INFN

ISTITUTO NAZIONALE DI FISICA NUCLEARE
Laboratori Nazionali di Frascati

FRASCATI PHYSICS SERIES

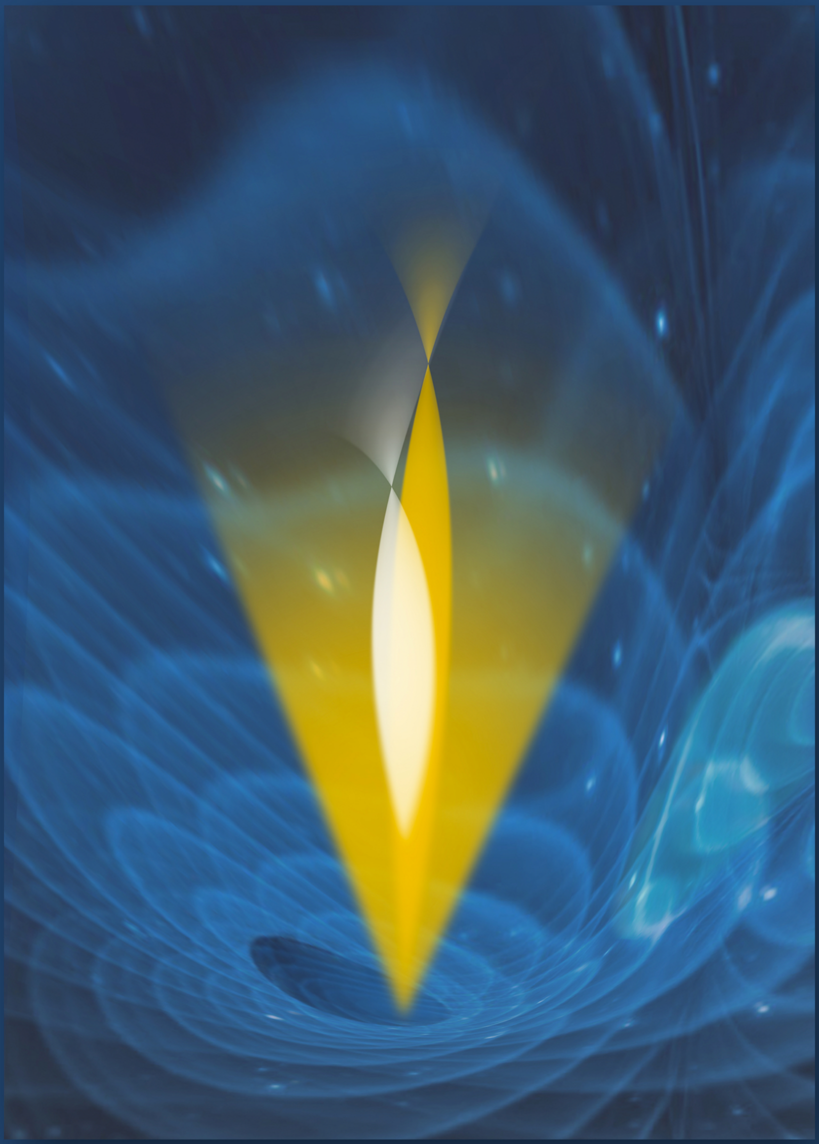

PHOTON 2019

International Conference on the Structure and the Interactions of the Photon

Satellite Workshop: Photon Physics and Simulation at Hadron Colliders

Editors:

G. Corcella, E. De Lucia, P. Di Nezza, P. Gianotti, G. Pancheri

FRASCATI PHYSICS SERIES

Series Editor
Paola Gianotti

Technical Editor
Lia Sabatini

Cover by Claudio Federici

Volume LXIX

Istituto Nazionale di Fisica Nucleare – Laboratori Nazionali di Frascati
Divisione Ricerca
Ufficio Biblioteca e Pubblicazioni
P.O. Box 13, I-00044 Frascati Roma Italy
email: library@lists.lnf.infn.it

ISBN 978-88-86409-70-4

PHOTON 2019

International Conference on the Structure and the Interactions of the Photon.

Satellite Workshop: Photon Physics and Simulation at Hadron Colliders.

June 2019

Frascati Physics Series Vol. 69 (2019)
PHOTON 2019 - International Conference on the Structure and the Interactions of the Photon
Jun 3-7, 2019

FOREWORD

PHOTON 2019, International Conference on the Structure and the Interactions of the Photon, including the 23rd International Workshop on Photon-Photon Collisions, and the International Workshop on High Energy Photon Colliders, was held at the INFN Frascati National Laboratories (Italy) from 3rd to 7th of June, 2019. The latest Photon conferences took place at CERN (2017), Novosibirsk (2015), Paris (2013), Spa (2011), Hamburg (2009), Paris (2007), Warsaw (2005), Frascati (2003), Ascona (2001), Freiburg (2000), Ambleside (1999), and Egmond aan Zee (1997).

In addition to a number of general talks and overviews of current options at future colliders, the topics of the conference included photon processes in electron-positron (e^+e^-), proton-proton (pp) and nucleus-nucleus (AA) collisions, presented in the four following sessions:

- Gamma-Hadron Collisions,
- Gamma-Gamma Collisions,
- Astrophysical Gamma,
- Gamma final states.

This year's edition also featured a two-day workshop on Photon Physics and Simulation at Hadron Colliders, focused on photon phenomenology at the LHC, with presentations during the last two days of the Conference, included in these Proceedings.

The conference was attended by 98 participants, with contributions from experimental groups, simulation collaborations and theoretical talks. A group of participants is included in the official Conference photograph shown Fig. 1. These Proceedings include 38 contributions submitted and presented in the four different sessions and in the satellite workshop.

Figure 1: *A group of Conference participants in front of the High Energy Building, INFN Frascati National Laboratories, credits C. Federici.*

1 History

PHOTON 2019 took place marking 60 years since the Frascati electro-synchrotron started operating in February 1959. Its building and completion led the country to became a full fledged member and early protagonist of the world-wide machine builders club, which, from mid-1970's, with the discovery of the J/Ψ, until 2012, with the discovery of the Higgs boson, provided the experimental confirmation of the Standard Model of elementary particles. It can be said that the Frascati synchrotron paved the way to the development of collider physics as it was through its construction that a generation of experimenters and technical staff was trained in the Frascati National Laboratories, providing the extraordinary expertise which, in 1960, would allow the construction of AdA, the first electron-positron collider. AdA had limited c.m. energy and luminosity, but was able to prove the feasibility of this type of machines, which were then successfully built through the following ten years.

A visual history of the construction of the 1100 MeV electron-synchrotron, in itself a first in the world in 1959 - albeit for a short time, can be found at the site `http://w3.lnf.infn.it/multimedia/index.php?/category/8`, where an extensive collection of period photographs follows the construction of the synchrotron from the scale model to the final commissioning. This series of photographs is also very instructive as it illustrates, in a relatively small scale, how a particle accelerator is built from its table-top model to the very end.

The construction of an Italian National Laboratory, already envisioned by Enrico Fermi in 1937, was decided in 1953, in the general context of the scientific and technological reconstruction of Europe, after the devastation of WWII. Thus, to accompany the creation of CERN, the construction of national laboratories where scientific and technological know-how would be developed was set in motion. In Italy Edoardo Amaldi and Gilberto Bernardini were the movers for the establishment of a laboratory which could house a modern particle accelerator. The chosen site was near the town of Frascati, on the vulcanic hills overlooking the city of Rome from the South-Est. The direction of such laboratory and the construction of an electro-synchrotron were given to Giorgio Salvini, who brought the task to completion in February 1959, leading a team of technicians, scientists and engineers shown in the left panel of Fig. 2, and which he had personally assembled with a talent search through all the Universities and Technical Schools of Italy. The completion of the task was proudly announced through a memo shown in the right hand side of Fig. 2.

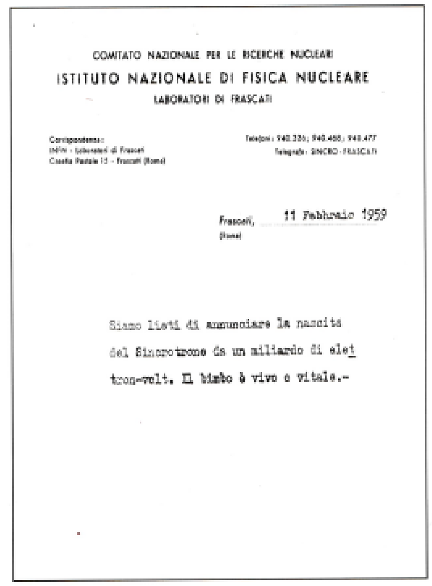

COMITATO NAZIONALE PER LE RICERCHE NUCLEARI
ISTITUTO NAZIONALE DI FISICA NUCLEARE
LABORATORI DI FRASCATI

Corrispondenza:
INFN - Laboratori di Frascati
Casella Postale 13 - Frascati (Roma)

Telegrafo: SINCRO-FRASCATI

Frascati, 11 Febbraio 1959
(Roma)

Siamo lieti di annunciare la nascita del Sincrotrone da un miliardo di elettron-volt. Il bimbo è vivo e vitale.-

Figure 2: *Left: a photo of the Frascati staff who built the electro-synchrotron, with G. Salvini, director of the Laboratories, at the center. Right: copy of the memo sent to announce the commissioning of the electro-synchrotron on February 1959: "We are pleased to announce the birth of the one billion electro-synchrotron. The baby is alive and well." See also A. Ghigo's talk at the Conference site,* `https://agenda.infn.it/event/16289/contributions/90052/`.

The synchrotron was a great success, widely followed by the Italian press. The president of the Republic inaugurated it and Giorgio Salvini, the director of the Laboratories, started a series of physics lectures in the National Television, inspiring a whole new generation of students to enrol and study physics. Visitors came from all over the world to see this machine, which had reached the highest energy in the world, with electrons accelerated up to 1.1 MeV. Fig. 3 shows a photograph of the synchrotron and Salvini with some visitors.

The electro-synchrotron jump-started the technological and scientific revolution which would bring the Frascati Laboratories to be the site where the first electron-positron collider was proposed and built. The operation of this new type of accelerators owed its feasibility to theory, on the one hand, and to highly specialized accelerator technology, such as vacuum technique, high frequency power sources, etc.. Both happened to be present in Frascati when AdA's proposal was put forward by Bruno Touschek [1], an Austrian born theoretical physicist, who had learnt the art of making electron accelerators from the Norwegian Rolf Widerøe, the inventor of betatron[2].

[1]E. Amaldi, *The Bruno Touschek legacy (Vienna 1921 - Innsbruck 1978)*, CERN Yellow Report CERN-81-19, 1981.

[2]R. Widerøe, *The infancy of particle accelerators. Life and work of Rolf Widerøe*, Ed. P. Waloschek,

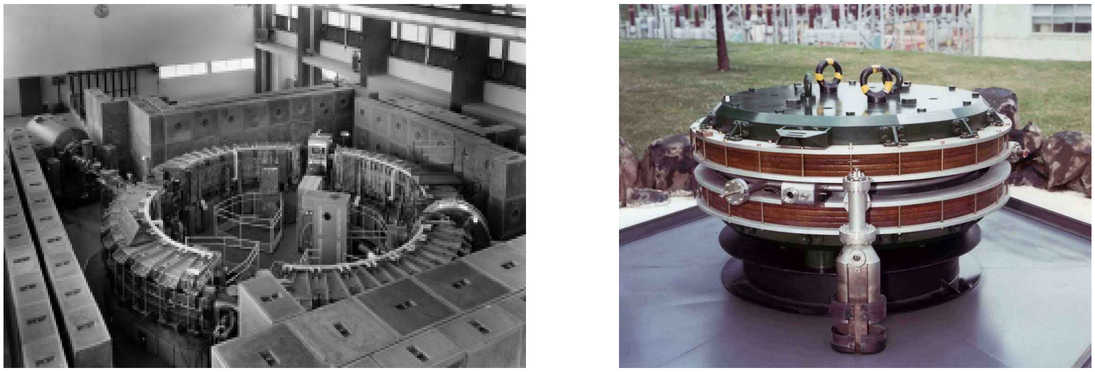

Figure 3: *Left, a photograph of the Frascati electro-sychrotron taken on April 4th 1959, a few month after its official commissioning day. Right, the first electron-positron collider AdA (Anello di Accumulazione).*

Meeetings to discuss the future of the Laboratory were held not long after the successful operation of the synchrotron. On February 17th 1960, Touschek proposed to build AdA, the actual project was then presented by Touschek in its details on March 7th, and financing was informally approved by the end of the month. From March to December, an exceptional team of scientists and technicians laboured to develop the extreme requirement for the machine to work, among them the characteristics of the magnet in which the AdA chamber would be embedded, insuring that electrons and positrons would travel along the same orbit in opposite directions, and the high vacuum, 10^{-9} *torr*, never reached before in a laboratory, required to keep the positron beam alive avoiding collisions with extraneous particles. The assembled team, which included C. Bernadini, G. F. Corazza, G. Ghigo and R. Querzoli, was driven by Touschek's absolute faith in the feasibility of AdA and succeeded in having the first electrons circulating in AdA in February 1961: the possibility of high-energy physics exploration with particle colliders was born. The full feasibility of AdA as proof-of-concept for electron positron colliders as exceptional tool for high-energy physics research took place in the following two years, when AdA was brought to France, at the Laboratoire de l'Accélérateur Linéair d'Orsay, where the Touschek effect was discovered [3].

Photons were the protagonists of postwar physics, with the development and exploitation of Quantum Elecrodynamics and the commissioning into operation of electron accelerators such as the electro-synchrotron which could produce powerful photon beams and, through them, study the proton structure. While these experiments exploited the photon in its virtual space-like aspect, Touschek proposed to exploit the time-like channel and study new particle production through annihilation channels such as shown in the left panel of Fig. 4, together with a photograph of Bruno Touschek, in 1955. Among the three processes indicated in this first draft, it is to be noticed the process $e^+e^- \to \gamma\gamma$, proposed as a monitor to calibrate the production of new particles. In the sketch of the proposal, the term *luminosity* to indicate the extraction of the interaction rate in storage rings may have made its first appearance.

When, at the end of 1960, it appeared clear that AdA would work, and that it could be possible to think ahead towards more powerful applications of the storage ring idea, Touschek prepared a short memo, in which he proposed to build ADONE, a bigger AdA, to reach an energy range allowing production of all known particles, 3 GeV in the electron-positron center of mass. The project was approved in its general lines in 1961 and experiments started in 1969, among them first observations of multi-hadronic

1994.

[3] C. Bernardini *et al.*, *Lifetime and beam size in a storage ring*, Phys. Rev. Letters 10, 407 (1963).

production, and of $\gamma\gamma$ collisions, which, together with Novosibirsk, sparked the beginning of the present Conference series.

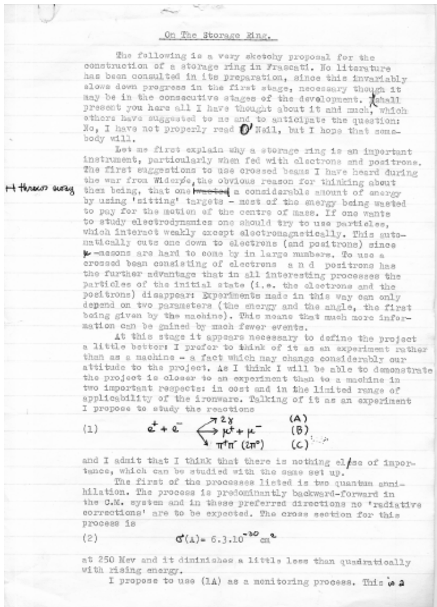

On The Storage Ring.

The following is a very sketchy proposal for the construction of a storage ring in Frascati. No literature has been consulted in its preparation, since this invariably slows down progress in the first stage, necessary though it may be in the consecutive stages of the development. I shall present you here all I have thought about it and much, which others have suggested to me and to anticipate the question: No, I have not properly read O'Neil, but I hope that somebody will.

Let me first explain why a storage ring is an important instrument, particularly when fed with electrons and positrons. The first suggestions to use crossed beams I have heard during the war from Widerøe, the obvious reason for thinking about them being, that one ~~wasted~~ + throws away a considerable amount of energy by using 'sitting' targets – most of the energy being wasted to pay for the motion of the centre of mass. If one wants to study electrodynamics one should try to use particles, which interact weakly except electromagnetically. This automatically cuts one down to electrons (and positrons) since μ-mesons are hard to come by in large numbers. To use a crossed beam consisting of electrons and positrons has the further advantage that in all interesting processes the particles of the initial state (i.e. the electrons and the positrons) disappear: Experiments made in this way can only depend on two parameters (the energy and the angle, the first being given by the machine). This means that much more information can be gained by much fewer events.

At this stage it appears necessary to define the project a little better: I prefer to think of it as an experiment rather than as a machine – a fact which may change considerably our attitude to the project. As I think I will be able to demonstrate the project is closer to an experiment than to a machine in two important respects: in cost and in the limited range of applicability of the ironware. Talking of it as an experiment I propose to study the reactions

$$(1) \qquad e^+ + e^- \rightarrow \begin{cases} 2\gamma & (A) \\ \mu^+ + \mu^- & (B) \\ \pi^+\pi^-\ (2\pi^0) & (C) \end{cases}$$

and I admit that I think that there is nothing else of importance, which can be studied with the same set up.

The first of the processes listed is two quantum annihilation. The process is predominantly backward-forward in the C.M. system and in these preferred directions no 'radiative corrections' are to be expected. The cross section for this process is

$$(2) \qquad \sigma(A) = 6.3.10^{-30}\ cm^2$$

at 250 Mev and it diminishes a little less than quadratically with rising energy.

I propose to use (1A) as a monitoring process. This is a

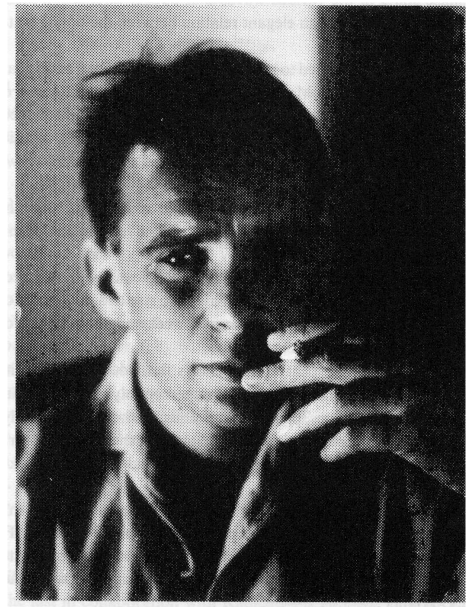

Figure 4: *At left, the first sketch of AdA's proposal, from a notebook dated 18.2.1960, and, at right a photograph of Bruno Touschek in 1955 from Amaldi's CERN Yellow Report CERN-81-19, 1981.*

We recall that this Conference is part of a series that was initiated in 1973 in Paris as *International Colloquium on Photon-Photon Collisions at Electron-Positron Storage Rings.* The first accelerators to produce results about $\gamma\gamma$ collisions were three electron-positron colliders, respectively from the USSR, Italy and France: VEPP2, ADONE and ACO. In Spring 1971, news from the experiments measuring photon-photon interactions in electron-positron colliders spread through the international particle physics community, first from Novosibirsk, followed by Frascati a few months later, and then from Orsay. It was therefore high time to have an International Colloquium on photon-photon collisions in electron-positron storage rings, as envisaged by the maximal authority on photon photon collision in Europe, Paul Kessler, the theoretician from the Collège de France in Paris, who, together with Jacques Parisi, led the gamma-gamma group of younger colleagues dedicated to this type of higher order QED calculations[4]. For a number of years the Conference mostly focused only on photon-photon, then the name underwent a change, including the structure and the interaction of the photon, as HERA's came up contributing to understand the hadronic nature of the photon.

After the closing of LEP, new results for gamma-gamma interactions at high energy were not available for quite some time. LHC has changed the picture, as photon processes at LHC are now being measured, promising in-depth studies of photon densities and hadronic structure. Even gamma-gamma elastic scattering, 60 years ago belonging only to theoretical studies, is now explored with hadron colliders and will be presented in these Proceedings.

[4] N. Arteaga-Romero, A. Jaccarini, P. Kessler (College de France), J. Parisi, *Photon-photon collisions, a new area of experimental investigation in high-energy physics*, Phys.Rev. **D3**, 1569 (1971).

2 Acknowledgements

We thank all the staff of LNF whose efforts were essential to the success of this edition of the Photon Conference. Particular thanks are due to the Research Division personnel and to Ms. Cristina D'Amato, who managed the secretariat with great dedication and efficiency.

3 Committees

International Advisory Committee

Stan Brodsky (SLAC), David d'Enterria (CERN), Albert de Roeck (CERN), Pasquale Di Nezza (INFN), Victor Fadin (INP), Alex Finch (Lancaster), Ilya Ginzburg (NSC), Jeffrey Gronberg (LNLL), Jack Gunion (UC Davis), Kaoru Hagiwara (KEK), Frederic Kapusta (LPNHE), Uri Karshon (Weizman Inst.) Michael Klasen (Münster), Eric Laenen (NIKEF), Michelangelo Mangano (CERN), Klaus Moening (DESY), Giulia Pancheri (INFN), Krzysztof Piotrzkowski (Louvain), Mariangela Settimo (SUBATECH, Nantes), Stefan Soldner-Rembold (Manchester), Tohru Takahashi (Hiroshima), Valery I. Telnov (NSK), Sadaharu Uehara (KEK), Mayda Velasco (Northwestern), Shin-Shan Yu (Taiwan), Fabian Zomer (LAL)

Local Organizing Committee

Gennaro Corcella, M. Cristina D'Amato (Secretary), Erika De Lucia, Pasquale Di Nezza (co-Chair), Paola Gianotti, Giulia Pancheri (co-Chair)

Conveners

* Gamma-Gamma Collisions

Lucian Harland-Lang (Oxford U.), Cheng-Ping Shen (Beihang U.)

* Gamma-Hadron Collisions

Aurore Courtoy (UNAM, Mexico City), Marco Battaglieri (INFN Genoa)

* Astrophysical Gamma

Alejandro Ibarra (TUM Munich), Luca Latronico (INFN Turin)

* Gamma Final States

German Sborlini (ICAS-UnSam, Buenos Aires & IFIC, Valencia), Mauro Raggi (Sapienza Rome U.)

* Future Perspectives

Gudrid Moortgat-Pick (DESY), David d'Enterria (CERN)

For the Workshop on Photon Physics and Simulation at Hadron Colliders:

Leonardo Carminati (Milan U.), Leandro Javier Cieri (Zurich U.), Giancarlo Ferrera (Milan U.)

CONFERENCES IN THIS SERIES

- **PHOTON 2019**
  International Conference on the Structure and Interactions of the Photon
  Including the 23rd International Workshop on Photon-Photon Collisions
  Frascati, Italy, 3-7 June 2019
- **PHOTON 2017**
  International Conference on the Structure and Interactions of the Photon
  Including the 22nd International Workshop on Photon-Photon Collisions and the International Workshop on High Energy Photon Colliders
  CERN, Switzerland, 22-26 May 2017
- **PHOTON 2015**
  International Conference on the Structure and Interactions of the Photon
  Including the 21st International Workshop on Photon-Photon Collisions and the International Workshop on High Energy Photon Colliders
  Novosibirsk, Russia, 15-19 June 2015
- **PHOTON 2013**
  International Conference on the Structure and Interactions of the Photon
  Including the 20th International Workshop on Photon-Photon Collisions and the —nternational Workshop on High Energy Physics and the High Energy Photon Linear Collider
  Paris, France, 20-24 May 2013
- **PHOTON 2011**
  International Conference on the Structure and Interactions of the Photon
  Including the 15th International Workshop on Photon-Photon Collisions
  SPA, Belgium, 22-27 May 2011
- **PHOTON 2009**
  International Conference on the Structure and Interactions of the Photon
  Including the 15th International Workshop on Photon-Photon Collisions
  Hamburg, Germany, 11-15 May 2009
- **PHOTON 2007**
  International Conference on the Structure and Interactions of the Photon
  Including the 15th International Workshop on Photon-Photon Collisions
  Paris, France, 9-13 July 2007
- **PHOTON 2005**
  International Conference on the Structure and Interactions of the Photon
  Including the 15th International Workshop on Photon-Photon Collisions
  Warsaw, Poland, 30 August-8 September 2005
- **PHOTON 2003**
  International Conference on the Structure and Interactions of the Photon
  Including the 15th International Workshop on Photon-Photon Collisions
  Frascati, Italy, 7-11 April 2003

- **PHOTON 2001**
  International Conference on the Structure and Interactions of the Photon
  Including the 14th International Workshop on Photon-Photon Collisions
  Ascona, Switzerland, 2-7 September 2001
- **PHOTON 2000**
  International Conference on the Structure and Interactions of the Photon
  Including the 13th International Workshop on Photon-Photon Collisions
  Ambleside, UK, 26-31 August 2000
- **PHOTON 99**
  International Conference on the Structure and Interactions of the Photon
  Including the 12th International Workshop on Photon-Photon Collisions
  Freiburg im Breisgau, Germany, 23-27 May 1999
- **PHOTON 97**
  International Conference on the Structure and Interactions of the Photon
  Including the 11th International Workshop on Photon-Photon Collisions
  Egmond aan Zee, The Netherlands, 10-15 May 1997
- **PHOTON 95**
  Incorporating the 10th International Workshop on Gamma-Gamma collisions and Related Processes
  Sheffield, UK, 8-13 April 1995
- **PHOTON-PHOTON 1992**
  9th International Workshop on Photon-Photon Collisions
  San Diego, USA, 22-26 March 1992
- 8th International Workshop on Photon-Photon Collisions
  Jerusalem, Israel, 24-28 April 1988
- 7th International Workshop on Photon-Photon Collisions
  Paris, France, 1-5 April 1986
- 6th International Workshop on Photon-Photon Collisions
  Lake Tahoe, USA,10-13 September 1984
- 5th International Workshop on Photon-Photon Collisions
  Aachen, Germany, 13-16 April 1983
- 4th International Workshop on Gamma-Gamma Interactions
  Paris, France, 6-9 April 1981
- International Workshop on Gamma-Gamma Collisions
  Amiens, France, 8-12 April 1980
- International Conference on Two Photon Interactions
  Lake Tahoe, USA, 30 August-1 September 1979
- International Colloquium on Photon-Photon Collisions in Electron-Positron Storage Rings
  Paris, France, 3-4 September 1973

CONTENTS

Frascati Physics Series Vol. 69 (2019)
PHOTON 2019 - International Conference on the Structure and the Interactions of the Photon
Jun 3-7, 2019

TOWARDS HARDWARE ACCELERATION FOR PARTON DENSITIES ESTIMATION

Stefano Carrazza
Juan Cruz-Martinez
Jesús Urtasun-Elizari
Emilio Villa
TIF Lab, Dipartimento di Fisica, Università degli Studi di Milano and INFN Sezione di Milano, Via Celoria 16, 20133, Milano, Italy

Abstract

In these proceedings we describe the computational challenges associated to the determination of parton distribution functions (PDFs). We compare the performance of the convolution of the parton distributions with matrix elements using different hardware instructions. We quantify and identify the most promising data-model configurations to increase PDF fitting performance in adapting the current code frameworks to hardware accelerators such as graphics processing units.

1 Introduction

The determination of parton distribution functions (PDFs) is a particular topic which strongly relies on three dynamic and time dependent factors: new experimental data, higher order theoretical predictions and fitting methodology. In this environment, there are two main tasks for PDF fitters such as the NNPDF collaboration [1–3], MMHT [4] or CTEQ [5]. The first task consists in maintaining and organizing a workflow which incrementally implements new features proposed by the respective experimental and theoretical communities. The second task of a PDF fitter corresponds to investigating new numerical and efficient approaches to PDF-fitting methodology. While the former relies almost exclusively on external groups and communities, the later is under full control of the PDF fitting collaborations, and in most cases it reflects the differences among them.

As a real example of the previous description we show in figure 1 a non-exhaustive timeline for PDF determinations with QED corrections. Since 2004 we have observed at least three different fitting approaches to the determination of the photon PDF, starting from the model-based approach where the photon PDF is modelled by an ad-hoc distribution [6, 7], then to a data-driven approach, where the photon PDF is extracted directly from data [8–10], and finally to a more precise procedure involving theory

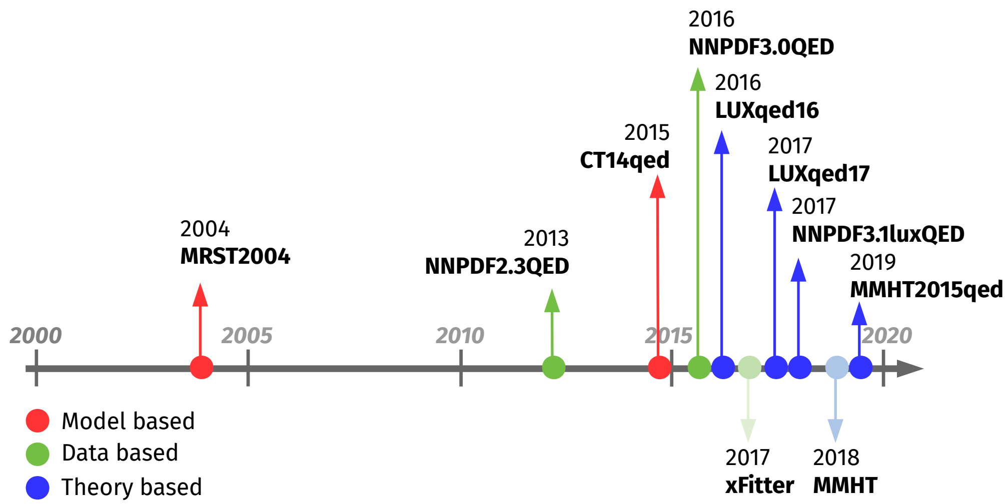

Figure 1: Illustrative timeline of PDF releases with QED corrections since 2004. Arrows pointing up refer to publications providing PDF sets as deliverables.

calculations [11–15]. Improvements in terms of PDF quality and physics content are however accompanied by a negative performance trend associated to longer fitting times and increased computational cost due to larger datasets and increasingly complex procedures. This in turn makes more difficult the task of developing and testing novel fitting procedures.

In this proceedings we describe a new approach to deal with this growing trend in computational resources for PDF determination. We focus our discussion on the new methodology recently presented by the N3PDF team within the NNPDF collaboration and summarized in the next paragraphs.

2 A deep learning approach to PDFs

In Ref. [16] we presented a new approach to PDF fits based on deep learning techniques in the context of the NNPDF methodology. We implement a new efficient computing framework based on graph generated models for PDF parametrization and gradient descent optimization called `n3fit`. The best model configuration is derived from a robust cross-validation mechanism through a hyperparametrization tune procedure. From a practical point of view the `n3fit` code uses Keras [17] and TensorFlow (TF) [18] as backends.

From a technical perspective, one of the most relevant achievements of `n3fit` is the reduction of computational time required to obtain PDF sets based on the NNPDF3.1 dataset [19]. In figure 2 we show the running time (in hours) required to fit 100 PDF replicas using the new `n3fit` fitting code and we compare it to the latest `NNPDF3.1` algorithm. On the left plot, we show a fit to DIS-only data, while in the right plot we have a global fit. In both cases we observe an improvement of between one to two orders of magnitude, *e.g.* the new `n3fit` code takes in average one hour to complete a global fit whereas the old code could take more than 40 hours. These improvements are partially due to the new minimizer (based on gradient descent instead of on genetic algorithms) in combination with multi-threading CPU calculations when executing the TensorFlow graph model.

The great performance improvement observed with `n3fit` suggests that we may find new code

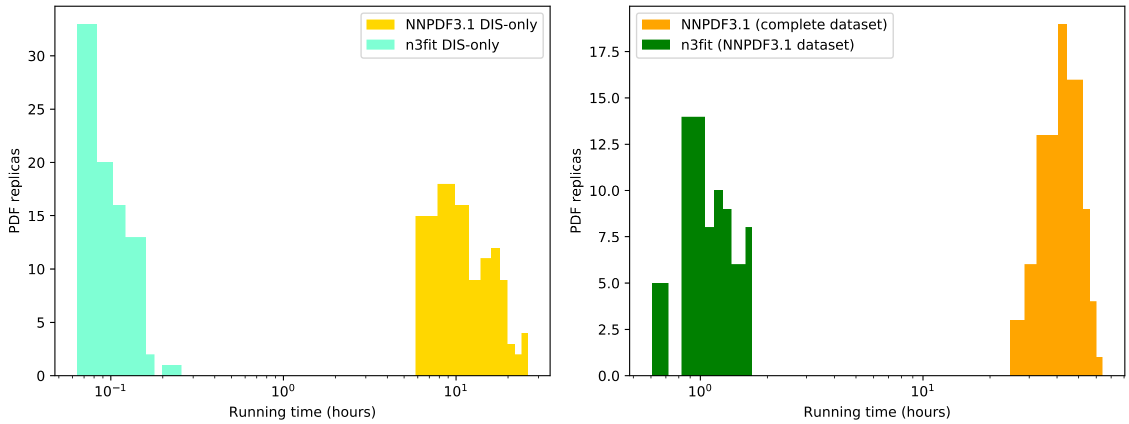

Figure 2: Fitting time distribution per replica PDF for NNPDF and `n3fit` codes for DIS-only (left plot) and global datasets (right plot).

strategies which take advantage of hardware acceleration. At this point, one may ask if it is possible to improve the performance from the default TensorFlow graph optimization for CPU and eventually use hardware accelerators such as graphic processing units (GPUs), field-programmable gate arrays (FPGAs), or tensor processing units (TPUs).

3 Hardware accelerating PDF determination

The first step towards faster fits consists in profiling the code and isolate the most time consuming operations during PDF fits. Fortunately, the answer to this question is simple and involves the computation of physical observables through PDF and matrix-element convolutions,

$$\sigma^N = \sum_{i,j,\alpha,\beta} f_\alpha(x_i) f_\beta(x_j) \mathrm{FK}^N_{ij\alpha\beta} \,, \tag{1}$$

where $f_\alpha(x_i)$ stands for the PDF of a particular flavor species α evaluated in the point x_i of the grid in x. $\mathrm{FK}^N_{ij\alpha\beta}$ is a Fast Kernel (FK) table which contains the information about the partonic cross section, following the description presented in [16]. In the case of hadronic observables the evaluation of predictions produces a vector of N observables, σ^N, by building a neural network that generates the PDFs sampling from a grid in x, representing the fractions of momenta that a particular parton could carry, and then convoluting the result with an FK table containing the partonic information.

Given that TensorFlow relies on symbolic computation and graph generation to represent a model, as a first step we investigate if the memory usage it requires is higher than the one needed by a custom code specialized in convolutions. We wrote a custom operator in `C++` for TensorFlow that performs the convolution and its corresponding gradient, directly without graph evaluations. In table 1 we cross-check the implementation by looking at examples of convolution and gradient computation for DIS and hadronic observables. The ratio between both implementations confirms excellent numerical agreement. The memory usage for the default TensorFlow implementation and the custom convolution code are shown in table 2. We observe a reduction of 3.2 GB and 5.9 GB of resident memory when using our custom operator, when loading all NNPDF3.1 hadronic and global data respectively. The reduction of memory usage is a great benefit because it gives the possibility to run PDF fits in consumer level hardware and,

		TensorFlow [pb]	Custom [pb]	Ratio
DIS	Convolution	1.9207904	1.9207904	1.0000000
		2.4611666	2.4611664	0.9999999
		1.3516952	1.3516952	1.0000000
	Gradient	1.8794115	1.8794115	1.0000000
		1.505316	1.505316	1.0000000
		2.866085	2.866085	1.0000000
Hadronic	Convolution	8.142365	8.142366	1.0000001
		8.947762	8.947762	1.0000000
		7.4513326	7.4513316	0.9999999
	Gradient	18.525095	18.525095	1.0000000
		19.182995	19.182993	0.9999999
		19.551006	19.551004	0.9999999

Table 1: Example of convolution and gradient computations for both DIS and hadronic observables. The ratio between TensorFlow and the custom computation confirms excellent numerical agreement.

		TensorFlow	Custom Convolution	Difference (TensorFlow - custom)
Hadronic	Virtual	17.7 GB	13.8 GB	3.9 GB
	RES	12.1 GB	8.39 GB	3.2 GB
Global	Virtual	23.5 GB	19.7 GB	3.8 GB
	RES	18.4 GB	12.5 GB	5.9 GB

Table 2: Memory usage after model generation and fit for both hadronic and global (DIS + hadronic) data.

most importantly, load all data in the limited memory space available in hardware accelerators. Once the memory saving is obtained, the performance can also be improved by multi-threading our custom operator on the CPU.

After the memory usage analysis, we carried out a time-performance comparison running the convolution both on CPU and GPU. Shifting the computation from CPU to GPU one can take advantage of the parallelization over the increased number of cores. In table 3 we show the overall running time for several examples of toy PDF and FK tables based on hadronic observables. The numbers include the computation time as well as the time required for the memory transfer to the GPU.

The performance of Advanced Vector Extensions (AVX) on CPU, OpenCL [20] on GPU and TF both on CPU and GPU are compared. As it is shown in table 3, AVX and TF running on CPU are faster up to a certain number of columns (for the FK table) or rows (for the PDFs matrices). Once the size of the operation is big enough, AVX is over one order of magnitude slower than OpenCL and even two orders of magnitude slower than TF on GPU. TF on CPU is more resilient than our AVX implementation and it is competitive with the GPU convolutions for a larger range of dimensions.

According to these results, for given dimensions of the FK table and the PDF matrices, it is convenient to carry out the PDF fits on GPU devices, parallelizing, for instance, over the different PDF replicas, allowing the fit of all of them to run simultaneously. In other words, hardware accelerators become competitive tools for PDF fitting once the penalty introduced by the memory transfer between devices is overcome.

Size of the PDF	Size of the FK Table	TensorFlow CPU [s]	AVX [s]	TensorFlow GPU [s]	OpenCL [s]
35721×1	8×35721	$1.10 \cdot 10^{-2}$	$1.57 \cdot 10^{-4}$	$4.14 \cdot 10^{-1}$	~ 1
$10^6 \times 1$	8×10^6	$4.70 \cdot 10^{-2}$	$5.00 \cdot 10^{-3}$	$4.49 \cdot 10^{-1}$	~ 1
$10^7 \times 1$	8×10^7	$3.20 \cdot 10^{-1}$	$5.70 \cdot 10^{-2}$	$7.90 \cdot 10^{-1}$	1.38
$10^8 \times 1$	8×10^8	2.90	$5.70 \cdot 10^{-1}$	4.21	6.31
35721×10^2	8×35721	$6.90 \cdot 10^{-2}$	$1.60 \cdot 10^{-2}$	$4.31 \cdot 10^{-1}$	~ 1
35721×10^3	8×35721	$1.50 \cdot 10^{-1}$	$1.69 \cdot 10^{-1}$	$5.63 \cdot 10^{-1}$	~ 1
35721×10^4	8×35721	1.12	1.73	1.92	1.76
$35721 \times 5 \cdot 10^4$	10×35721	5.33	8.93	7.83	5.80
35721×1	$10^2 \times 35721$	$2.80 \cdot 10^{-2}$	$2.43 \cdot 10^{-3}$	$4.24 \cdot 10^{-1}$	~ 1
35721×1	$10^3 \times 35721$	$1.30 \cdot 10^{-1}$	$2.14 \cdot 10^{-2}$	$5.60 \cdot 10^{-1}$	~ 1
35721×1	$10^4 \times 35721$	1.14	$2.16 \cdot 10^{-1}$	1.93	1.76
35721×10^2	$10^2 \times 35721$	$6.20 \cdot 10^{-2}$	$1.86 \cdot 10^{-1}$	$4.32 \cdot 10^{-1}$	~ 1
35721×10^3	$10^3 \times 35721$	$3.00 \cdot 10^{-1}$	21.61	$7.19 \cdot 10^{-1}$	5.25
$35721 \times 2 \cdot 10^3$	$2 \cdot 10^3 \times 35721$	5.06	86.13	1.38	15.97

Table 3: Time performances achieved with AVX, TensorFlow (both on CPU and GPU) and OpenCL for the given sizes of the FK table and the PDF matrix. In green it is highlighted the lowest value within each row. Time is given in seconds. The base FK table used in this comparison consists on 49 flavour combinations and an grid in x of size 27 (35721 elements in total).

4 Outlook and future developments

The results presented in this proceedings strongly suggest that PDF fits can benefit from hardware accelerators such as GPUs, and in future, FPGAs or TPUs thanks to the possibility of offloading the most time-consuming tasks to the accelerator. However, we should notice that, in order to achieve performance improvements, some precautions are required by defining the sizes of FK tables and the number of PDFs which we would like to convolute simultaneously. In future work we are planning to extend the `n3fit` framework to support GPU hardware.

Acknowledgements

S.C. acknowledges the NVIDIA Corporation for the donation of a Titan V GPU used for this research. S.C., J.CM. and J.U. are supported by the European Research Council under the European Unions Horizon 2020 research and innovation Programme (grant agreement number 740006). S.C. is supported by the UNIMI Linea 2A grant "New hardware for HEP".

References

1. R. Abdul Khalek *et al.* [NNPDF Collaboration], arXiv:1906.10698 [hep-ph].
2. R. Abdul Khalek *et al.* [NNPDF Collaboration], arXiv:1905.04311 [hep-ph].
3. R. D. Ball *et al.* [NNPDF Collaboration], Eur. Phys. J. C **78** (2018) no.5, 408 doi:10.1140/epjc/s10052-018-5897-7 [arXiv:1802.03398 [hep-ph]].

4. L. A. Harland-Lang, A. D. Martin, P. Motylinski and R. S. Thorne, Eur. Phys. J. C **75** (2015) no.5, 204 doi:10.1140/epjc/s10052-015-3397-6 [arXiv:1412.3989 [hep-ph]].

5. T. J. Hou *et al.*, arXiv:1908.11238 [hep-ph].

6. A. D. Martin, R. G. Roberts, W. J. Stirling and R. S. Thorne, Eur. Phys. J. C **39** (2005) 155 doi:10.1140/epjc/s2004-02088-7 [hep-ph/0411040].

7. C. Schmidt, J. Pumplin, D. Stump and C. P. Yuan, Phys. Rev. D **93** (2016) no.11, 114015 doi:10.1103/PhysRevD.93.114015 [arXiv:1509.02905 [hep-ph]].

8. R. D. Ball *et al.* [NNPDF Collaboration], Nucl. Phys. B **877** (2013) 290 doi:10.1016/j.nuclphysb.2013.10.010 [arXiv:1308.0598 [hep-ph]].

9. V. Bertone and S. Carrazza, PoS DIS **2016** (2016) 031 doi:10.22323/1.265.0031 [arXiv:1606.07130 [hep-ph]].

10. F. Giuli *et al.* [xFitter Developers' Team], Eur. Phys. J. C **77** (2017) no.6, 400 doi:10.1140/epjc/s10052-017-4931-5 [arXiv:1701.08553 [hep-ph]].

11. A. Manohar, P. Nason, G. P. Salam and G. Zanderighi, Phys. Rev. Lett. **117** (2016) no.24, 242002 doi:10.1103/PhysRevLett.117.242002 [arXiv:1607.04266 [hep-ph]].

12. A. V. Manohar, P. Nason, G. P. Salam and G. Zanderighi, JHEP **1712** (2017) 046 doi:10.1007/JHEP12(2017)046 [arXiv:1708.01256 [hep-ph]].

13. V. Bertone *et al.* [NNPDF Collaboration], SciPost Phys. **5** (2018) no.1, 008 doi:10.21468/SciPostPhys.5.1.008 [arXiv:1712.07053 [hep-ph]].

14. R. Nathvani, R. Thorne, L. Harland-Lang and A. Martin, PoS DIS **2018** (2018) 029 doi:10.22323/1.316.0029 [arXiv:1807.07846 [hep-ph]].

15. L. A. Harland-Lang, A. D. Martin, R. Nathvani and R. S. Thorne, arXiv:1907.02750 [hep-ph].

16. S. Carrazza and J. Cruz-Martinez, Eur. Phys. J. C **79** (2019) no.8, 676 doi:10.1140/epjc/s10052-019-7197-2 [arXiv:1907.05075 [hep-ph]].

17. F. Chollet et al., *Keras* (2015) `https://keras.io`

18. M. Abadi, A. Agarwal, P. Barham, E. Brevdo, Z. Chen, C. Citro, G.S. Corrado, A. Davis, J. Dean, M. Devin et al., *TensorFlow: Large-scale machine learning on heterogeneous systems* (2015), software available from tensorflow.org, `http://tensorflow.org/`

19. R. D. Ball *et al.* [NNPDF Collaboration], Eur. Phys. J. C **77** (2017) no.10, 663 doi:10.1140/epjc/s10052-017-5199-5 [arXiv:1706.00428 [hep-ph]].

20. J.E. Stone, D. Gohara and G. Shi, Computing in Science Engineering (2010) 12 no.3, 66 doi:10.1109/MCSE.2010.69

Frascati Physics Series Vol. 69 (2019)
PHOTON 2019 - International Conference on the Structure and the Interactions of the Photon
Jun 3-7, 2019

PERSPECTIVES OF PHOTON PHYSICS AT FUTURE COLLIDERS

Michael Klasen
Institut für Theoretische Physik, Westfälische Wilhelms-Universität Münster,
Wilhelm-Klemm-Straße 9, 48149 Münster, Germany

Abstract

We review current results on physics with photons at the LHC and discuss realistic perspectives of photon physics at future colliders. In particular, we focus on Standard Model (SM) measurements with photons at the upcoming high-luminosity and a possible high-energy LHC as well as jet measurements at an Electron-Ion Collider (EIC) to be constructed either at BNL or at JLAB and their potential to constrain nuclear parton densities. We also discuss future searches for physics beyond the SM with photons in the high-luminosity phase of the LHC.

1 Motivation

Discussions of physics with photons at future colliders have traditionally focused on photon-photon interactions at linear e^+e^- colliders like TESLA or CLIC [1], their low background, and their superior precision for measurements of the properties of the Higgs boson or yet to be discovered physics beyond the Standard Model (BSM) like supersymmetric (SUSY) particles [2]. Unfortunately, the Large Hadron Collider (LHC) has so far produced no evidence for BSM particles, so that the decision to build a linear collider is still pending. The LHC has, however, produced many interesting events with single photons, diphotons and photons plus jets in pp, pPb and PbPb collisions. They have led to a large variety of results ranging from the discovery of the Higgs boson [3] to the determination of the effective temperature of the quark-gluon plasma (QGP) [4]. In addition, ultraperipheral collisions (UPCs) at the LHC have led to measurements of exclusive dilepton and quarkonium photoproduction and even the discovery of light-by-light scattering [5].

The upgrade of the LHC to its high-luminosity (HL) phase is currently underway, and plans are being made to install stronger magnets in the existing tunnel for a high-energy (HE) machine with

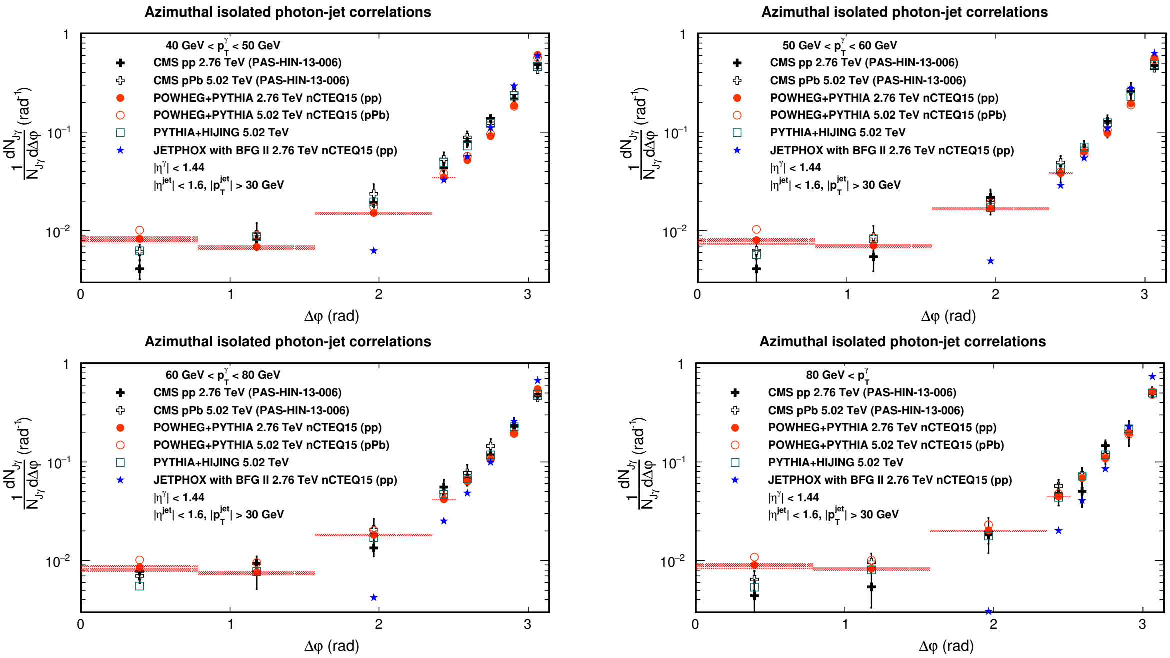

Figure 1: Relative azimuthal angle distributions of jets and photons in pp (open circles) and pPb (full circles) collisions at the LHC with a centre-of-mass energy per nucleon of $\sqrt{s_{NN}} = 2.76$ and 5.02 TeV, respectively, in four different bins of photon transverse momentum. CMS 2013 data (black) [9] are compared to predictions in LO with PYTHIA+HIJING (green), NLO with JETPHOX (blue), and NLO+PS with POWHEG+PYTHIA (red) [8].

increased centre-of-mass energy from 13 TeV to as much as 27 TeV in pp, 17 TeV in pPb and 10.6 TeV in PbPb collisions. At the same time, plans to supplement the existing Relativistic Heavy Ion Collider (RHIC) at BNL with a circular electron accelerator or to extend the upgraded Continuous Electron Beam Accelerator Facility (CEBAF) at JLAB with a heavy-ion storage ring are well advanced. In both incarnations, such an Electron Ion Collider (EIC) would greatly improve our knowledge of nuclear matter, probed by the real and virtual photons emitted from the electron. It is therefore appropriate to explore the impact of photons in these realistic future collider scenarios, i.e. on future SM studies at the HL/HE LHC and EIC as well as on BSM physics at the HL LHC.

2 SM physics with photons at the high-luminosity and high-energy LHC

2.1 Prompt photon production

The LHC collaborations ALICE, ATLAS and CMS have recently produced a large variety of interesting prompt photon results in pp, pPb and PbPb collisions at different centre-of-mass energies [6]. They serve to test both the QCD and electroweak sectors of the SM, to constrain the parton distribution functions (PDFs) in protons and nuclei and to determine the background for new physics searches with ever higher precision. To fully exploit the potential of these data, one must not only cleanly eliminate the meson decay contributions by data-driven subtraction methods or with infrared-safe photon isolation criteria, but also confront them with theoretical calculations at next-to-next-to-leading order (NNLO) or using resummation and parton showers (PS) [7].

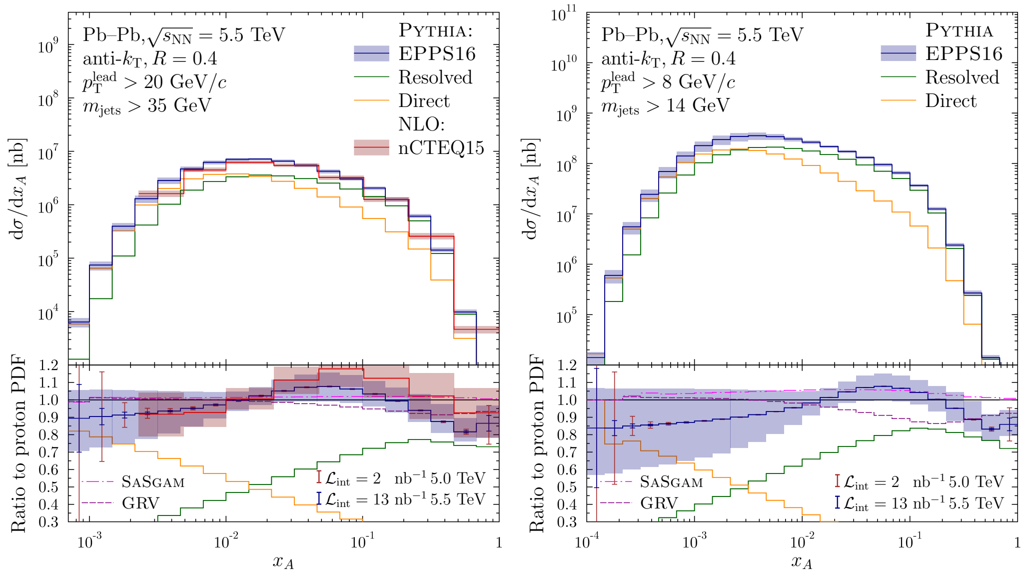

Figure 2: Photonuclear dijet cross sections in ultraperipheral PbPb collisions at $\sqrt{s_{NN}} = 5.5$ TeV with leading jet p_T cut of 20 GeV (left) and 8 GeV (right). Results based on PYTHIA simulations are calculated with EPPS16 nuclear modification (blue), and the contributions from resolved (green) and direct (orange) photons are separately shown. Ratio plots show also results with different photon PDF sets and the expected statistical uncertainties corresponding to the LHC (brown) and the Run 3 and Run 4 (dark blue) luminosities. Corresponding results based on NLO calculations for PbPb collisions at $\sqrt{s_{NN}} = 5.02$ TeV with nCTEQ15 nPDFs (red) are shown for a leading jet p_T cut of 20 GeV [14].

This has recently been demonstrated with the implementation of photons in POWHEG, the successful application of this new calculation to data from ALICE, ATLAS and CMS, and predictions for future measurements with LHCb [8]. An observable that is particularly sensitive to QCD effects beyond next-to-leading order (NLO) is the photon-jet azimuthal distribution, measured by CMS in pp and pPb collisions [9] and shown in Fig. 1. While the NLO JETPHOX calculations do not describe the data below $\Delta\phi_{J\gamma} = 2\pi/3$, as the maximum number of jets is limited to two at NLO, the POWHEG predictions agree quite well with the data. No significant energy dependence or cold nuclear effects are yet observed with this limited statistics, making its increase at the HL LHC mandatory. Exploratory studies have shown that the HL LHC can reach inclusive photon and diphoton transverse momenta up to 5 and 2 TeV, i.e. far beyond the current reach of about 1 TeV and 700 GeV, respectively [10], and the kinematic reach would obviously be even larger at a HE LHC. This would give access to proton PDFs over a wide range in x from less than 10^{-4} to 0.5.

2.2 Inclusive photoproduction

Collisions with an tagged proton or intact nucleus, small multiplicity, or a substantial rapidity gap on one side of the detector system allow for the identification of inclusive photoproduction events and thus the use of the LHC as a photon-proton or photon-ion collider. The inclusive photoproduction of dijets has already been observed by ATLAS [11] and been shown to agree well with NLO QCD calculations [12]. With a future precision of 5%, these data would have the potential to reduce the nuclear PDF uncertainties at $x \sim 10^{-3}$ by more than a factor of two [13].

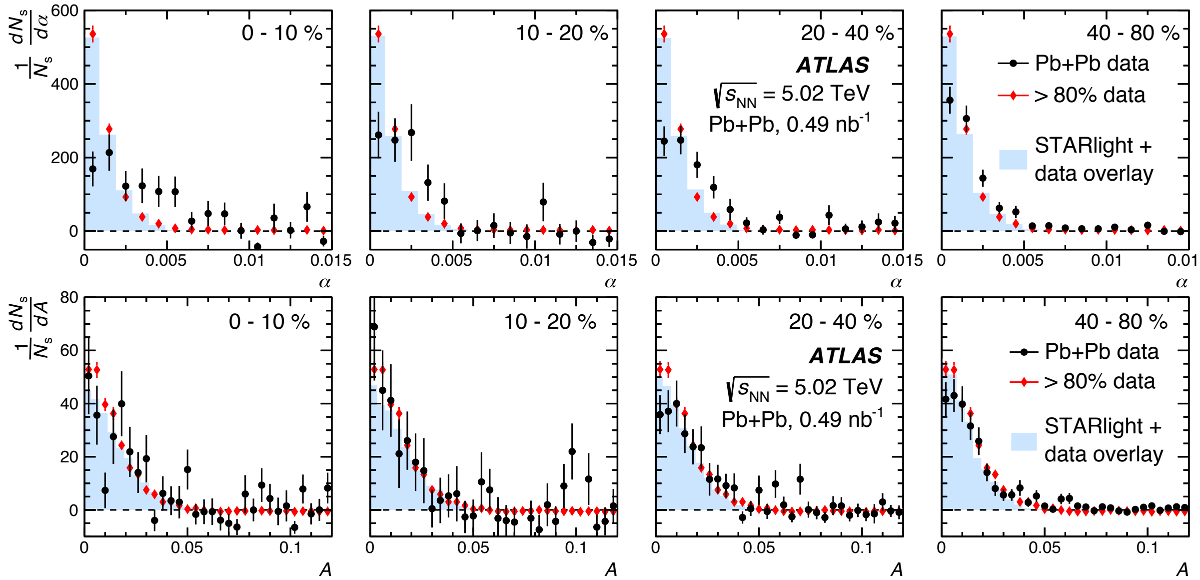

Figure 3: Acoplanarity (α, top) and lepton energy imbalance (A, bottom) as a function of centrality for dimuon pairs with pair mass above 10 GeV observed in the ATLAS detector [15].

Fig. 2 extends these studies to the HL LHC with centre-of-mass energy per nucleon of 5.5 TeV [14]. The reach in x_A would be extended by an order of magnitude and the reduction of the uncertainty could reach a factor of four, if the jet p_T is not only measured above 20 GeV (left), but down to 8 GeV (right). In the complementary kinematic region of large x_A, the small-x region of the photon PDFs, on which little is known, could be probed. This is demonstrated with two different parametrisations, which are still both consistent with current data. At a HE-LHC, the centre-of-mass energies per nucleon of 10.6 TeV in PbPb and 17 TeV in pPb collisions would obviously allow to extend the kinematic reach even further, and open heavy-quark production would shed further light on the heavy quark content of protons and nuclei.

2.3 Exclusive photoproduction

When the hadrons on both sides are tagged or separated from the central hard event by a rapidity gap, photon-photon collisions lead to the exclusive production of lepton pairs. Their theoretical description within QED requires not only accounting for form factors, but also absorptive effects from the additional scattering of pomerons. Muon pairs with invariant mass above 10 GeV have been measured by ATLAS not only in ultraperipheral, but also peripheral and central PbPb collisions [15]. For the former, the leptons are mostly back-to-back as expected, and the acoplanarity distribution (α, top) and lepton energy imbalance (A, bottom) agree well with the STARlight predictions in Fig. 3. In central collisions, however, the acoplanarity peak at $\alpha = 0$ is reduced, indicating electromagnetic rescattering in the created QGP, while A remains unchanged, so that no significant energy loss through bremsstrahlung occurs. A HL LHC would reach higher invariant masses of up to 100 GeV, corresponding to photon-photon interactions near or even in the nuclei and thus increased interactions with the QGP and/or nuclear magnetic field [14]. At low mass, electron pairs are expected to interact more than muons or even taus. At higher order, also the production of four leptons can be considered [16].

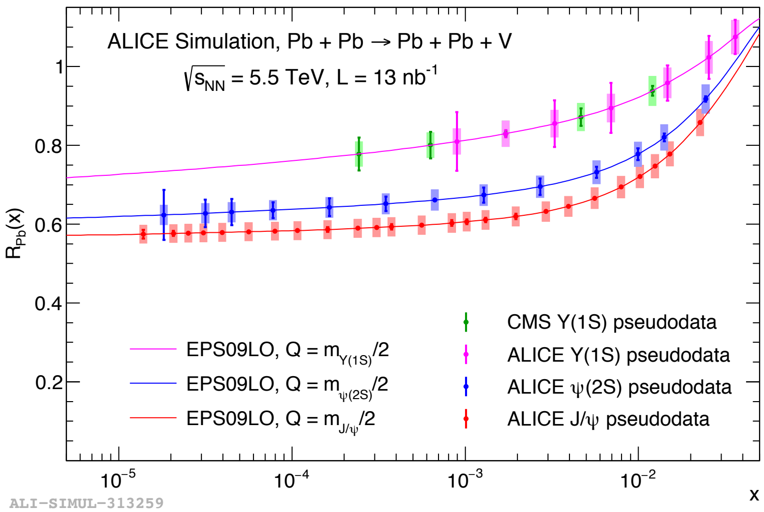

Figure 4: Pseudodata projections for the nuclear suppression factor by ALICE and CMS measured with the photoproduction of three heavy vector mesons in PbPb ultraperipheral collisions. The pseudodata points are derived from EPS09-based photoproduction cross section projections [19].

Exclusive dijets are produced not only by photon, but also pomeron interactions and could therefore in the future be used to determine for the first time diffractive PDFs of nuclei [17]. At leading twist, diffraction can be related to nuclear shadowing, and more evidence for the latter has recently been obtained by ALICE from exclusive production of ρ, J/ψ and ψ' mesons [18]. Their different masses would allow to probe in the future more precisely the evolution of nuclear shadowing with Q^2 [19], as is shown in Fig. 4. It assumes that a total integrated luminosity of 13 nb^{-1} could be reached with yearly PbPb runs at the end of 2021-2023 and 2027-2029. These measurements would be particularly interesting in view of establishing deviations from DGLAP and evidence for BFKL evolution or saturation effects. Finally, the production of W-boson and top-quark pairs as well as Higgs bosons would allow to search more precisely for deviations of the electroweak couplings of these particles from the SM predictions [20].

3 SM physics with photons at the EIC

Plans to build an EIC at either BNL or JLAB are well advanced. It would allow for a diverse physics program impacting nuclear, heavy-ion and high-energy physics with studies of sea quark and gluon distributions, their spins and the emergence of nuclear properties through electromagnetic, i.e. photon, interactions [21].

As two examples, we discuss here the impact of inclusive jets and dijets in deep-inelastic scattering (DIS) and photoproduction on the determination of nuclear PDFs. Both processes have recently been calculated at approximate NNLO (aNNLO). Fig. 5 (top left) shows the p_T distribution of inclusive jets in DIS for different EIC designs, where the eRHIC option with a 21 GeV electron and a 100 GeV per nucleon ion beam allows to reach p_T values of up to 35 GeV. The K factors as a function of p_T at NLO and aNNLO (top right) are very similar, which demonstrates good perturbative stability, as are the Q^2 evolutions predicted by nCTEQ15 and EPPS16 (bottom left), both based on DGLAP. However, the two nuclear PDF uncertainty bands do not overlap at x below 10^{-3}, demonstrating the potential EIC impact [22].

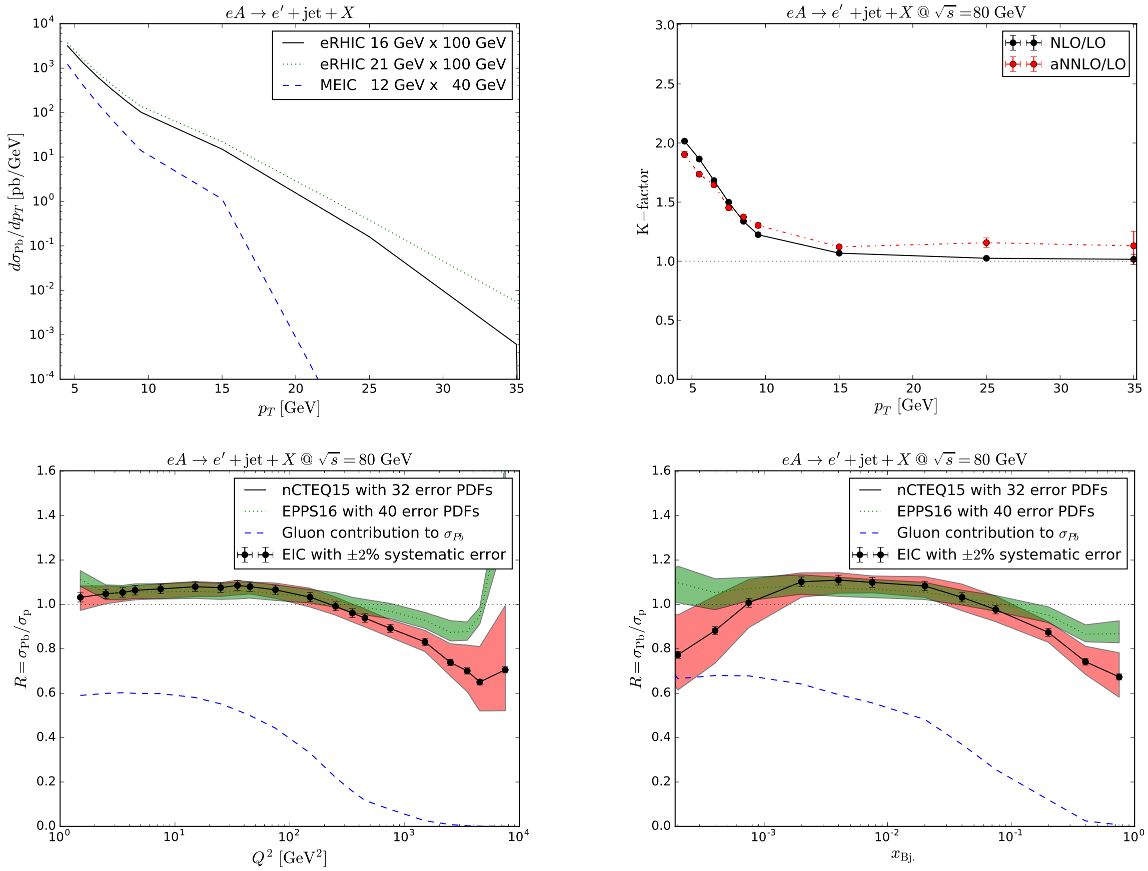

Figure 5: Top left: p_T distribution of inclusive jets in DIS for different EIC designs. Top right: K factors as a function of p_T at NLO and aNNLO. Bottom left: Q^2 evolution as predicted by nCTEQ15 and EPPS16. Bottom right: Nuclear PDF uncertainty bands as a function of the reconstructed parton momentum fraction in the lead nucleus [22].

Similar distributions are shown in Fig. 6 for dijet photoproduction. The average p_T of the two jets is now restricted to below 20 GeV (top left). The nuclear modifications depend strongly on the nucleus (top right) and are modelled differently by nCTEQ15 and EPPS16 (bottom left). Due to the reduced partonic centre-of-mass energy, the nuclear PDF sensitivity does not extend to x values below 10^{-2}. An alternative process to constrain in particular the nuclear gluon density would again be exclusive quarkonium photoproduction, also at the EIC [24].

4 BSM physics with photons at the high-luminosity and high-energy LHC

The searches for anomalous couplings of weak gauge or Higgs bosons and top quarks already briefly mentioned above are mainly motivated by the hierarchy and unification problems of the SM. Another major motivation for BSM searches comes from dark matter (DM), whose existence is largely undisputed, but whose nature remains to be elucidated. We therefore focus in this section on three different DM candidates, all related to photons: weakly interacting massive particles (WIMPs) and their future constraints from monophotons; prospects for dark photon searches; and axion-like particle (ALP) contributions to

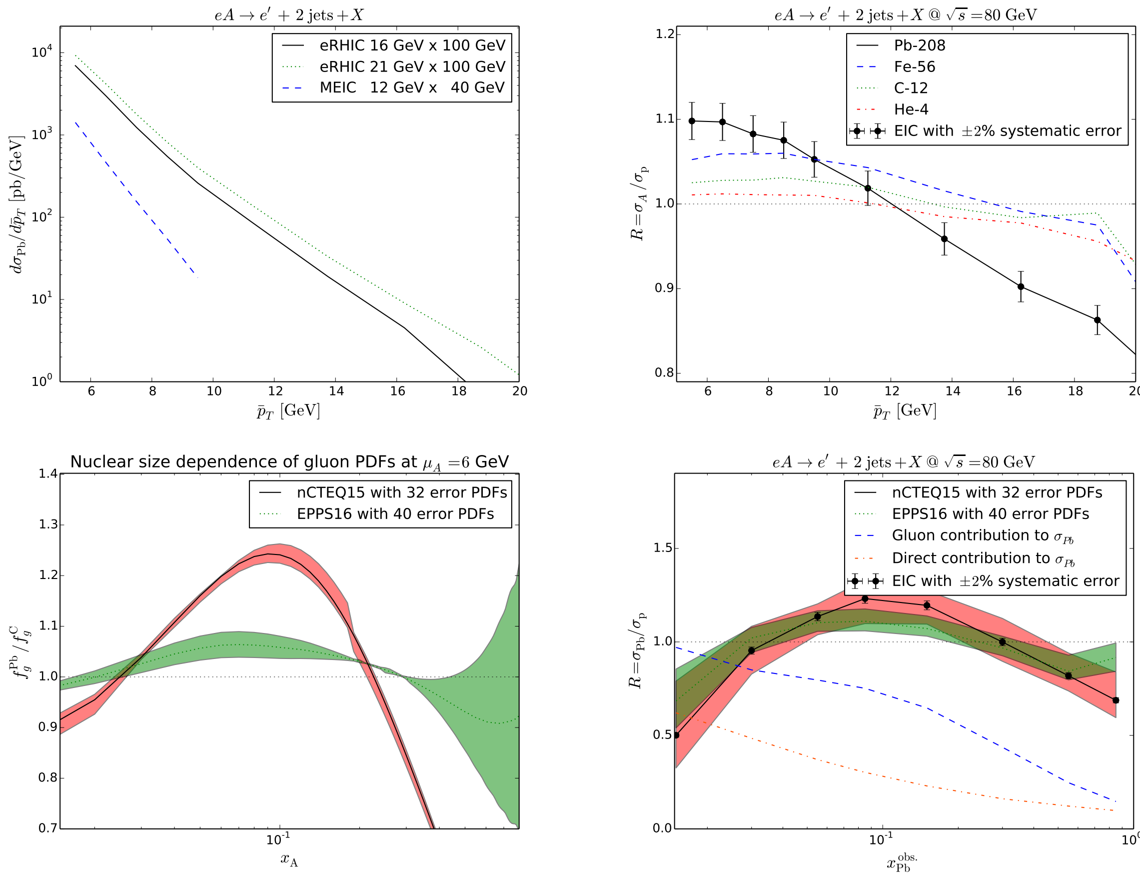

Figure 6: Top left: Average p_T distribution of dijets in photoproduction for different EIC designs. Top right: Ratios of different nuclear over free proton cross sections as a function of p_T. Bottom left: Ratios of lead and carbon over free proton cross sections as a function of the reconstructed parton momentum fraction in the nucleus. Bottom right: Nuclear PDF uncertainty bands as a function of the reconstructed parton momentum fraction in the lead nucleus [23].

light-by-light scattering at the HL and HE LHC.

4.1 Future dark matter searches with monophotons

Monophoton searches at the LHC can be competitive to other processes, in particular monojets, when DM is part of an electroweak multiplet, since photons induce a different dependence on model parameters like the electroweak representation or mass splitting. For example, DM is part of a Higgsino triplet $(\chi^0, \chi^\pm)$ in anomaly-meadiated SUSY-breaking models [25] and of scalar or fermion singlets, doublets or triplets in minimal DM models with a SM mediator [26]. Even when DM and its charged multiplet partners have identical masses at tree-level, electroweak loops always induce a mass splitting, e.g. of $m_{\chi^\pm} = m_{\chi^0} + 165$ MeV for triplets, making the neutral partner lighter and the heavier ones decay like $\chi^\pm \to \chi^0$ + soft charged pions. The DM particle itself is usually stabilised against decay into SM particles by assuming a symmetry like R parity or $U(1)_{B-L}$. The observed thermal relic density can then be obtained for masses $m_{\chi^0} \leq 3$ TeV.

DM signals from monophoton searches at the LHC not only have to be discriminated against the

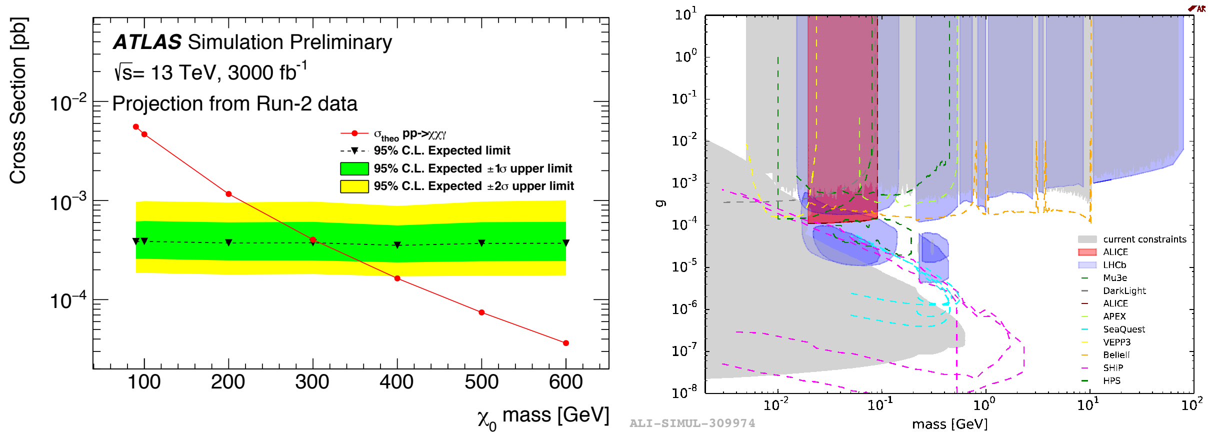

Figure 7: Left: Expected upper limits at 95% C.L. on the production cross section of dark matter as a function of χ^0 mass in monophoton final state. Results are shown for an integrated luminosity of 3 ab^{-1}. The red line shows the theoretical cross section [27]. Right: 90% of C.L. constrained by ALICE and LHCb in HL LHC era. Constraints by ALICE are based on 6 pb^{-1}, 0.3 pb^{-1}, 10 nb^{-1}, 0.3 pb^{-1}, and 3 nb^{-1} of pp, pPb, and PbPb collisions at 0.5 T, and pPb and PbPb collisions at 0.2 T and by LHCb are based on 15 fb^{-1} [14].

irreducible background $Z(\rightarrow \nu\nu)\gamma$, but also from W/Z + jet, tt, ZZ/WW production with electrons or jets faking photons. This is achieved with kinematic cuts like $\not{E}_T > 150$ GeV, $p_T^\gamma > 150$ GeV, $|\eta^\gamma| < 2.37$ and a photon isolation from $\not{E}_T$ by $\Delta\phi > 0.4$. The LHC can then set stronger limits than LEP ($m_{\chi^0} > 90$ GeV) as shown in Fig. 7 (left), reaching DM masses of 300 GeV for an integrated luminosity of 3 ab^{-1} [27].

4.2 Prospects for dark photon searches

Dark photons A' from $U(1)$ gauge extensions of the SM have gained in popularity as the neutral SM gauge and Higgs bosons have become more and more excluded as mediators for WIMP DM in the mass region between a few GeV and TeV. They are parametrised by their mass, obtained from spontaneous symmetry breaking, and mixing parameter g with the SM photon. ALICE has searched for possible decays of $\pi^0 \rightarrow \gamma A'(\rightarrow e^+e^-)$ by examining the electron-positron invariant mass between 20 and 90 MeV in pp and pPb collisions, and its upgrade will greatly improve the efficiency. LHCb has good capabilities to measure muon pairs and thus searches for prompt-like and long-lived dark photons produced in pp collisions and decaying as $A' \rightarrow \mu^+\mu^-$ between 214 MeV and 70 GeV. As Fig. 7 (right) shows, smaller couplings g will be probed at the HL LHC, closing potentially the wedge in the 20 to 90 MeV mass region.

4.3 BSM perspectives in light-by-light scattering

The Z^4 enhancement in PbPb collisions at the LHC leads to $4.5 \cdot 10^7$ more initial photon pairs than obtained in pp collisions, albeit with a softer spectrum. Both ATLAS and CMS have now observed light-by-light scattering, i.e. the exclusive production of diphotons in UPCs. Apart from model-independent searches for anomalous couplings, they allow in particular to hunt for light ALPs, which arise in solutions of the strong CP problem, through the identification of invariant mass peaks that should be clearly visible above the steeply falling QED background, as shown in Fig. 8 (left). Upper limits can then be set on the product of the production cross section and decay branching ratio into diphotons. In Fig. 8

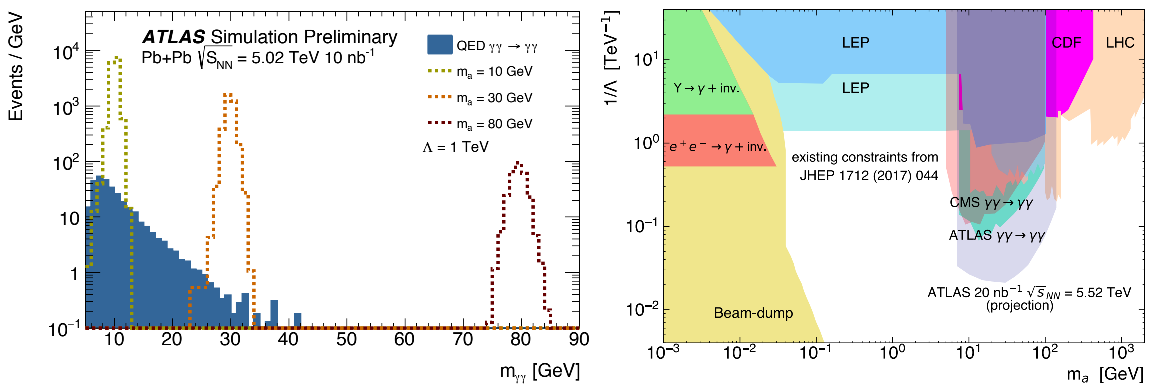

Figure 8: Left: Mass distribution for the ALP signal shown for three values of the ALP mass $m_a = 10$, 30 and 80 GeV (in red). Also shown (in blue) is the QED background. All ALP mass points are generated with $\Lambda = 1$ TeV. Right: Compilation of exclusion limits obtained by different experiments. In light grey, the projected ATLAS 20 nb^{-1} limit at $\sqrt{s_{NN}} = 5.52$ TeV is presented [14].

(right), existing exclusion limits on the ALP coupling, $1/\Lambda$, as a function of its mass m_a are supplemented with a projected ATLAS limit derived from PbPb collisions at 5.52 TeV. These results demonstrate that heavy-ion collisions have unique sensitivity to ALP searches in the mass range from 7 to 140 GeV [14].

Many theory papers have been written on BSM searches at photon colliders around the year 2000 in view of the expected construction of a linear collider. As an example, the testable scale of non-commutative QED was foreseen at $\Lambda_{\rm NC} \geq 1.5\sqrt{s_{ee}}$. However, a few studies have also been performed for the LHC. E.g., monopole mass limits of $M < n \cdot 7.4$, 10.5, 19 TeV were expected for $J_M = 0$, 1/2, 1 at $\sqrt{s_{pp}} = 7$ TeV, and limits of $M_{\rm Pl.} \geq 5...8\sqrt{s_{\gamma\gamma}}$ were predicted for $D = 4 + (2, 4, 6)$ dimensional gravity. With the discovery of the Higgs boson, "unparticles" are now all but forgotten [14]. Nevertheless, contrary to standard SUSY LHC searches, photon-photon collisions might indeed be sensitive in compressed mass scenarios where e.g. $m_{\tilde{l}} \sim m_{\tilde{\chi}^0}$ [28]. The search for monopoles with ATLAS, where the current mass limit from 13 TeV pp collisions lies at 2 TeV, has proven more difficult than expected, but is ongoing with the dedicated experiment MoEDAL and might in the future benefit from the enhanced photon luminosity in PbPb collisions [29].

5 Conclusion

In conclusion, we have tried to present a balanced and realistic discussion of physics opportunities with photons at future colliders, focusing on either existing (SM) physics at colliders with advanced funding decisions or on BSM physics at the HL LHC already under construction. Particular attention has been spent on the unique potential of photons to constrain the proton and in particular nuclear structure at high energy as well as their role in searches for DM, currently our clearest hint of physics beyond the SM. Photons also play of course a crucial role in astroparticle physics, but a thorough discussion of cosmic rays, the upcoming CTA telescope and the fascinating perspectives of multimessenger astronomy were unfortunately beyond the scope of this conference summary talk.

Acknowledgements

The author thanks the organisers of the Photon 2019 conference for the kind invitation, V. Guzey, T. Jezo, C. Klein-Bösing, F. König, K. Kovarik, H. Poppenborg, J. Potthoff and J.P. Wessels for their collaboration, and the DFG for financial support under contract KL 1266/9-1.

References

1. B. Badelek *et al.* [ECFA/DESY Photon Collider Working Group], Int. J. Mod. Phys. A **19** (2004) 5097; E. Accomando *et al.* [CLIC Physics Working Group], hep-ph/0412251.

2. S. Berge, M. Klasen and Y. Umeda, Phys. Rev. D **63** (2001) 035003; S. Berge and M. Klasen, Phys. Rev. D **66** (2002) 115014; S. Berge and M. Klasen, Eur. Phys. J. C **30** (2003) 123.

3. G. Aad *et al.* [ATLAS Collaboration], Phys. Lett. B **716** (2012) 1; S. Chatrchyan *et al.* [CMS Collaboration], Phys. Lett. B **716** (2012) 30

4. M. Klasen, C. Klein-Bösing, F. König and J. P. Wessels, JHEP **1310** (2013) 119.

5. M. Aaboud *et al.* [ATLAS Collaboration], Nature Phys. **13** (2017) 852; A. M. Sirunyan *et al.* [CMS Collaboration], arXiv:1810.04602 [hep-ex].

6. E. Masson [ALICE Collaboration], N. Saoulidou [on behalf of the ATLAS and CMS Collaborations], talks at this conference.

7. L. Cieri, M. Höfer, F. Siegert, talks at this conference.

8. T. Jezo, M. Klasen, F. König, JHEP **1611** (2016) 033; M. Klasen, C. Klein-Bösing, H. Poppenborg, JHEP **1803** (2018) 081.

9. CMS Collaboration, CMS-PAS-HIN-13-006.

10. P. Azzi *et al.*, *Standard Model Physics at the HL-LHC and HE-LHC*, arXiv:1902.04070 [hep-ph].

11. ATLAS Collaboration, *Photo-nuclear dijet production in ultra-peripheral Pb+Pb collisions*, ATLAS-CONF-2017-011.

12. V. Guzey and M. Klasen, Phys. Rev. C (in press), arXiv:1811.10236 [hep-ph].

13. V. Guzey and M. Klasen, Eur. Phys. J. C **79** (2019) 396.

14. Z. Citron *et al.*, *Future physics opportunities for high-density QCD at the LHC with heavy-ion and proton beams*, arXiv:1812.06772 [hep-ph].

15. M. Aaboud *et al.* [ATLAS Collaboration], Phys. Rev. Lett. **121** (2018) 212301.

16. F. Kapusta, talk at this conference.

17. V. Guzey and M. Klasen, JHEP **1604** (2016) 158.

18. M. Broz [ALICE], talk at this conference. See also I. Babiarz, V. Goncalvez, V. Khoze and A. Luszczak, talks at this conference.

19. V. Guzey, E. Kryshen, M. Strikman and M. Zhalov, Phys. Lett. B **726** (2013) 290.

20. D. d'Enterria, A. Szczurek, talks at this conference.

21. E. Aschenauer, talk at this conference.

22. M. Klasen, K. Kovarik and J. Potthoff, Phys. Rev. D **95** (2017) 094013.

23. M. Klasen and K. Kovarik, Phys. Rev. D **97** (2018) 114013.

24. A. Luszczak, talk at this conference.

25. B. Fuks, B. Herrmann and M. Klasen, Phys. Rev. D **86** (2012) 015002; B. Fuks, M. Klasen, S. Schmiemann and M. Sunder, Eur. Phys. J. C **78** (2018) 209.

26. M. Klasen, C. E. Yaguna and J. D. Ruiz-Alvarez, Phys. Rev. D **87** (2013) 075025; M. Klasen, C. E. Yaguna, J. D. Ruiz-Alvarez, D. Restrepo and O. Zapata, JCAP **1304** (2013) 044; S. Esch, M. Klasen, D. R. Lamprea and C. E. Yaguna, Eur. Phys. J. C **78** (2018) 88; S. Esch, M. Klasen and C. E. Yaguna, JHEP **1810** (2018) 055; J. Fiaschi, M. Klasen and S. May, JHEP **1905** (2019) 015.

27. X. Cid Vidal *et al.*, *Beyond the Standard Model Physics at the HL-LHC and HE-LHC*, arXiv:1812.07831 [hep-ph].

28. L. Harland-Lang, talk at this conference.

29. O. Gould, talk at this conference.

Frascati Physics Series Vol. 69 (2019)
PHOTON 2019 - International Conference on the Structure and the Interactions of the Photon
Jun 3-7, 2019

LIGHT DARK STATES ASSOCIATED WITH PHOTONS: AN OVERVIEW OF DARK-SECTOR PHYSICS

Xiaoyong Chu
Institute of High Energy Physics, Austrian Academy of Sciences, Nikolsdorfer Gasse 18, 1050 Vienna, Austria

Abstract

There exist various motivations to consider a dark sector beyond the Standard Model (SM). Such a dark sector is assumed to be coupled very weakly, or even feebly, to the known particles via a portal, but can contain its own interaction structures and provide possible candidates for dark matter. Due to its suppressed coupling to the SM particles, the phenomenology and detection strategies of this dark sector are dramatically different from those of conventional new physics, such as TeV supersymmetry and technicolor scenarios. These proceedings review recent developments on dark sector physics, especially those connected to the photon directly, including dark photon, dark current, and axion-like particles.

1 Introduction

With the discovery of the Higgs boson at LHC [1, 2], the SM sector becomes eventually self-contained, to some extent. Still, there are several mysteries in the observed Universe that hint at underlying theories of particle physics. One of them is the existence of dark matter, whose gravitational effects have been observed undoubtedly [3]. Nevertheless, so far the search for non-gravitational signatures of dark matter has not led to any convincingly positive results in direct and indirect searches, and in collider experiments. Thus, a new paradigm of new physics (or more specifically, dark matter physics) has gradually emerged, which suggests that, in contrast to conventional theories beyond SM, there may exist dark particles that only couple to the SM sector via very weaker portals, and, at the same time, are able to explain the dark matter and other observed anomalies. This paradigm is now referred to as dark sector physics.

The possibility of a dark sector is motivated by both UV-scale theories such as string landscape [4], and experimental observations more than just dark matter. For instance, two well-known scenarios in dark sector physics predict the dark photon via kinetic mixing [5] and the axion [6, 7, 8, 9]. The former has attracted a lot of attention recently, because not only such a mixing is theoretically interesting [10], but it can also explain the long-standing anomaly in the muonic anomalous magnetic dipole moment, i.e. the $(g-2)_\mu$, measurements [11, 12], and be relevant for the hypothesis of strongly self-interacting dark matter too [13, 14]. As for the axion, while it was originally proposed to explain the strong CP problem, similar Nambu–Goldstone bosons, namely axion-like particles, can obviously appear in general theories that contain a broken global $U(1)$ symmetry, and thus couple to photons at loop level (or via anomalies).

This review mainly covers the two scenarios of dark sector physics, focusing on recent studies of possible signatures and experimental constraints raised from their interactions with the SM photon.

2 Gauge kinetic mixing

As stated above, a dark photon A', corresponding to a broken or unbroken dark gauge group $U(1)_D$, can couple to the SM photon via gauge kinetic mixing. Without further specifying the UV origin of this mixing, one writes the relevant interactions in terms of renomalizable operators at low energies:

$$\mathcal{L}_D \ni -\frac{\epsilon}{4} F^{\mu\nu} F'_{\mu\nu} + i g_D A'_\mu J^\mu_D \,, \tag{1}$$

where J^μ_D represents the content of dark current, such as $\bar{\chi}\gamma^\mu\chi$ from a dark fermion that charged under the gauge group. Here the kinetic mixing parameter ϵ quantifies the portal interaction between the SM and dark sectors, and thus can be constrained by experimental results once the masses of dark sector particles (A', χ, ...) are presumed.

2.1 Dark photons

In the case of a massive dark photon, A' may be produced on-shell via the photon mixing in laboratory experiments with interacting SM fermions,[1] making its search straightforward, and the signatures depend on its lifetime and decay products. If $m_{A'}$ is above tens of GeV, it only appears in high-energy colliders, such as LEP and LHC, similarly to TeV new physics. In contrast, if A' is lighter than several GeV, low-energy experiments at intensity frontier, including BaBar, Belle and fixed-target experiments, are more competitive, as effectively much larger integrated luminosities can be achieved in these experiments.

If the dark photon decays visibly, which is the case if $m_{A'}$ is larger than twice the electron mass and it does not decay into dark currents with sufficiently high branching fractions, one strategy is to record its decay products ($e^\pm$, $\mu^\pm$, ..) and then reconstruct the invariant mass of the dark photon. The other one is to look for displaced vertices in far-end detectors. In the opposite case, where A' decays invisibly into dark currents or neutrinos, one can only look for the excess of missing-energy/momentum events, especially in electron-beam experiments. Since no signals have been found, all the experiments put constraints on the dark photon, requiring the mixing parameter $\epsilon \leq 10^{-3}$ for $m_{A'}$ below several GeV, as summarized in recent reviews [15, 16, 17].

To address the $(g-2)_\mu$ anomaly, the parameter region of interest is the one corresponding to dark-photon masses in the MeV–GeV range with values of the mixing parameter ϵ around 10^{-3}–10^{-2}. At present, this parameter region has been mostly excluded by NA48/2 if A' decays visibly [18], or by the BaBar results if A' decays invisibly [19]. However, it is still too early to conclude that the dark photon cannot solve the $(g-2)_\mu$ anomaly any more, due to several potential caveats. One is that the bounds on visible mode rely on the reconstruction of the invariant-mass peak under the assumption of two-body decays of the dark photon. More importantly, those experimental bounds can only directly constrain

[1] If $m_{A'} \ll 1\,\mathrm{GeV}$, A' is also produced in supernova and stars, leading to very stringent constraints.

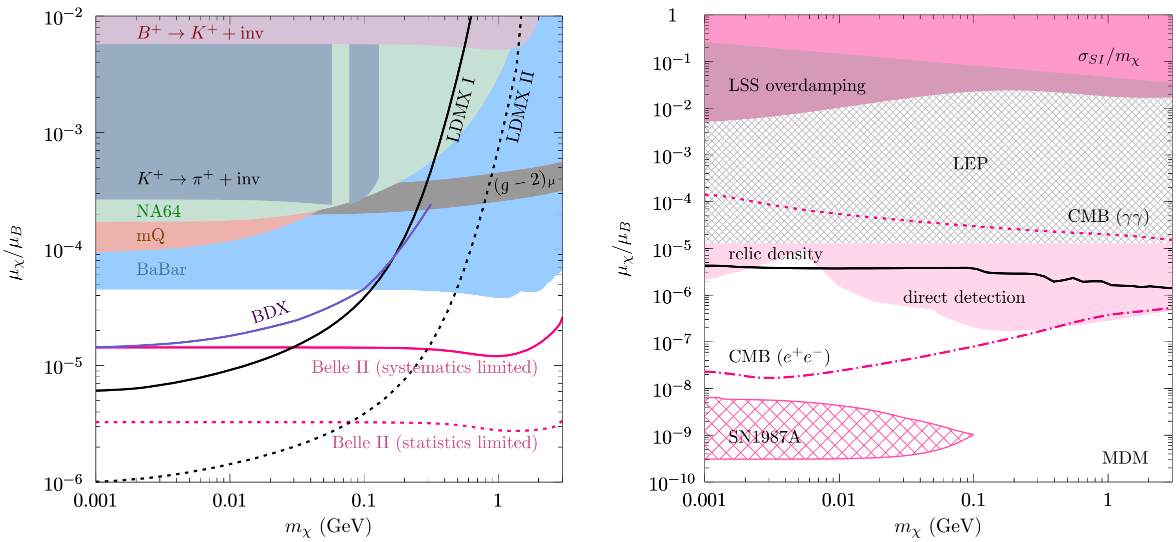

Figure 1: *Constraints on the MDM coupling of a dark Dirac fermion from intensity frontier experiments including projections (left), and conventional dark matter searches and cosmology (right). See* [25].

the coupling of A' to electrons (or nucleons), instead of its coupling to muons. See e.g. [20, 21] and references therein for quantitative studies.

2.2 Dark currents coupled to a photon

If the dark photon is massless, the detection strategy changes conceptually. The reason is that when all four gauge degrees of freedom in the mixing are degenerate/massless, one can always define the two degrees of freedom that couple to the charged SM particles as the *physical* photon so that the *physical* dark photon does not couple to the electromagnetic (EM) current. As a result, it becomes extremely difficult to search for the dark photon, which is not produced directly. Instead, one has to look for signatures caused by dark currents, whose coupling to the EM current is unaffected by the degeneracy.

The associated EM interactions for a Dirac fermion in dark sector can be written as

$$\mathcal{L}_D \ni \epsilon e\, \bar{\chi}\gamma^\mu \chi A_\mu + \frac{1}{2}\mu_\chi\, \bar{\chi}\sigma^{\mu\nu}\chi F_{\mu\nu} + \frac{i}{2}d_\chi\, \bar{\chi}\sigma^{\mu\nu}\gamma^5\chi F_{\mu\nu} - a_\chi\, \bar{\chi}\gamma^\mu\gamma^5\chi\partial^\nu F_{\mu\nu} + b_\chi\, \bar{\chi}\gamma^\mu\chi\partial^\nu F_{\mu\nu}\,. \tag{2}$$

The first term, corresponding to a milli-charged interaction, has been repeatedly studied in the literature. While its current bound is about $\epsilon \leq 10^{-3}$ for $m_\chi \leq 0.1\,\text{GeV}$ and becomes much weaker for higher m_χ, this will be improved by one to two orders of magnitude in future experiments [22, 23]. Meanwhile, we have updated the bounds on other EM form factors, among which the magnetic dipole moment (MDM) interactions is shown in Fig. 1 as an example; for more details see [24, 25, 26].

If the particle content of the dark current contains the dark matter, more constraints can be derived from direct detection experiments, and cosmological/astrophysical considerations, such as observables from large scale structure (LSS). These are also taken into account in right panel of Fig. 1. Notice that the bounds from CMB [27] and Voyager 1 [28] (also the benchmark relic density lines) only apply to symmetric dark matter, as they assume (thermal) pair annihilation.

3 Axion-Like Particles (ALPs)

While the coupling of an axion (or, more generally, an ALP) to photons is model-dependent [29, 30, 31], the interaction term is usually parametrized by a dimension-five operator

$$\mathcal{L}_D \ni -\frac{g_{a\gamma\gamma}}{4} a F^{\mu\nu} \tilde{F}_{\mu\nu} \equiv g_{a\gamma\gamma} a \, \mathbf{E} \cdot \mathbf{B} \,, \tag{3}$$

where $g_{a\gamma\gamma}$ is expressed in GeV^{-1} . To be conservative, here we only consider this interaction term while neglecting any other possible portals that connect the ALPs with the SM sector. Again, the detection strategies depend on the mass of the presumed ALP particle.

3.1 Very heavy ALPs

Similarly to the case of dark photons, a heavy ALP can be searched for in both high-energy colliders and low-energy intensity-frontier experiments. One can measure either the decay production of the ALP or the missing energy, according to whether it decays visibly or invisibly. Two main differences from dark-photon searches are the following: 1) There exists a three-photon channel in electron/proton collider searches [32, 33], e.g., $e^- e^+ \to \gamma + a^* \to \gamma\gamma\gamma$; 2) The ALP can be produced in light-by-light scattering with ultra-peripheral nucleus collisions, significantly enhancing its production rate [34]. Therefore, while fixed-target experiments dominate the bounds for m_a from MeV to GeV [35], heavy-ion experiments most likely will provide the strongest bounds for m_a above several GeV, probing the value of $g_{a\gamma\gamma}$ below 10^{-5}–$10^{-4}\,\mathrm{GeV}^{-1}$ in the future.

3.2 Ultra-light ALPs

The most appealing signatures of ultra-light ALPs are the photons from axion-photon conversion in magnetic fields, as suggested by Eq. (3). The source axion can be generated from a high-power laser [36] inside the Sun (i.e. helioscope) or from the dark matter axions of the Milky Way halo (i.e. haloscope). Moreover, the conversion of photons into axions also affects the polarization and energy spectra of cosmic photons during their propagation to our detectors from, e.g., the last scattering surface and high-redshift astrophysical objects. This detection strategy, together with stellar cooling arguments, in general provide the strongest constraints on m_a below MeV or so. For detailed discussions, see e.g. [37, 38, 39].

4 Sterile Neutrino, Light Scalar and More

Another very interesting dark-sector scenario is the so-called ν minimal SM [40]. It introduces three sterile neutrinos of keV–GeV mass scales that mix with the SM neutrinos via tiny mixing angles, in order to obtain both dark matter relic abundance and baryon asymmetry of the Universe. Such sterile neutrinos can decay into a SM neutrino and a photon, leading to observable signatures, although their lifetime can be extremely long due to the small mixing angles.

Also, a light scalar s can couple to the EM field strength via a dimension-five operator $sF^{\mu\nu}F_{\mu\nu}$. The consequence of this operator is the rescaling of the fine-structure constant, whose signatures can be looked for in precision experiments, such as atomic clocks [41].

Before the conclusion, it is worth emphasizing that while this review focuses on the coupling of the dark sector particles to the photon, other kinds of interactions are also very interesting and may lead to different experimental signatures, such as those of Higgs portal, fermionic portal and so on. For more general reviews on dark-sector physics, see [42, 16, 17].

5 Conclusions

There exist both theoretical motivations and experimental hints of the existence of a dark sector, which may contain the dark matter particle and its own interaction structures, but only couples to the SM sector via a very weak portal. Such a new paradigm leads to new detection strategies for physics beyond SM. This paper reviews the recent progress of the experimental efforts to probe the interaction of this dark sector with photons. It shows that astrophysical observations and intensity-frontier experiments can play a very important role in probing light dark particles. Moreover, multi-messenger observations will be crucial to exclude or confirm dark-sector physics scenarios in the future.

6 Acknowledgements

The author thanks Jui-Lin Kuo, Josef Pradler, and Lukas Semmelrock for collaboration on some of the work presented here, which is supported by the New Frontiers program of the Austrian Academy of Sciences. The author also thanks the organizers of PHOTON 2019 for the invitation to give an overview on dark-sector physics.

References

1. G. Aad *et al.* [ATLAS Collaboration], Phys. Lett. B **716** (2012) 1 [arXiv:1207.7214 [hep-ex]].

2. S. Chatrchyan *et al.* [CMS Collaboration], Phys. Lett. B **716** (2012) 30 [arXiv:1207.7235 [hep-ex]].

3. P. A. R. Ade *et al.* [Planck Collaboration], Astron. Astrophys. **571**, A16 (2014) [arXiv:1303.5076 [astro-ph.CO]].

4. J. Halverson and P. Langacker, PoS TASI **2017** (2018) 019 [arXiv:1801.03503 [hep-th]].

5. B. Holdom, Phys. Lett. **166B** (1986) 196.

6. R. D. Peccei and H. R. Quinn, Phys. Rev. Lett. **38** (1977) 1440.

7. R. D. Peccei and H. R. Quinn, Phys. Rev. D **16** (1977) 1791.

8. S. Weinberg, Phys. Rev. Lett. **40** (1978) 223.

9. F. Wilczek, Phys. Rev. Lett. **40** (1978) 279.

10. K. R. Dienes, C. F. Kolda and J. March-Russell, Nucl. Phys. B **492** (1997) 104 [hep-ph/9610479].

11. P. Fayet, Phys. Rev. D **75** (2007) 115017 [hep-ph/0702176 [hep-ph]].

12. M. Pospelov, Phys. Rev. D **80** (2009) 095002 [arXiv:0811.1030 [hep-ph]].

13. N. Arkani-Hamed, D. P. Finkbeiner, T. R. Slatyer and N. Weiner, Phys. Rev. D **79** (2009) 015014 [arXiv:0810.0713 [hep-ph]].

14. J. L. Feng, M. Kaplinghat and H. B. Yu, Phys. Rev. Lett. **104** (2010) 151301 [arXiv:0911.0422 [hep-ph]].

15. M. Raggi and V. Kozhuharov, Riv. Nuovo Cim. **38** (2015) no.10, 449.

16. J. Alexander *et al.*, arXiv:1608.08632 [hep-ph].

17. J. Beacham *et al.*, arXiv:1901.09966 [hep-ex].

18. M. Raggi [NA48/2 and NA62 Collaborations], J. Phys. Conf. Ser. **800** (2017) no.1, 012032.

19. J. P. Lees *et al.* [BaBar Collaboration], Phys. Rev. Lett. **119** (2017) no.13, 131804 [arXiv:1702.03327 [hep-ex]].

20. C. Y. Chen, M. Pospelov and Y. M. Zhong, Phys. Rev. D **95** (2017) no.11, 115005 [arXiv:1701.07437 [hep-ph]].

21. G. Mohlabeng, Phys. Rev. D **99** (2019) no.11, 115001 [arXiv:1902.05075 [hep-ph]].

22. A. Haas, C. S. Hill, E. Izaguirre and I. Yavin, Phys. Lett. B **746** (2015) 117 [arXiv:1410.6816 [hep-ph]].

23. A. Ball *et al.*, arXiv:1607.04669 [physics.ins-det].

24. K. Sigurdson, M. Doran, A. Kurylov, R. R. Caldwell and M. Kamionkowski, Phys. Rev. D **70** (2004) 083501 Erratum: [Phys. Rev. D **73** (2006) 089903] [astro-ph/0406355].

25. X. Chu, J. Pradler and L. Semmelrock, Phys. Rev. D **99** (2019) no.1, 015040 [arXiv:1811.04095 [hep-ph]].

26. X. Chu, J. L. Kuo, J. Pradler and L. Semmelrock, arXiv:1908.00553 [hep-ph].

27. M. Boudaud, J. Lavalle and P. Salati, Phys. Rev. Lett. **119** (2017) no.2, 021103 [arXiv:1612.07698 [astro-ph.HE]].

28. H. Liu, T. R. Slatyer and J. Zavala, Phys. Rev. D **94** (2016) no.6, 063507 [arXiv:1604.02457 [astro-ph.CO]].

29. W. A. Bardeen and S.-H. H. Tye, Phys. Lett. **74B** (1978) 229.

30. D. B. Kaplan, Nucl. Phys. B **260** (1985) 215.

31. M. Srednicki, Nucl. Phys. B **260** (1985) 689.

32. K. Mimasu and V. Sanz, JHEP **1506** (2015) 173 [arXiv:1409.4792 [hep-ph]].

33. J. Jaeckel and M. Spannowsky, Phys. Lett. B **753** (2016) 482 [arXiv:1509.00476 [hep-ph]].

34. S. Knapen, T. Lin, H. K. Lou and T. Melia, Phys. Rev. Lett. **118** (2017) no.17, 171801 [arXiv:1607.06083 [hep-ph]].

35. L. Harland-Lang, J. Jaeckel and M. Spannowsky, Phys. Lett. B **793** (2019) 281 [arXiv:1902.04878 [hep-ph]].

36. S. L. Adler, J. Gamboa, F. Mendez and J. Lopez-Sarrion, Annals Phys. **323** (2008) 2851 [arXiv:0801.4739 [hep-ph]].

37. G. G. Raffelt, Lect. Notes Phys. **741** (2008) 51 [hep-ph/0611350].

38. D. J. E. Marsh, Phys. Rept. **643** (2016) 1 [arXiv:1510.07633 [astro-ph.CO]].

39. P. W. Graham, I. G. Irastorza, S. K. Lamoreaux, A. Lindner and K. A. van Bibber, Ann. Rev. Nucl. Part. Sci. **65** (2015) 485 [arXiv:1602.00039 [hep-ex]].

40. T. Asaka, S. Blanchet and M. Shaposhnikov, Phys. Lett. B **631** (2005) 151 [hep-ph/0503065].

41. M. S. Safronova, D. Budker, D. DeMille, D. F. J. Kimball, A. Derevianko and C. W. Clark, Rev. Mod. Phys. **90** (2018) no.2, 025008 [arXiv:1710.01833 [physics.atom-ph]].

42. S. Alekhin *et al.*, Rept. Prog. Phys. **79** (2016) no.12, 124201 [arXiv:1504.04855 [hep-ph]].

Frascati Physics Series Vol. 69 (2019)
PHOTON 2019 - International Conference on the Structure and the Interactions of the Photon
Jun 3-7, 2019

Status of the anomalous magnetic moment of the muon in spring 2019

Pere Masjuan
Grup de Física Teòrica, Departament de Física, Universitat Autònoma de Barcelona
Institut de Física d'Altes Energies (IFAE), The Barcelona Institute of Science and Technology (BIST)
Campus UAB, E-08193 Bellaterra (Barcelona), Spain

Abstract

In this talk we review the recent progress on the numerical determination of the Hadronic contributions to the anomalous magnetic moment of the muon. Special emphasis on the role of experimental data on the light-by-light scattering is made.

1 Introduction

The anomalous magnetic moment of the muon $(g-2)_\mu$ is one of the most accurately measured quantities in particle physics, and as such is a very promising signal of new physics if a deviation from its prediction in the Standard Model is found. The present experimental value for $a_\mu = (g-2)_\mu/2$, is given by $a_\mu^{\rm EXP} = 11659209.1(6.3)\times10^{-10}$, as an average of $a_{\mu^+} = 11659204(7.8)\times10^{-10}$ and $a_{\mu^-} = 11659215(8.5)\times10^{-10}$ [1, 2]. Since statistical errors are the largest source of uncertainties, a new measurement with a precision of 1.6×10^{-10} is been pursuit at FNAL [3] nowadays and at JPARC in a near future [4]. In particular, the new experiment at FNAL [3] pretends to reduce the overall error by storing 20 times more muons, by producing a more stable magnetic field (better and more carefully measured), and by improving the precision of the frequency measurement (via high-fidelity recording of muon decay).

At the level of the experimental accuracy, the QED contributions has been completed up to the fifth order $\mathcal{O}(\alpha_{em}^5)$, giving the QED contribution $11658471.885(4)\times10^{-10}$ [5], using the Rydberg constant and the ratio m_{Rb}/m_e as inputs [2]. Also electroweak contributions are necessary, since they reach $15.4\pm0.1\times10^{-10}$ [6]. Hadronic contributions in terms of the hadronic vacuum polarization (HVP) and the hadronic light-by-light scattering (HLBL) represent the main uncertainty in the Standard Model. In this talk, we will attempt to update the hadronic contributions to a_μ.

A white paper by the newly created *The Muon g-2 Theory Initiative* trying to get a *consensus* is on its way, accompanying the aforementioned experimental effort, and paving the path to new physics [7]. The results here described update Refs. [8] reaching spring 2019 only. We propose a particular procedure to combine the different results in the literature concerning hadronic contributions to the muon $(g-2)$.

2 The Hadronic Vacuum Polarization (HVP)

The hadronic vacuum polarization contributions are calculated utilising dispersion integrals and the experimentally measured cross section $\sigma^0_{\mathrm{had},\gamma}(s) \equiv \sigma^0(e^+e^- \to \gamma^* \to \mathrm{hadrons} + \gamma)$, where the superscript 0 denotes the bare cross section and the subscript γ indicates the inclusion of effects from final state photon radiation. At leading order, the dispersion relation reads

$$a_\mu^{\mathrm{had,\,LO\,VP}} = \frac{\alpha^2}{3\pi^2}\int_{s_{\mathrm{th}}}^{\infty}\frac{\mathrm{d}s}{s}R(s)K(s)\,, \tag{1}$$

where $\alpha = \alpha(0)$, $s_{\mathrm{th}} = m_\pi^2$, $R(s)$ is the hadronic R-ratio given by

$$R(s) = \frac{\sigma^0_{\mathrm{had},\gamma}(s)}{\sigma_{\mathrm{pt}}(s)} \equiv \frac{\sigma^0_{\mathrm{had},\gamma}(s)}{4\pi\alpha^2/(3s)}\,, \tag{2}$$

where $K(s)$ is a well known kernel function [9] and behaves as $1/s$, thus causing the HVP contributions to be dominated by the low-energy domain. At next-to-leading order, the data input is identical, but modified kernel function. Notice that final state radiative corrections and vacuum polarization corrections are taken into account. At spring 2019, two different results confront each other: DHMZ17 yields $693.1 \pm 3.4 \times 10^{-10}$ [10] and KNT18 yields $693.3 \pm 2.5 \times 10^{-10}$ [11]. Both using the same data sets, do not find yet perfect agreement, even though the distance among them have been reduced since their last respective publications (DHMZ10 yielding $692.3 \pm 4.2 \times 10^{-10}$ [12], and HLMNT11 $694.9 \pm 4.3 \times 10^{-10}$ [13]). The central value is in agreement, the error is still slightly different, but most important, reduced by $30-40\%$ in both cases. Nonetheless, the central values is a coincidence. Such value is obtained after summing up the different exclusive channels accounting for the inclusive measurement. When exploring in detail each individual contribution, the agreement is not that good. The largest difference occurs in the $\pi\pi$ channel, where the mean value in KNT18 is lower by almost 1σ of the DHMZ17 analysis. Notice that the KNT18 is also lower to the previous HLMNT11 result due to the new, precise and highly correlated radiative return data from KLOE and BESIII and the capability of the new data combination method to utilise the correlations to their full capacity. The difference between KNT18 and DHMZ17 in this $\pi\pi$ channel is larger than the global error of the sum of all channels. This difference which comes from how choices with regard to data combination affect results is a systematic error that should be taken into account to get a final HVP result. We propose to consider the individual differences in each channel as a systematic error. For example, the $\pi\pi$ from KNT18 reads $503.74 \pm 1.96 \times 10^{-10}$, while from DHMZ17 reads $507.14 \pm 2.58 \times 10^{-10}$, a difference of -3.40×10^{-10}, a 1.05σ effect. The systematic difference -3.40×10^{-10} translates into a systematic error that should be add as well. We opt to combine statistical errors uncorrelated (they are correlated though in a way we cannot guess) and the -3.40×10^{-10} as a 100% correlated systematic error (accounting for the unknown statistical correlation) to yield in the $\pi\pi$ case $504.98 \pm 3.74 \times 10^{-10}$. Doing so for all channels returns the final value $a_\mu^{\mathrm{had,\,LO\,VP}} = +693.47 \pm 4.36 \times 10^{-10}$. Using the same set of data and procedure, we would obtain $a_\mu^{\mathrm{had,\,NLO\,VP}} = -9.82 \pm 0.04 \times 10^{-10}$ but also $a_\mu^{\mathrm{had,\,NNLO\,VP}} = +1.24 \pm 0.01 \times 10^{-10}$ [14], in agreement with KNT18. The final result is then

$$a_\mu^{\mathrm{had,\,Total\,VP}} = +684.89 \pm 4.33 \times 10^{-10}\,. \tag{3}$$

3 The Hadronic Light-by-Light contribution (HLBL)

For the HLBL, two reference numbers can be found in the literature: $a_\mu^{\rm HLBL} = (11.6 \pm 4.0) \times 10^{-10}$ [15] but also $(10.5 \pm 2.5) \times 10^{-10}$ [16]. The overall HLBL contribution is twice the order of the present experimental error, thus we really need to reduce the errors down to 10%. The progress on the field is captured in [17] and the aforementioned theory initiative (https://indico.fnal.gov/conferenceDisplay.py?confId=13795).

The HLBL cannot be directly related to any measurable cross section and requires knowledge of QCD at all energy scales. Since this is not known yet, one needs to rely on hadronic models to compute it. Such models introduce systematic errors which are difficult to quantify. Using the large-N_c and the chiral counting, de Rafael proposed [18] to split the HLBL into a set of different contributions: pseudo-scalar exchange (PS, dominant [15, 16]), charged pion and kaon loops, quark loop, and higher-spin exchanges. The large-N_c approach however has at least two shortcomings: firstly, it is difficult to use experimental data in a large-N_c world. Secondly, calculations carried out in the large-N_c limit demand an infinite set of resonances. As such sum is not known, one truncates the spectral function in a resonance saturation scheme, the Minimal Hadronic Approximation (MHA) [31]. The resonance masses used in each calculation are then taken as the physical ones from PDG [2] instead of the corresponding masses in the large-N_c limit. Both problems might lead to large systematic errors not included so far [22, 24, 25, 28].

Actually, most of the results in the literature follow de Rafael's proposal finding values for $a_\mu^{\rm HLbL}$ between 6×10^{-10} and up to 14×10^{-10} (see [19, 20, 21, 15, 16, 32, 22, 23, 25, 27, 24, 26, 28, 29], including full and partial contributions to $a_\mu^{\rm HLbL}$). Such range almost reaches ballpark estimates based on the Laporta and Remiddi (LR) [33] analytical result for the heavy quark contribution to the LBL. The idea in such ballparks is to extend the perturbative result to hadronic scales low enough for accounting at once the whole HLBL. The free parameter is the quark mass m_q. The recent estimates using such methodology [34, 23] found $m_q \sim 0.150 - 0.250$ GeV after comparing the particular model with the HVP. The value for the HLBL is around $a_\mu^{\rm HLBL} = 12 - 17 \times 10^{-10}$, which seems to indicate that subleading pieces of the standard calculations are not negligible.

Jegerlehner and Nyffeler's review [15] together with the *Glasgow consensus* written by Prades, de Rafael, and Vainshtein [16] represent, in our opinion, the two reference numbers. They agree well since they only differ by few subtleties. For the main contribution, the pseudoscalar, one needs a model for the pseudoscalar Transition Form Factor (TFF). They both used the model from Knecht and Nyffeler [20] based on MHA, but differ on how to implement the high-energy QCD constrains coming from the VVA Green's function. In practice, this translates on whether the piece contains a pion pole or a pion exchange. The former would imply that the exchange of heavier pseudoscalar resonances is effectively included in PS [21], while the latter demands its inclusion. The treatment of errors, summed linearly [15] or in quadrature [16], is also a difference. All in all, even though the QCD features for the HLbL are well understood [15, 16], the details of the particular calculations are important to get the numerical result to the final required precision. We think we need more calculations, closer to experimental data if possible.

Dispersive approaches [35, 29] relies on the splitting of the former tensor into several pieces according to low-energy QCD, which most relevant intermediates states are selected according to their masses [18, 36]; see Refs. [29] for recent advances. An advantage we see in this approach is that by decomposing the HLBL tensor in partial waves, a single contribution may incorporate pieces that were separated so far, avoiding potential double counting. The example is the $\gamma\gamma \to \pi\pi$ which includes the two-pion channel, the pion loop, and scalar and tensor contributions.

Finally, there have been different proposals to perform a first principles evaluation by using lattice

QCD [37]. They studied a non-perturbative treatment of QED which later on was checked against the perturbative simulation. With that spirit, they considered that a QCD+QED simulation could deal with the non-perturbative effects of QCD for the HLBL. Whereas yet incomplete and with some progress still required, promising advances have been reported already [37].

The lack of experimental data, specially on the doubly virtual TFF, is an obstacle for calculations. Fortunately, data on the TFF when one of the photons is real is available, from different collaborations, for π^0, η and η'. It is common to factorize the TFF, and describe it based on a rational function. One includes a modification of its numerator to fulfil high-energy QCD constraints. Although the high-energy region of the model is not very important, it still contributes around 20%. More important is the double virtuality, especially if one uses the same TFF model (as it should) for predicting the $\pi^0 \to e^+e^-$ decay. Current models cannot accommodate its experimental value (see [38]). The worrisome fact is that modifying the model parameters to match such decay and going back to the HLBL, would result in a dramatic decrease of the HLBL value [38].

While the HLBL requires knowledge at all energies, it is condensed in the Q^2 region from 0 to 2 GeV^2, in particular above around 0.5 GeV^2. Therefore a good description of TFF in such region is very important. Such data are not yet available, but any model should reproduce the available one. That is why the authors of [22, 23, 24, 28], in contrast to other previous approaches, did not used data directly but the low-energy parameters (LEP) of the Taylor expansion of the TFF and reconstructed it *via* the use of Padé approximants (PA) and Canterbury approximants (CA) for the two dimensional case [38]. As demonstrated in Ref. [28], the pseudoscalar TFF is Stieltjes functions for which the convergence of PA's sequence is guaranteed in advanced. As such, a comparison between two consecutive elements in this sequence estimates the systematic error yield by the method. In other words, PA for the TFFs take full advantage of analyticity and unitary of these functions to correctly extrapolate low- and high-energy regions. The LEPs were obtained in [22] for the π^0, in [39] for the η-TFF and in [40] for the η'-TFF, taking into account the $\eta - \eta'$ mixing [40, 41] and the determinations of the double virtual π^0 [38] and η, η' [42] TFFs. Ref. [28] collects the most updated results for the space- and time-like TFF together with $\gamma\gamma$ decays from 13 different collaborations, to yield a most precise PS contribution to the HLBL.

The aforementioned White Paper pretends a consensus for the HLBL with the following criteria: *i*) the TFF normalisation should be given by real-photon decay and should follow high-energy constraints. *ii*) At least space-like experimental data for the single-virtual TFF must be reproduced. *iii*) Systematic uncertainties must be assessed with reasonable procedure. Among all the aforementioned calculations only two of them satisfy the criteria for the π^0 and only one for the $\eta(')$. For the π^0, Ref [28] yields $a_\mu^{\mathrm{HLBL},\pi^0} = 6.36 \pm 0.36 \times 10^{-10}$ which was later on corroborated by [30] yielding $a_\mu^{\mathrm{HLBL},\pi^0} = 6.26^{+0.30}_{-0.25} \times 10^{-10}$. Taken the difference among them as a purely systematic 100% correlated error, we can combine them to obtain $a_\mu^{\mathrm{HLBL},\pi^0} = 6.30 \pm 0.24 \times 10^{-10}$. Adding the $a_\mu^{\mathrm{HLBL},\eta} = 1.63 \pm 0.19 \times 10^{-10}$ and $a_\mu^{\mathrm{HLBL},\eta'} = 1.45 \pm 0.17 \times 10^{-10}$ from Ref. [28] the final PS contribution would result in:

$$a_\mu^{\mathrm{HLBL,PS}} = 9.38 \pm 0.67 \times 10^{-10} \,. \tag{4}$$

In conclusion, new experimental data used to update the PS in Ref. [28] seem to reveal larger contributions from pseudsocalar mesons, and that the TFF is more important than expected. Also, systematic errors are important and difficult to evaluate, but PAs can help. Lattice QCD seems promising but only in the long run. Dispersion relations are useful at low energies but a consensus will be needed in order to combine with other contributions. On top, ballpark predictions coincide on drawing larger values, indicating the need to better understand the whole HLBL.

Acknowledgements

P.M is supported the Beatriu de Pinós postdoctoral program co-funded by the Agency for Management of University and Research Grants of the Government of Catalonia and by the COFUND program of the Marie Sklodowska-Curie actions under the framework program Horizon2020 of the European Commission.

References

1. G. Bennett, et al.,Phys.Rev.Lett. 92 (2004) 161802;Phys.Rev. D73 (2006) 072003.

2. M. Tanabashi *et al.* [Particle Data Group], Phys. Rev. D **98** (2018) no.3, 030001.

3. R. Carey, et al, 2009; B. Lee Roberts [Fermilab P989 Collaboration], Nucl. Phys. Proc. Suppl. **218** (2011) 237; J. L. Holzbauer, J. Phys. Conf. Ser. **770** (2016) no.1, 012038.

4. M. Abe *et al.*, PTEP **2019** (2019) no.5, 053C02.

5. T. Aoyama,*et al*, Phys.Rev.Lett. 109 (2012) 111808.

6. Gnendiger, *et al*, Phys.Rev. D88 (5) (2013) 053005.

7. M. Lindner, M. Platscher and F. S. Queiroz, Phys. Rept. **731** (2018) 1.

8. P. Masjuan, Nucl. Part. Phys. Proc. **260** (2015) 111; CERN Proc. **1** (2018) 257.

9. S. Brodsky, De Rafael, Phys.Rev.**168** (1968)1620; B. Lautrup, De Rafael, Phys.Rev. **174** (1968)1835.

10. M. Davier, A. Hoecker, B. Malaescu and Z. Zhang, Eur. Phys. J. C **77** (2017) no.12, 827.

11. A. Keshavarzi, D. Nomura and T. Teubner, Phys. Rev. D **97** (2018) no.11, 114025.

12. M. Davier, A. Hoecker, B. Malaescu and Z. Zhang, Eur. Phys. J. C **71** (2011) 1515 Erratum: [Eur. Phys. J. C **72** (2012) 1874].

13. K. Hagiwara,*et al*, J.Phys. G38 (2011) 085003.

14. A. Kurz, T. Liu, P. Marquard and M. Steinhauser, Phys. Lett. B **734** (2014) 144.

15. F. Jegerlehner, A. Nyffeler, Phys.Rept. 477 (2009) 1–110.

16. J. Prades, E. de Rafael, A. Vainshtein, arXiv:0901.0306.

17. P. Masjuan *et al.*, arXiv:1306.2045 [hep-ph]. C. Aubin *et al.*, arXiv:1407.4021 [hep-ph].

18. E. de Rafael, Phys.Lett. B322 (1994) 239–246.

19. J. Bijnens, E. Pallante, J. Prades, Phys.Rev.Lett. 75 (1995) 1447–1450; Nucl.Phys. B474 (1996) 379–420; Nucl.Phys. B626 (2002) 410–411. M. Hayakawa, T. Kinoshita, A. Sanda, Phys.Rev.Lett. 75 (1995) 790–793; Phys.Rev. D54 (1996) 3137–3153; Phys.Rev. D57 (1998) 465–477. D. K. Hong, D. Kim, Phys.Lett. B680 (2009) 480–484. A. Dorokhov, A. Radzhabov, A. Zhevlakov, Eur.Phys.J. C71 (2011) 1702. P. Roig, A. Guevara and G. López Castro, Phys. Rev. D **89** (2014) no.7, 073016.

20. M. Knecht, A. Nyffeler, Phys.Rev. D65 (2002) 073034.

21. K. Melnikov, A. Vainshtein, Phys.Rev. D70 (2004) 113006.

22. P. Masjuan, Phys.Rev.D 86 (2012) 094021.

23. P. Masjuan and M. Vanderhaeghen, J. Phys. G **42** (2015) no.12, 125004.

24. R. Escribano, P. Masjuan, P. Sanchez-Puertas, Phys.Rev. D89 (3) (2014) 034014.

25. P. Masjuan, E. Ruiz Arriola, W. Broniowski, Phys.Rev. D87 (2013) 014005.

26. F. Jegerlehner, EPJ Web Conf. **118** (2016) 01016.

27. J. Bijnens and J. Relefors, JHEP **1609** (2016) 113.

28. P. Masjuan and P. Sanchez-Puertas, Phys. Rev. D **95** (2017) no.5, 054026

29. G. Colangelo, M. Hoferichter, M. Procura and P. Stoffer, Phys. Rev. Lett. **118** (2017) no.23, 232001

30. M. Hoferichter, B. L. Hoid, B. Kubis, S. Leupold and S. P. Schneider, JHEP **1810** (2018) 141.

31. S. Peris, M. Perrottet, E. de Rafael, JHEP 9805 (1998) 011. P. Masjuan, S. Peris, JHEP 0705 (2007) 040; Phys.Lett. B663 (2008) 61–65; Phys.Lett. B686 (2010) 307–312.

32. M. Hayakawa and T. Kinoshita, Phys. Rev. D **57** (1998) 465 Erratum: [Phys. Rev. D **66** (2002) 019902]; M. Knecht, A. Nyffeler, M. Perrottet and E. de Rafael, Phys. Rev. Lett. **88** (2002) 071802; I. R. Blokland, A. Czarnecki and K. Melnikov, Phys. Rev. Lett. **88** (2002) 071803; A. E. Dorokhov and W. Broniowski, Phys. Rev. D **78** (2008) 073011; A. Nyffeler, Phys. Rev. D **79** (2009) 073012; L. Cappiello, *et al.*,Phys.Rev. D83 (2011) 093006. K. Kampf and J. Novotny, Phys. Rev. D **84** (2011) 014036; A. E. Dorokhov, A. E. Radzhabov and A. S. Zhevlakov, Eur. Phys. J. C **75** (2015) no.9, 417;

33. S. Laporta, E. Remiddi,Phys.Lett. B301 (1993) 440–446.

34. A. Pivovarov, Phys.Atom.Nucl. 66 (2003) 902–913. J. Erler, G. Toledo Sanchez, Phys.Rev.Lett. 97 (2006) 161801. R. Boughezal, K. Melnikov, Phys.Lett. B704 (2011) 193–196. D. Greynat, E. de Rafael, JHEP 1207 (2012) 020.

35. G. Colangelo, M. Hoferichter, M. Procura and P. Stoffer, JHEP **1509** (2015) 074;

36. T. Kinoshita, B. Nizic and Y. Okamoto, Phys. Rev. D **31** (1985) 2108.

37. T. Blum, S. Chowdhury, M. Hayakawa and T. Izubuchi, Phys. Rev. Lett. **114** (2015) no.1, 012001. T. Blum, N. Christ, M. Hayakawa, T. Izubuchi, L. Jin and C. Lehner, Phys. Rev. D **93** (2016) no.1, 014503. T. Blum, N. Christ, M. Hayakawa, T. Izubuchi, L. Jin, C. Jung and C. Lehner, Phys. Rev. Lett. **118** (2017) no.2, 022005.

38. P. Masjuan and P. Sanchez-Puertas, arXiv:1504.07001 [hep-ph].

39. R. Escribano, P. Masjuan and P. Sanchez-Puertas, Eur. Phys. J. C **75** (2015) no.9, 414

40. R. Escribano, S. Gonzàlez-Solís, P. Masjuan and P. Sanchez-Puertas, Phys.Rev.D **94** (2016) **5**, 054033

41. P. Bickert, P. Masjuan and S. Scherer, Phys. Rev. D **95** (2017) no.5, 054023

42. P. Masjuan and P. Sanchez-Puertas, JHEP **1608** (2016) 108

43. G. Colangelo, M. Hoferichter, A. Nyffeler, M. Passera and P. Stoffer, Phys. Lett. B **735** (2014) 90

Frascati Physics Series Vol. 69 (2019)
PHOTON 2019 - International Conference on the Structure and the Interactions of the Photon
Jun 3-7, 2019

GRAVITATIONAL FORM FACTORS AND INTERNAL FORCES IN HADRONS

Maxim V. Polyakov
Petersburg Nuclear Physics Institute, Gatchina, 188300, St. Petersburg, Russia
Institut für Theoretische Physik II, Ruhr-Universität Bochum, D-44780 Bochum, Germany
Peter Schweitzer
Department of Physics, University of Connecticut, Storrs, CT 06269, USA

Abstract

Matrix elements of the energy momentum tensor (EMT) bear fundamental information like mass, spin and D-term of a particle which is the "last unknown global property." Recent progress on EMT form factors of hadrons, their interpretations and applications as well as the experimental status is given.

1 Introduction

Matrix elements of the EMT [1] yield fundamental particle properties like mass and spin as well as the D-term [2] which is related to the stress-tensor components of the EMT and gives access to mechanical properties of the system [3, 4]. EMT form factors can be accessed through studies of generalized parton distributions (GPDs) in hard exclusive reactions [5, 6]. While a model-independent extraction of GPDs is a challenging long-term task, accessing information on the D-term may be possible sooner thanks to its relation to the subtraction constant in fixed-t dispersion relations in deeply virtual Compton scattering (DVCS) [3, 7]. The physics of EMT form factors has important applications. The purpose of this article is to provide an overview of the latest developments and experimental status.

2 EMT form factors of hadrons

The nucleon form factors of the symmetric EMT $\hat{T}_{\mu\nu} = \hat{T}^Q_{\mu\nu} + \hat{T}^G_{\mu\nu}$ are defined as

$$\langle p', s'|\hat{T}_{\mu\nu}(0)|p, s\rangle = \bar{u}'\left[A(t)\,\frac{\gamma_{\{\mu}P_{\nu\}}}{2} + B(t)\,\frac{i\,P_{\{\mu}\sigma_{\nu\}\rho}\Delta^\rho}{4m} + D(t)\,\frac{\Delta_\mu\Delta_\nu - g_{\mu\nu}\Delta^2}{4m}\right]u\,, \tag{1}$$

with $P = \frac{1}{2}(p'+p)$, $\Delta = p'-p$, $t = \Delta^2$, $a_{\{\mu}b_{\nu\}} = a_\mu b_\nu + a_\nu b_\mu$ and a covariant normalization of the states is used with the nucleon spinors $\bar{u}(p,s)\,u(p,s) = 2\,m$. Spin-0 hadrons like the pion have only the 2 total EMT form factors $A(t)$ and $D(t)$. Hadrons with spin $J \geq 1$ have more form factors [8, 9].

The quark and gluon QCD operators $\hat{T}^a_{\mu\nu}$ $(a = Q,\, G)$ are each gauge invariant. Their form factors $A^a(t,\mu)$, etc depend on renormalization scale μ and additional form factors appear, e.g. as the structure $m\,\bar{c}^a(t,\mu)\,g_{\mu\nu}$ in (1), with $\sum_a \bar{c}^a(t,\mu) = 0$.

3 Relation to GPDs and 2D interpretation

GPDs provide a practical way to access EMT form factors through the DVCS process $eN \to e'N'\gamma$ or hard exclusive meson production. For the nucleon the second Mellin moments of unpolarized GPDs yield

$$\int \mathrm{d}x\; x\, H^a(x,\xi,t) = A^a(t) + \xi^2 D^a(t), \quad \int \mathrm{d}x\; x\, E^a(x,\xi,t) = B^a(t) - \xi^2 D^a(t). \tag{2}$$

The Fourier transform $H^a(x,b_\perp) = \int d^2\Delta_\perp/(2\pi)^2\, e^{-i\vec{\Delta}_\perp\vec{b}_\perp}\, H^a(x,\xi,-\vec{\Delta}_\perp^2)|_{\xi=0}$ is the probability to find a parton carrying the momentum fraction x and located at the distance $b_\perp$ from the hadron's (transverse) center-of-mass on the lightcone [10]. The 2D interpretation of EMT form factors was also discussed [11].

4 The static EMT and 3D interpretation

In the Breit frame characterized by $P = (E,0,0,0)$ and $\Delta = (0,\vec{\Delta})$ with $t = -\vec{\Delta}^2$ and $E = \sqrt{m^2 + \vec{\Delta}^2/4}$ one can define the static EMT [3]

$$T^a_{\mu\nu}(\vec{r},\vec{s}) = \int \frac{d^3\vec{\Delta}}{(2\pi)^3 2E}\; e^{-ir\vec{\Delta}} \langle p'|\hat{T}^a_{\mu\nu}(0)|p\rangle, \tag{3}$$

where $\vec{s}$ is the polarization vector of the states $|p\rangle$, $|p'\rangle$ in the respective rest frames. The 00-component of (3) is the energy density which only can be defined for the total system, and yields $\int d^3r\, T_{00}(r) = m$. Decomposition of the nucleon mass in terms of quark and gluon contributions was discussed in [12]. The $0k$-components yield the spatial distribution of the nucleon spin density $J^i_a(\vec{r},\vec{s}) = \epsilon^{ijk} r^j T^{0k}_a(\vec{r},\vec{s})$. This 3D density has a monopole term [3], and a quadrupole term [13] which are related to each other [14]. The ij-components of (3) define the stress tensor which can be decomposed in contributions from shear forces $s(r)$ and pressure $p(r)$ as follows [3]

$$T^{ij}(\vec{r}) = \left(\frac{r^i r^j}{r^2} - \frac{1}{3}\,\delta^{ij}\right) s(r) + \delta^{ij}\, p(r)\,. \tag{4}$$

For the nucleon the 3D interpretation is subject to small relativistic corrections [15] and becomes exact in the large-N_c limit. The shear forces can be defined separately for quarks and gluons in terms of $D^{Q,G}(t)$. For the "partial" pressures from quarks and gluons one also needs $\bar{c}^{Q,G}(t,\mu)$.

EMT conservation relates $s(r)$ and $p(r)$ as $\frac{2}{3}\,s'(r) + \frac{2}{r}\,s(r) + p'(r) = 0$. Notice that $s(r) = 0$ would imply $p(r) =$ constant and isotropic matter, cf. (4). Thus, the shear forces are responsible for structure formation [11]. Another consequence of EMT conservation is the von Laue condition [17],

$$\int_0^\infty \mathrm{d}r\, r^2 p(r) = 0, \tag{5}$$

implying that $p(r)$ must have at least one node. In all model studies so far $p(r)$ was found positive in the inner region (repulsion towards outside) and negative in the outer region (attraction towards inside).

The D-term can be expressed in two equivalent ways as $D = -\frac{4}{15}\, m \int d^3r\; r^2\, s(r) = m \int d^3r\; r^2\, p(r)$. The stress tensor in (4) has two eigenvalues related to normal (dF_r) and tangential (dF_ϕ, dF_θ) forces

$$\frac{dF_r}{dS_r} = \frac{2}{3}s(r) + p(r), \quad \frac{dF_\theta}{dS_\theta} = \frac{dF_\phi}{dS_\phi} = -\frac{1}{3}s(r) + p(r) \tag{6}$$

with eigenvectors $\vec{e}_r$ and $\vec{e}_{\theta,\phi}$. The degeneracy is lifted for spin $J \geq 1$. In a stable system the normal force $dF_r/dS_r = \frac{2}{3}s(r)+p(r) > 0$. Otherwise the system would collapse. This mechanical stability requirement can be written as $\int_0^R dr\, r^2 p(r) > 0$ (for any R), thus complementing the von Laue condition (5). It also determines the D-term of a stable system to be negative [18], $D < 0$. The positivity of $\frac{2}{3}s(r) + p(r)$ allows us to define the mechanical radius [19]

$$\langle r^2 \rangle_{\rm mech} = \frac{\int d^3r\; r^2\; \left[\frac{2}{3}s(r) + p(r)\right]}{\int d^3r\; \left[\frac{2}{3}s(r) + p(r)\right]} = \frac{6D}{\int_{-\infty}^0 dt\; D(t)}\,. \tag{7}$$

Interestingly the mechanical radius is given by an "anti-derivative" of $D(t)$ at $t = 0$ unlike e.g. the proton mean charge square radius $\langle r^2 \rangle_{\rm charge} = 6G'_E(0)/G_E(0)$ given in terms of the electric form factor $G_E(t)$.

One can also consider forces in lower-dimensional subsystems [4]. The 2D pressure $p^{(2D)}(r) = -\frac{1}{3}s(r) + p(r)$ satisfies $\int_0^\infty dr\, r\, p^{(2D)}(r) = 0$ and corresponds to the tangential forces in (6). Similarly the 1D pressure $p^{(1D)}(r) = -\frac{4}{3}s(r) + p(r)$ satisfies $\int_0^\infty dr\, p^{(1D)}(r) = 0$. Generically, for a spherically symmetric mechanical system in nD one can express its pressure and shear forces in terms of pressure in kD spherical subsystem as follows:

$$p^{(nD)}(r) = \frac{k}{n}\; p^{(kD)}(r) + \frac{k(n-k)}{n}\; \frac{1}{r^k} \int_0^r dr'\; r'^{\,k-1} p^{(kD)}(r'), \tag{8}$$

$$s^{(nD)}(r) = -\frac{k}{n-1}\; p^{(kD)}(r) + \frac{k^2}{n-1}\; \frac{1}{r^k} \int_0^r dr'\; r'^{\,k-1} p^{(kD)}(r'). \tag{9}$$

Such relations can be useful, e.g. in holographic approaches to QCD. The concepts can be generalized to higher spins [9]. The energy density and pressure in the center of a hadron are given by [4]

$$T_{00}(0) = \frac{m}{4\pi^2} \int_{-\infty}^0 dt\; \sqrt{-t}\; \left[A(t) - \frac{t}{4m^2} D(t)\right], \quad p(0) = \frac{1}{24\pi^2 m} \int_{-\infty}^0 dt\; \sqrt{-t}\;\; tD(t). \tag{10}$$

5 The D-term in theory and experiment

In contrast to the constraints $A(0) = 1$ and $B(0) = 0$ resulting from properties of the states under Lorentz transformations [20], the form factor $D(t)$ is not constrained (not even at $t = 0$) by general principles. It is not related to external properties like Lorentz transformations but reflects internal dynamics inside the hadron. The value $D = D(0)$ is therefore not known for (nearly) any particle.

In free field theories one finds $D = -1$ for free Klein Gordon fields [1, 15], and $D = 0$ for free Dirac fields [21]. For Goldstone bosons of spontaneous chiral symmetry breaking it is predicted in the chiral limit that $D_{\rm Goldstone} = -1$ from soft pion theorems for EMT form factors [22] or pion GPDs [2]. Corrections due to finite masses are expected to be small for pions and larger for kaons and η [23, 15].

For large nuclei in the liquid drop model [3] $p(r) = p_0\theta(r-R) - \frac{p_0 R}{3}\delta(r-R)$ and $s(r) = \gamma\delta(r-R)$ with nucleus radius $R = R_0 A^{1/3}$ and surface tension γ related by the Kelvin relation $p_0 = 2\gamma/R$ [24]. It is predicted $\langle r^2 \rangle_{\rm mech} = \frac{3}{5}R^2$ and $D = -\frac{4}{5}\, m\, \gamma\, \frac{4\pi}{3}\, R^4 \propto A^{7/3}$ which is supported in Walecka model [25].

The D-term of the nucleon was studied in the chiral quark soliton model [26] which predicts $D \approx -3.5$ and $\langle r^2 \rangle_{\rm mech} \approx 0.75\, \langle r^2 \rangle_{\rm charge}$. Studies were also reported in Skyrme models including nuclear

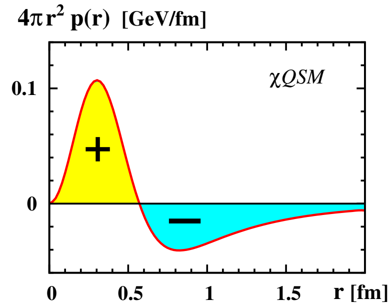

Figure 1: Pressure in chiral quark soliton (χQSM) [26] and realization of the von Laue condition (5).

medium corrections [27], bag model [28], a Nambu–Jona-Lasinio diquark approach [29], using dispersion relations [30], chiral perturbation theory [31], lattice QCD [32], and QCD lightcone sum rules [33]. D-terms of mesons [34], Q-balls [35], photons [36] and Δ-resonance [18] were also studied.

A first extraction of the quark contribution to the pion D-term from the BELLE data [37] on $\gamma^*\gamma \to 2\pi^0$ gave [38] $D^Q(0) \approx -0.75$ with unestimated uncertainties. For the D-term of the nucleon phenomenological fits indicate that $D^Q < 0$ with large uncertainties [39]. The D-term can be accessed in DVCS with help of fixed-t dispersion relations [3, 7] which relate the real and imaginary parts of the complex DVCS Compton form factors with a subtraction constant $\Delta(t,\mu)$ related to $D^Q(t,\mu) = \frac{2}{5}\,\Delta(t,\mu)/(e_u^2+e_d^2) = \frac{18}{25}\,\Delta(t,\mu)$ under certain assumptions (large-N_c limit, $\mu \to \infty$). An analysis of the JLab data [40] performed under such assumptions and additional constraints gave a first insight on $\Delta(t,\mu)$ of the nucleon [41]. Relaxing these assumptions and constraints at the current stage yields much larger uncertainties [42] though the method in principle works.

6 Applications and Conclusions

The EMT form factors have important applications including hard exclusive reactions, the description of hadrons in strong gravitational fields, hadronic decays of heavy quarkonia [22], and the description of exotic hadrons with hidden charm as hadroquarkonia [43, 18].

Unlike the EMT form factors $A(t)$ and $B(t)$ related to the generators of the Poincaré group and ultimately to the mass and spin of a particle, the form factor $D(t)$ is related to the internal forces and opens a new window for studies of the hadron structure and visualization of internal hadronic forces.

7 Acknowledgements

This work was supported by NSF (grant no. 1812423) and by CRC110 (DFG).

References

1. I. Y. Kobzarev and L. B. Okun, Zh. Eksp. Teor. Fiz. **43**, 1904 (1962) [Sov. Phys. JETP **16**, 1343 (1963)]. H. Pagels, Phys. Rev. **144**, 1250 (1966).

2. M. V. Polyakov and C. Weiss, Phys. Rev. D **60**, 114017 (1999).

3. M. V. Polyakov, Phys. Lett. B **555**, 57 (2003).

4. M. V. Polyakov and P. Schweitzer, Int. J. Mod. Phys. A **33**, 1830025 (2018).

5. D. Müller et al, Fortsch. Phys. **42**, 101 (1994). X. D. Ji, Phys. Rev. Lett. **78**, 610 (1997). A. V. Radyushkin, Phys. Lett. B **380**, 417 (1996). J. C. Collins, L. Frankfurt and M. Strikman, Phys. Rev. D **56**, 2982 (1997).

6. K. Goeke, M. V. Polyakov, M. Vanderhaeghen, Prog. Part. Nucl. Phys.**47**, 401 (2001). M. Diehl, Phys. Rept. **388** (2003) 41. A. V. Belitsky and A. V. Radyushkin, Phys. Rept. **418**, 1 (2005). S. Boffi and B. Pasquini, Riv. Nuovo Cim. **30**, 387 (2007).

7. O. V. Teryaev, hep-ph/0510031. I. V. Anikin and O. V. Teryaev, Phys. Rev. D **76**, 056007 (2007). M. Diehl and D. Y. Ivanov, Eur. Phys. J. C **52**, 919 (2007). A. V. Radyushkin, Phys. Rev. D **83**, 076006 (2011).

8. W. Cosyn, S. Cotogno, A. Freese and C. Lorcé, Eur. Phys. J. C **79**, 476 (2019). M. V. Polyakov and B. D. Sun, Phys. Rev. D **100**, 036003 (2019).

9. M. V. Polyakov and P. Schweitzer, PoS SPIN **2018**, 066 (2019) [arXiv:1812.06143].

10. M. Burkardt, Phys. Rev. D **62**, 071503 (2000); Int. J. Mod. Phys. A **18**, 173 (2003).

11. C. Lorcé, H. Moutarde and A. P. Trawiński, Eur. Phys. J. C **79**, 89 (2019).

12. X. D. Ji, Phys. Rev. Lett. **74**, 1071 (1995); Phys. Rev. D **52**, 271 (1995). C. Lorcé, Eur. Phys. J. C **78**, 120 (2018).

13. C. Lorcé, L. Mantovani and B. Pasquini, Phys. Lett. B **776**, 38 (2018).

14. P. Schweitzer and K. Tezgin, Phys. Lett. B **796**, 47 (2019).

15. J. Hudson and P. Schweitzer, Phys. Rev. D **96**, 114013 (2017).

16. M. V. Polyakov and H. D. Son, JHEP **1809**, 156 (2018).

17. M. von Laue, Ann. Phys. (Leipzig) 340, 524 (1911).

18. I. A. Perevalova, M. V. Polyakov and P. Schweitzer, Phys. Rev. D **94**, 054024 (2016).

19. M. V. Polyakov and P. Schweitzer, arXiv:1801.05858 [hep-ph].

20. P. Lowdon, K. Y. J. Chiu and S. J. Brodsky, Phys. Lett. B **774**, 1 (2017). S. Cotogno, C. Lorcé and P. Lowdon, Phys. Rev. D **100**, 045003 (2019). C. Lorcé and P. Lowdon, arXiv:1908.02567 [hep-th].

21. J. Hudson and P. Schweitzer, Phys. Rev. D **97**, 056003 (2018).

22. V. A. Novikov and M. A. Shifman, Z. Phys. C **8**, 43 (1981). M. B. Voloshin and V. I. Zakharov, Phys. Rev. Lett. **45**, 688 (1980). M. B. Voloshin and A. D. Dolgov, Sov. J. Nucl. Phys. **35**, 120 (1982) [Yad. Fiz. **35**, 213 (1982)]. H. Leutwyler and M. A. Shifman, Phys. Lett. B **221**, 384 (1989).

23. J. F. Donoghue and H. Leutwyler, Z. Phys. C **52**, 343 (1991).

24. W. Thomson (Lord Kelvin), Proc. Roy. Soc. London **9** (1858) 255.

25. V. Guzey and M. Siddikov, J. Phys. G **32**, 251 (2006).

26. V. Y. Petrov et al, Phys. Rev. D **57**, 4325 (1998). P. Schweitzer, S. Boffi, M. Radici, Phys. Rev. D **66**, 114004 (2002). J. Ossmann et al, Phys. Rev. D **71**, 034011 (2005). K. Goeke et al, Phys. Rev. D **75**, 094021 (2007); Phys. Rev. C **75**, 055207 (2007). M. Wakamatsu, Phys. Lett. B **648**, 181 (2007).

27. C. Cebulla, K. Goeke, J. Ossmann and P. Schweitzer, Nucl. Phys. A **794**, 87 (2007). J. H. Jung, U. Yakhshiev and H. C. Kim, J. Phys. G **41**, 055107 (2014). H. C. Kim, P. Schweitzer and U. Yakhshiev, Phys. Lett. B **718**, 625 (2012). J. H. Jung, U. Yakhshiev, H. C. Kim, P. Schweitzer, Phys. Rev. D **89**, 114021 (2014).

28. X. D. Ji, W. Melnitchouk and X. Song, Phys. Rev. D **56**, 5511 (1997). M. J. Neubelt, A. Sampino, J. Hudson, K. Tezgin and P. Schweitzer, PoS DIS **2019**, 210 (2019) [arXiv:1907.11185].

29. A. Freese and I. C. Cloët, arXiv:1907.08256 [nucl-th].

30. B. Pasquini, M. V. Polyakov and M. Vanderhaeghen, Phys. Lett. B **739**, 133 (2014).

31. A. V. Belitsky and X. Ji, Phys. Lett. B **538**, 289 (2002). S. I. Ando, J. W. Chen and C. W. Kao, Phys. Rev. D **74**, 094013 (2006). M. Diehl, A. Manashov, A. Schäfer, Eur. Phys. J. A **29**, 315 (2006).

32. P. Hägler *et al.*, Phys. Rev. D **68**, 034505 (2003). M. Göckeler *et al.*, Phys. Rev. Lett. **92**, 042002 (2004). P. Hägler *et al.*, Phys. Rev. D **77**, 094502 (2008). P. E. Shanahan and W. Detmold, Phys. Rev. D **99**, 014511 (2019), Phys. Rev. Lett. **122**, 072003 (2019).

33. I. V. Anikin, Phys. Rev. D **99**, 094026 (2019). K. Azizi and U. Özdem, arXiv:1908.06143 [hep-ph].

34. A. Freese and I. C. Cloët, Phys. Rev. C **100**, 015201 (2019).

35. M. Mai and P. Schweitzer, Phys. Rev. D **86**, 076001 (2012); Phys. Rev. D **86**, 096002 (2012). M. Cantara, M. Mai and P. Schweitzer, Nucl. Phys. A **953**, 1 (2016). I. E. Gulamov et al, Phys. Rev. D **92**, 045011 (2015). E. Nugaev and A. Shkerin, arXiv:1905.05146.

36. S. Friot, B. Pire and L. Szymanowski, Phys. Lett. B **645**, 153 (2007). I. R. Gabdrakhmanov and O. V. Teryaev, Phys. Lett. B **716**, 417 (2012).

37. M. Masuda *et al.* [Belle Collaboration], Phys. Rev. D **93**, 032003 (2016).

38. S. Kumano, Q. T. Song and O. V. Teryaev, Phys. Rev. D **97**, 014020 (2018).

39. K. Kumerički, D. Müller and K. Passek-Kumerički, Nucl. Phys. B **794**, 244 (2008). K. Kumerički and D. Müller, Nucl. Phys. B **841**, 1 (2010). D. Müller et al, Nucl. Phys. B **884** (2014) 438. K. Kumerički and D. Müller, EPJ Web Conf. **112**, 01012 (2016) [arXiv:1512.09014].

40. F. X. Girod *et al.* [CLAS Collaboration], Phys. Rev. Lett. **100**, 162002 (2008). H. S. Jo *et al.* [CLAS Collaboration], Phys. Rev. Lett. **115**, 212003 (2015).

41. V. D. Burkert, L. Elouadrhiri and F. X. Girod, Nature **557**, no. 7705, 396 (2018).

42. K. Kumerički, Nature **570**, no. 7759, E1 (2019).

43. M. I. Eides, V. Y. Petrov and M. V. Polyakov, Phys. Rev. D **93**, 054039 (2016); M. I. Eides, V. Y. Petrov and M. V. Polyakov, Eur. Phys. J. C **78**, 36 (2018); arXiv:1904.11616. J. Y. Panteleeva et al, Phys. Rev. C **99**, 045206 (2019).

Frascati Physics Series Vol. 69 (2019)
PHOTON 2019 - International Conference on the Structure and the Interactions of the Photon
Jun 3-7, 2019

COMBINATION AND QCD ANALYSIS OF CHARM AND BEAUTY PRODUCTION CROSS-SECTION MEASUREMENTS IN DEEP INELASTIC ep SCATTERING AT HERA

Uri Karshon
Weizmann Institute of Science, Rehovot, Israel
On behalf of the H1 and ZEUS Collaborations

Abstract

Measurements of open charm and beauty production cross sections in ep deep inelastic scattering (DIS) at HERA from the H1 and ZEUS Collaborations are combined. Reduced cross sections are obtained in a restricted kinematic range. Perturbative QCD calculations are compared to the combined data. Next-to-leading order QCD analysis is performed using these data together with combined inclusive HERA DIS cross sections. The running charm and beauty quark masses are determined.

1 Introduction and motivation

Deep inelastic scattering at HERA is a kinematic regime where the scattered electron is detected and the exchanged photon virtuality, Q^2, is above a few GeV^2. In leading-order (LO) QCD, the dominant process in heavy quark (HQ) production (charm c or beauty b) in DIS is boson-gluon fusion (BGF), where at least 2 heavy quarks are present in the final state. At HERA the charm contribution to the inclusive DIS cross section is up to 30%. The HQ production, which is directly sensitive to the gluon density in the proton and to the masses of the heavy quarks, enables testing QCD by comparing data to next-to-leading order (NLO) predictions. Multiple hard scales in this process (Q^2, m_{HQ} and $p_T(HQ)$) allow perturbative calculations to be made.

The HERA ep collider operated with electrons or positrons at 27.5 GeV and protons at 820 or 920 GeV. About 130 pb^{-1} of data were taken between 1995 - 2000 ("HERA I") and $\approx$ 380 pb^{-1} were taken between 2003 - 2007 ("HERA II") by each of the two main experiments H1 and ZEUS.

2 Heavy quark production in DIS

Several NLO schemes for HQ production in ep collisions exist:

1) “Massive” or Fixed Flavour Number Scheme (FFNS), where $Q^2 \approx m_{HQ}^2$. In this scheme three active quark flavours (u, d, s) in the proton are considered, the heavy quarks are produced only perturbatively in the hard scattering and mass effects are correctly included.

2) “Massless” or Zero-Mass Variable Flavour Number Scheme (ZM-VFNS), where $Q^2 \gg m_{HQ}^2$. Here the heavy quarks are treated as massless partons, the HQ density is added as an extra flavour in the proton and a resummation of large logarithms of Q^2/m_{HQ}^2 is performed.

At intermediate Q^2 both schemes should be merged:

3) General-Mass Variable Flavour Number Scheme (GM-VFNS). This scheme is equivalent to FFNS for $Q^2 \approx m_{HQ}^2$ and to ZM-VFNS for $Q^2 \gg m_{HQ}^2$. In between, various schemes interpolate differently from each other.

3 Combination of charm and beauty data

The double differential cross section $\frac{d^2\sigma^{Q\bar{Q}}}{dx_{B_j}dQ^2}$ can be expressed as:
$\frac{2\pi\alpha^2}{x_{B_j}Q^4}[(1+(1-y)^2)\sigma_{red}^{Q\bar{Q}}]$, where x_{B_j} is the Bjorken x variable, $y = Q^2/(sx_{B_j})$ is the inelasticity and s is the total energy squared of the ep system.

The heavy quark reduced cross sections, $\sigma_{red}^{Q\bar{Q}}$, were measured in the kinematic range $2.5 < Q^2 < 2000$ GeV^2; $3 \cdot 10^{-5} < x_{B_j} < 5 \cdot 10^{-2}$.

Thirteen charm + beauty data sets of D^*, D^+, D^0, μ and lifetime tags from various HERA I and HERA II analyses were combined [1]. Correlations of statistical and systematic uncrtainties for all data sets were taken into account. The combined data are compared to QCD predictions using various parton density functions (PDF) within the FFNS and VFNS schemes.

In fig. 1 the charm and beauty reduced cross sections are shown as a function of x_{B_j} for various Q^2 values for the combined (full circles) and for separate H1 and ZEUS measurements. The combined results uncertainties are much smaller than each most precise separate data set.

4 Comparison with QCD predictions

In Fig. 2 the ratio of the combined reduced charm cross sections to the FFNS predictions are compared to various schemes and PDF sets at NLO and approximate next-to-next-to-leading order (NNLO). Both FFNS and VFNS describe the data reasonably well. The x_{B_j} slope is steeper than the NLO predictions and it does not improve for approximate NNLO. For the reduced beauty cross sections all predictions are in good agreement with the data within large uncertainties.

Proton PDFs with NLO+NNLO fixed order supplemented by next-to-leading log (NLL) low-x resummation (FONLL-C scheme, Ball et al., arXiv:1710.05935) improve the agreement at low-x (see Fig. 3). A comparison of the data to this scheme for $Q^2 < 32$ GeV^2 yields a better description of the x_{B_j} slope for the NNLO calculation with and without the low-x resummation (NLL). The predictions are mostly below the data mainly for NNLO+NLL. The overall description is not improved w.r.t. the FFNS reference calculation. The best description of the charm data is given by NLO FFNS.

5 QCD analysis

The combined HQ production together with the combined inclusive DIS (with $Q^2_{min} = 3.5$ GeV^2) were used to perform a simultaneous NLO fit to determine the running HQ masses $m_c(m_c)$ and $m_b(m_b)$. The fit includes PDFs in FFNS and c, b quarks running masses in the $\overline{MS}$ scheme. The HQ running masses are free paramenters in the fit.

The result of the fit ("HERAPDF-HQMASS") yields:
$m_c(m_c) = 1.29^{+0.05}_{-0.04}(exp./fit)^{+0.06}_{-0.01}(mod.)^{+0.00}_{-0.03}(par.)$ GeV and
$m_b(m_b) = 4.05^{+0.10}_{-0.11}(exp./fit)^{+0.09}_{-0.03}(mod.)^{+0.00}_{-0.03}(par.)$ GeV. The uncertainties come from the fit, the model uncertainty and the PDF parameterisation. The results are consistent with the world average PDG2016.

Fig.4 left gives the ratios of combined reduced charm cross sections and HERAPDF-HQMASS fit to the nominal FFNS prediction. Both the FFNS predictions and the HERAPDF-HQMASS calculations describe the data almost identically. The steeper x_{B_j} slope persists also after the fit. For beauty, there is good agreement between data and theory within the large uncertainties.

The inclusive DIS cross section constrains the gluon density in the proton indirectly via scaling violation and directly via higher order corrections. Heavy flavour production via BGF probes the gluon directly. The x of the incoming gluon is different from x_{B_j}, which is measured at the photon vertex. In LO the gluon x is given by $x = x_{B_j}(1 + (\bar{s}/Q^2)$, where $\bar{s}$ is the invariant mass of the HQ pair. Due to the high precision of $\sigma^{c\bar{c}}_{red}$, the impact of charm measurement on the gluon determination in the QCD fit can be enhanced. A cut of $x_{B_j} > 0.01$ on the inclusive data in the fit reduces the impact of inclusive data in the determination of the gluon density function. The resulting function $xg(x, \mu_f^2)$, where $\mu_f^2 = 1.9$ GeV^2 is the starting scale, is shown in Fig.5 with no cut on x_{B_j} and with a cut $x_{B_j} > 0.01$ on inclusive data only. The low x gluon density function with the cut describes the charm data much better.

In Fig.4 right the ratios of combined reduced charm cross sections and HERAPDF-HQMASS fit to the nominal FFNS prediction based on HERAPDF-HQMASS are given with a cut $x_{B_j} > 0.01$ on the inclusive data. This fit rises more strongly towards small x and describes the data much better. No significant improvement is obtained for the beauty data. The heavy-quark masses obtained from this fit are consistent with the previous ones.

The ratios of combined inclusive DIS reduced cross section for neutral current (NC) e^+p, $\sigma^+_{r,NC}$, to the NC FFNS reference cross section, $\sigma^{+nom}_{r,NC}$, and to the HERAPDF-HQMASS fit without and with the $x_{B_j} > 0.01$ cut for the inclusive data are shown in Fig.6. The predictions based on NC FFNS and on HERAPDF-HQMASS agree with the inclusive measurements. However, the calculations with the $x_{B_j} > 0.01$ cut for inclusive data fail to describe the low-x inclusive data. It is impossible to resolve the difference in describing simultaneously the inclusive and charm measurements by changing the gluon density. It is unlikely that including NNLO, which gives a poorer description than NLO for the charm data, will alter this conclusion.

6 Summary

- Final combined H1 + ZEUS charm and beauty results in DIS with the full HERA data, including all correlations, yield tight constraints on QCD.
- The charm results yield a better precision of $\approx 20\%$ compared to previous results. The beauty results are combined for the first time.
- The charm data are described reasonably well by FFNS (best) and by VFNS. There is however $\approx 3\sigma$ tension in the x-slope with respect to the inclusive data.
- The beauty data are well described by all QCD predictions within the large experimental uncertainties.

- A simultaneous fit of inclusive, charm and beauty data yields accurate results for $m_c(m_c)$ and $m_b(m_b)$, which are consistent with PDG and with previous measurements.
- The x-slope tension between the charm data and the inclusive data cannot be solved by varying the gluon density, adding higher orders or resumming $\log 1/x$ terms. Further investigations are needed.

References

1. H. Abramowicz et al, H1 and ZEUS Collaborations, Eur.Phys.J. **C78**, 473 (2018).

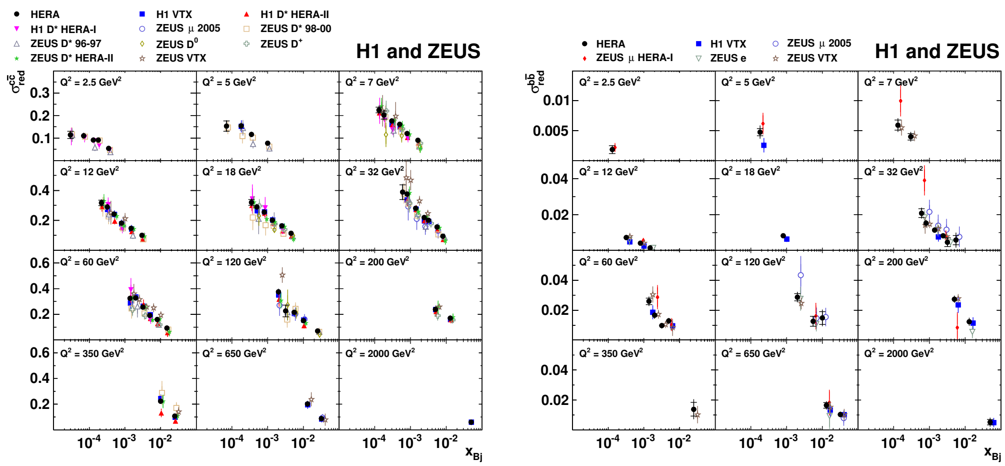

Figure 1: *Combined and separate H1 and ZEUS reduced charm (left) and beauty (right) production cross sections as a function of* x_{B_j} *for various* Q^2 *values.*

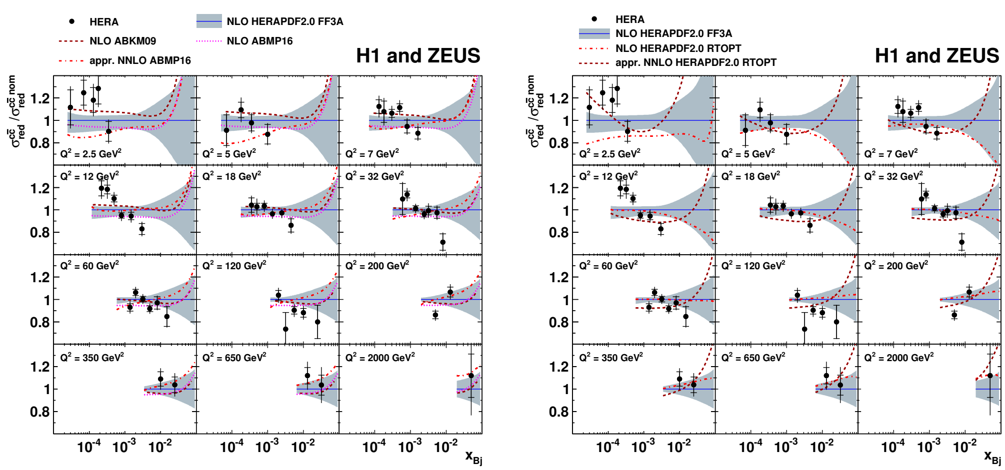

Figure 2: *Ratio of reduced charm cross sections as a function of* x_{B_j} *for various* Q^2 *values with respect to the FFNS NLO predictions compared to NLO and approximate NNLO FFNS (left) and VFNS (right) predictions.*

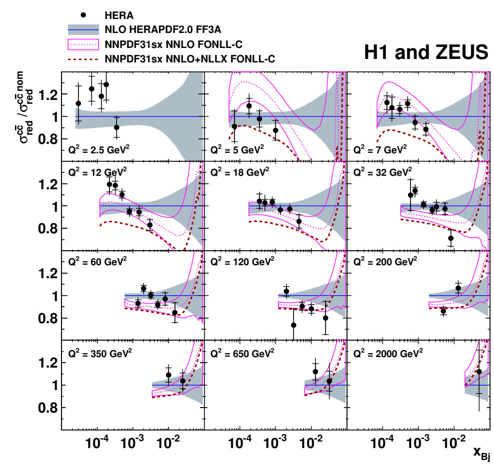

Figure 3: *Ratio of reduced charm cross sections as a function of x_{B_j} for various Q^2 values with respect to the FFNS NLO predictions compared to the FONLL-C scheme with (NNLO+NLL) and without (NNLO) low-x resummation.*

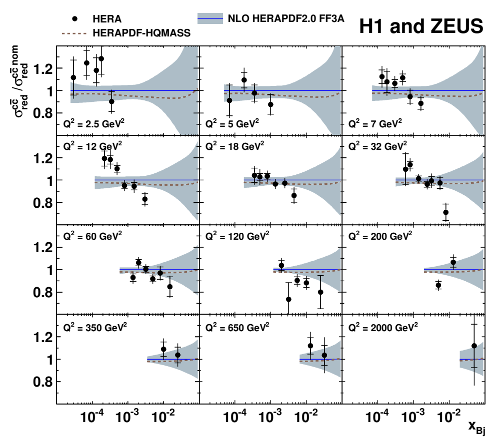

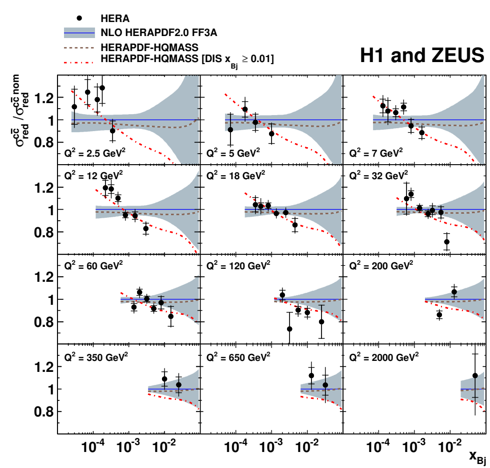

Figure 4: *Ratios of charm data and HERAPDF-HQMASS fit to the FFNS NLO predictions (left) and with $x_{B_j} > 0.01$ for the inclusive DIS data (right).*

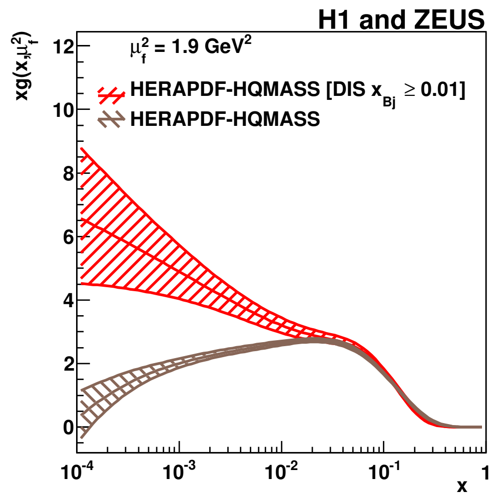

Figure 5: *The gluon density function $xg(x, \mu_f^2)$ as a function of x with and without a cut $x_{B_j} > 0.01$.*

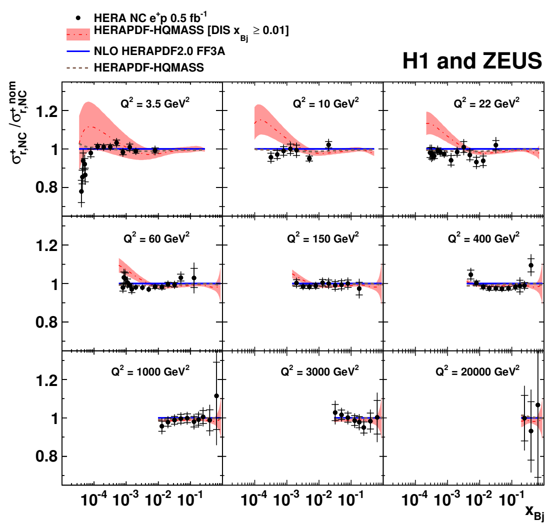

Figure 6: *Ratio of the combined reduced neutral current cross sections, $\sigma^+_{r,NC}$, to the NC FFNS reference cross section, $\sigma^{+\,nom}_{r,NC}$, and to the HERAPDF-HQMASS fit without and with a $x_{B_j} > 0.01$ cut on the inclusive data.*

Frascati Physics Series Vol. 69 (2019)
PHOTON 2019 - International Conference on the Structure and the Interactions of the Photon
Jun 3-7, 2019

TWO-PHOTON PROCESSES AT BELLE

Wenbiao Yan (For Belle Collaboration)
University of Science and Technology of China

Abstract

In this talk. We presented several measurement two-photon processes at Belle. With partial-wave amplitudes analysis in $\gamma\gamma \to K_S^0 K_S^0$, relative phase $\phi_{a_2(1320)}$ between $f_2(1270)$ and $a_2(1320)$ is extracted, and consistent with theory prediction. The $\Gamma_{\gamma\gamma}\mathcal{B}(K\bar{K})$ for $f_0(1710)$ is measured for the first time. The helicity-0, -1, and -2 components of $f_2(1270)$ TFF are measured for the first time in $\gamma\gamma^\star \to 2\pi^0$, Q^2 dependence of $f_0(980)$ and $f_2(1270)$ TFF are compared with theory prediction. A search for tetraquark is searched in $\gamma\gamma \to p\bar{p}K^+K^-$ process.

1 Introduction

In e^+e^- collider, two virtual photon from incident electron and positron have interaction, and produce hadrons. This two-photon process provide an important platform to investigate nature of strong interaction at low energy scale. Measurements of exclusive final states in two-photon process provides valuable information on resonances, QCD prediction and hadron production mechanics.

In this talk, we concentrate on measurement by no-tag method, where either a scattered electron or positron is detected, and single-tag method, where there are one detected scattered electron or positron. Many two-proton processes have been done by Belle, Table 1 summaries published results on two-photon process by Belle. The measurements have been preformed with Belle detector [1] at asymmetric e+e- collider KEKB [2].

2 $\gamma\gamma \to K_S^0 K_S^0$ process

The $e^+e^- \to (e^+e^-)K_S^0 K_S^0$ have been studied by no-tag method [3], in W region from (close) its threshold to 4.0GeV, and in angular range $|\cos\theta^\star| < 0.8$, where W is total energy of parent photons

Table 1: *The published results on two-photon process by Belle.*

	GeV	fb^{-1}	Reference
$\gamma J/\psi$	3.2-3.8	32.6	PLB540, 33 (2002)
K^+K^-	1.4-2.4	67	EPCJ 32, 323 (2003)
$\pi^+\pi^-/K^+K^-$	2.4-4.1	87.7	PLB 615, 39 (2005)
$p\bar{p}$	2.03-4.0	89	PLB 621, 41 (2005)
$D\bar{D}$	3.7-4.3	395	PRL 96, 082003 (2006)
$\pi^+\pi^-$	0.8-1.5	85.9	PRD 75, 051101 (2007)
$K_S^0K_S^0$	2.4-4.0	397.6	PLB 651, 15 (2007)
four mesons	1.4-3.4	395	EPCJ 53, 1 (2008)
$\pi^0\pi^0$	0.6-4.0	95	PRD 78, 052004 (2008)
$\pi^0\pi^0$	0.6-4.1	223	PRD 79, 052009 (2009)
$\eta\pi^0$	0.84-4.0	223	PRD 80, 032001 (2009)
$\phi J\psi$	4.2-5.0	825	PRL 104, 112004 (2010)
$\omega J\psi$	3.9-4.2	694	PRL 104, 092002 (2010)
$\eta\eta$	1.096-3.8	393	PRD 82, 114031 (2010)
$\omega\omega, \omega\phi, \phi\phi$	< 4.0	870	PRL 108, 232001 (2012)
π^0	$4 < Q^2 < 40\text{GeV}^2$	759	PRD 86, 092007 (2012)
$\eta'\pi^+\pi^-$	1.4-3.4	673	PRD 86, 052002 (2012)
$K_S^0K_S^0$	1.04-4.0	972	PTEP 2013, 123C01 (2013)
$\pi^0\pi^0$	$Q^2 < 30\text{GeV}^2$	759	PRD 93, 032002 (2016)
$p\bar{p}K^+K^-$	3.2-5.6	980	PRD 93, 112017 (2016)

and $\theta^\star$ is scattering angle of K_S^0 in their center-of-mass reference frame. Figure 1 shows W dependence of $\gamma\gamma \to K_S^0K_S^0$ integrated cross section ($|\cos\theta^\star| < 0.8$), where prominent peak near 1.3GeV is due to interference between $f_2(1270)$ and $a_2(1320)$, prominent peak around 1.5GeV it due to $f_2'(1525)$ and prominent peak around 1.8GeV.

A partial-wave amplitudes analysis was performed for $\gamma\gamma \to K_S^0K_S^0$, only partial waves of with even angular momentum contribute. In energy region $W < 3$GeV, there are only S, D & G waves are considered in fitting of differential cross section for obtaining information on partial waves.

2.1 Relative phase $\phi_{a_2(1320)}$ between $f_2(1270)$ and $a_2(1320)$

A fit was preformed in region $1.15 \leq W \leq 1.65$ GeV to determine resonance parameters of $f_2'(1525)$, and relative phase $\phi_{a_2(1320)}$ between $f_2(1270)$ and $a_2(1320)$. Two solutions are obtained, and main difference is values of $\Gamma_{\gamma\gamma}\mathcal{B}(\mathcal{KK})$, 113 and 48 eV, which are refereed as H (high) and L (low) respectively. Finally, the phase between $f_2(1270)$ and $a_2(1320)$ is combined statistically for solutions H & L, and is $(172.6^{+6.0+12.2}_{-0.7-7.0})^o$. This confirms destructive interference in $K_S^0K_S^0$ mode, and agrees with theory predictions [4].

2.2 $f_J(1710)$ formation in $K_S^0K_S^0$

In order to extract contribution of $f_J(1710)$, a fit was preformed in region $1.2 \leq W \leq 2.0$ GeV by fixing resonance parameters of $f_2'(1525)$ and $\phi_{a_2(1320)}$ in solutions H & L (see section 2.1). Table 2 summaries fitted results, fitted resonance parameters of $f_0(1710)$ are consistent with that of PDG [5], the $f_0(1710) \to K_S^0K_S^0$ is confirmed in two-photon process. The $\Gamma_{\gamma\gamma}\mathcal{B}(K\bar{K})$ for $f_0(1710)$ is measured for the first time. Because total width and $\Gamma_{\gamma\gamma}\mathcal{B}(K\bar{K})$ of $f_0(1710)$ are much larger than those expected for a pure glueball state, $f_0(1710)$ is unlikely to be glueball.

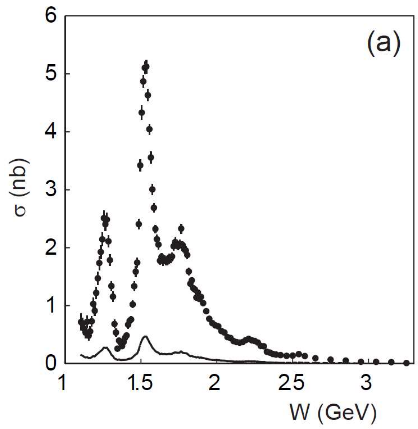

Figure 1: W *dependence of* $\gamma\gamma \to K_S^0 K_S^0$ *integrated cross section* ($|\cos\theta^\star| < 0.8$).

Table 2: *Fitted parameters for the* $f_0(1710)$ *fit and* $f_2(1710)$ *fit. Taken from* [3].

Parameter	$f_0(1710)$ fit				$f_2(1710)$ fit	
	fit-H	fit-L	H,L combined	PDG	fit-H	fit-L
χ^2/ndf	694.2/585	701.6/585	–	–	796.3/585	831.5/585
Mass(f_J) (MeV/c^2)	1750^{+5+29}_{-6-18}	1749^{+5+31}_{-6-42}	1750^{+6+29}_{-7-18}	1720 ± 6	1750^{+6}_{-7}	1729^{+6}_{-7}
$\Gamma_{\rm tot}(f_J)$ (MeV)	138^{+12+96}_{-11-50}	145^{+11+31}_{-10-54}	139^{+11+96}_{-12-50}	135 ± 6	132^{+12}_{-11}	150 ± 10
$\Gamma_{\gamma\gamma}\mathcal{B}(K\bar{K})_{f_J}$ (eV)	12^{+3+227}_{-2-8}	21^{+6+38}_{-4-26}	12^{+3+227}_{-2-8}	unknown	$2.1^{+0.5}_{-0.3}$	1.6 ± 0.2

A fit with a tensor meson (labeled $f_2(1710)$) for structure around 1.8GeV, which can be $a_2(1700)$ or $f_2(1810)$, was also preformed. Compared with that of $f_0(1710)$ fit, the unique best fit has poor χ^2, thus, $f_2(1710)$ fit is not favored by the data.

2.3 W-dependence of cross section

The study of W dependence of cross section in high W region is a good place to test pQCD prediction. The cross sections integrated with $|\cos\theta^\star|$ region, are fitted by aW^{-n}. Table 3 summaries fitted slope parameter n in different fit ranges. The n between 10 and 11 in $K_S^0 K_S^0$ is larger than that of $\pi^+\pi^-$ and K^+K^- processes, and is in reasonable agreement with pQCD prediction $n = 10$ [6]

3 $\gamma\gamma^\star \to 2\pi^0$ process

The cross section of $\gamma\gamma^\star \to 2\pi^0$ has been measured by single-tag method [7] for Q^2 up to 30 GeV^2, where Q^2 is negative of invariant mass squared of tagged photon, in kinematic range $0.5 < W < 2.1$GeV and $|\cos\theta^\star| < 1.0$ for total energy and pion scattering angle in $\gamma\gamma^\star$ center-of-mass frame, respectively. Figure 2 displays cross section of $\gamma\gamma^\star \to 2\pi^0$, integrated in $|\cos\theta^\star|$ region, as function of W for nine Q^2 bins. The $f_2(1270)$ and $f_0(980)$ are evident. In order to obtain transition form factors (TFF) of meson, a partial-wave amplitudes analysis was preformed in energy region $W \leq 1.5$GeV. The $f_2(1270)$ TFF with helicity-0, -1, and -2 components are measured for the first time. Figure 3 (a) shows Q^2 dependence

Table 3: *Fitted slope parameter n in different fit ranges. Taken from* [3].

W range (GeV)	$\vert\cos\theta^*\vert$ range	n	Note
$2.6-4.0$ (excluding $3.3-3.6$)	< 0.8	$11.0 \pm 0.4 \pm 0.4$	
$2.6-3.3$	< 0.8	$10.0 \pm 0.5 \pm 0.4$	
$2.6-3.3$	< 0.6	$11.8 \pm 0.6 \pm 0.4$	
$2.4-4.0$ (excluding $3.3-3.6$)	< 0.6	$10.5 \pm 0.6 \pm 0.5$	Belle 2007

of helicity-2 components of $f_2(1270)$ TFF, where solid line shows predicted Q^2 dependence by Ref. [8], dashed line and dotted-dashed line are predictions by Eq.(1) and Eq.(2) in Ref. [9], respectively. The theory prediction by Ref. [8] and Eq.(2) in Ref. [9] agree well with data. Figure 3 (b) compare measured helicity-1 components of $f_2(1270)$ TFF with prediction by Ref. [8] (solid line), which is a factor of 1.5-2 larger than measured helicity-0 data. Figure 3 (c) displays Q^2 dependence of $f_0(980)$ TFF with prediction for scalar meson in Ref. [8] (solid line), which agree fairly well with Belle data for $Q^2 \leq 10\text{GeV}^2$, but has less steeper Q^2 dependence for $Q^2 > 10\text{GeV}^2$.

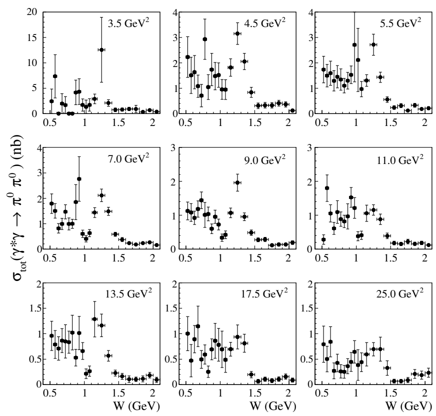

Figure 2: *The W dependence of integrated cross sections. Taken from* [7].

4 $\gamma\gamma \to p\bar{p}K^+K^-$ process

The LHCb Collaboration observed a narrow pentaquark state $P_c(4312)^+$, and two peak structure of $P_c(4450)^+$ in $J/\psi p$ at $\Lambda_b^0 \to J/\psi pK^-$ [10]. Because valence quark of $J/\psi p$ is $c\bar{c}uud$, these particles at least have five quarks. Another un-confirmed $\Theta(1540)^+$ in reaction $\gamma n \to nK^+K^-$ [11] [12], is an candidate for $uudd\bar{s}$ pentaquark state. The two-photon process provides additional method to confirm or search for pentaquark states.

The $\gamma\gamma \to p\bar{p}K^+K^-$ process and its intermediate states are measured for the first time with a $980fb^{-1}$ data at Belle [13] by no-tag method. Figure 4 (a-b) shows invariant mass of $pK^-(\bar{p}K^+)$ and K^+K^-, respectively, where a clear $\Lambda(1520)$ and ϕ are clearly observed. However, no evidence are seen for $\Theta(1540)^0 \to pK^-(\bar{p}K^+)$, $\Theta(1540)^{++} \to pK^+$ and $\Theta(1540)^{--} \to \bar{p}K^-$ (Figure 4 (c)). The sum of ϕp or $\phi\bar{p}$ invariant mass spectrum is shown in Figure 4 (d). No significant evidence of $s\bar{s}$ partner of P_c pentaquark states is observed. Finally, cross sections of $\gamma\gamma \to p\bar{p}K^+K^-$ process and its intermediate

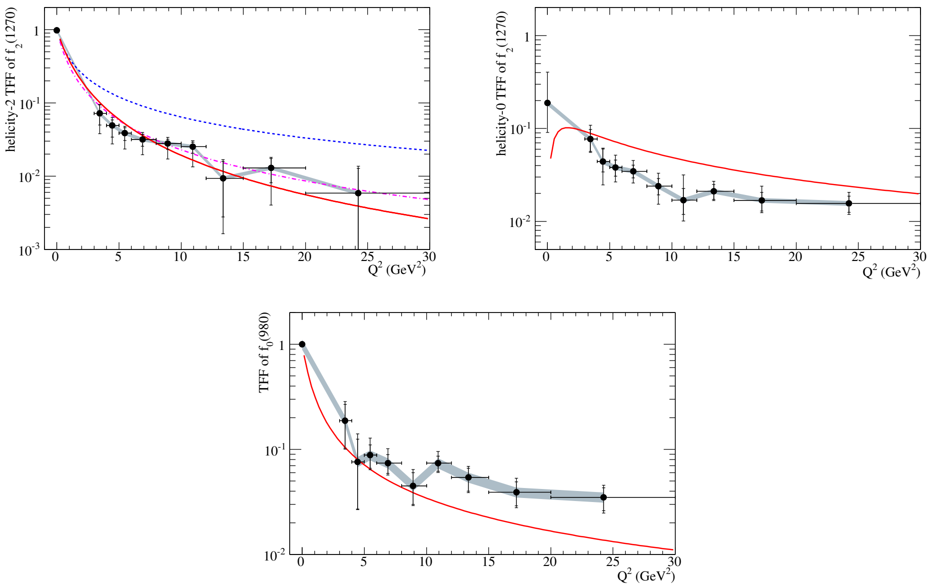

Figure 3: *(a) The Q^2 dependence of measured helicity-2 $f_2(1270)$ TFF (top left). (b) The Q^2 dependence of measured helicity-0 $f_2(1270)$ TFF (top right). (c) The Q^2 dependence of measured $f_0(980)$ TFF (bottom). Taken from* [7].

processes are also measured.

5 Summary

A partial-wave amplitudes analysis was conducted for $\gamma\gamma \to K_S^0 K_S^0$, relative phase $\phi_{a_2(1320)}$ between $f_2(1270)$ and $a_2(1320)$ is $(172.6^{+6.0+12.2}_{-0.7-7.0})^o$, and agrees with theory prediction. The $\Gamma_{\gamma\gamma}\mathcal{B}(K\bar{K})$ for $f_0(1710)$ is measured for the first time. The fitted slope parameter of W dependence of integrated cross section in high W region, is consistent with pQCD prediction The helicity-0, -1, and -2 components of $f_2(1270)$ TFF are measured for the first time in $\gamma\gamma^\star \to 2\pi^0$ process, Q^2 dependence of $f_0(980)$ and $f_2(1270)$ TFF are compared with theory prediction. There is no significant evidence of $\Theta(1540)$ and $s\bar{s}$ partner of P_c pentaquark states in $\gamma\gamma \to p\bar{p}K^+K^-$ process. With planed 50 ab^{-1} data at Belle II, we could have more deep understanding of two-photon process, and one can refer to Prof. Boris Shwartz's talk in this workshop [14].

6 Acknowledgements

This work is supported by National Natural Science Foundation of China under Contract NO. 11675166.

References

1. J. Brodzicka *et al* (Belle Collaboration), Prog. Theor. Exp. Phys. **2012**, 04D001 (2012).
2. T. Abe *et al*, Prog. Theor. Exp. Phys. **2013**, 03A003 (2012).

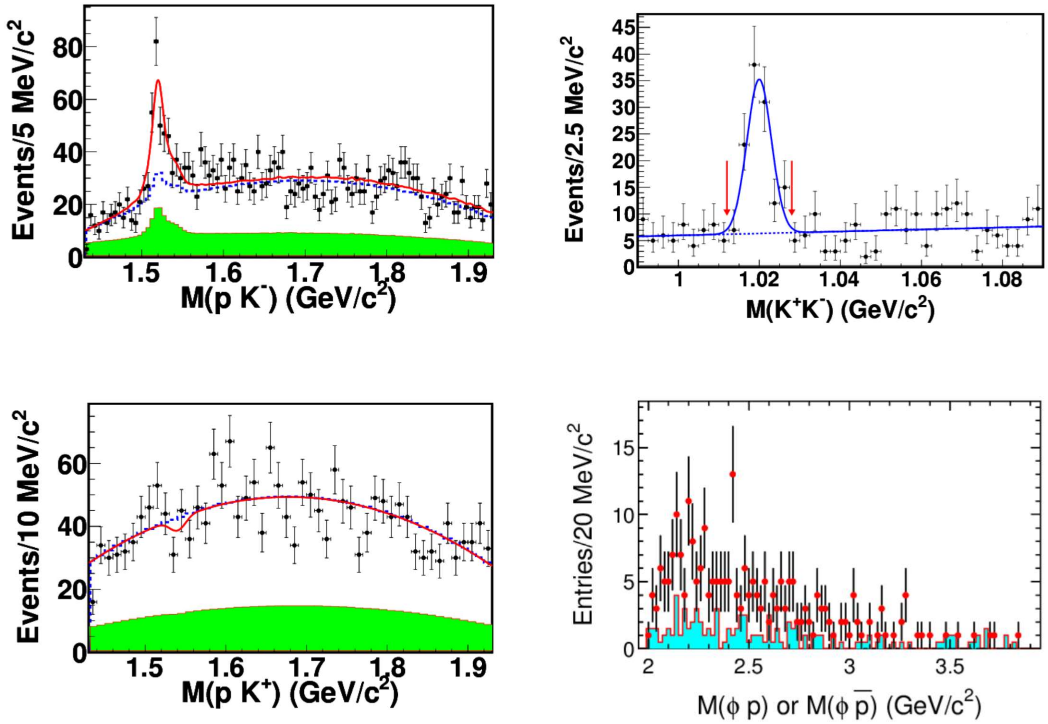

Figure 4: *(a) $pK^-(\bar{p}K^+)$ invariant mass spectrum (top left), (b)K^+K^- invariant mass spectrum (top right), (c) pK^+ invariant mass spectrum (bottom left), (d) ϕp or $\phi\bar{p}$ invariant mass spectrum (bottom right), Taken from* [13].

3. S. Uehara *et al* (Belle Collaboration), Prog. Theor. Exp. Phys. **2013**, 123C01 (2013).

4. H. Lipkin, Phys. Lett. B **59** 269 (1975).

5. M. Tanabashi *et al.* (Particle Data Group), Phys. Rev. D **98**, 030001 (2018).

6. V. L. Chernyak, arXiv:1212.1304[hep-ph]

7. M. Masuda *et al* (Belle Collaboration), Phys. Rev. D **93**, 032003 (2016).

8. G. A. Schuler *et al*, Nucl. Phys. B **523**, 423 (1998).

9. V. Pascalutsa *et al*, Phys. Rev. D **85**, 116001 (2012).

10. R. Aaij *et al* (LHCb Collaboration), Phys. Rev. Lett. **122**, 222001 (2019).

11. T. Nakano *et al* (LEPS Collaboration), Phys. Rev. Lett. **91**, 012002 (2003).

12. T. B. Liu *et al*, Int. J. Mod. Phys. A **29**, 1430020 (2014).

13. C.P. Shen *et al* (Belle Collaboration), Phys. Rev. D **93**, 112017 (2016).

14. Boris Shwartz, proceeding in this workshop.

Frascati Physics Series Vol. 69 (2019)
PHOTON 2019 - International Conference on the Structure and the Interactions of the Photon
Jun 3-7, 2019

RECENT RESULTS ON TWO-PHOTONS PROCESSES AT BABAR

Peter A. Lukin*
on behalf of the BaBar Collaboration
Russia, 630090, Novosibirsk, Lavrentyeva Avenue, 11, Budker Institute of Nuclear Physics
Russia, 630090, Novosibirsk, Pirogova street, 1, Novosibirsk State University

Abstract

We report the results of study of the process $e^+e^- \to e^+e^-\eta'$ in the double-tag mode and measure for the first time the $\gamma^\star\gamma^\star \to \eta'$ transition form factor $F_{\eta'}(Q_1^2, Q_2^2)$ in the momentum-transfer range $2 < Q_1^2, Q_2^2 < 60$ GeV^2, obtained with the BaBar detector at center-of-mass energies near 10.6 GeV.

1 Introduction

We report on the measurement of the $\gamma^\star\gamma^\star \to \eta'$ transition form factor (TFF) by using the two-photon-fusion reaction $e^+e^- \to e^+e^-\eta'$. The TFF is defined via the amplitude for the $\gamma^\star\gamma^\star \to \eta'$ transition

$$T = -i4\pi\alpha\epsilon_{\mu\nu\beta\gamma}\varepsilon_1^\mu\varepsilon_2^\nu q_1^\beta q_2^\gamma F_{\eta'}(Q_1^2, Q_2^2), \tag{1}$$

where α is the fine structure constant, $\epsilon_{\mu\nu\alpha\beta}$ is the totally antisymmetric Levi-Civita tensor, $\varepsilon_{1,2}$ and $q_{1,2}$ are the polarization vectors and four-momenta, respectively, of the space-like photons, $Q_{1,2}^2 = -q_{1,2}^2$, and $F_{\eta'}(Q_1^2, Q_2^2)$ is the transition form factor.

We measure the differential cross section of the process $e^+e^- \to e^+e^-\eta'$ in the double-tag mode, in which both scattered electrons[1] are detected (tagged). The tagged electrons emit highly off-shell photons with momentum transfers $q_{e^+}^2 = -Q_{e^+}^2 = (p_{e^+} - p'_{e^+})^2$ and $q_{e^-}^2 = -Q_{e^-}^2 = (p_{e^-} - p'_{e^-})^2$, where $p_{e^\pm}$ and $p'_{e^\pm}$ are the four-momenta, respectively, of the initial- and final-state electrons. We measure for the first time $F_{\eta'}(Q_1^2, Q_2^2)$ in the kinematic region with two highly off-shell photons $2 < Q_1^2, Q_2^2 < 60$ GeV^2. The η' transition form factor $F_{\eta'}(Q^2, 0)$ in the space-like momentum transfer region and in the

*Speaker. E-mail: P.A.Lukin@inp.nsk.su

[1] Unless otherwise specified, we use the term "electron" for either an electron or a positron.

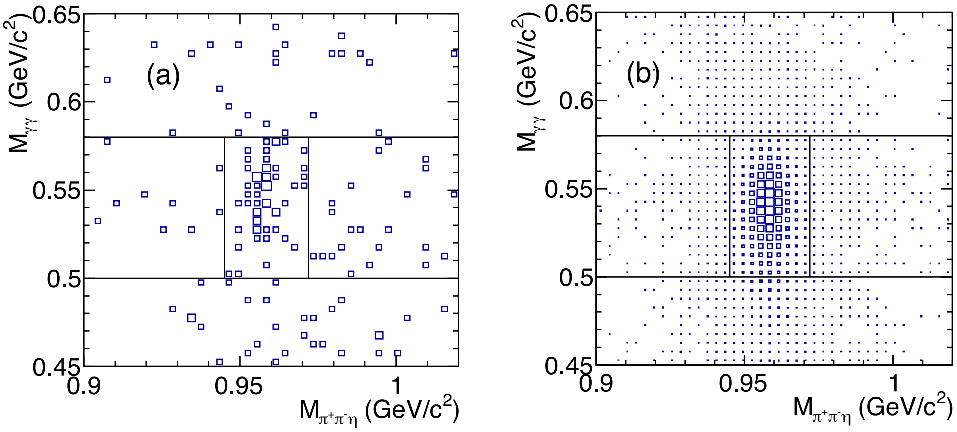

Figure 1: *Distribution of the η candidate mass ($M_{\gamma\gamma}$) versus the η' candidate mass ($M_{\pi^+\pi^-\eta}$) for data (a) and signal MC simulation (b). The horizontal lines indicate the boundaries of the selection condition applied. The vertical lines correspond to the restriction $0.945 < M_{\pi^+\pi^-\eta} < 0.972$ GeV/c^2 that is used for the plot of $Q^2_{e^-}$ versus $Q^2_{e^+}$ distribution in Fig. 2.*

single-tag mode was measured in several previous experiments [1, 2, 3, 4, 5]. The most precise data at large Q^2 were obtained by the CLEO [4] experiment, and then by the BaBar [5] experiment, in the momentum transfer ranges $1.5 < Q^2 < 30$ GeV^2 and $4 < Q^2 < 40$ GeV^2, respectively. Many theoretical models exist for the description of the TFFs of pseudoscalar mesons, $F_P(Q_1^2, 0)$ and $F_P(Q_1^2, Q_2^2)$ (see for example Refs. [6, 7, 8, 9]). Measurement of the TFF at large Q_1^2 and Q_2^2 allows the predictions of models inspired by perturbative QCD (pQCD) to be distinguished from those of the vector dominance model (VDM) [10, 11, 12]. In the case of only one off-shell photon, both classes of models predict the same asymptotic dependence $F_P(Q^2, 0) \sim 1/Q^2$ as $Q^2 \to \infty$, while for two off-shell photons the asymptotic predictions are quite different, $F(Q_1^2, Q_2^2) \sim 1/(Q_1^2 + Q_2^2)$ for pQCD, and $F(Q_1^2, Q_2^2) \sim 1/(Q_1^2 Q_2^2)$ for the VDM model.

2 Data set and event selection

The data used in this analysis were collected with the BaBar detector at the PEPII asymmetric-energy e^+e^- collider, at the SLAC National Accelerator Laboratory. A total integrated luminosity of 468.6 fb^{-1} [13] is used. The decay chain $\eta' \to \pi^+\pi^-\eta \to \pi^+\pi^-2\gamma$ is used to reconstruct the η' meson candidate. Two photon candidates are combined to form an η candidate. We apply a kinematic fit to the two photons, with an η mass constraint to improve the precision of their momentum measurement. An η' candidate is formed from a pair of oppositely charged pion candidates and an η candidate. The final selection uses tagged electrons and is based on variables in the c.m. frame of the initial e^+ and e^-. The total momentum of the reconstructed $e^+e^-\eta'$ system ($P^\star_{e^+e^-\eta'}$[2]) must be less than 0.35 GeV/c. The total energy of the $e^+e^-\eta'$ system must be in the range of 10.30–10.65 GeV. To reject background from QED events, requirements on the energies of the detected electron and positron are applied. The distribution of the η candidate mass versus the η' one for the selected data and simulated signal samples is shown in Fig. 1. A clustering of events in the central region of the data distribution corresponds to

[2] The superscript asterisk indicates a quantity calculated in the e^+e^- c.m. frame

the two-photon η' production. To further suppress background we require that the invariant mass of the η candidate be in the range 0.50–0.58 GeV/c^2, as shown by the horizontal lines in Fig. 1.

Data events that pass all selection criteria are divided into five ($Q^2_{e^-}$, $Q^2_{e^+}$) regions, as illustrated on Fig. 2 for events with $0.945 < M_{\pi^+\pi^-\eta} < 0.972$ GeV/c^2. Because of the symmetry of the process under the exchange of the e^- with the e^+, regions 3 and 4 each include two disjunct regions, mirror symmetric with respect to the diagonal. The number of signal events ($N_{\rm events}$) in each ($Q^2_{e^-}$, $Q^2_{e^+}$) region is obtained from a fit to the $\pi^+\pi^-\eta$ invariant mass spectrum with a sum of signal and background distributions. The total number of signal events is $46.2^{+8.3}_{-7.0}$. The total systematic uncertainty related to the description of the background and signal is 3.7% and the total systematic uncertainty of the detection efficiency is 11%. Following the methods developed in the single-tag analysis of Ref. [5], we have studied possible sources of peaking background.

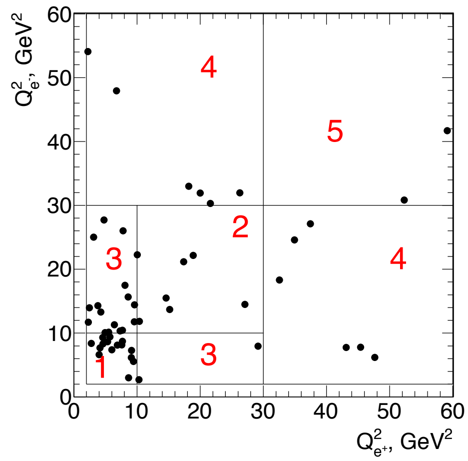

Figure 2: *The $Q^2_{e^-}$ versus $Q^2_{e^+}$ distribution for data events. The lines and numbers indicate the five regions used for the study of the dynamics of TFF a function of $Q^2_{e^-}$ and $Q^2_{e^+}$.*

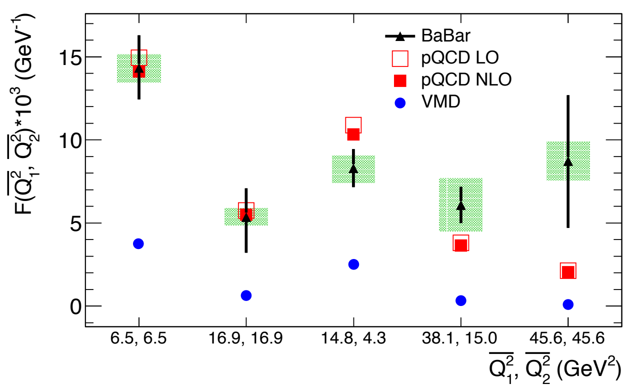

Figure 3: *Comparison of the measured $\gamma^\star\gamma^\star \to \eta'$ transition form factor (triangles, with error bars representing the statistical uncertainties) with the LO (open squares) and NLO (filled squares) pQCD predictions and the VDM predictions (circles).*

3 Cross section and form factor

The cross section in the entire range of momentum transfer $2 < Q_1^2, Q_2^2 < 60$ GeV^2 is $\sigma = 11.4^{+2.8}_{-2.4}$ fb, where the uncertainty is statistical. The systematic uncertainty includes the uncertainty in the number of signal events associated with background subtraction (Sec. 2), the uncertainty in the detection efficiency, the uncertainty in the calculation of the radiative correction (1%) [14], and the uncertainty in the integrated luminosity (1%) [13]. The total systematic uncertainty (12%) is the sum in quadrature of all the systematic contributions. The model uncertainty is described in [15].

The obtained values of the transition form factor are published in [15] and are represented in Fig. 3 by the triangles. The error bars attached to the triangles indicate the statistical uncertainties. The quadratic sum of the systematic and model uncertainties is shown by the shaded rectangles. The open and filled squares in Fig. 3 correspond to the LO and NLO pQCD predictions, respectively. The NLO correction is relatively small. The measured TFF is, in general, consistent with the QCD prediction. The circles in Fig. 3 represent the predictions of the VDM model, which exhibits a clear disagreement with the data.

4 Summary

So, we have studied for the first time the process $e^+e^- \to e^+e^-\eta'$ in the double-tag mode and have measured the $\gamma^\star\gamma^\star \to \eta'$ transition form factor in the momentum-transfer range $2 < Q_1^2, Q_2^2 < 60$ GeV^2. The measured values of the form factor are in agreement with the pQCD prediction and contradict the prediction of the VDM model.

5 Acknowledgements

We are grateful for the extraordinary contributions of our PEPII colleagues in achieving the excellent luminosity and machine conditions and we have received support from the Russian Foundation for Basic Research (grant No. 18-32-01020).

References

1. C. Berger *et al.* (PLUTO Collaboration), Phys. Lett. B **142**, 125 (1984).
2. H. Aihara *et al.* (TPC/Two Gamma Collaboration), Phys. Rev. D **38**, 1 (1988); Phys. Rev. Lett. **64**, 172 (1990).
3. H.-J. Behrend *et al.* (CELLO Collaboration), Z. Phys. C **49** (1991) 401.
4. J. Gronberg *et al.* (CLEO Collaboration), Phys. Rev. D **57**, 33 (1998).
5. P. del Amo Sanchez *et al.* (BaBar Collaboration),Phys. Rev. D **84**, 052001 (2011).
6. G. Kopp, T. F. Walsh, and P. M. Zerwas, Nucl. Phys. B **70**, 461 (1974).
7. S. Berman and D. Geffen, Nuovo Cim. **18**, 1192 (1960).
8. P. Kroll, Nucl. Phys. B (Proc. Suppl.) **219-220**, 2 (2011).
9. S. Agaev *et al.*, Phys. Rev. D **90**, 074019 (2014).
10. B.-l. Young, Phys. Rev. **161**, 1620 (1967).
11. L. G. Landsberg, Phys. Rep. **128**, 301 (1985).
12. A. Dorokhov, M. Ivanov, and S. Kovalenko, Phys.Lett. B **677**, 145 (2009).
13. J. P. Lees *et al.* (BaBar Collaboration), Nucl. Instrum. Methods Phys. Res., Sect. A **726**, 203 (2013).
14. S. Ong and P. Kessler, Phys. Rev. D **38**, 2280 (1988).
15. Lees J. P. *et al.* (BaBar Collaboration), Physical Review D **98**, 112002 (2018).

Frascati Physics Series Vol. 69 (2019)
PHOTON 2019 - International Conference on the Structure and the Interactions of the Photon
Jun 3-7, 2019

$\gamma - \gamma$ PHYSICS AT KLOE-2

Dario Moricciani on behalf of KLOE-2 collaboration
INFN-Laboratori Nazionali di Frascati

Abstract

The precision measurement of the $\pi^0 \to \gamma\gamma$ width allows to gain insights into the low-energy QCD dynamics. The precision needed (1%) in order to test theory predictions can be achieved by studying the π^0 production through $\gamma\gamma$ fusion in the $e^+e^- \to e^+e^-\gamma^*\gamma^* \to e^+e^-\pi^0$ reaction. The KLOE-2 experiment has the capability of performing such measurement thanks to a new detector, the High Energy Tagger (HET), installed along the DAΦNE beamline, which allows to tag the final state leptons and to reduce the background coming from Φ meson decays. The HET detector measures the deviation of leptons from their main orbit by determining their position and timing.

1 Introduction

One of the main goals of KLOE-2 is the precision measurement of the π^0 width, $\Gamma_{\pi^0\to\gamma\gamma}$, which is a strong test of low-energy QCD. The $\Gamma_{\pi^0\to\gamma\gamma}$ is predicted with 1.4% precision ($\Gamma^{\mathrm{Th.}}_{\pi^0\to\gamma\gamma} = 8.09 \pm 0.11$ eV [1, 2]) while the most precise experimental measurement ($\Gamma^{\mathrm{Exp}}_{\pi^0\to\gamma\gamma} = 7.82 \pm 0.22$ eV [3]), obtained with the Primakoff conversion, has 2.8% precision [1].

To achieve the precision needed to test QCD it is usefull the π^0 production through $\gamma\gamma$ fusion in the reaction $e^+e^- \to e^+e^-\gamma^*\gamma^* \to e^+e^-\pi^0$. This task can be achieved by the KLOE-2 experiment thanks to the installation, in both arms of the DAΦNE layout, of two tagger stations in order to detect high energy scattered electrons coming from interaction point. About 10^4 events are expected to be detected in a three-fold coincidence between the KLOE central detector (KLOEcd) and the two HET stations, with an integrated luminosity of 5 fb^{-1} [5].

[1]The PDG value is $\Gamma^{\mathrm{PDG}}_{\pi^0\to\gamma\gamma} = 7.63 \pm 0.16$ eV [4]

The KLOE-2 experiment also aims also to perform the first measurement of the $F_{\pi^0\gamma^*\gamma}$ form factor at low transferred momentum ($Q^2 \leq 0.1\,\mathrm{GeV}^2$) in the space-like region. This quantity may have an impact on the value and precision of the contribution of one-neutral pion exchange to the hadronic light-by-light scattering, $a_\mu^{\mathrm{LbyL};\pi^0}$, a term of the muon anomaly calculation, g-2 [5].

2 The HET Detector

The HET is a position detector able to measure the deviation of the off-energy leptons from their main orbit in DAΦNE. The HET stations are placed inside roman pots at the exit of the dipole magnets, 11 m away from the IP, on both the positron and the electron arm, as shown in figure 1. The sensitive area is made up of a set of 28 plastic scintillators (EJ-228), designed for ultra-fast timing and ultra-fast counting applications, with dimensions $(3\times5\times6)$ mm^3 each. One additional scintillator, of dimensions $(3\times50\times6)$ mm^3, whose acceptance covers all the others, is used to reinforce evidence for real particles crossing the detector.

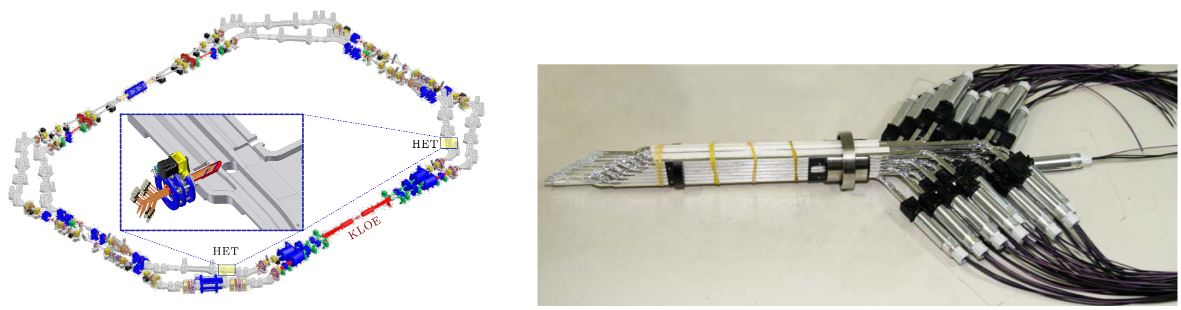

Figure 1: *(a) A drawing of the two HET detectors placed on DAΦNE lattice. (b) A picture of the HET detector assembled with the photomultipliers.*

The light emitted by each of the 28 scintillators is read out through a plastic light guide by a high quantum efficiency photomultiplier (35% for wavelengths between 300–400 nm) which matches well the scintillator spectrum. Figure 1 shows a picture of the HET detector assembled with the photomultipliers. The 28 scintillators are placed at different distances from the beam-line, in such a way that the measurement of the distance between the beam and the detected particle can be performed simply knowing which scintillator has been fired.

A dedicated DAQ electronic board, based on a Xilinx Virtex-5 FPGA, which uses custom logic to manage signals from DAΦNE, KLOE and HET, has been developed for this detector [6]. It provides a MultiHit TDC with a time resolution of 550(1) ps giving us the possibility to clearly identify the correct bunch crossing ($\Delta T_{\mathrm{bunch}} = 2.7$ ns) and reproduce the DAΦNE bunch structure. In Figure 2 it is shown the TDC spectrum for a special run where specific bunch pattern in DAΦNE beam was filled.

3 Data Analysis

The counting rate of the HET is largely dominated by leptons coming from Bhabha scattering at very low angle that we have studied to validate the MonteCarlo transport through the DAΦNE beam line and to monitor the stability of the operation during data acquisition. The effective cross section, defined as product of the low-angle Bhabha cross section, the HET acceptance, and the detector efficiency, $\sigma\times A\times\varepsilon$,

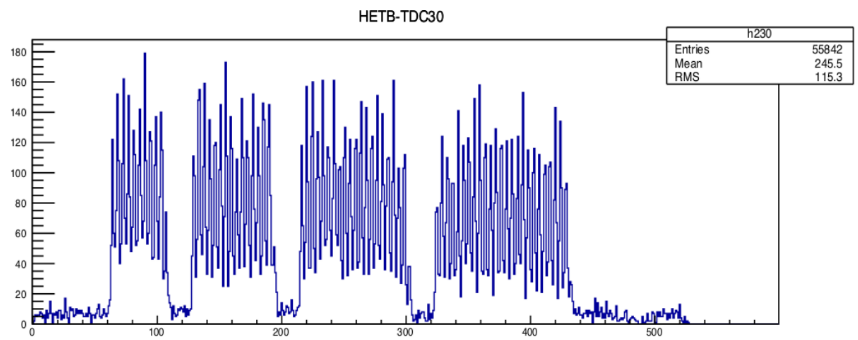

Figure 2: *TDC spectrum (TDC counts) for DAΦNE specific run: not all the bunches where filled*

is of the order of 10 mbarn, with large variations on the scintillators closest to the beam. A sub-set of scintillators with optimal stability over a time-scale of several months has been identified in each station, and used in the π^0 search. A KLOE-2 data sample of 0.5 fb^{-1} has been analysed by selecting events having:

- two clusters in the KLOE barrel calorimeter associated to the same bunch in DAΦNE, within 25 ns from the trigger time;
- at least one hit scintillator in the HET, associated with a bunch in DAΦNE within 25 ns from the bunch which produce the trigger.

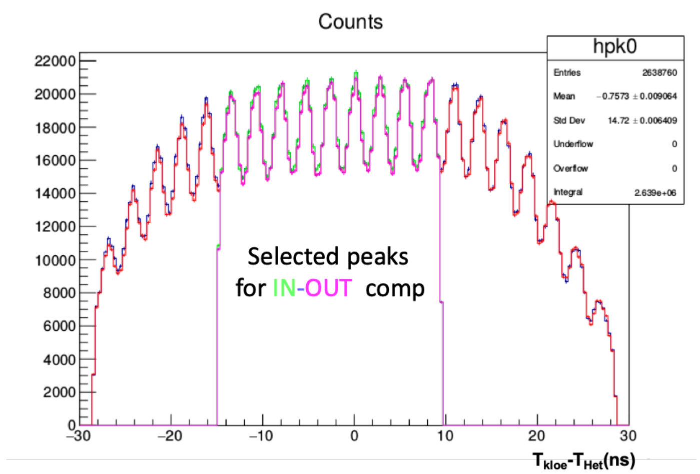

Figure 3: *Counting rate as function of $T_{Kloe} - T_{Het}$*

Bhabha scattering completely overwhelms $\gamma\gamma$ signal and HET-KLOE coincidences are dominated by accidentals even at one-bunch-crossing level. Since the HET data acquisition (DAQ) window is about 3 times larger than the KLOE one HET events that are "out-of-time" with respect to KLOE DAQ are used for the precision measurement of the accidentals during data taking. Real coincidences are expected to emerge from the subtraction of the accidentals with respect to the events in "overlapping-window". Statistical evidence ($> 5\ \sigma$) of real coincidences has been observed, as shown in Figure 3.

In Figure 4 are shown the invariant mass distributions of the two γ's detected in KLOE for the events in the "overlapping-window" and "out-of-time-window; this plot and similar ones are used to validate the analysis procedure.

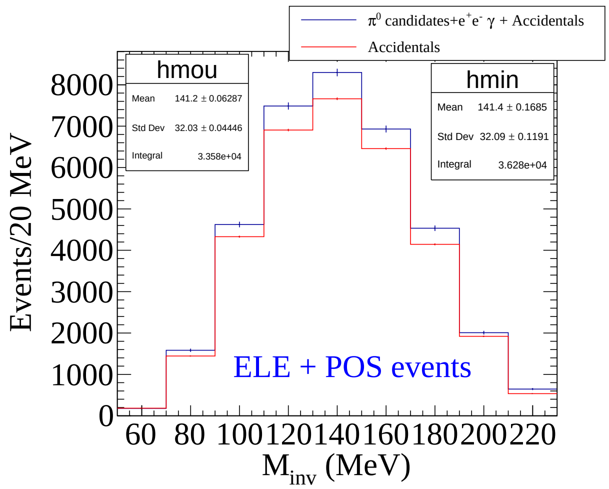

Figure 4: *Invariant mass of two γ's in KLOE for "overlapping-windows" and "out-of-time window". We add events where final leptons are tagged in the electron or positron HET stations.*

MonteCarlo generation of the signal is based on `Ekhara` [7] and lepton transport along the beam line has been developed on `BDSIM` [8]. A multi-variate analysis trained with the MonteCarlo signal, and taking accidentals from the data in the "out-of-time" window, is being performed in order to separate $\gamma\gamma$ processes from radiative Bhabha's.

More data are being reconstructed and more efforts are being devoted to accidental reduction, that is the crucial issue to be solved for a precision measurement of the π^0 radiative width.

References

1. K. Kampf, B. Moussallam, Phys. Rev. D **79** (2009) 076005.
2. J. Bijnens, K. Kampf, Nucl. Phys. B Proc. Suppl. **207-208** (2010) 220.
3. H. Primakoff, Phys. Rev. **81** (1951) 899.
4. Particle Data Group, Chin. Phys. C **40** (2016) 100001.
5. D. Babusci *et al.*, Eur. Phys. J. C **72** (2012) 1917.
6. A. Balla *et al.* Nucl. Instr. and Meth. A **739** (2014) 75.
7. H. Czyz *et al.*, Comp. Phys. Comm. **234** (2019) 245.
8. I. Agapov *at al.* Nucl. Inst. and Meth. **606** (2009) 708.

Frascati Physics Series Vol. 69 (2019)
PHOTON 2019 - International Conference on the Structure and the Interactions of the Photon
June 3-7, 2019

TRANSITION FORM FACTOR MEASUREMENTS AT BESIII

Christoph Florian Redmer
Institute for Nuclear Physics, Johannes Gutenberg-University Mainz, 55099 Mainz, Germany

Abstract

Motivated by the recent developments in data-driven approaches to improve the hadronic light-by-light scattering calculations of the Standard Model prediction of the anomalous magnetic moment of the muon a_μ, the BESIII collaboration has embarked on a dedicated two-photon physics program. The momentum dependence of transition form factors of single pseudoscalar mesons, as well as of multi-meson systems is studied. Based on the high statistics data, collected at the τ-charm factory BESIII operated at the BEPCII accelerator in Beijing, the information can be provided in the relevant momentum region for a_μ. In this presentation we discuss recent results, the current status of ongoing measurements, and the prospects for $\gamma\gamma$ collision studies at BESIII.

1 Introduction

The anomalous magnetic moment of the muon a_μ is defined as the relative deviation of the muon's Landé factor g_μ from the Dirac solution, which predicts a value of $g = 2$. It is one of the most precisely known observables in the Standard Model, and is determined in theory and experiment to a precision of 0.5 ppm [1, 2]. However, there is a long standing discrepancy of more than three standard deviations between the Standard Model prediction and the direct measurement of a_μ. Since it can be a hint for New Physics, the discrepancy triggered a worldwide effort to increase the accuracy in both theory and experiment. In the course of this endeavor, two new direct measurements of a_μ are planned, which aim at improving the accuracy of the current value by a factor four. The E989 experiment at Fermilab [3] reuses the storage ring of the BNL E821 experiment. Due to a higher beam intensity and an improved apparatus, a first result with a statistical accuracy equivalent to the BNL result is expected by the end of 2019. A second experiment is planned at J-PARC, Tokai, which makes use of ultra-cold muon beams eliminating the need for focusing electric fields in the experimental apparatus [4]. Thus, the measurement will be a systematically independent cross check of the Fermilab result.

In the same way the direct measurement is improved, also the Standard Model prediction needs to be improved. While the absolute value of a_μ is almost completely determined from quantum electrodynamics (QED), its uncertainty is completely dominated by the hadronic contributions to the quantum corrections. These cannot be calculated perturbatively due to the running of the strong coupling constant at the relevant energy scale. Non-perturbative efforts like lattice QCD have not yet reached the necessary precision [5]. Other non-perturbative approaches need information from experiments as input to provide a prediction of the hadronic contributions. Generally, the hadronic contributions to a_μ are separated into two parts, the hadronic vacuum polarization (HVP) and the hadronic light-by-light scattering (HLbL) contributions. While the former can at leading order be systematically improved with the help of a dispersion integral [6], which takes cross sections measured at e^+e^- colliders as input, the calculations of the latter process are more involved. The contribution of HLbL can be split up in a dominating contribution of pseudoscalar meson pole exchanges, a contribution of pion and kaon loops, and minor contributions due to scalar and axial resonances as well as quark loops [7]. Recently, dispersive frameworks have been devised, which allow to determine the two leading contributions in a data-driven way [8]. The relevant experimental inputs are transition form factors of pseudoscalar mesons at arbitrary virtualities, and the partial waves of the process $\gamma^*\gamma^* \to \pi\pi$. It can be shown that information on these observables at small spacelike momentum transfer, below approximately $1\,\mathrm{GeV}^2$, is most relevant [9]. However, existing data is scarce and is mostly acquired at B-factories with large momentum transfers [10, 11]. The BESIII experiment can provide data in the relevant momentum range with high accuracy.

2 The BESIII detector at BEPCII

The BESIII detector is a magnetic spectrometer [12] located at the Beijing Electron Positron Collider (BEPCII) [13]. The cylindrical core of the BESIII detector consists of a helium-based multilayer drift chamber (MDC), a plastic scintillator time-of-flight system (TOF), and a CsI(Tl) electromagnetic calorimeter (EMC), which are all enclosed in a superconducting solenoidal magnet providing a 1.0 T magnetic field. The solenoid is supported by an octagonal flux-return yoke with resistive plate counter muon identifier modules interleaved with steel. The acceptance of charged particles and photons is 93% over 4π solid angle. The charged-particle momentum resolution at $1\,\mathrm{GeV}/c$ is 0.5%, and the dE/dx resolution is 6% for the electrons from Bhabha scattering. The EMC measures photon energies with a resolution of 2.5% (5%) at 1 GeV in the barrel (end cap) region. The time resolution of the TOF barrel part is 68 ps, while that of the end cap part is 110 ps. The end cap TOF system is upgraded in 2015 with multi-gap resistive plate chamber technology, providing a time resolution of 60 ps [14].

BEPCII provides e^+e^- collisions at center of mass energies between 2.0 GeV and 4.6 GeV. The design luminosity of the machine of $10^{33}\mathrm{cm}^{-2}\mathrm{s}^{-1}$ at the center of mass energy $\sqrt{s} = 3.773\,\mathrm{GeV}$ has been achieved. The data taking campaigns focus on the many aspects of the BESIII physics program of charmonium spectroscopy, open charm physics, light hadron spectroscopy and precise τ-mass and R scan measurements. The worlds largest data sets on e^+e^- collisions in the τ-charm region have been acquired. As of 2019, these correspond in total to an integrated luminosity of more than $20\,\mathrm{fb}^{-1}$, which includes among others a sample of 10^{10} J/ψ decays recorded on disk [15].

3 Transition Form Factors of Pseudoscalar Mesons

At BESIII, transition form factors (TFF) of pseudoscalar mesons can be measured in three different reactions. Dalitz decays of pseudoscalar mesons, as well as their radiative production in e^+e^- annihilations allow to determine TFF in the timelike regime. The meson mass puts a lower and upper limit on the momentum transfer range accessible in the respective process. The spacelike regime of the momentum dependence of TFFs can be studied in two-photon fusion reactions. In an e^+e^- collision both leptons can exchange a photon, which in turn fuse and form mesons of the quantum numbers $J^{PC} = 0, 2^{\pm +}$. These states are not directly accessible in the dominating annihilation processes, where only a single photon is exchanged. The cross section of these two-photon reactions is directly proportional to the square of the TFF, which in turn is a function of the virtualities of the two photons. The virtuality can be measured as it corresponds to the momentum transfer $q^2 = -Q^2$ of the scattered leptons. Limitations in the accessible range of Q^2 come from the detector acceptance. Like most detectors at e^+e^- colliders, at BESIII the region of polar angles below $\cos\theta \geq 0.93$ is not covered by detector elements, due to the beam optics necessary to establish the collisions. Unfortunately, the differential cross section of two-photon fusion reactions is peaked towards small scattering angles of the leptons. A practical way to still learn about the momentum dependence of meson TFFs are single-tagged measurements. In this analysis technique, apart from the produced meson, only one of the two scattered leptons is required to be registered in the active detector volume. The four-momentum of the second lepton is reconstructed from energy and momentum conservation. By requiring the polar angle of the missing momentum to be small, also the momentum transfer of the respective lepton will be small. In the selected two-photon events a virtual and a quasi-real photon are exchanged. The measured TFF $F_{p\gamma^*\gamma^*}(Q_1^2, Q_2^2)$ of a meson p depends now only on a single virtuality $F_{p\gamma^*\gamma}(Q_1^2, Q_2^2 = 0) \equiv F_{p\gamma^*\gamma}(Q^2)$.

As a first measurement at BESIII the spacelike TFF of π^0 is measured in a single-tagged analysis of $2.318\,\mathrm{fb}^{-1}$ taken at $\sqrt{s} = 3.773\,\mathrm{GeV}$. The meson is reconstructed from its dominating decay mode in two photons. The selected event topology of an electron or positron and at least two photons has a dominating background contribution from radiative Bhabha scattering. Apart from the single-tag condition explained above, these events can be effectively rejected with conditions on the helicity angle of the photons assigned to the π^0 candidate, as well as their polar angle difference in the lab frame. The latter condition addresses effects of cluster splitting observed for high energetic photons. An additional condition, successfully used by the BaBar collaboration to reduce background contributions of radiative effects in two-photon events [11)], turned out to efficiently remove remaining background contributions from annihilation reactions producing $q\bar{q}$ continuum events. Remaining background contributions are subtracted from the differential momentum transfer distribution, by fitting the π^0 peak above the continuous background distribution in the two photon invariant mass distribution for each bin in Q^2. The background subtracted distribution is normalized to the respective bin widths, the detection efficiency, and the integrated luminosity of the data, in order to determine the differential cross section. The TFF is extracted by dividing out the pointlike cross section using Monte Carlo generated distributions based on the Ekhara 3.0 event generator [16)].

Figure 1 shows the preliminary result of the spacelike π^0 TFF measurement. Momentum transfers from $0.3\,\mathrm{GeV}^2$ to $3.1\,\mathrm{GeV}^2$ are covered. The left panel compares the BESIII measurement to previous results in the same region of momentum transfer. At largest values of Q^2 the accuracy is compatible with the results of the CLEO collaboration [10)], while below $1.5\,\mathrm{GeV}^2$ the accuracy of BESIII exceeds that of all previous measurements. Furthermore, the range of available information is extended, as the CELLO result only provided data down to $0.5\,\mathrm{GeV}^2$ [10)]. The center panel of fig.1 confronts the preliminary

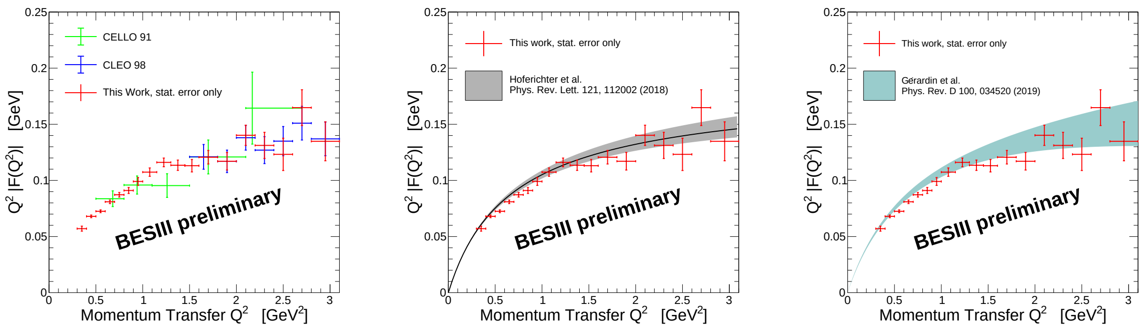

Figure 1: *The preliminary result of the π^0 TFF measurement.* **Left:** *A comparison to previous measurements* [10]. **Center:** *A comparison to the prediction of a dispersive construction of the TFF* [17]. **Right:** *A comparison to a lattice calculation of the TFF* [18].

BESIII result with a prediction of the pion TFF, which is constructed in dispersive theory from existing time-like data [17]. The data show good agreement, although especially at smaller values of Q^2 the data rather seem to follow the edge of the error band of the prediction than its central value. In the right panel of fig.1 the preliminary data are compared to the lattice calculation [18] of the singly-virtual pion TFF. A similar relation between experiment and theory as for the dispersive calculation is observed, where the data points rather agree with the edge of the error band corresponding to one standard deviation. The preliminary BESIII result does not yet include a proper treatment of radiative effects. This will be taken into account using full calculations of radiative corrections implemented in the Ekhara 3.0 event generator [16].

4 Transition Form Factors of the Two-Pion System

With the exception of a recent Belle result on neutral pion pairs [19], all information on the two-photon production of pion pairs has been acquired in collisions of quasi-real photons [20]. Additionally, information on the two pion systems with small invariant masses barely exists. At BESIII a single-tagged analysis has been started, using a combined data set of $7.5\,\mathrm{fb}^{-1}$ at $3.773 \leq \sqrt{s}\,[\mathrm{GeV}] \leq 4.6$, with the aim to measure $\gamma\gamma^* \to \pi^+\pi^-$ over a wide range of the parameter space relevant for the data-driven calculations of the HLbL contributions to a_μ. The strategy of the analysis follows the techniques successfully applied for single pseudoscalar mesons. The dominating background contributions come from two distinct sources. On the one hand, the conventionally applied means of particle identification cannot sufficiently separate pions from muons, which leads to a strong contribution of the reaction $e^+e^- \to e^+e^-\mu^+\mu^-$. On the other hand, the radiative Bhabha scattering process, where the photon couples to a ρ meson, which in turn decays into charged pion pairs, leads to an irreducible background of the reaction $e^+e^- \to e^+e^-\rho \to e^+e^-\pi^+\pi^-$.

The former source of background is well understood in terms of existing Monte Carlo event generators [21]. These are used to train and apply machine learning techniques based on boosted decision trees in order to achieve a track based separation of pions and muons. In this way, the background from muon pair production can be efficiently suppressed. The irreducible source of background from pion production is subtracted from data using the precise knowledge of the pion form factor and its available parametrizations. Taking into account the $\gamma\gamma$ luminosity function, the background subtracted data allow to study the reaction $\gamma\gamma^* \to \pi^+\pi^-$ for the first time at momentum transfers between $0.2 \leq Q^2[\mathrm{GeV}^2] \leq 2.0$ at invariant masses starting from the two pion threshold up to $2\,\mathrm{GeV}$, at a full coverage of the pion helicity angle.

5 Outlook

The successful measurement of the pion TFF is being extended to other pseudoscalar mesons. The η meson has already been observed in the decay photon invariant mass spectrum used for the background subtraction in the π^0 TFF measurement. Additional, feasibility studies are performed, where the η production is tagged using the three pion decay modes. All tests indicate a TFF result covering the same Q^2 range as achieved for the π^0 with competitive accuracy. Similar studies have been done for the η' meson, where the decay mode $\eta' \to \pi^+\pi^-\eta$ is exploited. The studies also showed the feasibility of measurements of TFFs of axial and tensor mesons, since the $a_2(1360)$ is seen in the three pion invariant mass spectrum and the $f_1(1285)$ is seen in the $\pi^+\pi^-\eta$ invariant mass spectrum. A good knowledge of the contributions of these mesons to the HLbL contribution to a_μ is necessary to bring the precision of the Standard Model prediction of a_μ to the final accuracy aimed at by the new direct measurements. Similarly, the measurement of the two pion system is extended to neutral systems, including $\pi^0\eta$ and $\eta\eta$ final states.

So far only fractions of the complete data acquired at BESIII have been exploited. Feasibility studies have shown that by combining all data sets measurements of the doubly virtual TFF of pseudoscalar mesons are possible. Currently, only a single measurement of the η' TFF is published [22]. However, a region of momentum transfer is covered, which is of minor impact for the calculations of a_μ. At BESIII, the TFFs of π^0, η and η' will be measured at values of Q^2 around ($Q_1^2 \approx 1\,\mathrm{GeV}^2, Q_2^2 \approx 1\,\mathrm{GeV}^2$). The expected precision will allow for model independent determinations of the TFF, and is expected to have a considerable impact on the precision of the data-driven approaches to HLbL [9]. At the same time, additional tagging detectors at small angles are developed, which will extend the prospects for double-tagged two-photon measurements towards regions of smaller momentum transfer.

References

1. F. Jegerlehner and A. Nyffeler, Phys. Rept. **477**, 1 (2009).
2. G. W. Bennett *et al.*, [Muon g-2 Collaboration], Phys. Rev. D**73**, 072003 (2006).
3. J. Grange *et al.* [Muon g-2 Collaboration], arXiv:1501.06858 (2015).
4. Tsutomu Mibe [J-PARC g-2 Collaboration], Nucl. Phys. Proc. Suppl. **218**, 242-246 (2011).
5. T. Blum *et al.* [RBC and UKQCD Collaborations], Phys. Rev. Lett. **121**, 022003 (2018); T. Blum, S. Chowdhury, M. Hayakawa and T. Izubuchi, Phys. Rev. Lett. **114**, 012001 (2015).
6. M. Davier, A. Hoecker, B. Malaescu and Z. Zhang, Eur. Phys. J. C **77**, 827 (2017); A. Keshavarzi, D. Nomura and T. Teubner, Phys. Rev. D**97**, 114025 (2018).
7. E. de Rafael, Phys. Lett. B**322,** 239 (1994).
8. G. Colangelo, M. Hoferichter, M. Procura, and P. Stoffer, JHEP **1409**, 091 (2014); JHEP **1509**, 074 (2015); Phys. Rev. Lett. **118**, 232001 (2017); JHEP **1902**, 006 (2019).

9. A. Nyffeler, Phys. Rev. D**94**, 053006 (2016).

10. H. J. Behrend *et al.* [CELLO Collaboration], Z. Phys. C**49**, 401 (1991); J. Gronberg *et al.* [CLEO Collaboration], Phys. Rev. D**57**, 33 (1998);

11. B. Aubert *et al.* [BaBar Collaboration], Phys. Rev. D**80**, 052002 (2009); S. Uehara *et al.* [Belle Collaboration], Phys. Rev. D**86**, 092007 (2012).

12. M. Ablikim *et al.* [BESIII Collaboration], Nucl. Instrum. Meth. A **614**, 345 (2010).

13. C. H. Yu *et al.*, Proceedings of IPAC2016, Busan, Korea, 2016, doi:10.18429/JACoW-IPAC2016-TUYA01.

14. X. Li *et al.*, Radiat. Detect. Technol. Methods **1**, 13 (2017); Y. X. Guo *et al.*, Radiat. Detect. Technol. Methods **1**, 15 (2017).

15. M. Ablikim *et al.* [BESIII Collaboration], Chin. Phys. C**37**, 123001 (2013); Chin. Phys. C**39**, 093001 (2015); Chin. Phys. C**41**, 013001 (2017); Chin. Phys. C**42**, 023001 (2018).

16. H. Czyz and P. Kisza, Comput. Phys. Commun. **234**, 245 (2019).

17. M. Hoferichter, B. Hoid, B. Kubis, S. Leupold and S. P. Schneider, Phys. Rev. Lett. **121**, 112002 (2018); JHEP **1810**, 141 (2018).

18. A. Gérardin, H. B. Meyer and A. Nyffeler, Phys. Rev. D **100**, 034520 (2019).

19. M. Masuda *et al.* [Belle Collaboration], Phys. Rev. D**93**, 032003 (2016).

20. J. Boyer et al., Phys. Rev. D, **42**, 1350 (1990); H.-J. Behrend et al., [CELLO Collaboration], Z. Phys. C **56**, 381 (1992); T. Mori, et al., [Belle Collaboration], Phys. Rev. D **75**, 051101 (2007).

21. F.A. Berends, P.H. Daverveldt and R. Kleiss, Comp. Phys. Comm. **40**, 271 (1986); Comp. Phys. Comm. **40**, 285 (1986).

22. J. P. Lees *et al.* [BaBar Collaboration], Phys. Rev. D**98**, 112002 (2018).

Frascati Physics Series Vol. 69 (2019)
PHOTON 2019 - International Conference on the Structure and the Interactions of the Photon
Jun 3-7, 2019

OBSERVATION OF LIGHT-BY-LIGHT SCATTERING AND MEASUREMENTS OF PHOTON-PHOTON COLLISIONS AT ATLAS

Iwona Grabowska-Bold on behalf of the ATLAS Collaboration
AGH University of Science and Technology, Al. Mickiewicza 30, Kraków

Abstract

We present the observation of the light-by-light scattering process, $\gamma\gamma \to \gamma\gamma$, in lead-lead collisions at $\sqrt{s_{\mathrm{NN}}} = 5.02$ TeV. The analysis is conducted using 1.73 nb^{-1} of data collected in November 2018 by the ATLAS experiment at the LHC. Light-by-light scattering event candidates are selected in events with two photons produced exclusively, with small diphoton transverse momentum and small acoplanarity. After applying all selection criteria, 59 candidate events are observed for a background expectation of 12 ± 3 events. An excess of events over the expected background is found with an observed significance of 8.2 standard deviations. The fiducial cross-section is also measured and compared to the theoretical predictions.

In addition, we present the measurements of $\gamma\gamma \to W^+W^-$ and $\gamma\gamma \to \mu^+\mu^-$ in proton-proton collisions at ATLAS. The production of $\gamma\gamma \to \mu^+\mu^-$ is measured at a centre-of-mass energy of 13 TeV using 3.2 fb^{-1}. Fiducial and differential cross-sections are compared to theoretical predictions both with and without corrections for absorptive effects. Exclusive production of W^+W^- consistent with the Standard Model (SM) prediction is found with a 3σ significance using 20.2 fb^{-1} of data at a centre-of-mass energy of 8 TeV. The fiducial cross-section is measured and found to be in agreement with SM predictions. Constraints are placed on anomalous quartic gauge boson interactions.

1 Introduction

When proton–proton (pp) or lead-lead (Pb+Pb) beams collide at the LHC, photon–photon induced ($\gamma\gamma$) interactions occur at a perceptible rate and provide an unique opportunity to study high-energy electroweak processes. The electromagnetic (EM) field strengths of relativistic beams scale with the atomic number (Z). In the Equivalent Photon Approximation (EPA) [1, 2], the EM fields produced by the colliding beam can be treated as a beam of quasi-real photons with a small virtuality of $Q^2 < 1/R^2$, where R is the radius of the charge distribution. The cross-sections for processes $AA\gamma\gamma \to AAX\bar{X}$, where A stands for p or Pb beam and $X\bar{X}$ is a produced particle pair, can be calculated by convolving the respective photon flux with the elementary cross-section for the process $\gamma\gamma \to X\bar{X}$. Since the photon flux associated with each beam scales as Z^2, the cross-section is significantly enhanced in Pb+Pb collisions as compared to the pp system.

The ATLAS Collaboration [3] has measured a rare light-by-light process [4, 5], $\gamma\gamma \to \gamma\gamma$, in Pb+Pb collisions, while exclusive production of $W^\pm$ boson pairs [9], $\gamma\gamma \to W^+W^-$, and exclusive production of the dimuon system [11], $\gamma\gamma \to \mu^+\mu^-$, have been measured in pp collisions.

2 Observation of light-by-light scattering in Pb+Pb collisions

The observation of the light-by-light scattering process, $\gamma\gamma \to \gamma\gamma$, in Pb+Pb collisions at $\sqrt{s_{\mathrm{NN}}} =$ 5.02 TeV is reported [5] by the ATLAS experiment. A data sample corresponding to an integrated luminosity of 1.73 nb^{-1}, collected in November 2018, is analysed. It brings a factor of three improvement in the expected number of event candidates in comparison to the previous analysis based on the 2015 Pb+Pb data set, which established the strong evidence for that process [4] with a 4.4σ significance.

Light-by-light scattering candidates are selected in events with two photons produced exclusively, each with transverse energy $E_{\mathrm{T}}^{\gamma} > 3$ GeV and pseudorapidity $|\eta_\gamma| < 2.4$, diphoton invariant mass above 6 GeV, and small diphoton transverse momentum and acoplanarity, $A_\phi = (1 - |\Delta\phi|/\pi)$, where $\Delta\phi$ stands for the difference in azimuthal angles of two photon candidates. In order to suppress the $\gamma\gamma \to e^+e^-$ background, events are rejected if they have a charged-particle track with $p_{\mathrm{T}} > 100$ MeV, $|\eta| < 2.5$, and at least six hits in the pixel and microstrip detectors, including at least one pixel hit. To further suppress $\gamma\gamma \to e^+e^-$ events with poorly reconstructed charged-particle tracks, candidate events are required to have no "pixel tracks" matched to a photon candidate within $|\Delta\eta| < 0.5$.

A left panel of fig. 1 shows the acoplanarity distribution for events which pass the analysis selection after relaxing the A_ϕ requirement. Two sources of background contribute to the data sample: exclusive production of dielectrons, $\gamma\gamma \to e^+e^-$, and central exclusive production (CEP) of photon pairs, $gg \to \gamma\gamma$. In the high A_ϕ region, the data sample is dominated by backgrounds. Fractions of both background components are evaluated from dedicated control regions in the data.

After applying all selection criteria including a requirement on $A_\phi < 0.01$, 59 candidate events are observed for a background expectation of 12 ± 3 events. Uncorrected diphoton invariant mass, transverse momentum and rapidity distributions in data are shown in fig. 1. The data points are reasonably well described by a sum of signal and background components ($\gamma\gamma \to e^+e^-$ and CEP). The observed excess of events over the expected background has a significance of 8.2σ. The measured fiducial cross-section is 78 ± 13 (stat.) $\pm\, 7$ (syst.) $\pm\, 3$ (lumi.) nb, which can be compared with the predicted values of 45 ± 5 nb from Ref. [6], 51 ± 5 nb from Ref. [7] and 50 ± 5 nb from SuperChic3 Monte Carlo (MC) simulation [8]. The experiment-to-prediction ratios are 1.73 ± 0.40, 1.53 ± 0.33 and 1.56 ± 0.33, respectively. The measurement is statistically limited. The systematic uncertainty is dominated by uncertainties in the photon reconstruction efficiency (4%) and the trigger efficiency (2%).

3 Search for $\gamma\gamma \to W^+W^-$ in pp collisions

Searches for exclusively produced $W^\pm$ boson pairs in the process $pp\gamma\gamma \to ppW^+W^-$ have been performed using $e^\pm\mu^\mp$ final states [9]. The measurement uses 20.2 fb^{-1} of pp collisions collected by the ATLAS experiment in 2012 at a centre-of-mass energy $\sqrt{s} = 8$ TeV. The analysis selection requires event candidates

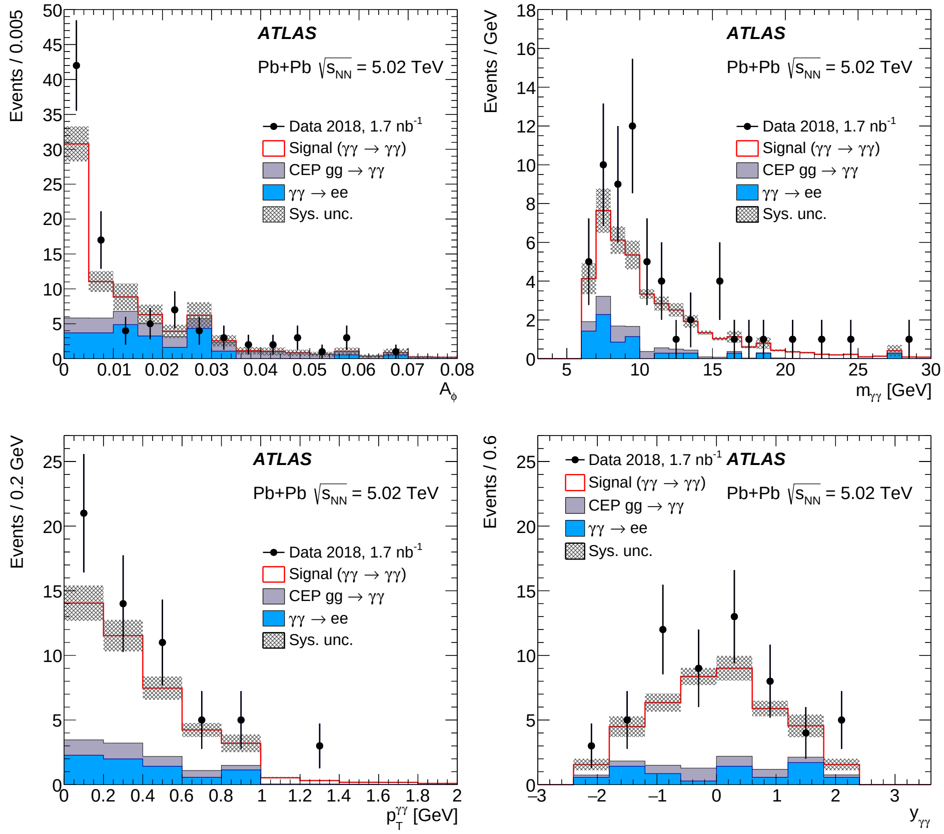

Figure 1: *(Upper, left) The diphoton acoplanarity A_ϕ distribution for events satisfying signal region selection, but before the $A_\phi < 0.01$ requirement is imposed. Data are shown as points, while the histograms represent the expected signal and background levels. Diphoton invariant mass (upper, right), transverse-momentum (botton, left) and rapidity (bottom, right) distributions for $\gamma\gamma \to \gamma\gamma$ event candidates. Taken from Ref.* [5]*.*

to be consistent with muon or electron decays of W boson pairs into oppositely charged different-flavour leptons. The p_{T} requirement imposed on the leading lepton is $p_{\mathrm{T}} > 25$ GeV, while the subleading lepton is required to pass $p_{\mathrm{T}} > 20$ GeV. The invariant mass of the dilepton system has to be greater than 20 GeV. To reduce $\gamma\gamma \to \tau^+\tau^-$ and $Z/\gamma^* \to \tau^+\tau^-$ contaminations, the magnitude of the transverse momentum of the dilepton system, $p_{\mathrm{T}}^{e\mu}$, is required to be greater than 30 GeV. Events with additional tracks originating from a vertex built from two lepton candidates are rejected. After all selection requirements are imposed, the total predicted background is 8.3 ± 2.6 events with the largest contribution from inclusive W^+W^- (80%) and exclusive $\gamma\gamma \to \tau^+\tau^-$ (17%) production, while 23 event candidates are observed in the data. A left panel of fig. 2 shows the $p_{\mathrm{T}}^{e\mu}$ distribution for all events passing the selection criteria. The cross-section is measured in the exclusive W^+W^- region and extrapolated to the full phase space $\sigma_{\gamma\gamma\to W^+W^-\to e^\pm\mu^\mp X} = 6.9 \pm 2.2$ (stat.) $\pm\, 1.4$ (syst.) fb. The statistical uncertainty dominates. The predicted cross-section is $\sigma^{\text{pred.}}_{\gamma\gamma\to W^+W^-\to e^\pm\mu^\mp X} = 4.4 \pm 0.3$ fb. The background-only hypothesis has a p-value about 0.0012, corresponding to a significance of 3.0σ.

Exclusive production of $W^\pm$ boson pairs allows to study $\gamma\gamma \to W^+W^-$ anomalous quartic gauge

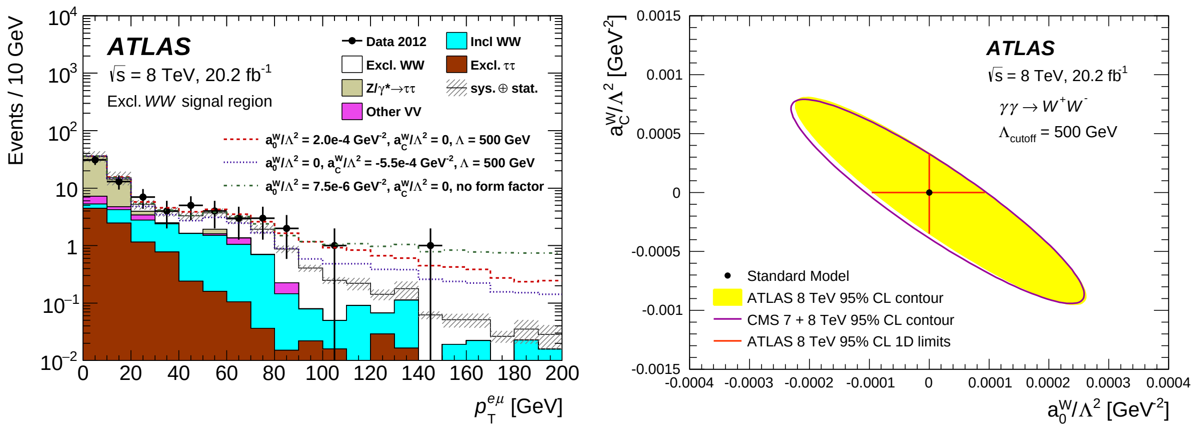

Figure 2: *(Left) The* $p_{\rm T}^{e\mu}$ *distribution for data compared to the SM prediction for events satisfying all the exclusive* W^+W^- *selection requirements apart from the one on* $p_{\rm T}^{e\mu}$ *itself. Also shown are various predictions for aQGC parameters* $a^W_{0,\rm C}$. *(Right) The observed log-likelihood 95% confidence-level contour and 1D limits for the case with a dipole form factor with* $\Lambda_{\rm cutoff} = 500$ *GeV. The CMS combined 7 and 8 TeV result is shown for comparison. Taken from Ref.* [9].

couplings (aQGC), which provide a window to further probe possible new physics extensions of electroweak theory. The aQGC limit setting is performed using the region $p_{\rm T}^{e\mu} > 120$ GeV where the aQGC contributions are expected to be important and SM backgrounds are suppressed. In the left panel of fig. 2, the $p_{\rm T}^{e\mu}$ distribution in data is compared to the SM prediction and various aQGC scenarios. The aQGCs enhance the exclusive signal at high $p_{\rm T}^{e\mu}$, while the background is negligible with $p_{\rm T}^{e\mu} > 80$ GeV. The 95% confidence-level (CL) limits on the couplings a_0^W/Λ^2 and a_C^W/Λ^2 are extracted with a likelihood test using the one observed data event as a constraint. To extract one-dimensional (1D) limits, one of the aQGCs is set to zero. 1D limits on the two aQGC parameters are shown in the right panel of fig. 2 for the case with a dipole form factor with $\Lambda_{\rm cutoff} = 500$ GeV, where $\Lambda_{\rm cutoff}$ defines the scale of possible new physics. The region outside the contour is ruled out at 95% confidence-level. The limits are comparable to the CMS combined 7 and 8 TeV results [10].

4 Measurement of $\gamma\gamma \to \mu^+\mu^-$ in pp collisions

Production of exclusive $\gamma\gamma \to \mu^+\mu^-$ events in pp collisions at a centre-of-mass energy of 13 TeV is measured [11] using data corresponding to an integrated luminosity of 3.2 fb^{-1}. The measurement is performed for a dimuon invariant mass of $12 < m_{\mu^+\mu^-} < 70$ GeV with a single-muon requirement of $|\eta^\mu| < 2.4$ and $p_{\rm T}^{\mu} > 6$ GeV. The analysis methodology is based on the earlier ATLAS measurement [12] of exclusive dimuon and dielectron production in pp collisions at a centre-of-mass energy $\sqrt{s} = 7$ TeV. To suppress pileup, events with more than two tracks reconstructed at a vertex formed by dimuon candidates are rejected. The transverse momentum requirement imposed on the dimuon system $p_{\rm T}^{\mu^+\mu^-} < 1.5$ GeV is introduced to suppress single-dissociative background which originates from events where one of outgoing protons dissociates. After the analysis criteria are imposed, 7 925 event candidates are selected. The sample consists of signal, as well as single- and double-dissociative background, and of dimuon pairs produced in the Drell-Yan process. Contributions from other background sources are found to be negligible.

The acoplanarity variable is not affected by the muon momentum scale and resolution uncertainties and provides a good separation of signal from background. Templates from MC simulation are used for the signal, single- and double-dissociative, and Drell-Yan processes. The expected number of signal events is extracted from the fit to the acoplanarity distribution. The purity of the data sample is found to be 50%.

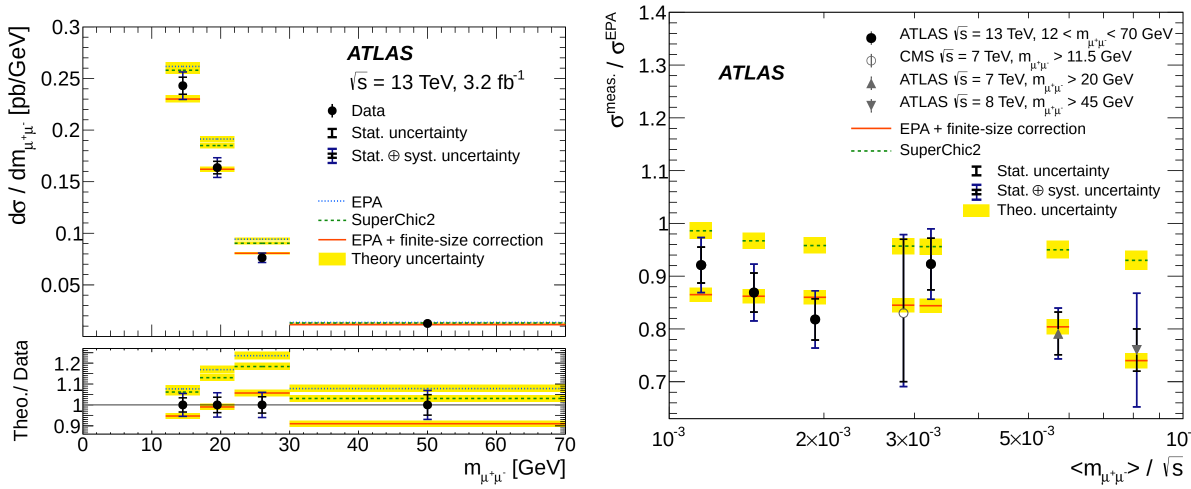

Figure 3: *(Left) The exclusive $\gamma\gamma \to \mu^+\mu^-$ differential fiducial cross-section as a function of dimuon invariant mass $m_{\mu^+\mu^-}$. The bottom panel shows the ratio of the predictions to the data. (Right) Comparison of the ratios of measured and predicted cross-sections to the bare EPA calculations as a function of the average dimuon invariant mass scaled by the pp centre-of-mass energy used. Data (markers) are compared to various predictions (lines). Full circle markers represent the four mass points presented in this report, while open circle, up-triangle and down-triangle depict the previous results obtained with $m_{\mu^+\mu^-} > 11.5$ GeV [13], $m_{\mu^+\mu^-} > 20$ GeV [12] and $m_{\mu^+\mu^-} > 45$ GeV [9] requirements on the dimuon invariant mass. The inner error bars represent the statistical uncertainties, and the outer bars represent the total uncertainty in each measurement. The yellow bands represent the theoretical uncertainty in the predictions. Taken from Ref. [11].*

The fiducial cross-section for exclusive dimuon production is measured to be $\sigma^{\text{fid.}}_{\gamma\gamma\to\mu^+\mu^-} = 3.12 \pm 0.07\ (\text{stat.}) \pm 0.14\ (\text{syst.})$ pb. This value can be compared to the bare EPA predictions, $\sigma^{\text{EPA}}_{\gamma\gamma\to\mu^+\mu^-} = 3.56 \pm 0.05$ pb, to the EPA predictions corrected for absorptive effects using the finite-size parameterisation, $\sigma^{\text{EPA,corr.}}_{\gamma\gamma\to\mu^+\mu^-} = 3.06 \pm 0.05$ pb, or to the SuperChic2 predictions, $\sigma^{\text{SC2}}_{\gamma\gamma\to\mu^+\mu^-} = 3.45 \pm 0.05$ pb. The absorptive effects are mainly related to additional gluon interactions between the protons (or proton remnants), which take place in addition to the QED process. The comparison between the measured differential cross-sections as a function of $m_{\mu^+\mu^-}$ and the theoretical predictions is shown in the left panel of fig. 3. The EPA predictions corrected for absorptive effects are in good agreement with the measured cross-sections. The total systematic uncertainty of the measurement is dominated by shape modelling uncertainties, which can be reduced by tagging outgoing protons with dedicated forward detectors in the future. A right panel of fig. 3 shows a ratio of the measured to predicted cross-sections as a function of the average $m_{\mu^+\mu^-}$ scaled by a given pp centre-of-mass energy for recent $\gamma\gamma \to \mu^+\mu^-$ measurements performed at the LHC [9, 11, 12, 13]. The deviations from unity of the ratios of measured cross-sections to the bare EPA-based predictions increase slightly with the energy scale $\langle m_{\mu^+\mu^-}\rangle/\sqrt{s}$. This indicates that the size of the absorptive corrections tends to increase with $\langle m_{\mu^+\mu^-}\rangle/\sqrt{s}$.

5 Summary

Photon-induced processes have been measured in Pb+Pb and *pp* collisions by the ATLAS experiment. Thanks to a factor of 10^8 enhancement of photon fluxes in Pb+Pb collisions in comparison to the *pp* system, a very rare process of light-by-light scattering could be observed for the first time at the LHC. The observation has been established with a 8.2σ significance over a background-only hypothesis. A search for exclusive $\gamma\gamma \to W^+W^-$ process has been conducted in *pp* collisions, and an evidence with a 3σ significance has been found. This process has also been used to set limits on anomalous quartic gauge boson interactions. The exlusive production of dimuons has been measured with high precision in *pp* collisions at 13 TeV. The proton absorptive effects have been found to play an important role in the data description.

6 Acknowledgements

This work was partly supported by the AGH UST statutory task No. 11.11.220.01/4 within subsidy of the Ministry of Science and Higher Education, by the National Science Centre of Poland under grant number UMO2016/23/B/ST2/01409, and by PL-GRID infrastructure.

References

1. M. S. Chen, I. Muzinich, H. Terazawa and T. Cheng, Phys. Rev. D **7**, 3485 (1973).
2. V. M. Budnev, I. F. Ginzburg, G. V. Meledin and V. Serbo, Nucl. Phys. B **63**, 519 (1973).
3. ATLAS Collaboration, J. Instrum. **3**, S08003 (2008).
4. ATLAS Collaboration, Nature Phys. **13**, 9 (2017).
5. ATLAS Collaboration, Phys. Rev. Lett. **123**, 052001 (2019).
6. D. d'Enterria and G. G. da Silveira, Phys. Rev. Lett. **111**, 080405 (2013), [Erratum: Phys. Rev. Lett. **116**, 129901 (2016)].
7. M. Klusek-Gawenda, P. Lebiedowicz and A. Szczurek, Phys. Rev. C **93**, 044907 (2016).
8. L. A. Harland-Lang, V. A. Khoze and M. G. Ryskin, , Eur. Phys. J. **C79**, 39 (2019).
9. ATLAS Collaboration, Phys. Rev. D **94**, 032011 (2016).
10. CMS Collaboration, J. High Energy Phys. **08**, 119 (2016).
11. ATLAS Collaboration, Phys. Lett. B **777**, 303 (2018).
12. ATLAS Collaboration, Phys. Lett. B **749**, 242 (2015).
13. CMS Collaboration, J. High Energy Phys. **01**, 052 (2012).

Frascati Physics Series Vol. 69 (2019)
PHOTON 2019 - International Conference on the Structure and the Interactions of the Photon
Jun 3-7, 2019

DIPHOTON ELASTIC SCATTERING IN UPC AT SMALLER $W_{\gamma\gamma}$

Antoni Szczurek
Institute of Nuclear Physics PAN, Kraków and University of Rzeszów

Abstract

We present a study of photon-photon scattering for invariant masses $W_{\gamma\gamma} < 5$ GeV. We extend earlier calculations of this cross section for $W_{\gamma\gamma} > 5$ GeV into the low mass range where photoproduction of the pseudoscalar mesons $\eta(548)$, $\eta^{'}(958)$ and other mesonic resonances contribute to the two-photon final states. We consider the dominant background of the two photon final state which arises from $\gamma\gamma$ decays of photoproduced $\pi^0\pi^0$-pairs. We discuss how to reduce the background by imposing cuts on different kinematical variables. We present results for ALICE and LHCb kinematics.

1 Introduction

The first evidence of diphoton measurements in ultra-peripheral heavy-ion collisions has been reported by the ATLAS and CMS Collaborations [1, 2]. These data are, however, restricted to photon-photon invariant masses $\mathrm{W}_{\gamma\gamma} > 5$ and 6 GeV for the CMS and ATLAS analyses, respectively. ATLAS comparison of its experimental results to the predictions from Ref. [3] show a reasonable agreement. Our result is also consistent with the CMS data [2].

In our recent paper [4] we examined the possibility of measuring photon-photon scattering in ultra-peripheral heavy-ion collisions at the LHC for $W_{\gamma\gamma} < 5$ GeV. At lower diphoton masses, photoproduction of meson resonances plays a significant role in addition to the Standard Model box diagrams [5], as well as double-photon fluctuations into light vector mesons [3] or two-gluon exchanges [6] may be important.

In our recent study we considered also the background from the $\gamma\gamma \to \pi^0(\to \gamma\gamma)\pi^0(\to \gamma\gamma)$ process measured, e.g., by the Belle [7] and Crystal Ball [8] collaborations. In Ref. [9] a multi-component model, which describes the Belle and Crystal Ball $\gamma\gamma \to \pi^0\pi^0$ data, was constructed.

2 Sketch of the formalism

In Fig. 1 we illustrate the signal ($\gamma\gamma \to \gamma\gamma$ scattering) which we take to be the dominant box mechanism (see [3]). Panel (b) shows a diagram for s-channel $\gamma\gamma \to$ pseudoscalar/scalar/tensor resonances which also contributes to the $\gamma\gamma \to \gamma\gamma$ process. We also show (diagram (c)) the $\gamma\gamma \to \pi^0\pi^0$ process, which leads to what we consider as the dominant background when only one photon from each $\pi^0 \to \gamma\gamma$ decay is detected.

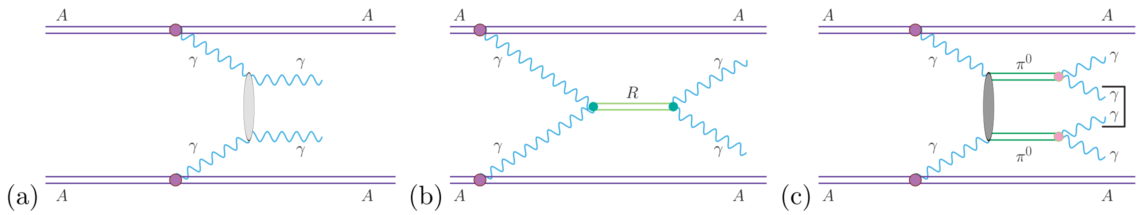

Figure 1: *The continuum $\gamma\gamma \to \gamma\gamma$ scattering (a), $\gamma\gamma \to$ resonances $\to \gamma\gamma$ (b), and the background mechanism (c).*

In our equivalent photon approximation (EPA) approach in impact parameter space, the phase space integrated cross section for $A_1A_2 \to A_1A_2X_1X_2$ reaction is expressed through, the five-fold integral

$$\sigma_{A_1A_2\to A_1A_2X_1X_2}\left(\sqrt{s_{A_1A_2}}\right) = \int \sigma_{\gamma\gamma\to X_1X_2}\left(W_{\gamma\gamma}\right) N\left(\omega_1, \mathbf{b_1}\right) N\left(\omega_2, \mathbf{b_2}\right) S^2_{abs}\left(\mathbf{b}\right) \times \mathrm{d}^2 b\, \mathrm{d}\bar{b}_x\, \mathrm{d}\bar{b}_y\, \frac{W_{\gamma\gamma}}{2} \mathrm{d}W_{\gamma\gamma}\, \mathrm{d}Y_{X_1X_2}\ , \tag{1}$$

where X_1X_2 is a pair of photons or neutral pions. $W_{\gamma\gamma} = \sqrt{4\omega_1\omega_2}$ and $Y_{X_1X_2} = \left(y_{X_1} + y_{X_2}\right)/2$ are invariant mass and rapidity of the outgoing X_1X_2 system. The energy of the photons is expressed through $\omega_{1/2} = W_{\gamma\gamma}/2\exp(\pm Y_{X_1X_2})$. $\mathbf{b_1}$ and $\mathbf{b_2}$ are impact parameters of the photon-photon collision point with respect to parent nuclei 1 and 2, respectively, and $\mathbf{b} = \mathbf{b_1} - \mathbf{b_2}$ is the standard impact parameter for the A_1A_2 collision. The absorption factor $S^2_{abs}\left(\mathbf{b}\right)$ assures UPC implying that the nuclei do not undergo nuclear breakup. The photon fluxes ($N\left(\omega_i, \mathbf{b_i}\right)$) are expressed through a nuclear charge form factor of the nucleus. In our calculations we use a realistic form factor which is a Fourier transform of the charge distribution in the nucleus. More details can be found e.g. in [10].

3 Results

In Table 1 we show the total cross sections in nb for different contributions to the diphoton final state. The cross sections are given in two ranges of di-photon invariant masses both for ALICE and LHCb acceptances. The rapidity coverage of ALICE is $|\eta_\gamma| < 0.9$ and LHCb $2 < \eta_\gamma < 4.5$.

In Fig.2 we show the distribution of the diphoton invariant mass, separately for the ALICE (left panel) and LHCb (right panel) kinematics. As a signal (solid line) here we included only fermionic box contributions. One can observe sharp peaks corresponding to the s-channel exchanges of many resonances specified in the figure. In the calculation presented in this figure only cuts on photon rapidities and transverse momenta were imposed. No experimental resolutions were included, therefore the peaks corresponding to mesons are fairly sharp. The dashed line represents the background due to incomplete registration of the $\pi^0\pi^0$ channel. The background is rather small above $M \sim 2.5$ GeV. Therefore a measurement of $\gamma\gamma \to \gamma\gamma$ scattering for subchannel energies $W > 3$ GeV should be possible. We remind

Table 1: Total nuclear cross section in nb for the Pb+Pb collisions at $\sqrt{s}_{NN} = 5.02$ TeV.

Energy	$W_{\gamma\gamma} = (0-2)$ GeV		$W_{\gamma\gamma} > 2$ GeV	
Region	ALICE	LHCb	ALICE	LHCb
boxes	4 890	3 818	146	79
$\pi^0\pi^0$ bkg	135 300	40 866	46	24
η	722 573	568 499		
$\eta'(958)$	54 241	40 482		
$\eta_c(1S)$			9	5
$\chi_{c0}(1P)$			4	2
$\eta_c(2S)$			2	1

that ATLAS and CMS could measure $\gamma\gamma \to \gamma\gamma$ scattering only for energies larger than 6 and 5 GeV, respectively.

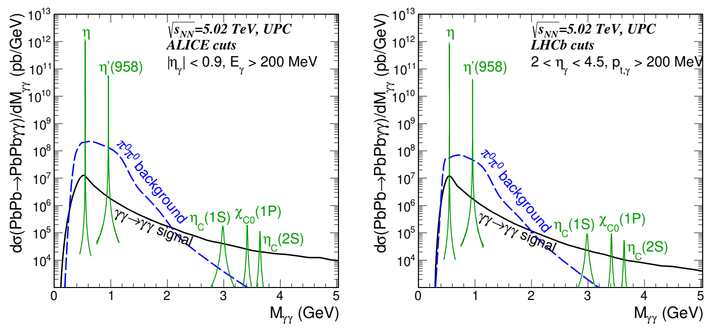

Figure 2: *Diphoton invariant-mass distribution for ALICE (left panel) and LHCb (right panel) kinematical conditions.*

How to reduce the unwanted background ? As an example in Fig.3 we show distribution in transverse momentum of the diphoton pair. The solid line represents the signal and the dashed line the background evaluated separately for the ALICE and LHCb experimental conditions. The smearing in $p_{t,\gamma\gamma}$ is caused by finite experimental energy resolution included in this calculation. It is clear that imposing extra cuts on transverse momenta of the pair of photons one can get rid off the unwanted background. Several other possibilities how to reduce the background were considered in our original paper [4].

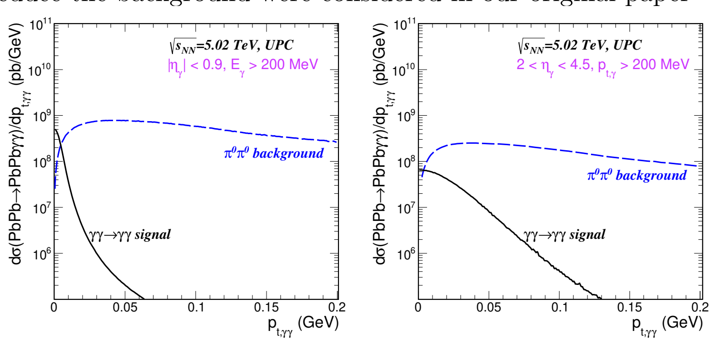

Figure 3: *Transverse momentum distribution of the diphoton pair for ALICE (left) and LHCb (right) kinematics.*

The effect of energy resolution on diphoton invariant-mass spectra is shown in Fig.4 for the ALICE case. Here we show also the effect of imposing a cut on so-called scalar asymmetry of outgoing photons (see [4]).

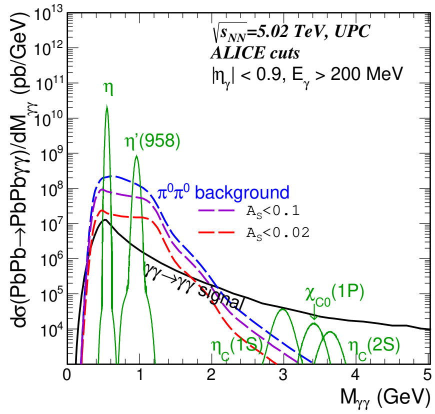

Figure 4: *Diphoton invariant mass for the ALICE conditions including experimental energy resolution. Here we show also effect of cuts on scalar asymmetry of outgoing photon transverse momenta.*

Acoplanarity is another variable which can be used to reduce the $\pi^0\pi^0$ background. In Fig.5 we demonstrate the effect of limiting the acoplanarity range. Even with drastic cuts on the acoplanarity it is very difficult to reduce the $\pi^0\pi^0$ background.

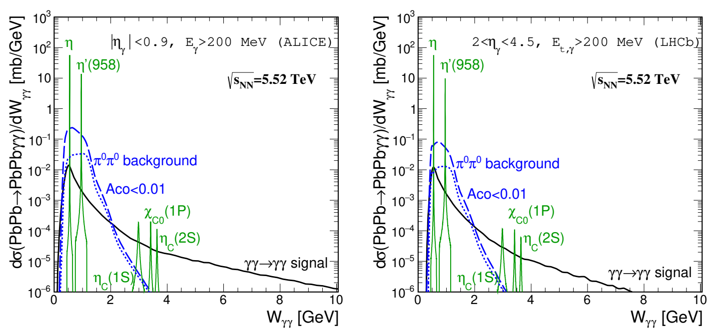

Figure 5: *Diphoton invariant-mass distribution for ALICE (left) and LHCb (right) kinematics. Here a cut on acoplanarity is imposed.*

In Fig.6 we show a similar result for Ar + Ar collisions. The situation looks similar to Pb + Pb collisions. Although the cross section for Ar + Ar collisions is much smaller than for Pb + Pb collisions, the reaction can be very useful due to higher integrated luminosity and consequent higher counting rate.

4 Conclusions

Here we have considered the possibility to study elastic $\gamma\gamma \to \gamma\gamma$ scattering in the diphoton mass range $W_{\gamma\gamma} < 5$ GeV at the LHC using ALICE or LHCb detectors. Our results show that the contributions of the pseudoscalar resonances $\eta(548)$ and $\eta'(958)$ are clearly visible on top of the diphoton mass continuum arising from fermion loop diagrams. We have made first predictions for cross sections as a function of diphoton mass for the typical acceptances in rapidity and transverse momentum of the ALICE and LHCb

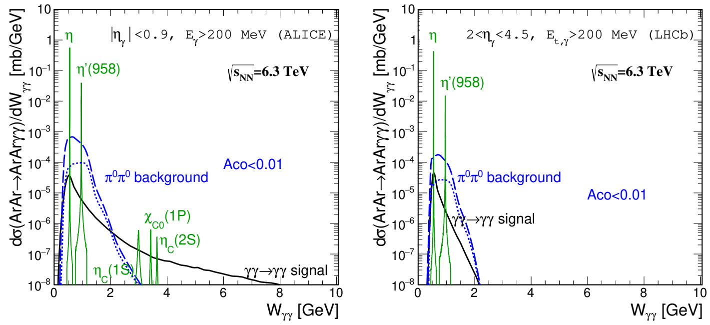

Figure 6: *Diphoton invariant-mass distributions for Ar + Ar collisions with the acoplanarity cut imposed.*

experiments. The evaluation of counting rates needs, however, Monte Carlo simulations which take into account detailed acceptances and realistic responses of the detectors used for measuring the two-photon final states.

In addition to the signal Pb Pb $\to$ Pb Pb $\gamma\gamma$ we considered also the background dominated by the Pb Pb $\to$ Pb Pb $\pi^0\pi^0$ reaction, when only two out of the four decay photons in the final state are registered. This background can be reduced by imposing cuts on scalar and vector asymmetry of transverse momentum of the two photons, acoplanarity, etc. We showed also that cuts on the sum of photon rapidities (or the rapidity of the diphoton system) can additionally be used to reduce the background.

5 Acknowledgements

I am indebted to Mariola Kłusek-Gawenda, Ronan McNuclty and Rainer Schicker for collaboration on the topic presented here. This work was supported by the Polish National Science Center grant DEC-2014/15/B/ST2/02528.

References

1. M. Aaboud et al. (ATLAS Collaboration), Nat. Phys. **13** (2017) 852.

2. A.M. Sirunyan et al. (CMS Collaboration), Phys. Lett. **B797** (2019) 134826.

3. M. Kłusek-Gawenda, P. Lebiedowicz and A. Szczurek, Phys. Rev. **C93** (2016) 044907.

4. M. Kłusek-Gawenda, R. McNulty, R. Schicker and A. Szczurek, Phys. Rev. **D99** (2019) 093013.

5. P. Lebiedowicz and A. Szczurek, Phys. Lett. **B772** (2017) 330.

6. M. Kłusek-Gawenda, W. Schäfer and A. Szczurek, Phys. Lett. **B761** (2016) 399.

7. S. Uehara et al. (Belle Collaboration), Phys. Rev. **D79** (2009) 052009.

8. H. Marsiske et al. (Crystal Ball Collaboration), Phys. Rev. **D41** (1990) 3324.

9. M. Kłusek-Gawenda and A. Szczurek, Phys. Rev. **C87** (2013) 054908.

10. M. Kłusek-Gawenda and A. Szczurek, Phys. Rev. **C82** (2010) 014904.

Frascati Physics Series Vol. 69 (2019)
PHOTON 2019 - International Conference on the Structure and the Interactions of the Photon
June 3-7, 2019

STUDY OF QED IN STRONG FIELD REGIME AT LUXE EXPERIMENT

Oleksandr Borysov on behalf of LUXE collaboration
Deutsches Elektronen-Synchrotron (DESY), Hamburg, 22607, Germany

Abstract

The LUXE experiment at DESY plans to use the European XFEL electron beam of 17.5 GeV in collision with a high intensity optical laser to study non-perturbative QED phenomena. The main focus of the experiment will be the measurement of the rate of laser assisted electron-positron pair production in collisions of high energy photons with an intensive laser beam and high intensity Compton scattering in electron-laser interaction. The design of the experimental setup, detector-system requirements and simulation results are presented and discussed.

1 Introduction

Quantum electrodynamics (QED) with a strong electromagnetic field has been studied since the formulation of the QED. The scale of the strong field is known as a Schwinger critical field

$$\mathcal{E}_{\rm cr} \equiv \frac{m_e^2 c^3}{e\hbar} \approx 1.3 \times 10^{16}\ \frac{\rm V}{\rm cm}\ . \tag{1}$$

where m_e and e are electron mass and charge, c is a speed of light and $\hbar$ is reduced Plank constant. This field accelerates electron to the energy equivalent to its mass at a distance of Compton wavelength $\lambdabar = \hbar/mc$. It leads to the vacuum instability with a possibility of spontaneous e^+e^--pair generation. The static field of this magnitude is not reachable in the lab, but such a regime of QED can be probed in collisions of high-energy electrons or photons with an intense laser beam where two phenomena have been extensively studied theoretically [1, 2, 3]: non-linear Compton scattering and laser-assisted e^+e^--pair production.

$$e^- + n\gamma_L \to e^-\gamma\,, \tag{2}$$

$$\gamma + n\gamma_L \rightarrow e^+e^- , \tag{3}$$

where n is the number of laser photons γ_L participating in the process. An experiment to study these processes was performed at SLAC by E144 collaboration [4].

The interaction between photons and laser field can be characterized by two dimensionless parameters. One of them is an intensity parameter related to the field strength:

$$\xi = \frac{e\mathcal{E}_{\mathrm{L}}}{m_e c\omega_L} = \frac{m_e c^2 \mathcal{E}_{\mathrm{L}}}{\hbar\omega_L \mathcal{E}_{\mathrm{cr}}} \tag{4}$$

where $\mathcal{E}_{\mathrm{L}}$ is the RMS electric field of the laser and ω_L its frequency. Another one is a photon recoil parameter:

$$\chi_\gamma = \frac{k_\gamma \cdot k_L}{m_e^2 c^4}\xi = (1+\cos\theta)\frac{\hbar\omega_\gamma}{m_e c^2}\frac{\mathcal{E}_{\mathrm{L}}}{\mathcal{E}_{\mathrm{cr}}}. \tag{5}$$

where θ is the angle between the laser propagation direction and the photon with momentum k_γ and frequency ω_γ. The areas in these parameters space studied by E144, recent experiment in Astra-Gemini laser facility [5], future planned experiments in European Extreme Light Infrastructure (ELI) [6] and LUXE (Laser und XFEL [7] Experiment) at DESY are shown in figure 1. The possibility to investigate

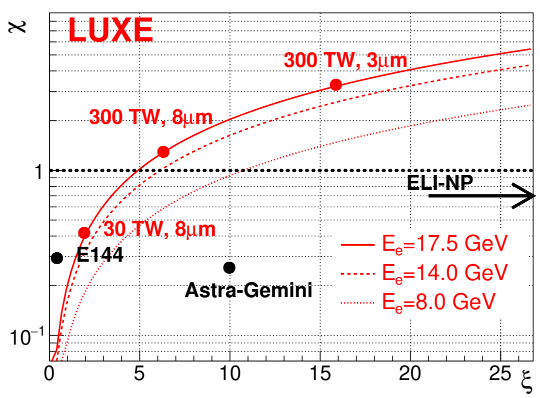

Figure 1: *The χ and ξ parameter space accessible by various experiments. The three red lines show the parameters accessible to LUXE for three possible electron beam energies. Indicated are power and transverse size at focus corresponding to the foreseen laser configurations of LUXE.*

experimentally new domains in (ξ, χ) space is mainly determined by the tremendous progress in laser technologies achieved in recent decades. The proposed experiment LUXE aims to study non-perturbative QED processes (equations (2), (3)) in collisions of the European XFEL electron beam with an optical laser. A sketch of the LUXE experimental setup for the laser-assisted pair-production measurements is presented in figure 2. In this scenario, the incident electrons of the XFEL beam hit a metal target to produce bremsstrahlung photons, which then interact with a laser pulse. The spectrometer located after the target, equipped with arrays of Cherenkov detectors, is intended to register conversion electrons and positrons to estimate the number of produced photons. Another spectrometer downstream of interaction point (IP) built of magnet and two identical detector systems is designed for positrons and electrons registration. Further downstream, the forwards photon detector system monitors bremsstrahlung photons and in scenario of nonlinear Compton study it measures photons produced in electron-laser interaction (2). This report describes the results of simulations obtained within the GEANT4 [8] framework to evaluate the feasibility of the LUXE experiment and optimize its setup. Main focus here is devoted to the design of the experiment intended to study e^+e^--pair production in collisions of bremsstrahlung photons with an intense laser beam.

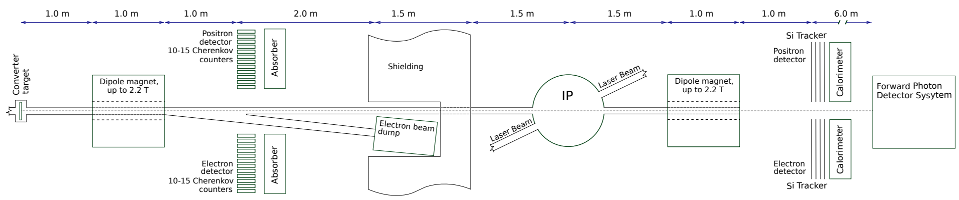

Figure 2: *Diagram of the LUXE experiment layout designed for e^+e^--pair production study.*

2 Simulation Model

For the bremsstrahlung production studies, the primary electrons are generated in accordance with the XFEL beam parameters: energy 17.5 GeV, emittance 1.4 mm mrad and number of electrons 6.25×10^9. Their values together with tentative numbers for the LUXE laser settings are presented in table 1. The process of the laser assisted pair production in collisions of bremsstrahlung photons and laser

Table 1: *LUXE laser and electron beam parameters at the IP.*

Parameter	Value
Laser pulse energy (J)	0.36 (phase 1), 3.6 (phase 2)
Laser transverse size, FWHM (μm)	8.0, 3.0
Laser pulse duration (fs)	35
Laser wavelength (nm)	800
Electron beam energy (GeV)	up to 17.5
Number of electrons ($\times 10^9$)	up to 6.25
Electron beam transverse size, $\sigma_{x,y}$ (μm)	5 - 20
Electron beam duration (fs)	80
Electron beam normalized emittance (mm mrad)	1.4
Crossing angle (rad)	0.35

beam was theoretically studied and results were presented in several papers [1, 2]. The spectrum of the bremsstrahlung photons was approximated using the following formula [9]:

$$\frac{dN_\gamma}{dE_\gamma} = \frac{X}{E_\gamma X_0} \left(\frac{4}{3} - \frac{4}{3} \frac{E_\gamma}{E_e} + \left(\frac{E_\gamma}{E_e} \right)^2 \right), \tag{6}$$

where E_e is the energy of the incident electron, X_0 the radiation length of the target material and X is the target thickness. It is valid for thin targets as it neglects the photon-to-e^+e^--pair conversions within the target, and thus tends to overestimate the rate of high-energy photons. Also, it does not contain information about the angular distribution of the bremsstrahlung photons. Considering a rather small transverse size of the laser pulse and a relatively large distance between the target and the IP, the number of bremsstrahlung photons crossing the laser pulse might be significantly smaller than the total number estimated from Eq. (6). Figure 3 shows the spectra of bremsstrahlung photons produced in the GEANT4 simulation for 35 μm ($1\% X_0$) thick tungsten target. The red line in the figure represents the spectrum of photons counted in the forward region with a position in the transverse plane limited to ± 1.5 m ($|x| < 1.5$ m and $|y| < 1.5$ m) at a distance of 2 m downstream of the target which corresponds to projected polar angles of about 37°. The blue line corresponds to a calculation using Eq. (6), which is in good agreement with the simulation. The green line shows the cross section for photons with a position in the transverse plane limited to ± 25 μm, which matches the transverse size of the LUXE laser beam with a reasonable overlap. The bottom ratio plot demonstrates that the number of photons which take part in the interaction with the laser beam constitutes only 5% of the total number of bremsstrahlung photons. The spacial distribution of photons in the IP plane is determined mainly by their angular spread in the production process and by multiple scattering of incident electrons in the target. Since the initial electron beam is focused onto the IP and has a Gaussian shape with rather small $\sigma = 5$ μm in the IP transverse plane, the contribution of the initial electron angles is less significant. The average

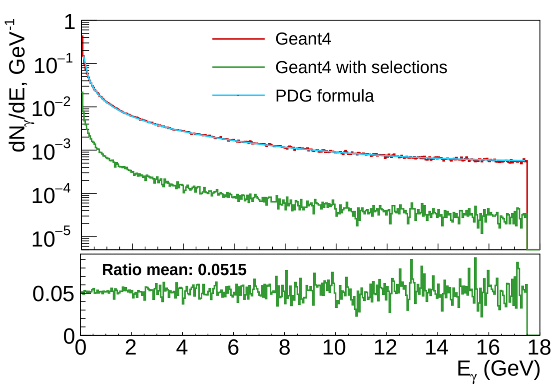

Figure 3: *Comparison of bremsstrahlung spectra obtained from Equation (6) and with GEANT4 simulation for a tungsten target of 35 μm (1%X_0) thickness. The green line shows the γ spectrum after imposing limits on the position in the transverse plane to ± 25 μm.*

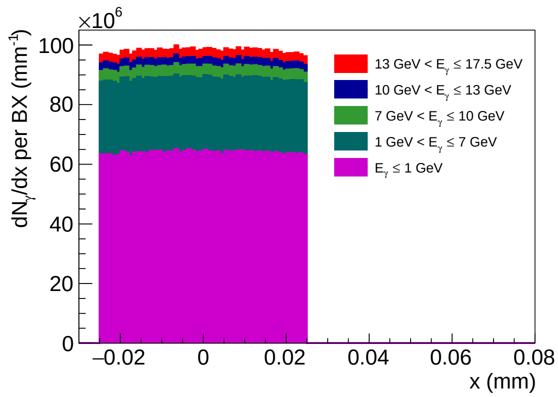

Figure 4: *Bremsstrahlung-photon position distribution in transverse coordinate x at the IP for $|y| < 25\mu m$.*

number of bremsstrahlung photons produced per bunch crossing (BX) is about 5.6×10^8, the number of positrons – 1.6×10^6 and the total number of electrons observed behind the target is 6.26×10^9. Good agreement between simulation and (6) for a thin target (1%X_0) is explained by the fact that the number of conversion positrons is 100 times smaller than the number of radiated photons. The number of positrons and electrons behind the target determines the choice of Cherenkov detectors for their registration (fig. 2).

The spectra of bremsstrahlung photons produced in GEANT4 simulations with aluminum, copper and tungsten targets of 1%X_0 thickness were studied and found to be identical above 1 GeV. The area below 1 GeV looks slightly different for these targets, with the total number of photons in this region 23% higher for copper and 50% for aluminum compared to tungsten. At the same time, it is shown [1)] that there is a lower bound on the energy of the photon for laser-assisted pair production: for the LUXE conditions, it is around 7 GeV. In this case the low-energy photons are only relevant for the possible background study and have no influence on the pair-production rate. For these reasons the tungsten is chosen as a target material. It has also other attractive properties: high melting-point temperature, high thermal conductivity and high sputtering resistance.

Another parameter which is important for the experiment is the distance between the target and the IP. It is mainly constrained on the low side by the technical requirements for the electron and laser design in the vicinity of the LUXE IP. It has also an effect on the thermal stability of the target because of the beam focusing. For a 5m distance, for example, the Gaussian distribution of the beam electrons in the transverse plane has $\sigma \approx 43$ μm and it decreases as the distance between the target and the IP becomes smaller, and consequently the heating power per unit volume increases.

The polar-angle distributions of the bremsstrahlung photons for different energy domains have similar shapes. The projected distribution in the transverse plane within $|y| < 25\ \mu$m in this area, shown in Figure 4, can be well approximated by a uniform distribution. Consequently the number of photons interacting with the laser beam is proportional to the solid angle covering the IP in the transverse plane. This property allows using a simple formula for estimating the number of photons colliding with the laser beam for different distances between target and IP,

$$N_\gamma(R) = \frac{R_0^2}{R^2} N_\gamma(R_0)\,, \tag{7}$$

where R is the distance between the target and IP and $N_\gamma(R_0)$ is the number of photons at distance R_0. Since the total number of photons in the forward region does not depend on the distance, a similar formula is applicable to the estimation of the fraction of photons crossing the IP area. Calculating the fraction of photons for a 5m distance using the number 5.15% for $R_0 = 2$m (Figure 3) gives a fraction of 0.82%, while the simulation gives 0.89%. A similar test for a 12m distance gives 0.15% considering $R_0 = 5$ m and the simulation result is 0.16%. It is clear that Eq. (7) is more accurate in the angular range where the curves in Figure 4 are better approximated by horizontal lines. The angular distribution of bremsstrahlung photons is significantly affected by the multiple scattering of the incident electrons in the target material.

The generated photons are used as an input for modeling the interaction with a laser pulse at the LUXE IP. A detailed description of the Monte Carlo (MC) code can be found in [10]. The spectra of positrons produced in collisions of bremsstrahlung photon with the laser beams of 2.0×10^{19} W/cm^2 ($\xi \approx 2.2$) and 10^{20} W/cm^2 ($\xi \approx 4.9$) are shown in figure 5. The average number of pairs expected in one BX as a function of the laser intensity is presented in Figure 6. One can see that the average number of electrons and positrons increases form about 10^{-2} to 10^3, with the spectra covering a range from 2 GeV to 14 GeV. With the magnet of 1.4T, at 1m distance from the magnet the simulation shows that the particles are spread over a distance of 50 cm with a maximum and average track densities of about 10 mm^{-2} and 1 cm^{-2}, respectively. This flux can be reliably registered in the tracker built of ALPIDE sensors [11], with pixel size of 27×29 μm^2 and a spatial resolution of $\sigma \sim 5\ \mu$m. Calorimeters combined with the tracking detectors provide efficient low-energy background rejection and improve spectra reconstruction.

3 Summary

LUXE [12] at DESY proposes to extend the scientific scope of the European XFEL to probe fundamental physics in a new regime of strong fields. An experimental study of laser-assisted pair production and high-intensity Compton scattering is feasible with the European XFEL beam. The conceptual design study of the LUXE experimental setup shows that the detector subsystems can be built using existing technologies for magnets, pixel tracking detectors, Cherenkov counters and calorimeters. The required lasers are available from the industry, but the technique and tools for their accurate power monitor need to be developed.

4 Acknowledgements

We thank the members of various DESY groups for support and DESY directorate for funding this work through the DESY Strategy Fund. This work has benefited from computing services provided by the German National Analysis Facility (NAF).

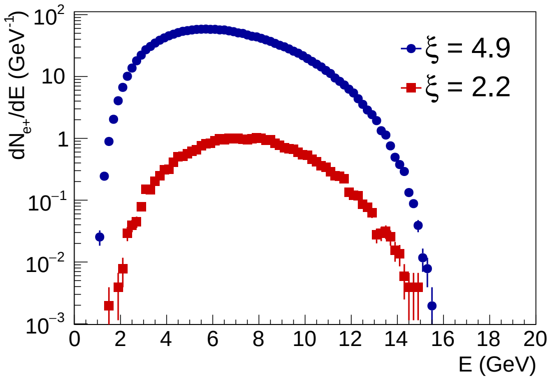

Figure 5: *Positron energy spectra for $\xi = 2.2$ and $\xi = 4.9$, and electron beam energy 17.5 GeV. Each spectrum is normalized to the average number of positrons produced in one BX.*

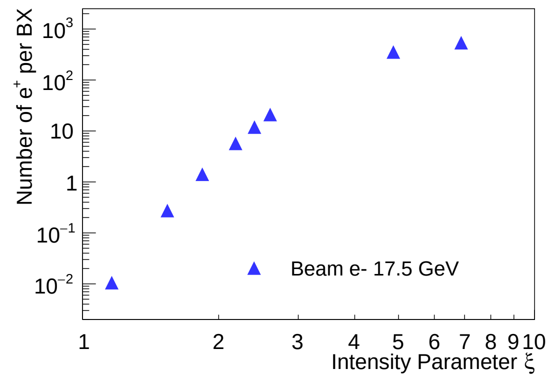

Figure 6: *Number of positrons per BX versus the mean value of ξ in γ laser collisions, for an electron beam of 17.5 GeV.*

References

1. A. Hartin, A. Ringwald, and N. Tapia, Measuring the boiling point of the vacuum of quantum electrodynamics, Phys. Rev. D **99** (2019) 036008. [arXiv:1807.10670].

2. T.G. Blackburn and M. Marklund, Nonlinear Breit-Wheeler pair creation with bremsstrahlung γ rays, Plasma Phys. Control. Fusion **60** (2018) 054009.

3. A. Di Piazza, C. Muller, K. Z. Hatsagortsyan, and C. H. Keitel, Extremely high-intensity laser interactions with fundamental quantum systems, Rev. Mod. Phys. **84** (2012) 1177. [arXiv:1111.3886].

4. C. Bamber et al. Studies of nonlinear QED in collisions of 46.6 GeV electrons with intense laser pulses, Phys. Rev. D **60**, (1999) 092004.

5. K. Poder *et al*, Experimental Signatures of the Quantum Nature of Radiation Reaction in the Field of an Ultraintense Laser, Phys. Rev. **X8** (2018), no. 3, 031004. [arXiv:1709.01861].

6. N. V. Zamfir, Extreme Light Infrastructure - Nuclear Physics (ELI-NP) European Research Centre, EPJ Web Conf. **66**, (2014) 11043.

7. M. Altarelli *et al*, European X-ray Free Electron Laser. Technical Design Report, ISBN 978-3-935702-17-1 (2006), DOI:10.3204/DESY_06-097.

8. J. Allison *et al*, Recent developments in GEANT4, NIM A **835**, 186 (2016).

9. M. Tanabashi *et al*, Particle Data Group, Phys. Rev. D **98** (2018) 030001.

10. A. Hartin, Strong field QED in lepton colliders and electron/laser interactions, Int. J. Mod. Phys. A **33**, no. 13, (2018) 1830011. [arXiv:1804.02934].

11. ALICE Collaboration. ALPIDE, the Monolithic Active Pixel Sensor for the ALICE ITS upgrade, Nucl. Instrum. Meth. A **824**, (2016) 434–438.

12. H. Abramowicz *et al*, Letter of Intent for the LUXE Experiment. [arXiv:1909.00860]; DESY-19-151.

Frascati Physics Series Vol. 69 (2019)
PHOTON 2019 - International Conference on the Structure and the Interactions of the Photon
Jun 3-7, 2019

PRODUCTION OF W^+W^- AND $t\bar{t}$ PAIRS VIA PHOTON-PHOTON MECHANISM IN PROTON-PROTON SCATTERING

Antoni Szczurek
Institute of Nuclear Physics PAN, Kraków
Marta Łuszczak
College of Natural Sciences, Institute of Physics, University of Rzeszów

Abstract

We review our recent results for production of W^+W^- and $t\bar{t}$ pairs via photon-photon fusion mechanism. A sketch of theoretical approach is presented. We include the transverse momenta of the photons in the calculation of photon fluxess. Then we present our results for the cross section (total and differential) of W^+W^- production. Results for different parametrizations of proton structure functions are used to calculate the inelastic fluxes of photons. A discussion on the rapidity gap survival probability, due to remnant fragmentation, is presented. A similar discussion is presented for $t\bar{t}$ production.

1 Introduction

It was realized rather recently that the electroweak corrections are important for precise calculations of cross sections in different processes. The $pp \to W^+W^-$ process is a good example (see e.g. [1]) and $\gamma\gamma \to W^+W^-$ is a relevant subprocess. This subprocess is important also in the context of searches beyond the Standard Model [2, 3]. By imposing special conditions on the final state, this contribution can be observed experimentally [4, 5].

In [6, 7] we developed a formalism tp calculate $pp \to l^+l^-$ processes, proceeding via photon-photon fusion. In [8] we used the same technique to calculate the cross section for $pp \to W^+W^-$ reaction proceeding via photon-photon fusion. In order to make reference to real "measurements" of the photon-photon contribution one has to include in addition the gap survival probability caused by extra emissions. In [9] we concentrated on the effect related to remnant fragmentation and its destroying of the rapidity gap.

In [10] we calculated the cross section for the photon-photon contribution to the $pp \to t\bar{t}$ reaction, including also the effects of gap survival probability.

Here we briefly review our results obtained in [8, 9, 10].

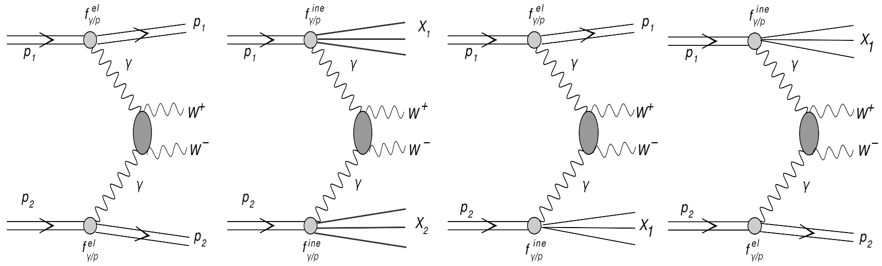

Figure 1: *Diagrams representing different types of photon-photon induced mechanisms for production of W^+W^- pairs.*

2 A skech of the formalism

In our analyses we included the different types of processes shown in Fig. 1.

In our approach we include transverse momenta of (virtual) photons. Then the differential cross section for W^+W^- production can be written as:

$$\frac{d\sigma^{(i,j)}}{dy_1 dy_2 d^2\vec{p}_{T1} d^2\vec{p}_{T2}} = \int \frac{d^2\vec{q}_{T1}}{\pi\vec{q}_{T1}^{\,2}} \frac{d^2\vec{q}_{T2}}{\pi\vec{q}_{T2}^{\,2}} \mathcal{F}^{(i)}_{\gamma^*/A}(x_1,\vec{q}_{T1})\, \mathcal{F}^{(j)}_{\gamma^*/B}(x_2,\vec{q}_{T2}) \frac{d\sigma^*(p_1,p_2;\vec{q}_{T1},\vec{q}_{T2})}{dy_1 dy_2 d^2\vec{p}_{T1} d^2\vec{p}_{T2}} , \quad (1)$$

where $i,j =$ elastic, inelastic and the longitudinal momentum fractions are expressed in terms of rapidities and transverse momenta of W bosons.

The elementary off-shell cross section in (1) is written as:

$$\frac{d\sigma^*(p_1,p_2;\vec{q}_{T1},\vec{q}_{T2})}{dy_1 dy_2 d^2\vec{p}_{T1} d^2\vec{p}_{T2}} = \frac{1}{16\pi^2(x_1x_2s)^2} \sum_{\lambda_{W^+}\lambda_{W^-}} |M(\lambda_{W^+},\lambda_{W^-})|^2\, \delta^{(2)}(\vec{p}_{T1}+\vec{p}_{T2}-\vec{q}_{T1}-\vec{q}_{T2}) \, .$$

Above the helicity-dependent off-shell matrix elements were calculated as:

$$\begin{aligned} M(\lambda_{W^+}\lambda_{W^-}) &= \frac{1}{|\vec{q}_{\perp 1}||\vec{q}_{\perp 2}|} \sum_{\lambda_1\lambda_2} (\vec{e}_\perp(\lambda_1)\cdot\vec{q}_{\perp 1})(\vec{e}_\perp{}^*(\lambda_2)\cdot\vec{q}_{\perp 2}) \mathcal{M}(\lambda_1,\lambda_2;\lambda_{W^+},\lambda_{W^-}) \\ &= \frac{1}{|\vec{q}_{\perp 1}||\vec{q}_{\perp 2}|} \sum_{\lambda_1\lambda_2} q^i_{\perp 1} q^j_{\perp 2}\, e_i(\lambda_1) e^*_j(\lambda_2) \mathcal{M}(\lambda_1,\lambda_2;\lambda_{W^+},\lambda_{W^-}) \, . \quad (2) \end{aligned}$$

Initial- and final-state helicity-dependent matrix elements were discussed e.g. in [11]. The k_t-factorization W-boson helicity dependent matrix elements were calculated with the help of the above [8].

The unintegrated inelastic flux of photons is expressed as:

$$\begin{aligned} \mathcal{F}^{\rm in}_{\gamma^*\leftarrow A}(z,\vec{q}_T) &= \frac{\alpha_{\rm em}}{\pi} \Bigg\{ \{(1-z) \left[\frac{\vec{q}_T^{\,2}}{\vec{q}_T^{\,2} + z(M_X^2 - m_p^2) + z^2 m_p^2} \right]^2 \frac{F_2(x_{\rm Bj},Q^2)}{Q^2 + M_X^2 - m_p^2} \\ &+ \frac{z^2}{4x_{\rm Bj}^2} \frac{\vec{q}_T^{\,2}}{\vec{q}_T^{\,2} + z(M_X^2 - m_p^2) + z^2 m_p^2} \frac{2x_{\rm Bj}F_1(x_{\rm Bj},Q^2)}{Q^2 + M_X^2 - m_p^2} \Bigg\} , \quad (3) \end{aligned}$$

The main ingredients of the formula are the F_1 and F_2 proton structure functions.

contribution	8 TeV	13 TeV
LUX-like		
$\gamma_{el}\gamma_{in}$	0.214	0.409
$\gamma_{in}\gamma_{el}$	0.214	0.409
$\gamma_{in}\gamma_{in}$	0.478	1.090
ALLM97 F2		
$\gamma_{el}\gamma_{in}$	0.197	0.318
$\gamma_{in}\gamma_{el}$	0.197	0.318
$\gamma_{in}\gamma_{in}$	0.289	0.701
SU F2		
$\gamma_{el}\gamma_{in}$	0.192	0.420
$\gamma_{in}\gamma_{el}$	0.192	0.420
$\gamma_{in}\gamma_{in}$	0.396	0.927
LUXqed collinear		
$\gamma_{in+el}\ \gamma_{in+el}$	0.366	0.778
MRST04 QED collinear		
$\gamma_{el}\gamma_{in}$	0.171	0.341
$\gamma_{in}\gamma_{el}$	0.171	0.341
$\gamma_{in}\gamma_{in}$	0.548	0.980
Elastic- Elastic		
$\gamma_{el}\gamma_{el}$ (Budnev)	0.130	0.273
$\gamma_{el}\gamma_{el}$ (DZ)	0.124	0.267

Table 1: *Cross sections (in pb) for different contributions and different F_2 structure functions: LUX, ALLM97 and SU, compared to the relevant collinear distributions with MRST04 QED and LUXqed distributions.*

The unintegrated elastic flux of photons is expressed as:

$$\begin{aligned}\mathcal{F}^{\rm el}_{\gamma^*\leftarrow A}(z,\vec{q}_T) &= \frac{\alpha_{\rm em}}{\pi}\Bigg\{(1-z)\left[\frac{\vec{q}_T^{\,2}}{\vec{q}_T^{\,2}+z(M_X^2-m_p^2)+z^2m_p^2}\right]^2\frac{4m_p^2G_E^2(Q^2)+Q^2G_M^2(Q^2)}{4m_p^2+Q^2} \\ &+ \frac{z^2}{4}\frac{\vec{q}_T^{\,2}}{\vec{q}_T^{\,2}+z(M_X^2-m_p^2)+z^2m_p^2}G_M^2(Q^2)\Bigg\}\ .\end{aligned} \tag{4}$$

In this case the main ingredients are G_E and G_M, the proton electromagnetic form factors.

To calculate the inelastic fluxes of photons, one needs the numerical representation of the proton structure functions. Different parametrizations of the F_2 structure functions are available in the literature, see e.g. [12, 13, 14].

3 Results

The integrated cross sections obtained in our approach are collected in Table 1.

Without any gap survival effects one has:

$$\sigma(inel.-inel.) > \sigma(inel.-el.) + \sigma(el.-inel.) > \sigma(el.-el.)\ . \tag{5}$$

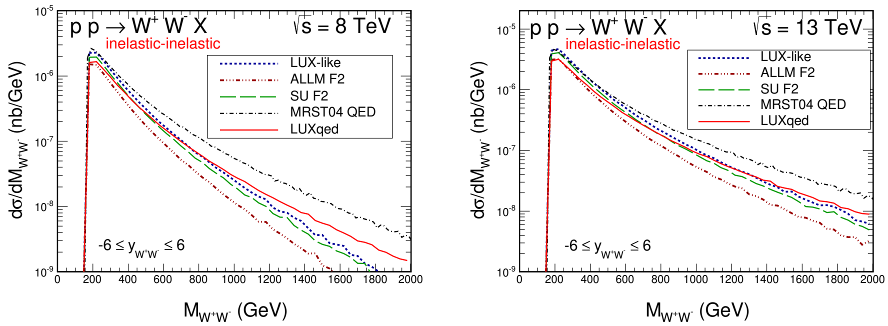

Figure 2: *M_{WW} invariant mass distribution for double dissociative contribution obtained with different parametrizations of structure functions.*

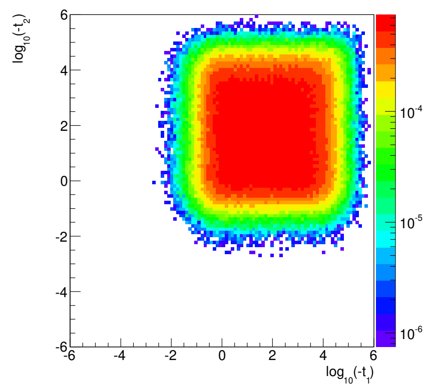

Figure 3: *Two-dimensional distribution in* $(\log_{10}(Q_1^2), \log_{10}(Q_2^2))$ *for double-dissociative processes.*

Many differential distributions were calculated in [8]. Here, in Fig. 3, we show only the invariant-mass distribution for double-dissociation processes (inelastic-inelastic) for different parametrizations of the structure functions taken from the literature.

The k_t-factorization result is similar to the collinear one for the same structure function (LUX-like). The rather old MRST04-QED collinear approach [15] predicted larger cross section. The reasons were discussed in [8].

As an example, in Fig. 3 we show the distribution of the photon virtualities. Rather large photon virtualities come into the game. Such large virtualities seem to contradict collinear approach.

The remnant fragmentation [9] was done with the help of PYTHIA 8 program. Including only parton (jet) emission is already a quite good approximation.

The gap survival probability for single dissociative process is calculated as:

$$S_R(\eta_{\rm cut}) = 1 - \frac{1}{\sigma} \int_{-\eta_{\rm cut}}^{\eta_{\rm cut}} \frac{\mathrm{d}\sigma}{\mathrm{d}\eta_{\rm jet}} \mathrm{d}\eta_{\rm jet} \; . \tag{6}$$

Jet emissions were considered also in [17]; the gap survival factor associated with jet emission is shown in Fig. 4. We find (see also Table 1)

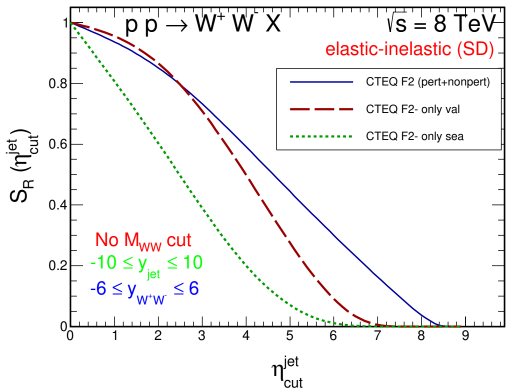

Figure 4: *Gap survival factor for single dissociative process associated with the jet emission. The solid line is for the full model, the dashed line for the valence contribution and the dotted line for the sea contribution.*

$$S_{R,DD} \approx (S_{R,SD})^2 \ . \tag{7}$$

Such an effect is expected when the two fragmentations are independent, which is the case in the model construction. So far we have not included the soft gap survival factors. They are relatively easy to calculate only for double-elastic (DE) contribution [16)]. For the "soft" gap survival factors we expect:

$$S_{soft}(DD) < S_{soft}(SD) < S_{soft}(DE) \ . \tag{8}$$

	8 TeV	13 TeV	8 TeV	13 TeV	8 TeV	13 TeV
$(2M_{WW}, 200$ GeV)	0.763(2)	0.769(2)	0.582(4)	0.591(4)	0.586(1)	0.601(2)
$(200, 500$ GeV)	0.787(1)	0.799(1)	0.619(2)	0.638(2)	0.629(1)	0.649(1)
$(500, 1000$ GeV)	0.812(2)	0.831(2)	0.659(3)	0.691(3)	0.673(2)	0.705(2)
$(1000, 2000$ GeV)	0.838(7)	0.873(5)	0.702(12)	0.762(8)	0.697(5)	0.763(6)
full range	0.782(1)	0.799(1)	0.611(2)	0.638(2)	0.617(1)	0.646(1)

Table 2: *Average rapidity gap survival factors: $S_{R,SD}(|\eta^{ch}| < 2.5)$, $(S_{R,SD})^2\,(|\eta^{ch}| < 2.5)$, $S_{R,DD}(|\eta^{ch}| < 2.5)$ related to remnant fragmentation for single dissociative and double dissociative contributions for different ranges of M_{WW}.*

Finally we wish to show also similar results for the $pp \to t\bar{t}$ reaction. In Table 3 we show the integrated cross section for different categories of processes. Rather small cross sections are obtained; it is not clear at present whether such a process can be identified experimentally.

As an example we show $t\bar{t}$ invariant mass distribution for inclusive case as well as when extra veto on (mini)jet is imposed. The inclusion of rapidity gap veto reduces the cross section. Whether the cross section corresponding to the photon-photon fusion can be measured requires special dedicated studies.

4 Conclusions

Helicity-dependent matrix elements for $\gamma^*\gamma^* \to W^+W^-$ (off-shell photons) have been derived and used in the calculation of cross sections for $pp \to W^+W^-$ reaction. We have obtained a cross section of about 1 pb at the LHC energies. Different combinations of the final states (elastic-elastic, elastic-inelastic, inelastic-elastic, inelastic-inelastic) have been considered. Several correlation observables have been studied. Large

Contribution	No cuts	$y_{\rm jet}$ cut
elastic-elastic	0.292	0.292
elastic-inelastic	0.544	0.439
inelastic-elastic	0.544	0.439
inelastic-inelastic	0.983	0.622
all contributions	2.36	1.79

Table 3: *Cross section for $t\bar{t}$ production in fb at $\sqrt{s}$ = 13 TeV for different components, without (left column) and with the extra condition on the outgoing jet $|y_{\rm jet}| > 2.5$ (right).*

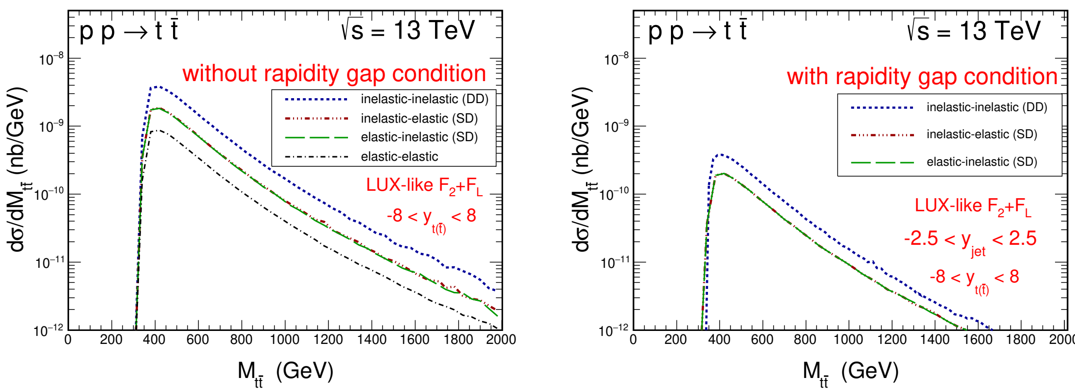

Figure 5: *$t\bar{t}$ invariant-mass distribution for different components defined in the figure. The left panel is without imposing the condition on the struck quark/antiquark and the right panel includes the condition.*

contributions from the regions of large photon virtualities Q_1^2 and/or Q_2^2 have been found putting in question the reliability of leading-order collinear-factorization approach.

We have discussed the quantity called "remnant gap survival factor" for the $pp \to W^+W^-$ reaction initiated via photon-photon fusion. We have calculated the gap survival factor for single dissociative process at parton level. In such an approach the outgoing parton (jet/mini-jet) is responsible for destroying the rapidity gap. We have found that the hadronisation only mildly modifies the gap survival factor calculated at parton level. We have found different values for double- and single-dissociative processes. In general, $S_{R,DD} < S_{R,SD}$ and $S_{R,DD} \approx (S_{R,SD})^2$. We expect that the factorisation observed here for the remnant dissociation and hadronisation will be violated when the soft processes are explicitly included. The larger $\eta_{\rm cut}$ (upper limit on charged particles pseudorapidity), the smaller rapidity gap survival factor S_R. This holds for both double and single dissociation. The present approach is a first step towards a realistic modelling of gap survival in photon induced interactions and definitely requires further detailed studies and comparisons to the existing and future experimental data. We have shown that rather large photon virtualities come into the game for W^+W^- production.

We have also calculated the cross sections for $t\bar{t}$ production via $\gamma\gamma$ mechanism in pp collisions, including the photon transverse momenta and using modern parametrizations of the proton structure functions. The contribution to the inclusive $t\bar{t}$ is only about 2.5 fb. We have found $\sigma_{tt}^{ela-ela} < \sigma_{tt}^{SD} < \sigma_{tt}^{DD}$. We have calculated several differential distributions. Some of them are not accessible in the standard equivalent-photon approximation. As for W^+W^- production, we have shown that rather large photon virtualities come into the game.

References

1. M. Łuszczak, A. Szczurek and Ch. Royon, JHEP **02**, 098 (2015).

2. E. Chapon, C. Royon and O. Kepka, Phys. Rev. D **81**, 074003 (2010), [arXiv:0912.5161 [hep-ph]].

3. T. Pierzchala and K. Piotrzkowski, Nucl. Phys. Proc. Suppl. **179-180**, 257 (2008) [arXiv:0807.1121 [hep-ph]].

4. V. Khachatryan *et al.* [CMS Collaboration], JHEP **1608**, 119 (2016) [arXiv:1604.04464 [hep-ex]].

5. M. Aaboud *et al.* [ATLAS Collaboration], Phys. Rev. D **94**, no. 3, 032011 (2016) [arXiv:1607.03745 [hep-ex]].

6. G. G. da Silveira, L. Forthomme, K. Piotrzkowski, W. Schäfer and A. Szczurek, JHEP **1502**, 159 (2015) [arXiv:1409.1541 [hep-ph]].

7. M. Łuszczak, W. Schäfer and A. Szczurek, Phys. Rev. D **93**, no. 7, 074018 (2016) [arXiv:1510.00294 [hep-ph]].

8. M. Łuszczak, W. Schäfer and A. Szczurek, "Production of W^+W^- pairs via $\gamma^*\gamma^* \to W^+W^-$ subprocess with photon transverse momenta", JHEP**05**, 064 (2018).

9. L. Forthomme, M. Łuszczak, W. Schäfer and A. Szczurek,
"Rapidity gap survival factors caused by remnant fragmentation for W^+W^- pair production via $\gamma^*\gamma^* \to W^+W^-$ subprocess with photon transverse momenta", Phys. Lett. **B789**, 300 (2019).

10. M. Luszczak, L. Forthomme, W. Schäfer and A. Szczurek.
"Production of $t\bar{t}$ pairs via $\gamma\gamma$ fusion with photon transverse momenta and proton dissociation", JHEP **02**, 100 (2019).

11. O. Nachtmann, F. Nagel, M. Pospischil and A. Utermann, Eur. Phys. J. C **45**, 679 (2006) [hep-ph/0508132].

12. H. Abramowicz and A. Levy, hep-ph/9712415.

13. A. Szczurek and V. Uleshchenko, Eur. Phys. **C12**, 663 (2000); Phys. Lett. **B475**, 120 (2000).

14. A.V. Manohar, P. Nason, G.P. Salam and G. Zanderighi, JHEP **12**, 046 (2017).

15. A. D. Martin, R. G. Roberts, W. J. Stirling and R. S. Thorne, Eur. Phys. J. C **39**, 155 (2005) [hep-ph/0411040].

16. P. Lebiedowicz and A. Szczurek, Phys. Rev. **D91**, 095008 (2015).

17. L. Harland-Lang, V.A. Khoze, M.G. Ryskin, Eur. Phys. J. **C76**, 255 (2016).

Frascati Physics Series Vol. 69 (2019)
PHOTON 2019 - International Conference on the Structure and the Interactions of the Photon
Jun 3-7, 2019

TOWARDS AN ANALYTICAL THRESHOLD FUNCTION OF THE TWO LEPTON PAIR PRODUCTION IN GAMMA-GAMMA COLLISIONS

Frédéric Kapusta
LPNHE, Paris

Abstract

The analytical asymptotic cross section for arbitrary masses was given a few years ago. Obtaining an analytical approach of the onset of the asymptotic regime is an interesting challenge.

1 Introduction

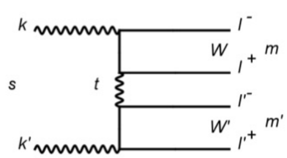

Figure 1: $\gamma\gamma \rightarrow l^+l^-l'^+l'^-$ *: peripheral contribution with kinematic notation*

An analytical expression of the asymptotic ($s = \infty$) cross-section, based on the 45 years old Kessler group factorization formula [1], which gives exact numerical values, was obtained by Wilfrid da Silva and I, more than ten years ago and presented at Photon2007 [2]. Although bremsstrahlung diagrams contribute at low s, an analytical description for $s > 1GeV^2$, with reasonable accuracy, might be useful for estimates in HEP and AstroParticle Physics. In the following I start with a toy model keeping $\ln * \ln$ terms. It is a nice playground for a QCD approach to perturbative and non perturbative regimes, but here it will be only a perturbative QED description. Using then exact expressions and keeping $\ln * \ln$ terms, a "non infinite s" expression is obtained with the help of a specific parametrization.

2 The ingredients

First is the factorization formula :

$$\frac{d\sigma}{dtdW^2dW'^2} = \frac{W^2W'^2}{8\pi^3s^2t^2}\left[(1+ch^2\theta)\sigma_T\sigma'_T + sh^2\theta(\sigma_T\sigma'_L + \sigma_L\sigma'_T) + ch^2\theta\sigma_L\sigma'_L\right] \tag{1}$$

where the $\gamma\gamma^* \to l\,\bar{l}$ transverse and longitudinal cross-section are given by :

$$\sigma_T = \frac{4\pi\alpha^2\beta W^2}{(W^2+t)^2}\left(\frac{3-\beta^4+2t^2/W^4}{2\beta}\ln\frac{1+\beta}{1-\beta} + 2\frac{t}{W^2} + \beta^2 - 2 - \frac{t^2}{W^4}\right) \tag{2}$$

and

$$\sigma_L = \frac{16\pi\alpha^2\beta t}{(W^2+t)^2}\left(1 - \frac{1-\beta^2}{2\beta}\ln\frac{1+\beta}{1-\beta}\right) \quad \text{with} \quad \beta = \sqrt{1-\frac{4m^2}{W^2}} \tag{3}$$

and

$$ch\theta = 2\omega - 1 \quad \text{with} \quad \omega = \frac{st}{(W^2+t)(W'^2+t)} \tag{4}$$

Introducing

$$x = \frac{t}{W^2+t} \quad \text{and} \quad x_0 = \frac{t}{4m^2+t} \tag{5}$$

and x', x'_0 similarly, the kinematical boundaries are given by :

$$x_0x'_0 \geq xx' \geq \frac{t}{s} \quad \text{implying} \quad w = \frac{st}{(4m^2+t)(4m'^2+t)} = \frac{s}{t}x_0x'_0 \geq 1 \tag{6}$$

3 A toy model

Modulo a factor $f(\omega) = (1 - \frac{1}{\omega} + \frac{1}{2\omega^2})$, when $\omega \to \infty$, the differential cross-section can be interpreted in terms of a central exchanged photon probing the QED partonic content of the two real photons :

$$\frac{d\sigma}{dtdxdx'} = 2\frac{4\pi\alpha^2}{t^2}\left[l(x,t) + \bar{l}(x,t)\right]\left[l'(x',t) + \bar{l}'(x',t)\right] \tag{7}$$

$$\begin{aligned} l(x,t) = \frac{\alpha}{2\pi}\{&[x^2+(1-x)^2]2\chi + (1-x)^2(1-th^4\chi)\chi - 4x(1-x)(1-th^2\chi)\chi \\ &-[1-8x(1-x)]th\chi - (1-x)^2(1-th^2\chi)th\chi\} \quad \text{where} \quad \chi(\beta) = \frac{1}{2}\ln\frac{1+\beta}{1-\beta} \end{aligned} \tag{8}$$

The idea is to keep only the $\chi(\beta)\chi(\beta')$ terms, under the assumption of $t \ll 4m^2$, $W^2 \gg 4m^2$ and $W'^2 \gg 4m'^2$. To ease the computation, the choice is to use :

$$l(x,t) = \frac{\alpha}{2\pi}ln\frac{W^2+t}{4m^2+t} = \frac{\alpha}{2\pi}ln\frac{x_0}{x} \tag{9}$$

Introducing $v = \frac{x}{x_0}$ we get :

$$\frac{d\sigma}{dt} = \frac{8\alpha^4}{\pi st}\int_{\frac{1}{w}}^{1} dv\frac{\ln v}{v}\int_1^{wu} d\omega \ln\frac{\omega}{wu} = \frac{8\alpha^4}{\pi st}F(w) \tag{10}$$

$$F(w) = w - 1 - \ln w - \frac{1}{2}\ln^2 w - \frac{1}{6}\ln^3 w = wG(w) \tag{11}$$

Keeping $f(\omega)$, we get instead :

$$G_f = 1 - \frac{3}{2\omega} + \frac{1}{2\omega^2} - \frac{1}{\omega}\left[\frac{1}{2}\ln\omega + \frac{3}{4\ln^2\omega} + \frac{1}{12}\ln^3\omega + \frac{1}{24}\ln^4\omega\right] \tag{12}$$

Some kinematics and notations have to be defined.

$$t_0 = 4mm' \quad s_0 = 4(m+m')^2 \quad s_1 = 4(m-m')^2 \tag{13}$$

Then for $w = 1$,

$$t_\pm = t_0 e^{\pm 2\zeta} \quad \text{with} \quad th\zeta = \sqrt{\frac{s-s_0}{s-s_1}} \tag{14}$$

Or with $u = th\zeta$ we have :

$$w(t) = \frac{s(1-u^2)}{s_0 - s_1 u^2} \quad \text{with} \quad 1 \le w \le \frac{s}{s_0} \tag{15}$$

Integrating with a reasonable approximation :

$$\sigma = \frac{16\alpha^4}{\pi s}\int_0^{u_0}\frac{2du}{1-u^2}wG(w) = \frac{16\alpha^4}{\pi}\int_0^{u_0}\frac{2du}{s_0 - s_1u^2}G(w) \simeq \frac{16\alpha^4}{\pi}\frac{1}{\sqrt{s_0 s_1}}\ln\frac{1+\sqrt{\frac{s_1}{s_0}}u_0}{1-\sqrt{\frac{s_1}{s_0}}u_0}G(s/s_0) \tag{16}$$

leads to the following threshold function :

$$\frac{\sigma(s)}{\sigma(\infty)} = \frac{\ln\frac{1+\sqrt{\frac{s_1}{s_0}}\sqrt{\frac{s-s_0}{s-s_1}}}{1-\sqrt{\frac{s_1}{s_0}}\sqrt{\frac{s-s_0}{s-s_1}}}}{\ln\frac{1+\sqrt{\frac{s_1}{s_0}}}{1-\sqrt{\frac{s_1}{s_0}}}}G(s/s_0) \tag{17}$$

4 Toy model results : $\gamma\gamma \to 4\mu$ and $\gamma\gamma \to 2\mu 2e$

The comparison with the exact numerical computation is given below, thanks to Mathematica [3)].

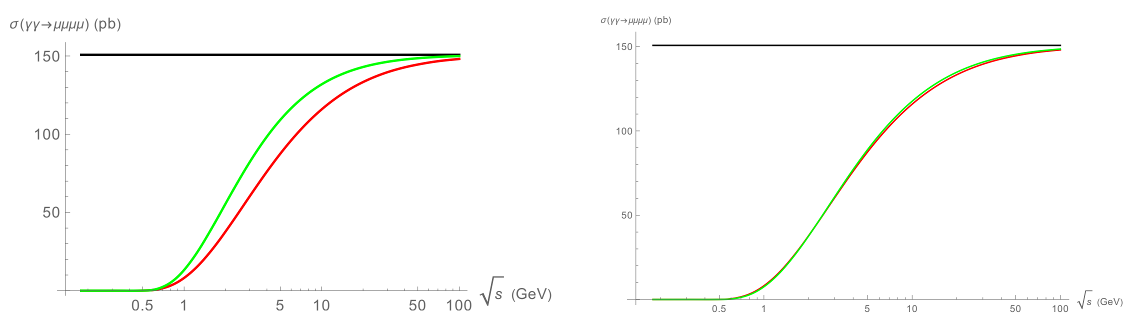

Figure 2: $\gamma\gamma \to 4\mu$: *left with* $G(\omega)$, *right with* $G_f(\omega)$. *Exact value in red, approximation in green*

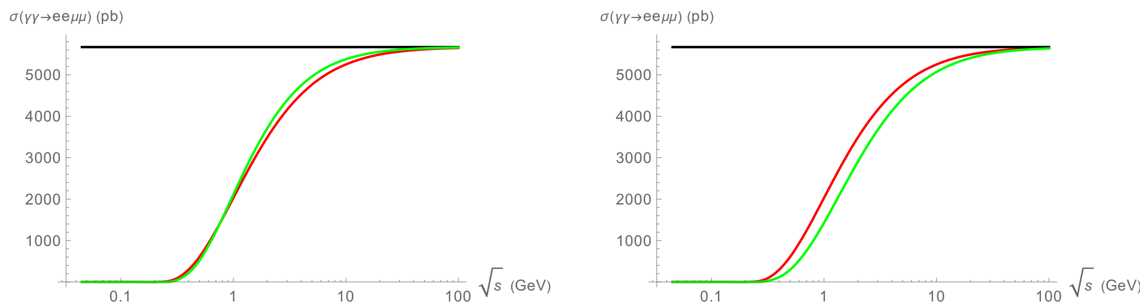

Figure 3: $\gamma\gamma \to 2e2\mu$: *left with* $G(\omega)$, *right with* $G_f(\omega)$. *Exact value in red, approximation in green*

5 Turning to the exact expressions

5.1 The $\ln * \ln$ term

We use now the exact expression of the argument of the log terms. The choice of good variables makes the approach easier. We have to compute :

$$\frac{d\sigma}{dtdxdx'} = \frac{32\alpha^4}{\pi t^2}\chi(\beta)\chi(\beta') \quad \text{where} \quad \chi(\beta) = \frac{1}{2}\ln\frac{1+\beta}{1-\beta} \tag{18}$$

First we consider :

$$\int_{\frac{t}{sx_0}}^{x_0'} dx' \int_{\frac{t}{sx'}}^{x_0} dx\chi(\beta)\chi(\beta') \tag{19}$$

Changing variables, we get :

$$\frac{t}{s}\int_1^w \frac{du}{u}\chi(\beta')\int_1^u d\omega\chi(\beta) \quad \text{using} \quad u = \frac{s}{t}x_0x' \tag{20}$$

where

$$\beta^2 = \frac{u-\omega}{u-\omega x_0} \quad \text{and} \quad \beta'^2 = \frac{w-u}{w-ux_0'} \tag{21}$$

Since

$$\frac{\omega}{u} = \frac{1-\beta^2}{1-\beta^2 x_0} = \frac{x}{x_0} \quad \text{and noting} \quad \beta_1^2 = \frac{u-1}{u-x_0} \tag{22}$$

the integration by parts on ω gives :

$$\int_1^u d\omega\chi(\beta) = -\chi(\beta_1) + \frac{u}{\sqrt{x_0}}\chi(\beta_1\sqrt{x_0}) \tag{23}$$

5.2 Keeping the leading term

Considering now :

$$\frac{t}{s}\int_1^w du\chi(\beta')\left[\frac{1}{\sqrt{x_0}}\chi(\beta_1\sqrt{x_0}) - \frac{1}{u}\chi(\beta_1)\right] \tag{24}$$

to a good approximation we put $\beta_1 = \beta_0$. Note that β_0 is the β_1 value for $u = w$.

$${\beta_0}^2 = \frac{w-1}{w-x_0} \quad \text{and similarly} \quad {\beta_0'}^2 = \frac{w-1}{w-x_0'} \tag{25}$$

Since

$$\frac{u}{w} = \frac{1-\beta'^2}{1-\beta'^2 x'_0} = \frac{x'}{x'_0} \tag{26}$$

we get in a similar way as above :

$$\int_1^w du\chi(\beta') = -\chi(\beta'_0) + \frac{w}{\sqrt{x'_0}}\chi(\beta'_0\sqrt{x'_0}) \tag{27}$$

We keep the leading term :

$$\sqrt{x_0}\chi(\beta_0\sqrt{x_0})\sqrt{x'_0}\chi(\beta'_0\sqrt{x'_0}) \tag{28}$$

which gives the correct expression when $s \to \infty$

$$\sqrt{x_0}\chi(\sqrt{x_0})\sqrt{x'_0}\chi(\sqrt{x'_0}) \tag{29}$$

and goes to 0 at threshold.

5.3 t integration with a trick

In the last integration to be performed

$$\sigma = \frac{32\alpha^4}{\pi}\int_{t_-}^{t_+}\frac{dt}{t^2}\sqrt{x_0}\chi(\beta_0\sqrt{x_0})\sqrt{x'_0}\chi(\beta'_0\sqrt{x'_0}) \tag{30}$$

we note that

$$X_0 = x_0\beta_0^2 = \frac{w-1}{\frac{w}{x_0}-1} \quad \text{and} \quad X'_0 = x'_0\beta'^2_0 = \frac{w-1}{\frac{w}{x'_0}-1} \tag{31}$$

which implies

$$\left(\frac{1}{X_0}-1\right)\left(\frac{1}{x'_0}-1\right) = \left(\frac{1}{x_0}-1\right)\left(\frac{1}{X'_0}-1\right) \tag{32}$$

The following parametrization

$$x_0 = \frac{sh^2\eta_0}{sh^2\eta} \quad \text{and} \quad x'_0 = \frac{ch^2\eta_0}{ch^2\eta} \quad \text{with} \quad th\eta_0 = \frac{m'}{m} \tag{33}$$

$$\text{satisfies} \quad \left(\frac{1}{x_0}-1\right)m'^2 = m^2\left(\frac{1}{x'_0}-1\right) \quad \text{and implies} \quad \left(\frac{1}{X_0}-1\right)m'^2 = m^2\left(\frac{1}{X'_0}-1\right) \tag{34}$$

which allows to write similarly

$$X_0 = \frac{sh^2\eta_0}{sh^2\psi} \quad \text{and} \quad X'_0 = \frac{ch^2\eta_0}{ch^2\psi} \tag{35}$$

5.4 Relation between ψ and η

$$\text{Since} \quad \left(\frac{1}{X_0}-1\right) = \left(\frac{w}{w-1}\right)\left(\frac{1}{x_0}-1\right) \quad \text{and} \quad \frac{w-1}{w} = \frac{t}{s}\left(1-\frac{t_-}{t}\right)\left(\frac{t_+}{t}-1\right) \tag{36}$$

one can express $\frac{t}{t_0} = \tau$ as a function of $sh^2\psi$

$$(\tau - \tau_{0-})(\tau_{0+} - \tau) = \frac{s}{t_0}\frac{sh\eta_0 ch\eta_0}{sh^2\psi - sh^2\eta_0} \tag{37}$$

having introduced $\tau_{0+} = e^{2\zeta}$ and $\tau_{0-} = e^{-2\zeta}$ and remembering that $t_0 = 4mm'$, $s_0 = 4(m+m')^2$ and $s_1 = 4(m-m')^2$ with $ch^2(\zeta) = \frac{s-s_1}{s_0-s_1}$ and $sh^2(\zeta) = \frac{s-s_0}{s_0-s_1}$ leading to

$$\tau_\pm = ch(2\zeta) \pm sh(2\zeta)\sqrt{K(\psi)} = \frac{sh\eta_0 ch\eta_0}{sh^2\eta - sh^2\eta_0} \quad \text{with} \quad K\left(\psi\right) = \frac{sh^2\psi - sh^2\psi_0}{sh^2\psi - sh^2\eta_0} \tag{38}$$

where

$$sh^2(\psi_0) = sh^2(\eta_0) + sh(\eta_0)ch(\eta_0)C(s) \quad \text{with} \quad C(s)\frac{s(s_0-s_1)}{(s-s_0)(s-s_1)} \tag{39}$$

and

$$e^{\psi_0} = \frac{1}{\sqrt{1-r^2}}\left[\sqrt{1+rC(s)} + \sqrt{r}\sqrt{r+C(s)}\right] \quad \text{with} \quad e^{-\eta_0} = \sqrt{\frac{1-r}{1+r}} \tag{40}$$

5.5 The volume element

Using the η parametrization with

$$\sqrt{x_0} = \frac{sh\eta_0}{sh\eta} \qquad \sqrt{x_0'} = \frac{ch\eta_0}{ch\eta} \qquad \frac{1}{\tau} = \frac{sh^2\eta - sh^2\eta_0}{sh\eta_0 ch\eta_0} \tag{41}$$

the volume element is simply

$$t_0\frac{dt}{t^2}\sqrt{x_0}\sqrt{x_0'} = 2d\eta \tag{42}$$

Since $\psi \to \eta$ when $s \to \infty$ we will use $2d\psi$ instead. Noting that we can write :

$$\frac{1+\sqrt{X_0}}{1-\sqrt{X_0}} = \frac{\left(1+e^{-(\psi-\eta_0)}\right)}{\left(1-e^{-(\psi-\eta_0)}\right)}\frac{\left(1-e^{-(\psi+\eta_0)}\right)}{\left(1+e^{-(\psi+\eta_0)}\right)} \tag{43}$$

and

$$\frac{1+\sqrt{X_0'}}{1-\sqrt{X_0'}} = \frac{\left(1+e^{-(\psi-\eta_0)}\right)}{\left(1-e^{-(\psi-\eta_0)}\right)}\frac{\left(1+e^{-(\psi+\eta_0)}\right)}{\left(1-e^{-(\psi+\eta_0)}\right)} \tag{44}$$

gluing everything we get :

$$t_0\int_{t_-}^{t_+}\frac{dt}{t^2}\sqrt{x_0}\chi(\beta_0\sqrt{x_0})\sqrt{x_0'}\chi(\beta_0'\sqrt{x_0'}) \simeq \int_{\psi_0}^{\infty} 2d\psi\frac{1}{4}\left[\ln^2\left|\frac{1+e^{-(\psi-\eta_0)}}{1-e^{-(\psi-\eta_0)}}\right| - \ln^2\left|\frac{1+e^{-(\psi+\eta_0)}}{1-e^{-(\psi+\eta_0)}}\right|\right] \tag{45}$$

5.6 The integration variable

For an integration between 0 and 1, just use $y = e^{-(\psi-\psi_0)}$.

$$t_0\int_{t_-}^{t_+}\frac{dt}{t^2}\sqrt{x_0}\chi(\beta_0\sqrt{x_0})\sqrt{x_0'}\chi(\beta_0'\sqrt{x_0'}) \simeq \int_0^1 2\frac{dy}{y}\frac{1}{4}\left[\ln^2\left|\frac{1+ye^{-(\psi_0-\eta_0)}}{1-ye^{-(\psi_0-\eta_0)}}\right| - \ln^2\left|\frac{1+ye^{-(\psi_0+\eta_0)}}{1-ye^{-(\psi_0+\eta_0)}}\right|\right] \tag{46}$$

With

$$P(th\eta) = \int_0^1\frac{dy}{y}\left[\ln^2\left|\frac{1+y}{1-y}\right| - \ln^2\left|\frac{1+ye^{-2\eta}}{1-ye^{-2\eta}}\right|\right] \tag{47}$$

where

$$P(u) = \ln^2 u \ln\frac{1+u}{1-u} - 2\ln u\left[\mathrm{Li}_2(u) - \mathrm{Li}_2(-u)\right] + 2\left[\mathrm{Li}_3(u) - \mathrm{Li}_3(-u)\right] = \Lambda_3(u) - \Lambda_3(-u) \tag{48}$$

$$t_0\int_{t_-}^{t_+}\frac{dt}{t^2}\sqrt{x_0}\chi(\beta_0\sqrt{x_0})\sqrt{x_0'}\chi(\beta_0'\sqrt{x_0'}) \simeq \frac{1}{2}\left[P(th\frac{\psi_0+\eta_0}{2}) - P(th\frac{\psi_0-\eta_0}{2})\right] \tag{49}$$

Notice that when $s \to \infty$, $\psi_0 \to \eta_0$ and we recover $P(th\eta_0)$ inside the brackets.

So the corresponding form factor is :

$$\frac{P(th\frac{\psi_0+\eta_0}{2}) - P(th\frac{\psi_0-\eta_0}{2})}{P(th\eta_0)} \tag{50}$$

5.7 The jacobian at low y

With the help of the following change of variables $y = e^{-(\psi-\psi_0)}$ and $z = e^{-(\eta-\eta_0)}$ we have :

$$\tau = \frac{z^2(1-e^{-4\eta_0})}{(1-z^2)(1-z^2e^{-4\eta_0})}K(\psi) = \frac{(1-y^2)(1-y^2e^{-4\psi_0})}{[1-y^2e^{-2(\psi_0+\eta_0)}][1-y^2e^{-2(\psi_0-\eta_0)}]} \tag{51}$$

And at low y, the jacobian behaves like :

$$\frac{dz^2}{z^2} \simeq \frac{dy^2}{a^2+y^2} \tag{52}$$

For large s, a^2 behaves like

$$a^2 \simeq \frac{(m+m')^2}{s} \tag{53}$$

and near threshold when $s \to s_0$

$$a^2 \simeq \sqrt{\frac{4t_0}{s-s_0}} \tag{54}$$

This explicit form of the jacobian explains the previous approximation in the large s limit.

5.8 The modified Kummer function

Before gluing everything for a comparison with the exact expression, we just have now to compute an integral of the following type :

$$P(\theta, \frac{1-b}{1+b}) = \int_0^1 2y\frac{dy}{a^2+y^2}\frac{1}{4}\ln^2\left|\frac{1+yb}{1-yb}\right| \quad \text{with} \quad e^{-i\theta} = \frac{1-iab}{1+iab} \quad \text{and} \quad u = \frac{1-b}{1+b} \tag{55}$$

We get

$$P(\theta,u) = \Lambda_3(u) - \frac{1}{2}\left[\Lambda_3(-ue^{i\theta}) + \Lambda_3(-ue^{-i\theta})\right] \tag{56}$$

$$\text{and define} \quad \mathrm{Li}_n(re^{i\theta}) + \mathrm{Li}_n(re^{-i\theta}) = 2\mathrm{Li}_n(r,\theta) \tag{57}$$

6 Discussion to conclude

We have already got an approximate expression corresponding to the $\frac{1}{3}5\sqrt{x_0}\chi(\beta_0\sqrt{x_0})$ piece, which might be sufficient for a reasonable limited accuracy.

Integrating the full $l(x,t)$ expression on x between 0 and x_0 leads to :

$$\frac{1}{3}\left[\left(5\sqrt{x_0} - \frac{1}{\sqrt{x_0}}\right)\chi(\beta_0\sqrt{x_0}) + \frac{\beta_0}{2}\frac{2 - x_0(3+\beta_0^4) + x_0^2(3-4\beta_0^2+3\beta_0^4)}{(1-\beta_0^2x_0)^2}\right] \tag{58}$$

When $\beta_0 = 1$, we get as expected :

$$\frac{1}{3}\left[1 + \left(5\sqrt{x_0} - \frac{1}{\sqrt{x_0}}\right)\chi(\sqrt{x_0})\right] \tag{59}$$

used to obtain the asymptotic cross section which can be written as :

$$\sigma_\infty = \frac{4\alpha^4}{9\pi m^2 th\eta_0}\left\{\left[\frac{25}{4} + \frac{19}{32}\left(\frac{1}{th\eta_0} - th\eta_0\right)^2\right]P(th\eta_0) + Q(th\eta_0)\right\} \tag{60}$$

with

$$Q(u) = \frac{19}{16}\left[2\left(\frac{1}{u} - u\right)\ln u - \left(\frac{1}{u} + u\right)\left(1 + \ln^2 u\right)\right] \tag{61}$$

Keeping only

$$\sigma_0 = \frac{25\alpha^4}{9\pi m^2} \frac{P(th\eta_0)}{th\eta_0} \tag{62}$$

gives for small $th\eta_0$

$$\frac{25\alpha^4}{18\pi m^2} \left(\ln^2 th\eta_0^2 - 2\ln th\eta_0^2 + 4\right) \tag{63}$$

instead of

$$\frac{28\alpha^4}{27\pi m^2} \left(\ln^2 th\eta_0^2 - \frac{103}{21}\ln th\eta_0^2 + \frac{485}{63}\right) \tag{64}$$

For equal masses, once divided by 2, obtain :

$$\sigma_0 = \frac{\alpha^4}{\pi m^2}\frac{175}{36}\zeta(3) \quad \text{instead of} \quad \frac{\alpha^4}{\pi m^2}\left(\frac{175}{36}\zeta(3) - \frac{19}{18}\right) \tag{65}$$

The expression to be tested against the numerical integration is then up to a factor $G(s/s_0)$:

$$\frac{P(th\frac{\psi_0+\eta_0}{2}) - P(th\frac{\psi_0-\eta_0}{2})}{P(th\eta_0)}\sigma_\infty \quad \text{or better} \quad \frac{P(\theta_+, th\frac{\psi_0+\eta_0}{2}) - P(\theta_-, th\frac{\psi_0-\eta_0}{2})}{P(th\eta_0)}\sigma_\infty \tag{66}$$

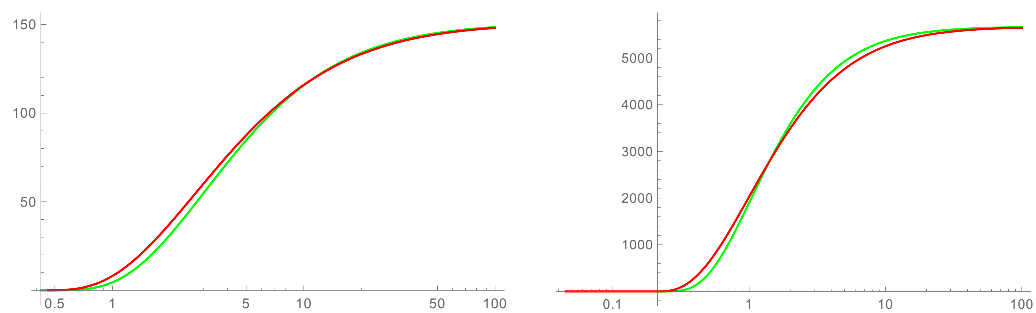

Figure 4: *left : $\gamma\gamma \to 4\mu$ with $G(\omega)$, right : $\gamma\gamma \to 2e2\mu$ with $G(\omega)$. Same display as in previous figures.*

Including more terms in the integration is left for future work.

References

1. C. Carimalo, G. Cochard, P. Kessler, J. Parisi and B. Roehner, Phys. Rev. **D10**, 1561 (1974).
2. W. da Silva, F. Kapusta, Phys. Lett. B, **B718**, 577 (2012).
3. Wolfram Research, Inc., Mathematica, Version 12.0, Champaign, IL (2019).

Frascati Physics Series Vol. 69 (2019)
PHOTON 2019 - International Conference on the Structure and the Interactions of the Photon
Jun 3-7, 2019

THE $\gamma^*\gamma^* \to \eta_c(1S, 2S)$ TRANSITION FORM FACTOR FROM QUARKONIUM WAVE FUNCTIONS

Izabela Babiarz[1]
[1] *The Henryk Niewodniczański Institute of Nuclear Physics Polish Academy of Sciences*
Victor P. Goncalves[2], Roman Pasechnik[3], Wolfgang Schäfer[1], Antoni Szczurek[1]
[2] *Instituto de Fisica e Matematica – Universidade Federal de Pelotas (UFPel),*
[3] *Department of Astronomy and Theoretical Physics,Lund University*

Abstract

We discuss $\gamma^*\gamma^* \to \eta_c(1S)$, $\eta_c(2S)$ transition form factor for both virtual photons. The general formula is given. We use different models for the $c\bar{c}$ wave function obtained from the solution of the Schrödinger equation for different $c\bar{c}$ potentials: harmonic oscillator, Cornell, logarithmic, power-law, Coulomb and Buchmüller–Tye. We showed some examples of wave functions in the Light Front representation as well as in the rest frame of $c\bar{c}$. We compare our results to the BaBar experimental data for $\eta_c(1S)$, with one real and one virtual photon, and to the values collected by the Particle Data Group for the form factor $F(0, 0)$, decay width $\Gamma_{\gamma\gamma}$ and decay constant f_{η_c}. We also consider the non-relativistic limit for $F(0, 0)$ with the wave function evaluated at the origin $R(0)$.

1 Introduction

In the last few years, the pseudoscalar charmonium states $\eta_c(1S)$ and its radial excitation $\eta_c(2S)$ have been paid a lot of attention from both theoretical [1, 2] and experimental [3, 4, 5] sides. So far the collaboration CLEO, BABAR, Belle, L3 Collaboration have extracted the transition form factor for light mesons $(\pi^0, \eta, \eta^{'})$ from events, where only one of the leptons in the final state could be measured. Similar researches were done for $\eta_c(1S)$ by the BABAR collaboration. The study of transition form factor for both-off shell photons is motivated by the possibility of accurate measurement of the double-tag mode, considering the high luminosity for Belle2.

The matrix element for the $\gamma^*\gamma^* \to \eta_c$ fusion can be written with the help of the form factor $F(Q_1^2, Q_2^2)$:

$$\mathcal{M}_{\mu\nu}(\gamma^*(q_1)\gamma^*(q_2) \to \eta_c) = 4\pi\alpha_{\rm em}\,(-i)\varepsilon_{\mu\nu\alpha\beta}q_1^\alpha q_2^\beta\, F(Q_1^2, Q_2^2)\,, \tag{1}$$

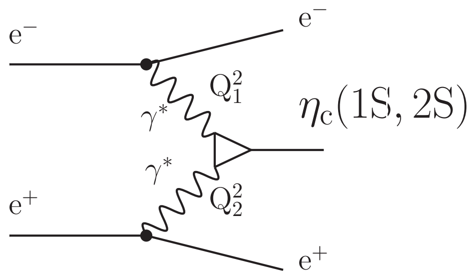

Figure 1: *Feynman diagram for the process $e^+e^- \to e^+e^-\eta_c(1S, 2S)$.*

where $Q_i^2 = -q_i^2 > 0\,, i = 1,2$ are space like virtualities of the photon. To describe the $\gamma^*\gamma^*$ transition we used Light-Front Wave Function $\psi(z, k_\perp)$ and $F(Q_1^2, Q_2^2)$ takes the form [6]:

$$F(Q_1^2, Q_2^2) \qquad = e_c^2\sqrt{N_c}4m_c \cdot \int \frac{dzd^2\mathbf{k}}{z(1-z)16\pi^3}\psi(z,\mathbf{k})\Big\{\frac{1-z}{(\mathbf{k}-(1-z)\mathbf{q}_2)^2 + z(1-z)\mathbf{q}_1^2 + m_c^2} + \frac{z}{(\mathbf{k}+z\mathbf{q}_2)^2 + z(1-z)\mathbf{q}_1^2 + m_c^2}\Big\}\,. \tag{2}$$

Here $(z, \mathbf{k})$ are light-front variables, z and $1 - z$ is are fraction of longitudinal momentum of η_c and $\mathbf{k}$ is the relative momentum of the quark and antiquark in the center-of-mass of the $c\bar{c}$ system. In Fig. 2 we present the dependence of the transition form factor onthe photon virtualities Q_1^2 and Q_2^2.

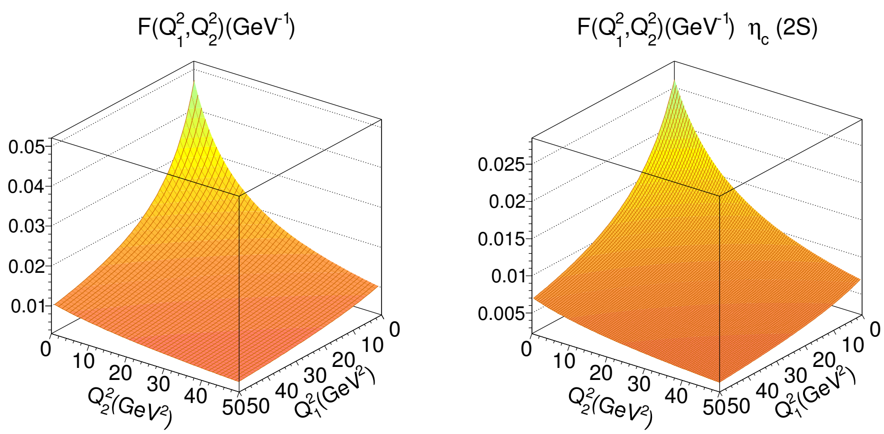

Figure 2: *Transition form factor for $\eta_c(1S)$ and $\eta_c(2S)$ for Buchmüller–Tye potential.*

2 Radial momentum-space wave function and Terentev prescription

The radial wave function in the rest frame of the quark-antiquark system is obtained from the Schrödinger equation:

$$\frac{\partial^2 u(r)}{\partial r^2} = (V_{\text{eff}}(r) - \epsilon)u(r)\,, \tag{3}$$

where $u(r) = \sqrt{4\pi}\, r\psi(r)$, and $V_{\rm eff}(r)$ is the effective potential, as described in Ref [7].

Then we transform $u(r)$ into the momentum space wave function

$$\int\limits_0^\infty |u(r)|^2 dr = 1 \quad \Rightarrow \quad \int_0^\infty |u(p)|^2 dp = 1\,. \tag{4}$$

One can notice in Fig. 3 that each wave function $u(p)$ has slightly different behaviour, dependent on the applied effective potential and related to the model c quark mass. For further calculation we used the

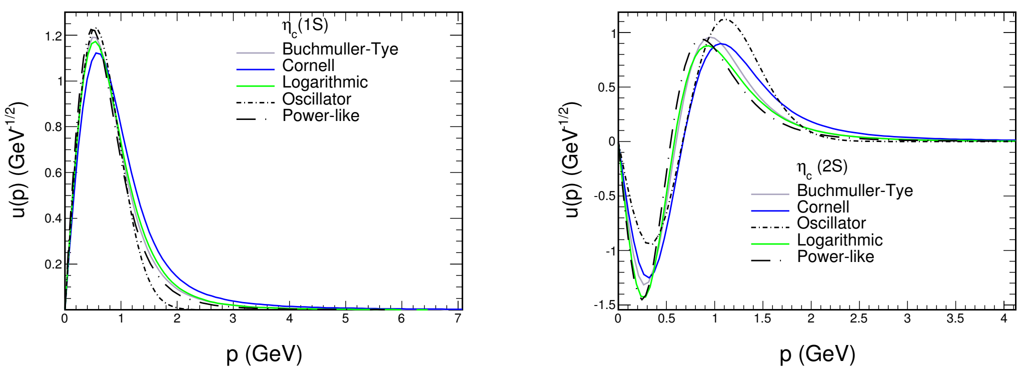

Figure 3: *Radial momentum-space wave function for different potentials. On the left-hand side the $\eta_c(1S)$ is presented, on the right-hand side the $\eta_c(2S)$.*

Terentev prescription, in order to obtain the Light-Front wave function:

$$\psi(z, k_\perp) = \frac{\pi}{\sqrt{2M_{c\bar{c}}}} \frac{u(p)}{p}\,, \tag{5}$$

using

$$p_\perp = k_\perp, \quad p_z = \left(z - \frac{1}{2}\right) M_{c\bar{c}}\,, \quad M_{c\bar{c}}^2 = \frac{k_\perp + m_c^2}{z(1-z)}\,. \tag{6}$$

Eq. (5) includes also the Jacobian factor of changing the variables of the integration. An example of the light cone wave function is shown in Fig. 4, for the Buchmüller–Tye potential model. One can observe that the wave function is strongly peaked around z equal to 1/2.

3 $F(0,0)$ transition for both on-shell photons

In order to write the formula for both on-shell photons, we can simplify Eq. (2):

$$F(0,0) = e_c^2 \sqrt{N_c}\, 4m_c \cdot \int \frac{dz d^2 k_\perp}{z(1-z)16\pi^3} \frac{\psi(z, k_\perp)}{k_\perp^2 + m_c^2}\,, \tag{7}$$

and then the relation between the two-photon decay width and $F(0,0)$ can be expressed by:

$$\Gamma(\eta_c \to \gamma\gamma) = \frac{\pi}{4} \alpha_{\rm em}^2 M_{\eta_c}^3 \, |F(0,0)|^2\,. \tag{8}$$

The so-called decay constant f_{η_c} can be extracted numerically by integrating over variable z in the equation:

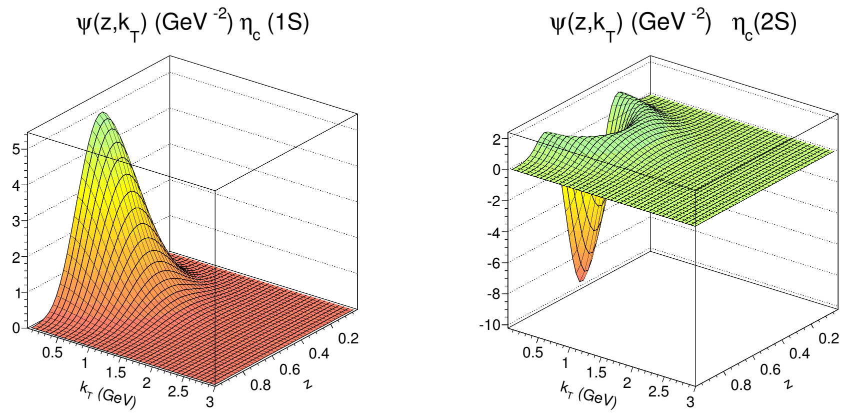

Figure 4: Radial light-front wave function for the Buchmüller–Tye potential.

$$f_{\eta_c}\varphi(z,\mu_0^2) = \frac{1}{z(1-z)}\frac{\sqrt{N_c}\,4m_c}{16\pi^3}\int d^2k_\perp\,\theta(\mu_0^2-k_\perp^2)\,\psi(z,k_\perp)\,, \tag{9}$$

with the following normalization of the distribution amplitude: $\int_0^1 dz\,\varphi(z,\mu_0^2) = 1\,.$

$F(0,0)$ can be rewritten in terms of the radial momentum-space wave function $u(p)$:

$$F(0,0) = e_c^2\sqrt{2N_c}\,\frac{2m_c}{\pi}\int_0^\infty \frac{dp\,p\,u(p)}{\sqrt{M_{c\bar{c}}^3}(p^2+m_c^2)}\,\frac{1}{2\beta}\log\left(\frac{1+\beta}{1-\beta}\right)\,, \tag{10}$$

In the non-relativistic (NR) limit, where $p^2/m_c^2 \ll 1, \beta \ll 1$, and $2m_c = M_{c\bar{c}}$ or $2m_c = M_{\eta_c}$, we obtain

$$F(0,0) = e_c^2\sqrt{N_c}\sqrt{2}\frac{4}{\pi\sqrt{M_{\eta_c}^5}}\int_0^\infty dp\,p\,u(p) = e_c^2\sqrt{N_c}\frac{4\,R(0)}{\sqrt{\pi M_{\eta_c}^5}}\,, \tag{11}$$

where $\beta = p/\sqrt{p^2+m_c^2}$ and R(0) is the radial wave function at the origin. The values of the transition form factor with both photons on-shell, decay constant as well as decay width $\Gamma_{\gamma\gamma}$ are collected in Table 1 for $\eta_c(1S)$ and in Table 2 for $\eta_c(2S)$.

Table 1: *Transition form factor* $|F(0,0)|$ *for* $\eta_c(1S)$ *at* $Q_1^2 = Q_2^2 = 0$.

potential type	m_c [GeV]	$\|F(0,0)\|$ [GeV^{-1}]	$\Gamma_{\gamma\gamma}$ [keV]	f_{η_c} [GeV]
harmonic oscillator	1.4	0.051	2.89	0.2757
logarithmic	1.5	0.052	2.95	0.3373
power-like	1.334	0.059	3.87	0.3074
Cornell	1.84	0.039	1.69	0.3726
Buchmüller–Tye	1.48	0.052	2.95	0.3276
experiment	-	0.067 ± 0.003 [8)]	5.1 ± 0.4 [8)]	0.335 ± 0.075 [9)]

We calculated the normalized transition form factor: $F(Q^2,0)/F(0,0)$ with the aim of comparing our results with the experimental data obtained by the BABAR collaboration [10)], see Fig. 5. The

Table 2: *Transition form factor $|F(0,0)|$ for $\eta_c(2S)$ at $Q_1^2 = Q_2^2 = 0$.*

potential type	m_c [GeV]	$\lvert F(0,0)\rvert$ [GeV^{-1}]	$\Gamma_{\gamma\gamma}$ [keV]	f_{η_c} [GeV]
harmonic oscillator	1.4	0.03492	2.454	0.2530
logarithmic	1.5	0.02403	1.162	0.1970
power-like	1.334	0.02775	1.549	0.1851
Cornell	1.84	0.02159	0.938	0.2490
Buchmüller-Tye	1.48	0.02687	1.453	0.2149
experiment [8]	-	0.03266 ± 0.01209	2.147 ± 1.589	-

right panel of Fig. 5 presents the prediction for the normalized transition form factor for $\eta_c(2S)$. Rather different results are obtained with each potential model. We noticed that the best description of the data is given by the model with $m_c = 1.334$ GeV. Moreover, we observed a strong dependence on the quark mass.

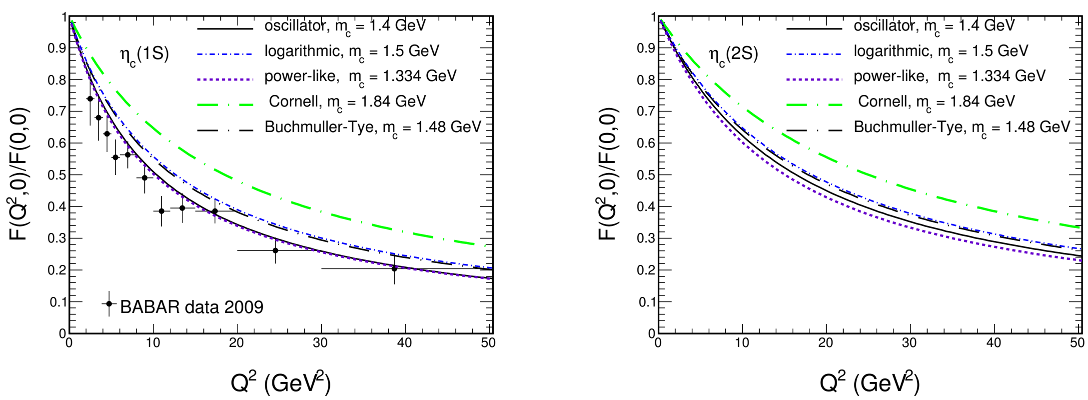

Figure 5: *Normalized transition form factor: $F(Q^2,0)/F(0,0)$ as a function of photon virtuality Q^2. The BABAR data are shown for comparison* [10]

4 Conclusion

The transition form factors for different wave functions, obtained as a solution of the Schrödinger equation for the $c\bar{c}$ system for different phenomenological $c\bar{c}$ potentials from the literature, were calculated in Ref [6], where more details and results can be found. We have studied the transition form factors for $\gamma^*\gamma^* \to \eta_c(1S, 2S)$ for two space-like virtual photons, which can be accessed experimentally in future measurements of the cross section for the $e^+e^- \to e^+e^-\eta_c$ process in the double-tag mode. The transition form factor for only one off-shell photon as a function of its virtuality has been studied and compared to the BaBar data for the $\eta_c(1S)$ case. The dependence of the transition form factor on the virtuality has been studied as well.

References

1. V. L. Chernyak *et al.*, Prog. Part. Nucl. Phys. **80**, 1 (2014).

2. H. Y. Ryu *et al.* Phys. Rev. D **98**, no. 3, 034018 (2018).
3. R. Aaij *et al.* [LHCb Collaboration], Phys. Lett. B **769**, 305 (2017).
4. Y. Hu [BESIII Collaboration], arXiv:1906.08998 [hep-ex].
5. Z. Metreveli, eConf C **070805**, 16 (2007).
6. I. Babiarz *et al.*, Phys. Rev. D **100**, no. 5, 054018 (2019).
7. J. Cepila *et al.*, Eur. Phys. J. C **79**, no. 6, 495 (2019).
8. M. Tanabashi *et al.* [Particle Data Group], Phys. Rev. D **98**, no.3, 030001 (2018).
9. K. W. Edwards *et al.* [CLEO Collaboration], Phys. Rev. Lett. **86**, 30 (2001).
10. J. P. Lees *et al.* [BaBar Collaboration], Phys. Rev. D **81**, 052010 (2010).

Frascati Physics Series Vol. 69 (2019)
PHOTON 2019 - International Conference on the Structure and the Interactions of the Photon
Jun 3-7, 2019

AXION-LIKE PARTICLES AND HIGH ENERGY ASTROPHYSICS

Giorgio Galanti*
INAF, Osservatorio Astronomico di Brera, Via E. Bianchi 46, I – 23807 Merate, Italy

Abstract

Axion-like particles (ALPs) are light, neutral, pseudo-scalar bosons predicted by several extensions of the Standard Model of particle physics – such as the String Theory – and are supposed to interact primarily only with two photons. In the presence of an external magnetic field, photon-ALP oscillations occur and can produce sizable astrophysical effects in the very-high energy (VHE) band ($100\,\mathrm{GeV} - 100\,\mathrm{TeV}$). Photon-ALP oscillations increase the transparency of the Universe to VHE photons partially preventing the gamma-gamma absorption caused by the Extragalactic Background Light (EBL). Moreover, they have important implications for active galactic nuclei (AGN) by modifying their observed spectra both for flat spectrum radio quasars (FSRQs) and BL Lacs. Many attempts have been made in order to constrain the ALP parameter space by studying irregularities in spectra due to photon-ALP conversion in galaxy clusters and the consequences of ALP emission by stars. Upcoming new VHE photon detectors like CTA, HAWC, GAMMA-400, LHAASO, TAIGA-HiSCORE, HERD and ASTRI will settle the issue.

1 Introduction

The detection of axion-like particles (ALPs) would represent a stunning development in particle physics, since it would drive fundamental research towards a very specific direction in order to understand the laws responsible for the evolution of our Universe. Furthermore, implications of the detection of an ALP would be dramatic in astroparticle physics, since ALP interaction with photons would modify many aspects of the gamma-ray propagation: the transparency of photons propagating in magnetized media, the emission models of active galactic nuclei (AGN), and the stellar evolution. In the following, we concentrate on the consequences of ALPs for very-high energy (VHE) astrophysics with arising features which may be observed by the above new generation of the VHE gamma-ray observatories.

*gam.galanti@gmail.com

2 Axion-like particles

Many extensions of the Standard Model (SM) of elementary particle physics such as the String Theory predict the existence of axion-like particles (ALPs), which are very light, neutral, pseudo-scalar bosons [1]. ALPs are a generalization of the *axion*, the pseudo-Goldstone boson related to the global Peccei-Quinn symmetry $U(1)_{PQ}$ proposed as a natural solution to the strong CP problem [2]. While for the axion its interaction with fermions, two gluons, and two photons must be considered, and a strict relationship between the axion mass and the two-photon coupling constant exists, ALPs differ from the axion in this respect: i) ALPs are supposed to couple primarily only to two photons while other interactions are discarded, ii) ALP mass m_a and the two-photon coupling constant $g_{a\gamma\gamma}$ are unrelated parameters. Thus, the Lagrangian describing the ALP field a reads

$$\mathcal{L}_{\rm ALP} = \frac{1}{2}\,\partial^\mu a\,\partial_\mu a - \frac{1}{2}\,m_a^2\,a^2 + g_{a\gamma\gamma}\,a\,\mathbf{E}\cdot\mathbf{B}\;, \tag{1}$$

where $\mathbf{E}$ and $\mathbf{B}$ are the electric and magnetic components of the electromagnetic tensor $F^{\mu\nu}$. As far as the actual value of m_a and $g_{a\gamma\gamma}$ is concerned, many bound have been derived as discussed in [3] and also below in the text.

Considering a photon-ALP beam, we denote by $\mathbf{B}$ an external magnetic field and by $\mathbf{E}$ the propagating photon field in eq.1: because the mass matrix of the $\gamma - a$ system is off-diagonal, the propagation eigenstates differ from the interaction eigenstates. As a result, in the presence of an external $\mathbf{B}$ field, photon-ALP oscillations take place. Furthermore, from eq.1 it follows that the only part of $\mathbf{B}$ which couples to a is the transverse component $\mathbf{B}_T$ belonging to the plane containing $\mathbf{E}$ and orthogonal to the photon momentum $\mathbf{k}$. From eq.1 it is possible to evaluate the photon survival probability $P_{\gamma\to\gamma}$ representing the observable quantity: indeed $P_{\gamma\to\gamma}$ is related to the optical depth τ by the relation $P_{\gamma\to\gamma} = e^{-\tau}$ [4]. In media magnetized by strong $\mathbf{B}$ such as inside the jet of AGN we must take into account also the one-loop QED vacuum polarization [5].

3 ALP impact in very-high-energy astrophysics

The existence of ALPs would have many implications in VHE astrophysics in each environment where magnetic fields are sufficiently strong and/or the path inside a magnetized medium is long. In this Section, we cursorily sketch the consequences of ALPs in these environments.

3.1 Active galactic nuclei

Active galactic nuclei (AGN) are powered by mass accreting onto supermassive black holes and in some cases they are characterized by the formation of two collimated relativistic oppositely oriented jets. An enormous amount of radiation is emitted from the inner regions. When one of the jets is occasionally pointing toward the Earth the AGN is called a blazar. Blazars are divided into two classes: flat spectrum radio quasars (FSRQs) and BL Lac objects (BL Lacs). FSRQs are more powerful and they are characterized by strong optical emission lines, while BL Lacs are less bright and they do not display significant emission lines.

In FSRQs the VHE photons produced at the jet base interact with the optical photons of the broad line region (BLR) thereby disappearing by producing an e^+e^- pair: in the BLR the optical depth τ is so high that no photon with energies above $\sim 20\,\text{GeV}$ is expected to leave the FSRQs. However, photons with energies up to $\sim 400\,\text{GeV}$ have been observed. In order to explain such a detection one is forced to place the emission region beyond the BLR in order to avoid absorption. If we want instead to place the emission region – as in the standard AGN models – not too far from the center, then photon-ALP oscillations inside the jet magnetic field $B_{\rm jet} = \mathcal{O}(1\,{\rm G})$ can be invoked in order to reduce the effective BLR optical depth [6]. In the left panel of fig.1 we can observe the dramatic reduction of the optical depth τ in the presence of photon-ALP interactions as compared to the standard τ: ALPs do not interact with BLR photons thereby increasing the effective VHE photon mean free path, thereby providing an explanation for photon emission well above 20 GeV without invoking ad hoc blazar emission models. A complete and physically motivated spectral energy distribution (SED) is plotted in figs.8-10 of [6].

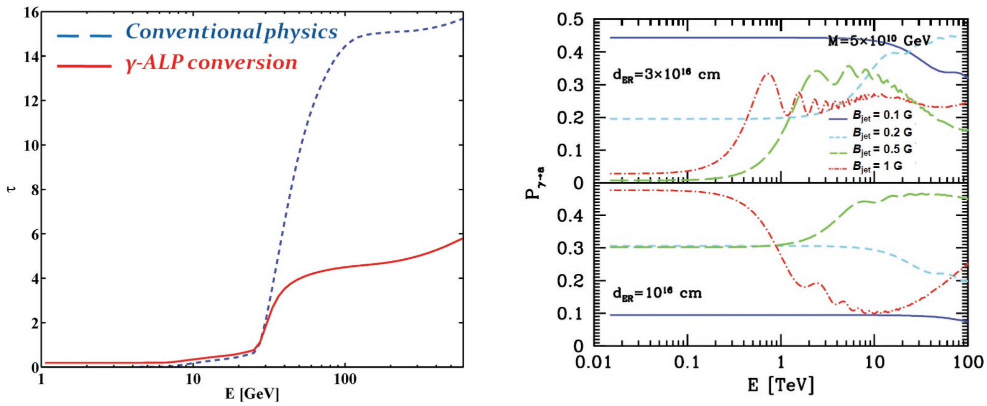

Figure 1: *Photon-ALP interaction in blazars. In the left panel, for FSRQs we report the BLR optical depth* τ *in the standard case and with photon-ALP interaction:* $g_{a\gamma\gamma} \simeq 10^{-11}\,{\rm GeV}^{-1}$ *and* $m_a < \mathcal{O}(10^{-10}\,{\rm eV})$ [6]. *In the right panel, for BL Lacs we plot the photon-to-ALP conversion probability* $P_{\gamma\to a}$ *with* $M \equiv 1/g_{a\gamma\gamma} = 5\times10^{10}\,{\rm GeV}$ *and different choices of the emission distance and of the jet magnetic field* $B_{\rm jet}$ [7].

BL Lacs do not present absorption regions as FSRQs so that VHE photons can escape from the central region unimpeded. In any case, photon-ALP conversion inside the jet magnetic field $B_{\rm jet} = (0.1-1)\,{\rm G}$ allows for the production of ALPs already in the source. The fraction of photon/ALP produced strongly depends on the values of the emission distance from the centre, on $B_{\rm jet}$ and on $g_{a\gamma\gamma}$ [7]. The right panel of fig.1 shows that the estimate for the produced ALPs is fairly large with a reasonable choice of the parameters.

3.2 Galaxy clusters

The emission of gamma-rays from the Perseus cluster – possessing a magnetic field $B_{\rm clus} = 1-10\,\mu{\rm G}$ – has been used in order to set constrains on m_a and $g_{a\gamma\gamma}$ by studying the possible photon-to-ALP conversion inside $B_{\rm clus}$ and back conversion inside the magnetic field of the Milky Way. A generic photon-ALP conversion probability is plotted versus the energy E in fig.7 of [8] with arbitrary reference energy $E_{\rm ref}$. When the ALP mass effect at low energies is important (see the oscillatory region at low energy in fig.7 of [8]) $P_{\gamma\to a}(E, m_a, g_{a\gamma\gamma}, B_{\rm clus})$ predicts spectral irregularities in observational data, which are related to the value of m_a and $g_{a\gamma\gamma}$. Since the observable spectrum $F_{\rm obs}$ is related to the intrinsic one $F_{\rm em}$ by $F_{\rm obs} = P_{\gamma\to\gamma}(m_a, g_{a\gamma\gamma})F_{\rm obs}$, with $P_{\gamma\to\gamma}$ denoting the photon survival probability in the presence of photon-ALP interaction, the statistical *no preference* for photon-ALP conversion to fit data constrains ALP parameters to: $g_{a\gamma\gamma} < 5\times10^{-12}\,{\rm GeV}^{-1}$ for $5\times10^{-10}\,{\rm eV} < m_a < 5\times10^{-9}\,{\rm eV}$ [9].

3.3 Extragalactic space

The propagation of the photon-ALP beam in extragalactic space is affected by the morphology and strength of the extragalactic magnetic field $\mathbf{B}_{\rm ext}$ which has large uncertainties in the range $10^{-7}\,{\rm nG} < B_{\rm ext} < 1.7\,{\rm nG}$ on the scale $\mathcal{O}(1\,{\rm Mpc})$. However, models contemplating galactic outflows especially from dwarf galaxies are generally believed to be the source of $\mathbf{B}_{\rm ext}$. Accordingly, $\mathbf{B}_{\rm ext}$ turns out to have a domain-like structure with $B_{\rm ext} = \mathcal{O}(1\,{\rm nG})$ and a coherence scale $\mathcal{O}(1\,{\rm Mpc})$. In extragalactic space photons are absorbed by scattering off the photons of the extragalactic background light (EBL) – which is the infrared/optical/ultraviolet radiation emitted by galaxies during the cosmic evolution – thereby producing an e^+e^- pair [10, 11]. This process is the analogous of the photons in FSRQs interacting with those of the BLR: thus, photon-ALP oscillations can increase the VHE photon mean free path enhancing the Universe transparency [4]. In addition, photon dispersion on the cosmic microwave background (CMB) plays a crucial role above 15 TeV, where the sharp discontinuous domain-like model for $\mathbf{B}_{\rm ext}$ gives unphysical results about the calculation of the photon survival probability $P_{\gamma\to\gamma}$ and – as reported in the left panel of fig.2 – a model which smoothly interpolates $\mathbf{B}_{\rm ext}$ from one domain to the next (with the orientation angle ϕ of the transverse component of $\mathbf{B}_{\rm ext}$ becoming a continuous function) is compelling [8]. As reported in the right panel of fig.2, we observe that, even in the presence of CMB photon dispersion,

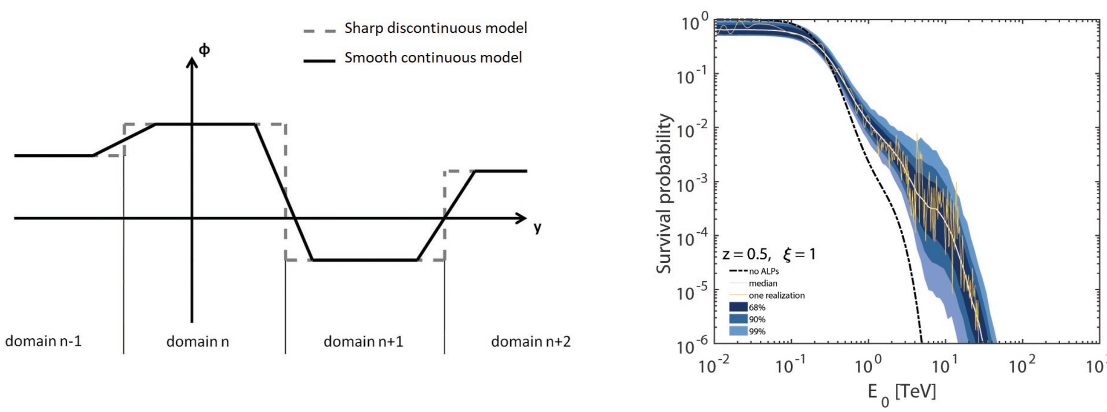

Figure 2: *Photon-ALP oscillations in extragalactic space. In the left panel, we plot the orientation angle ϕ of the transverse component of $\mathbf{B}_{\rm ext}$ crossing from a domain to the next in the domain-like smooth-edges (DLSME) model [8]. In the right panel, we report the photon survival probability $P_{\gamma\to\gamma}$ versus the observed energy E_0 in the standard case and as modified by photon-ALP interaction for a redshift $z = 0.5$ and $\xi = 1$: a single realization of $P_{\gamma\to\gamma}$ and its statistical properties are plotted. See [3] for details.*

$P_{\gamma\to\gamma}$ with photon-ALP oscillations at work is drastically increased as respect to the conventional physics prediction [3]. In the right panel of fig.2, we plot $P_{\gamma\to\gamma}$ for an hypothetical source at redshift $z = 0.5$ and $\xi \equiv (B_{\rm ext}/{\rm nG})(g_{a\gamma\gamma}10^{11}\,{\rm GeV}) = 1$. The behavior of $P_{\gamma\to\gamma}$ in the presence of photon-ALP oscillations depends on the choice of ξ and $P_{\gamma\to\gamma}$ gets increased more and more as the redshift grows [3].

3.4 Milky Way and total effect

Only the regular component of the Milky Way magnetic field $B_{\rm MW} \simeq 5\,\mu{\rm G}$ with coherence length $l_{\rm coh} \simeq 10\,{\rm kpc}$ gives a sizable contribution to the photon-ALP conversion: in any case, detailed sky maps of $B_{\rm MW}$

exist. By combining the photon/ALP propagation in the several magnetized environments crossed by the photon-ALP beam (the jet, the extragalactic space, the Milky Way) it is possible to obtain the observed SED for BL Lacs. In fig.3 we plot the SED of Markarian 501 (left panel) and 1ES 0229+200 (right panel) for reasonable values of m_a and of $g_{a\gamma\gamma}$ as discussed above. From fig.3 we see that conventional physics

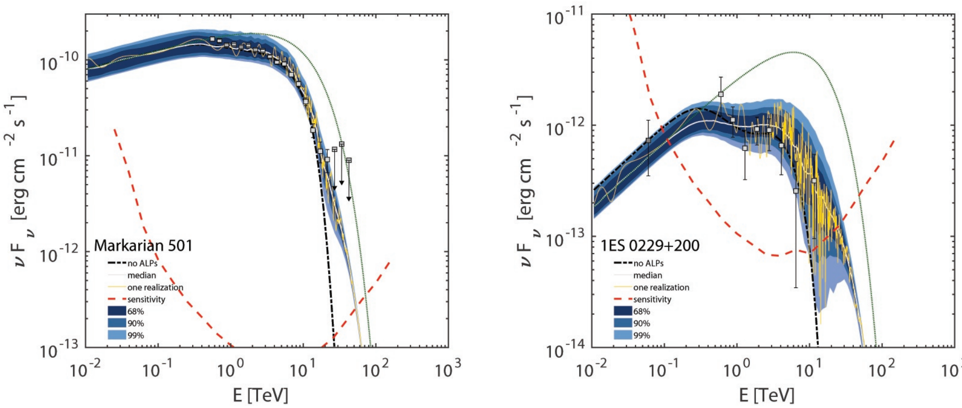

Figure 3: *Behavior of the observed SED of Markarian 501 (left panel) and 1ES 0229+200 (right panel) versus the observed energy E in the standard case and in the ALP scenario for reasonable values of m_a and of $g_{a\gamma\gamma}$* [12] *as discussed in previous sections.*

hardly explains the highest energy points in the spectra of Markarian 501 and of 1ES 0229+200, while the model including photon-ALP oscillations naturally matches the data. The photon-ALP interaction predicts features in BL Lac spectra (an energy-dependent oscillatory behavior and a photon excess above 20 TeV) that may be tested by the above new generation of the VHE gamma-ray observatories [12].

3.5 Main sequence and evolved stars

ALPs can be produced in the Sun via Primakoff scattering $p + \gamma \to p + a$, where p denotes a proton or a charged particle. The CAST experiment uses the fact that ALPs can then be reconverted back to photons inside the magnetic field of a decommissioned magnet of the LHC. However, no signal has been detected – which gives a firm bound about m_a and $g_{a\gamma\gamma}$: $g_{a\gamma\gamma} < 0.66 \times 10^{-10}\,\mathrm{GeV}^{-1}$ for $m_a < 0.02\,\mathrm{eV}$ [13].

ALPs similarly produced in main-sequence stars are a source of stellar cooling, which modifies stellar evolution as a function of m_a and $g_{a\gamma\gamma}$. As a consequence, also globular cluster star content gets accordingly modified: from a comparison with observational data bounds on ALP parameters can be derived as $g_{a\gamma\gamma} < 0.66 \times 10^{-10}\,\mathrm{GeV}^{-1}$ [14].

4 Discussion and conclusions

We have described some consequences of photon-ALP interaction in astrophysics but the list would be much longer: search for spectral irregularities of point sources in galaxy clusters in the X-ray energy band [15]; spectral distortions of the continuum thermal emission ($T \sim 2 - 8\,\mathrm{keV}$) of galaxy clusters [16]; study of the unexpected spectral line at 3.55 keV as dark matter decay into ALPs and subsequent conversion to photons [17]; in the VHE band hints about a better description of AGN spectral indices by introducing ALPs [18, 19]; search for a diffuse flux of photons coming from ALP-to-photon back-conversation concomitant with neutrino production in the extragalactic space [20].

In conclusion, we stress that many of the previous effects arise with the same choice of the ALP model parameters (m_a, $g_{a\gamma\gamma}$): this fact may be a possible first hint of the existence of an ALP. In any case, other possibilities that partially mimic ALP effects exist and have been compared in [21]. Astrophysical new data from the new generation of γ-ray observatories CTA, HAWC, GAMMA-400, LHAASO, TAIGA-HiSCORE, HERD and ASTRI will provide a check of the scenarios outlined above.

Acknowledgements

I thank M. Roncadelli and F. Tavecchio for a careful reading of the manuscript. I acknowledge contribution from the grant INAF CTA–SKA, “Probing particle acceleration and γ-ray propagation with CTA and its precursors” and INAF Main Stream project “High-energy extragalactic astrophysics: toward the CTA”.

References

1. A. Ringwald, Phys. Dark Univ. **1**, 116 (2012).
2. D. J. E. Marsch, Phys. Rep. **643**, 1 (2016).
3. G. Galanti and M. Roncadelli, J. High Energy Astrophys. **20**, 1 (2018).
4. A. De Angelis, G. Galanti and M. Roncadelli, Phys. Rev. D **84**, 105030 (2011).
5. G. G. Raffelt and L. Stodolsky, Phys. Rev. D **37**, 1237 (1988).
6. F. Tavecchio, M. Roncadelli, G. Galanti and G. Bonnoli, Phys. Rev. D **86**, 085036 (2012).
7. F. Tavecchio, M. Roncadelli and G. Galanti, Physics Letters B **744**, 375 (2015).
8. G. Galanti and M. Roncadelli, Phys. Rev. D **98**, 043018 (2018).
9. M. Ajello *et al.*, Phys. Rev. Lett. **116**, 161101 (2016).
10. A. De Angelis, G. Galanti and M. Roncadelli, Mon. Not. R. Astron. Soc. **432**, 3245 (2013).
11. G. Galanti, F. Tavecchio, F. Piccinini and M. Roncadelli, arXiv:1905.13713 (2019).
12. G. Galanti, F. Tavecchio, M. Roncadelli and C. Evoli, Mon. Not. R. Astron. Soc. **487**, 123 (2019).
13. V. Anastassopoulos *et al.*, Nat. Phys. **13**, 584 (2017).
14. A. Ayala *et al.*, Phys. Rev. Lett., **113**, 1302 (2014).
15. J. P. Conlon, F. Day, N. Jennings, S. Krippendorf and M. Rummel, JCAP **1707**, 005 (2017).
16. J. P. Conlon, M. C. D. Marsh and A. J. Powell, Phys. Rev. D **93**, 123526 (2016).
17. J. Jaeckel, J. Redondo and A. Ringwald, Phys. Rev. D **89**, 103511 (2014).
18. G. I. Rubtsov and S. V. Troitsky, JETP Lett., **100**, 355 (2014).
19. G. Galanti, M. Roncadelli, A. De Angelis and G. F. Bignami, arXiv:1503.04436 (2015).
20. H. Vogel, R. Laha and M. Meyer, arXiv:1712.01839 (2017).
21. G. Galanti, F. Tavecchio, M. Landoni, to appear (2019).

Frascati Physics Series Vol. 69 (2019)
PHOTON 2019 - International Conference on the Structure and the Interactions of the Photon
Jun 3-7, 2019

PHOTONS IN THE SCIENCE OF THE PIERRE AUGER OBSERVATORY

Sergio Petrera[1,2] for the Pierre Auger Collaboration[3,4]
[1] *Gran Sasso Science Institute (GSSI), L'Aquila, Italy*
[2] *INFN Laboratori Nazionali del Gran Sasso, Assergi (L'Aquila), Italy*
[3] *Observatorio Pierre Auger, Av. San Martín Norte 304, 5613 Malargüe, Argentina*
[4] *Full author list:* http://www.auger.org/archive/authors_2019_06.html

Abstract

In this paper, the connection between Pierre Auger Observatory measurements and photons is discussed. Three cases are presented: the search for photons in the ultrahigh-energy cosmic-ray radiation, the impact of the photon background in the cosmic ray propagation and the role of the ambient photon fields surrounding cosmic accelerators.

1 Introduction

The Pierre Auger Observatory 1) is the largest facility to detect cosmic rays built so far. It is located in the province of Mendoza, Argentina and has been in operation since 2004. Cosmic rays (CR) are studied by combining a Surface Detector (SD) and a Fluorescence Detector (FD) to measure extensive air showers. The SD consists of 1600 water-Cherenkov detectors on a 1500 m triangular grid (SD-1500) over an area of about 3000 km^2 and additional 61 detectors covering 23.5 km^2 on a 750 m grid (SD-750 or 'infill' array). The 24 fluorescence telescopes grouped in four FD buildings are located on the boundary of the observatory to overlook the whole atmospheric volume above the surface array. Three additional telescopes pointing at higher elevations (HEAT) are located near one of the FD sites (Coihueco) to detect lower energy showers. An array of radio antennas, Auger Engineering Radio Array (AERA) 1, 2), complements the data with the detection of the shower radiation in the hundred MHz region.

The design of the observatory has been conceived to exploit the 'hybrid' concept, the simultaneous detection of air showers by the surface array and fluorescence telescopes. The apparatus collects shower events of different classes depending on the on-time (generally called duty cycle) of the different detector components: the surface array is able to collect showers at any time, whereas the fluorescence detectors can operate only during clear moonless nights ($\approx 15\%$ duty cycle). After taking into account geometry and quality cuts applied at the event reconstruction level, the hybrid data-set is only a few percent. Therefore only a small part of the SD showers are actually reconstructed by the FD. Nonetheless, this sub-sample (the hybrid data-set) is very valuable, including events having both the footprint of the shower at the ground and the longitudinal profile measured. The hybrid approach has been a major breakthrough in the detection of UHE cosmic rays (UHE stands for $E > 10^{18}$ eV) since the method allows one to have the same energy scale in the surface detectors and the fluorescence telescopes and to derive the energy spectra entirely data-driven and free of model-dependent assumptions about hadronic interactions in air showers.

The science outcomes of the Pierre Auger Observatory are numerous and address several features of UHE cosmic rays, like the energy spectrum, the mass composition and the anisotropies in the arrival directions. It is beyond the purposes of this paper to show these results: the most recent ones can be found in ref. [3]. In this paper, I discuss how photons are related to the Auger results both as CR particles and as background fields. In particular, in Sec. 2, I summarize the advances in the search of UHE photons. The existence of these photons and their fraction to CR nuclear particles give remarkable hints about their origin. On the other hand, photons also affect UHECR observables (e.g. spectrum and composition) because cosmic rays interact with the photon fields present in the sources and the Universe. In Sec. 3, I discuss the impact of the photon background in the UHECR propagation, which connects the cosmic-ray sources to the observables we measure. Finally, in Sec. 4, I discuss the influence of the photon fields surrounding the cosmic-rays sources on the same observables.

2 Search for Ultrahigh-Energy Photons

A flux of photons with energies above 1 EeV is expected from the decay of π^0 particles produced by protons interacting with the cosmic microwave background (CMB) in the so-called Greisen-Zatsepin-Kuz'min (GZK) effect. In this scenario, called 'bottom-up', photons originate from the propagation of CR particles through the photon background and their flux is directly connected to the primary CR flux. The expected flux of GZK photons is estimated to be of the order of 0.01-0.1% of the total CR flux, depending on the astrophysical model [4, 5, 6] (e.g., mass composition and spectral shape at the source). Instead, a large flux of UHE photons is predicted in 'top-down' models: in this scenario [7, 8], ultrahigh-energy cosmic rays originate from the decay of supermassive particles, and these particles have decay branching ratios into photons (as well as neutrinos) comparable to that into hadrons. For this reason, UHE photon (and neutrino) limits are powerful tools to discriminate between the two scenarios. Further, it is worth noticing that a possible non-observation of UHE photons is meaningful for the physics foundations at the highest energies because it provides constraints to Lorentz Invariance Violation (LIV) [9], QED non-linearities [10] and space-time structures [11].

In the Pierre Auger Observatory, UHE cosmic rays are studied by observing the extensive air showers (EAS) originating from their interactions with the atmosphere. Therefore, the nature of the primary is analysed looking at mass parameters which exhibit different sensitivities to photon and hadron showers. EAS initiated by UHE photons have two remarkable features: a delayed development of the shower profile and a reduced muon content. To give an idea of the separation induced by the shower development, simulated proton and photon showers have average depths of the shower maximum, $X_{\max}$, that differ by about 200 g/cm^2 in the EeV (10^{18} eV) range. The lower muon content is instead detectable at the ground using the SD, where smaller footprints, steeper lateral distributions and faster rise-times are expected for photons. The observables used in the photon searches are different depending on the primary energy:

- At lower energies, hybrid events are numerous. For these events, the depth of the shower maximum,

$X_{\max}$, is the most sensitive mass parameter. Searches based on severe cuts on the measured $X_{\max}$ have been published [12, 13] where upper limits have been set for energies above 1, 2, 3, 5 and 10 EeV. The latest search based on the same event class mixes $X_{\max}$ with two SD observables, S_{b} and N_{stat}[1], which show sensitivity to the separation between photons and hadrons. A multivariate analysis based on the Boosted Decision Tree (BDT) technique has allowed us to improve the previous limits [14].

- At higher energies only SD observables are used to search for photon signatures. Upper photon flux limits for energies above 10^{19} eV have been published in [15, 16].

In figure 1 left panel, the Auger results on the integral photon flux are shown in comparison with the results from other experiments and model predictions. The achieved sensitivity allows testing photon fractions of about 0.1% at EeV energies and percent level at higher energies. This outcome rules-out early top-down models and challenges the most recent super-heavy dark matter models. Furthermore, these values initiate the exploration of the region of photon fluxes predicted in GZK astrophysical scenarios.

These searches address the diffuse photon flux. The Pierre Auger Collaboration also performed photon searches from sources. In [17], a blind search for point sources of EeV photons anywhere in the exposed sky was performed. The search is sensitive to a declination band from $-85°$ to $+20°$, in an energy range from $10^{17.3}$ eV to $10^{18.5}$ eV. No photon point source has been detected with the consequence that no celestial direction exceeds 0.25 eV cm^{-2} s^{-1} in energy flux. To reduce the statistical penalty of many trials as done in the blind directional search, a targeted search from different source classes was pursued in [18]. Several Galactic and extragalactic candidate objects are grouped in classes and are analyzed for a significant excess above the background expectation. No evidence for photon emission from candidate sources is found, and upper limits are given for the selected candidate sources. These

[1] See ref. [14] for their definition.

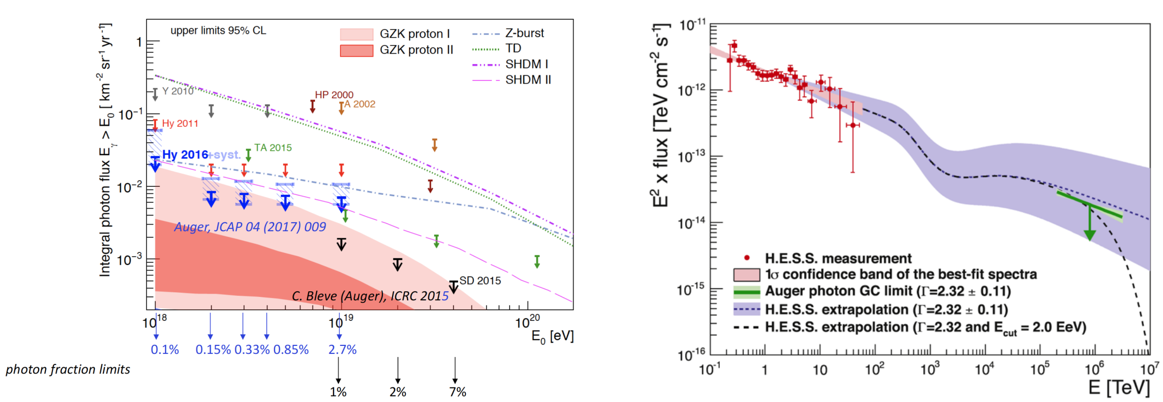

Figure 1: *Left: Upper limits on the integral photon flux from Auger for a photon flux* E^{-2} *and no background subtraction. The corresponding photon fractions are also given. Other limits from Telescope Array (TA), AGASA (A), Yakutsk (Y) and Haverah Park (HP) are shown for comparison. The shaded regions and the lines give the predictions for the GZK photon flux and for top-down models. References to data and models in* [14]. *Right: Photon flux as a function of energy from the Galactic center region. Measured data by H.E.S.S. are indicated, as well as the extrapolated photon flux at Earth in the EeV range. The Auger limit is indicated by a green line. A variation of the assumed spectral index by* ± 0.11 *according to systematics of the H.E.S.S. measurement is denoted by the light green and blue band. References in* [18].

limits significantly constrain predictions of EeV proton emission models from non-transient Galactic and nearby extragalactic sources. In fig. 1 right panel, the particular case of the Galactic center region is illustrated.

3 Photon background in the propagation of UHE cosmic rays

The cosmic-ray energy spectrum and composition measured by UHECR experiments are strongly affected by the propagation of particles from their sources to the Earth. Using propagation codes, it is possible to connect the injected spectrum/composition with the observed ones. Several investigations have been done in recent years to interpret UHECR data along this line [19]. Most of these studies converge to scenarios with sources injecting hard spectra with low rigidity cutoff and mixed composition, even though simplifying assumptions are used as uniform source distributions and 1D cosmic-ray propagation. All these results are strongly model dependent [20]: besides the hadronic interaction models which describe the shower development in the atmosphere, the other model uncertainties come from the photon background radiation which cosmic rays cross in their propagation and the cross sections of photo-disintegration of nuclei interacting with background photons. These uncertainties are sizeable and mainly due to the lack of data [21].

The Auger Collaboration has published a comprehensive study about the astrophysical implications from the combined fit of spectrum and composition data [22] above the ankle, discussing in detail the effects of theoretical uncertainties on the propagation of UHECRa and their interactions in the atmosphere as well as the dependence of the fit parameters on the experimental systematic uncertainties. In this study, we used a scenario in which the sources of UHECRs are of extragalactic origin, and nuclei are accelerated in electromagnetic processes with a rigidity-dependent maximum energy, $R_{\rm cut}$. Within this scenario a good description of the shape of the measured energy spectrum as well as the energy evolution of the $X_{\rm max}$ distributions can be achieved if the sources accelerate a primary nuclear mix consisting of H, He, N and Si, if the primary spectrum follows a power law $\propto E^{-\gamma}$ with a spectral index $\gamma \approx 1$ and if the maximum rigidity is about $10^{18.7}$ V. More details can be found in [22].

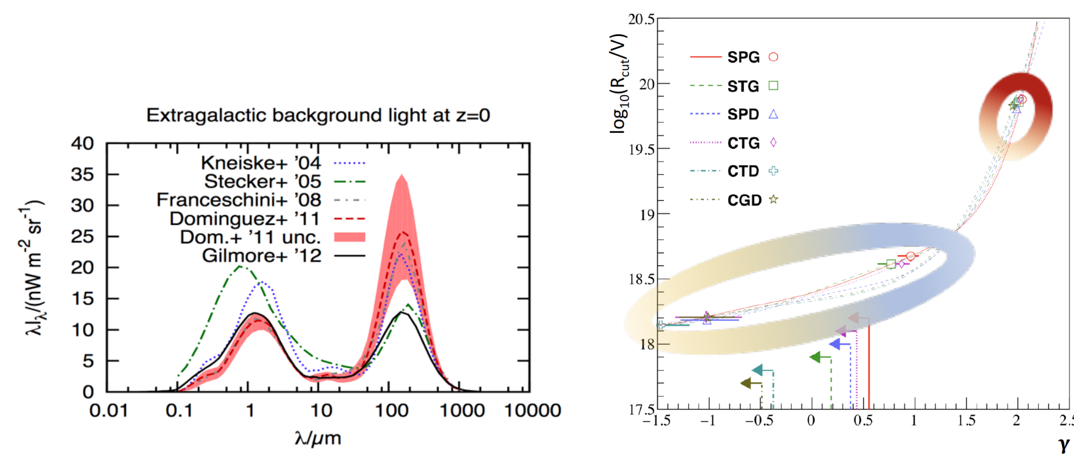

Figure 2: *Left: Intensity of the Extragalactic background light (EBL) at z= 0 for the models presented in ref.* [20]*. Right: The lines connecting the local minima for the six models given in ref.* [22]*. Symbols indicate the position of the minima of each model. Both the best fit at $\gamma \lesssim 1$ (enclosed in the elongated ellipse at left) and the second local minimum at $\gamma \approx 2$ (in the small ellipse at right) are shown.*

Here I want to focus on the impact of the photon backgrounds on these outcomes. In the energy range in which we are interested, the photon energy spectrum includes the cosmic microwave background radiation (CMB), and the infrared, optical and ultra-violet photons (commonly named extragalactic background light, EBL). The CMB has been measured extremely well, at least to the accuracy relevant for UHECR propagation. The EBL, which comprises the radiation produced in the Universe since the formation of the first stars, is relatively less known: several models of EBL have been proposed, among which there are sizeable differences (see fig. 2 left panel), especially in the far infrared and at high redshifts.

A quite general feature of the combined fit reported in [22] is a very definite correlation between the injection spectral index γ and the rigidity cutoff R_{cut}. Considering the deviance ($\approx \chi^2$) distribution there are in general two regions of local minima: one, which contains the best minimum, corresponds to a low value of R_{cut} and $\gamma \lesssim 1$; a second relative minimum appears, less extended, around the pair $\gamma \simeq 2$ and $\log_{10}(R_{\text{cut}}/\text{V}) \simeq 19.9$. In fig. 2 right panel, the positions of the minima of the combined fit are shown for the six different models used in [22]; in particular, the last letter in the model names refers to the EBL model used (G = Gilmore+ '12, D = Dominguez+ '11). One immediately notices the strong dependence of the best solution on the EBL model. Instead, the region of the second minimum appears to have a modest dependence on all model parameters. To explain, at least partly, the different dependence on the photon background it is worth noticing that interactions on EBL photons become dominant as we approach low spectral indexes ($\gamma \lesssim 1$) and rigidity cutoffs ($\log_{10}(R_{\text{cut}}/\text{V}) \lesssim 18.7$). As a consequence, better models of EBL spectrum and evolution would help to reduce the uncertainties on the astrophysical scenarios.

4 Photon fields in the CR source environments

As shown in the previous section, a combined fit of spectrum and composition measurements allows one interpret Auger data above the ankle. An extension to lower energies is possible in two alternative secenarios. In the first one, the light component below the ankle originates from a different population of sources [23]. In this model, the spectrum injected by the sources of this component is steeper than the one corresponding to the other population. In the second scenario, the light component originates from the photo-disintegration of high energy and heavier nuclei in the photon field present in the environment of the source. This scenario has been proposed as a general mechanism in [24] and also in the context of the UHECR acceleration in more specific astrophysical objects [25, 26, 28, 27]. It is worth pointing out that in this scenario we can also expect neutrinos emitted by the 'extended source' (i.e., including the radiation region surrounding the UHECR accelerator) allowing in this way multimessenger studies to discriminate among the different astrophysical models.

In ref. [24] it is shown that under certain hypotheses on the source parameters, the competition between interactions of nuclei emitted by the UHECR accelerator and the escape from the same region can generate *i.* a spectrum feature consistent with the observed UHECR ankle, *ii.* a mixed-composition escaping the source and *iii.* protons dominating in the ankle and sub-ankle regions. This fact is illustrated in fig. 3 where ^{28}Si nuclei are injected with a E^{-1} spectrum in a photon field represented by a broken power-law spectrum peaked at about 0.1 eV.

More studies are needed to understand if this promising scenario will give outcomes consistent with data in realistic astrophysical objects. In these studies a better description of the properties of the candidate source classes (luminosity and size of the accelerating region, shape of photon spectrum and its peak energy) is mandatory to improve the comparison with the available data.

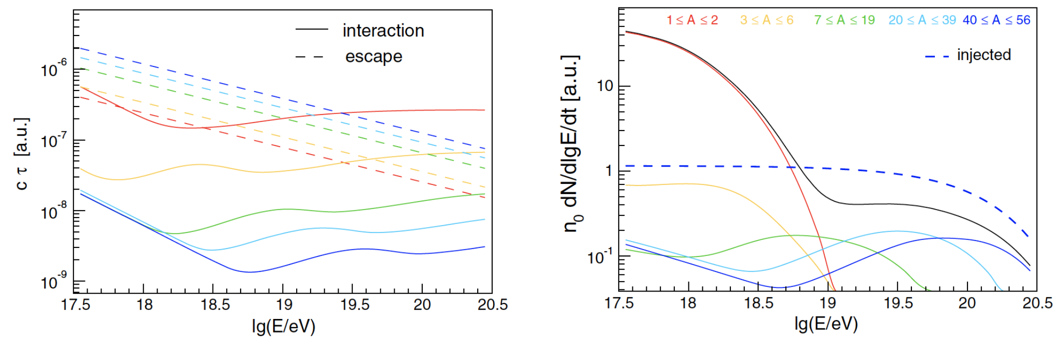

Figure 3: *Interaction and escape times for different nuclei (left). Case for injected* ^{28}Si *flux (dashed line) and escaping fluxes (solid lines). Parameters are given in* [24]*.*

References

1. A. Aab *et al.* [Pierre Auger Collaboration], Nucl. Instrum. Meth. A **798**, 172 (2015).
2. P. Abreu *et al.* [Pierre Auger Collaboration], JINST **7** P10011 (2012).
3. A. Castellina [Pierre Auger Collaboration], PoS ICRC **2019**, 004 (2019) [arXiv:1909.10791 [astro-ph.HE]]; A. Aab *et al.* [Pierre Auger Collaboration], arXiv:1909.09073 [astro-ph.HE].
4. G. Gelmini, O. E. Kalashev and D. V. Semikoz, J. Exp. Theor. Phys. **106**, 1061 (2008).
5. D. Hooper, A. M. Taylor and S. Sarkar, Astropart. Phys. **34**, 340 (2011).
6. B. Sarkar, K. H. Kampert and J. Kulbartz, Proc. 32nd Int. Cosmic Ray Conf., **2**, 198 (2011).
7. P. Bhattacharjee and G. Sigl, Phys. Rept. **327**, 109 (2000).
8. R. Aloisio, S. Matarrese and A. V. Olinto, JCAP **1508**, 024 (2015).
9. M. Galaverni and G. Sigl, Phys. Rev. Lett. **100**, 021102 (2008).
10. L. Maccione and S. Liberati, JCAP **0808**, 027 (2008).
11. L. Maccione, S. Liberati and G. Sigl, Phys. Rev. Lett. **105**, 021101 (2010).
12. J. Abraham *et al.* [Pierre Auger Collaboration], Astropart. Phys. **27**, 155 (2007)
13. J. Abraham *et al.* [Pierre Auger Collaboration], Astropart. Phys. **31**, 399 (2009).
14. A. Aab *et al.* [Pierre Auger Collaboration], JCAP **1704**, 009 (2017).
15. J. Abraham *et al.* [Pierre Auger Collaboration], Astropart. Phys. **29**, 243 (2008).
16. C. Bleve [Pierre Auger Collaboration], PoS ICRC **2015**, 1103 (2016).
17. A. Aab *et al.* [Pierre Auger Collaboration], Astrophys. J. **789**, 160 (2014).
18. A. Aab *et al.* [Pierre Auger Collaboration], Astrophys. J. **837**, L25 (2017).

19. References can be found e.g. in R. Aloisio, P. Blasi, I. De Mitri and S. Petrera, "Selected Topics in Cosmic Ray Physics," in *Multiple Messengers and Challenges in Astroparticle Physics* (Springer, 2018) 1-95 and arXiv:1707.06147 [astro-ph.HE].

20. R. Alves Batista, D. Boncioli, A. di Matteo, A. van Vliet and D. Walz, JCAP **1510**, 063 (2015).

21. For photo-disintegration uncertainties see e.g. D. Boncioli, A. Fedynitch and W. Winter, Sci. Rep. **7**, 4882 (2017).

22. A. Aab *et al.* [Pierre Auger Collaboration], JCAP **1704**, 038, (2017); Erratum: [JCAP **1803**, E02 (2018).

23. R. Aloisio, V. Berezinsky and P. Blasi, JCAP **1410**, 020 (2014).

24. M. Unger, G. R. Farrar and L. A. Anchordoqui, Phys. Rev. D **92**, 123001 (2015); M. S. Muzio, M. Unger and G. R. Farrar, arXiv:1906.06233 [astro-ph.HE].

25. N. Globus, D. Allard and E. Parizot, Phys. Rev. D **92**, 021302 (2015).

26. K. Fang and K. Murase, Phys. Lett. **14**, 396 (2018) [Nature Phys. **14**, 396 (2018)].

27. A. D. Supanitsky, A. Cobos and A. Etchegoyen, Phys. Rev. D **98**, 103016 (2018).

28. D. Biehl, D. Boncioli, A. Fedynitch and W. Winter, Astron. Astrophys. **611**, A101 (2018).

Frascati Physics Series Vol. 69 (2019)
PHOTON 2019 - International Conference on the Structure and the Interactions of the Photon
June 3-7, 2019

UNVEILING THE UNRESOLVED GAMA-RAY SKY THROUGH ITS ANISOTROPIES

Michela Negro
INFN Sez. di Torino - Via P. Giuria 1, 10125 Torino

Abstract

The gamma-ray sky has been revealed in the last decade by the *Fermi* Large Area Telescope (LAT), offering an outstanding picture of our Universe at the highest energies. The majority of this gamma-ray emission has been attributed to known processes involving cosmic-ray interactions with the interstellar medium within our Galaxy. Another important contribution is represented by the gamma-ray emission of known Galactic and extragalactic astrophysical sources. However, still an important fraction ($\sim$20%) of the total gamma-ray emission remains unresolved, and therefore we referred to it as the unresolved gamma-ray background (UGRB). Guaranteed contribution to this component is the cumulative emission of gamma-ray sources that are too faint to be resolved separately and hence lie below the current instrumental sensitivity. On the other hand, even more exotic scenarios involving dark matter particles may contribute as well, making the exact composition of the UGRB one of the main unanswered questions in gamma-ray astrophysics. The unprecedented large sample of high quality gamma-ray photons provided by the *Fermi*-LAT opened a new window on this study: the measurement and characterization of UGRB spatial anisotropies. In this talk I will give an overview of all the different techniques employed in the effort to give a definitive answer to the question of the UGRB composition.

1 Introduction

The UGRB is *nearly* isotropic, and this kind of topology can be easily explained by the cumulative emission of randomly distributed γ-ray sources whose flux is below the sensitivity of *Fermi*-LAT. Hence, these sources are too faint to be resolved separately, and this results in a global diffuse glow. Contribution from well-known extragalactic astrophysical source populations, such as blazars [1, 4] and misaligned AGNs (mAGNs) [2, 3] is guaranteed, them being quite rare objects generally speaking, but the brightest and the most numerous seen in γ-rays. Also, a non-negligible contribution is expected from SFGs [4, 5, 6], which are not very bright in the γ-band but extremely abundant in the Universe and may contribute mostly at low energies ($<$ 10 GeV). Minor contributions from an unresolved population of Galactic millisecond pulsars (MSPs) can be expected [7, 8], as well as from galaxy clusters [9, 10, 1], Type Ia supernovae [11, 12], and GRBs [13, 14]. Furthermore, more exotic scenarios may contribute as well: despite a huge current experimental effort aimed to search for evidence of annihilating or decaying WIMPs through the detection of γ-rays (primarily or secondarily produced), no signal has been robustly associated with DM up to now, so if present it is most probably unresolved and contributes to the UGRB. The first measurement of the UGRB, (as opposed to the EGB, which was measured already by EGRET and SAS-2) in terms of intensity energy spectrum, was performed by the *Fermi*-LAT collaboration in 2010 [15], and from that time on there has been a wide interest to interpret the results, even more accentuated when new measurements, also exploiting different approaches than the intensity spectrum (as we will see in the next section), have been released. Despite the extensive interpretation campaign, the exact composition of the UGRB remains one of the main unanswered questions of γ-ray astrophysics. The interest in finding a definitive answer is attributable to the need to constrain the faint end of the luminosity function of the UGRB contributors, which could also tell something about the cosmological evolution of the classes of objects involved. Since these objects, as we said before, are too faint to be resolved individually, the study of the UGRB may represent the only source of information about them. In addition, the UGRB characterization might shed some light on the nature of DM, constraining the parameter space of mass and annihilation cross-sections or decay lifetimes of weakly interacting massive particles (WIMPs).

2 Autocorrelation

In addition to the mean flux of the UGRB one could extract valuable information from the study of the angular scale and the amplitude of its intensity fluctuations. The technique exploited to perform this analysis is the autocorrelation, both in terms of auto-correlation function (ACF) and angular power spectrum (APS). The final result of this study is an anisotropy energy spectrum, which is sensitive to all the components of the UGRB whose distribution carries a non-negligible small-scale anisotropy content. In Fig. 1 it is reported the result from [20], in which *Fermi*-LAT data between 0.5 GeV and 1 TeV have been analyzed by means of a sophisticated tool to compute the angular power spectrum from UGRB maps. The analysis not only includes the autocorrelation of the unresolved background with itself for each energy bin, but also encompasses all the cross-correlations between different energy bins. The results supports the scenario in which two major and distinct populations are responsible for the observed tiny intensity fluctuations. The two populations emerge at different energies, the transition occurring at ~ 4 GeV. In particular the best-fit model given by a double power law with exponential cutoff, suggests the presence of a bulk of BL Lac type blazars above a few GeV, while at lower energies, a population with a softer spectrum, like possibly misaligned AGNs, FSRQs, SFGs, or even more likely a combination of them, appears to dominate the UGRB. The detection of the high-energy cutoff, once confirmed that it is due to the absorption of energetic γ rays from the EBL, might shed light about the cosmic evolution of the particular contributors dominating at those energies. A proper physical interpretation of this measurement is still a work in progress.

3 Cross-correlation with LSS probes

In addition to the estimation of global UGRB quantities (resulting from the previously listed techniques), it is possible to benefit from an extremely powerful tool to directly characterize the unresolved content, namely cross-correlations of the UGRB with other observables. This technique estimates both cross-correlation functions (CCF) and cross-correlation angular power spectra (CAPS), looking for a non-null signal, which would give immediate evidence of whether the considered observable contributes or not to the UGRB. Cross-correlations with the UGRB have been done considering different large scale structures (LSS) probes, such as galaxy catalogs, galaxy cluster catalogs, cosmic shear and lensing potential of the cosmic-microwave background (CMB).

Cross-correlation with galaxy catalogs. Literature counts several works devoted to the evaluation of the cross-correlation signal between the UGRB and different galaxy catalogs, e.g. [16], [17], [18], and [19]. In particular in [18] exploited a tomographic approach to study the evolution of the cross-correlation signal with the redshift (namely the distance of the galaxies). They clearly detected a change over redshift in the spectral and clustering behavior of the γ-ray sources contributing to the UGRB. In [19] it is presented the cross-correlation between the *Fermi*-LAT sky maps and the 2MPZ catalog through which they investigated the nature of the local $z < 0.2$ γ-ray Universe. They went beyond the tomographic approach by investigating the cross-correlation of the UGRB with different sub-selections of the 2MPZ catalog: three bins in absolute B-band luminosity to investigate the star formation activity, three bins in K-band luminosity to trace the mass of the objects and a low-B/high-K sample as ideal target for DM searches (objects with high-K and low-B luminosities being massive and with a low level of star formation activity). They found that the signal was dominated by AGN emission, while blazars and SFGs provide a subdominant contribution.

Cross-correlation with galaxy cluster catalogs. Clusters of galaxies are the product of hierarchical structure formation processes driven by gravitational instability. Clusters of galaxies are not isolated objects, but live in the nodes of a complex cosmic web, surrounded by filaments that host populations of astrophysical objects. Currently several catalogs of galaxy clusters are available, and in particular in [21] the cross-correlation signal with three different catalogs has been investigated: WHL12 ($0.05 < z < 0.8$), redMaPPer ($0.08 < z < 0.55$), and PlanckSZ ($z < 0.5$). They detected a clear non-zero cross-correlation signal for all the catalogs considered and quantified the statistical significance in terms of number of sigmas in the three energy bins: for WHL12 they found $N_\sigma = 3.7, 4.4$, and 2.9; for redMaPPer they found $N_\sigma = 3.3, 5.0$, and 2.7; for PlanckSZ, due to the limited number of clusters, they opted for considering one single energy bin ($E > 1$ GeV) finding $N_\sigma = 3.7$. Another recent work, [22], investigated the cross-correlation of the UGRB with the Subaru Hyper Suprime-Cam (HSC) catalog, which provides a wide and homogeneous measurement of the large-scale structure distribution up to redshift 1.1. They investigated the cross-correlation signal in two different redshift bins ($0.1 < z < 0.6$ and $0.6 < z < 1.1$). They found a signal with a significance of $2.0 - 2.3\sigma$ for all redshift and low-redshift cluster samples, and a weaker signal with significance of $1.6 - 1.9\sigma$ for the high-redshift sample.

Cross-correlation with cosmic shear. The cosmic shear is a statistical measurement of the distortion of images of distant galaxies due to weak lensing. The same distribution of matter responsible for the lensing traces the γ-ray emission, either because of DM annihilation (and/or decay) or because of astrophysical γ-ray emitters hosted by DM structures, hence one expects correlation between the two fields. The first measurement of the cross-correlation of the extragalactic gamma-ray sky with cosmic shear was performed by [23], and recently the same group published the updated results exploiting the

Subaru Hyper Suprime-Cam (HSC) SSP survey [24]. The conclusion of that work was that given the current statistical significance of the signal results are compatible with having no signal, the hope being to get more information from the HSC final data. Ref [25] is an investigation of the cross-correlation of the UGRB with other galaxy cluster surveys, in particular: the Canada-France-Hawaii Telescope Lensing Survey (CFHTLenS), the Red Cluster Sequence Lensing Survey (RCSLenS), and the Kilo Degree Survey (KiDS). They found no cross-correlation signal and no improvement was achieved by exploiting of a tomographic approach. A very recent work related to this measurement is [26], which exploiting 9 years of Fermi-LAT data and the Dark Energy Survey (DES), for the first time has detected a non-null cross-correlation signal. In particular, based on a signal-to-noise ratio of 4.5, their results show that the signal is mostly localized at small angular scales and high γ-ray energies, with a hint of correlation at extended separation.

Cross-correlation with CMB. CMB photons traveling toward us from the last scattering surface encounters a super-clusters and super-voids of matter along its journey, and undergo the so-called *integrated Sachs-Wolfe* (ISW) effect, caused by the expansion of the Universe at late cosmological time, when the Universe itself became Dark Energy (DE)-dominated. The net result of this effect is that the CMB temperature appear slighlty warmer/colder in correspondence of a super-cluster/super-void than it would otherwise. The same superclusters being expected to produce γ-rays, measuring the cross-correlation between the CMB map and the UGRB can potentially probe the properties of DE in the local Universe. This was investigated in [16] for the first time. Unfortunately they found a cross-correlation signal consistent with zero; the poor data statistics of the γ data (at that time) may have contributed to this negative result, and we cannot exclude that a future more updated work could lead to a non-null correlation. Recently [27] explored the possibility to find correlation between the UGRB and the *lensing potential* of the CMB: the gravitational lensing induced by LSS perturbs the statistical properties of the CMB and imprints some distortions on its anisotropy pattern, in such a way that the radiation detected today is not exactly that emitted at recombination. They found a preference for a signal with the correct features expected from the extragalactic γ-ray emission with a 3.0σ significance.

Fig. 2, therefore, shows the significance of cross-correlation signals between the UGRB and several LSS probes denoted by different colors: the widths of the bars illustrate the redshift ranges considered and beside each bar we indicate the energy range relative to the found cross-correlation signal.

4 Conclusion

The great interest in unveiling the UGRB composition is evident from the several different techniques that have been exploited to achieve that goal. We mentioned the study of its intensity energy spectrum, but other techniques, which exploits the statistical features of the field, are the 1-point probability distribution function (or 1-point PDF), the autocorrelation, and the cross-correlation with other observables tracing the large scale structures of the Universe. In this contribution we focused on the autocorrelation measurement and the cross-correlations of the UGRB with galaxy catalogs, galaxy cluster catalogs, CMB, CMB lensing potential and weak lensing. Combining all the results from those analyses will be the ultimate effort towards the unveiling of the nature of the unresolved gamma-ray emission.

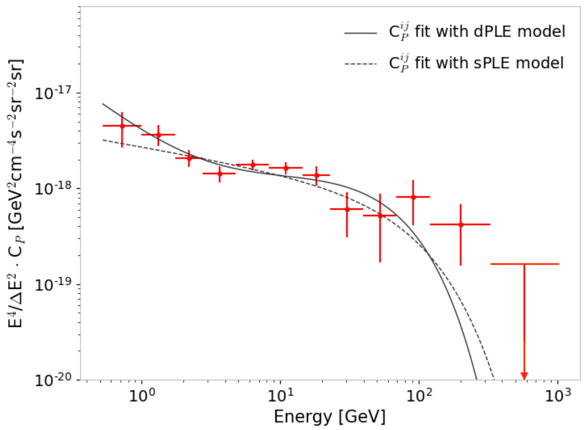

Figure 1: *UGRB Autocorrelation energy spectrum.*

5 Acknowledgements

The *Fermi*-LAT Collaboration acknowledges support for LAT development, operation and data analysis from NASA and DOE (United States), CEA/Irfu and IN2P3/CNRS (France), ASI and INFN (Italy), MEXT, KEK, and JAXA (Japan), and the K.A. Wallenberg Foundation, the Swedish Research Council and the National Space Board (Sweden). Science analysis support in the operations phase from INAF (Italy) and CNES (France) is also gratefully acknowledged. This work performed in part under DOE Contract DE-AC02-76SF00515.

References

1. Ando, S. *et al*, Mon. Not. Roy. Astron. Soc., 376, 4 (2007).

2. Inoue Y., Ap. J., 733, 66 (2011).

3. Di Mauro, M. *et al*, Ap. J., 780, 161 (2014).

4. Stecker, F. W. and Venters, T. M., Ap. J., 736 (2011).

5. Fields, B. D. *et al*, Phys. Rev. Lett. **13**, 138 (1964).

6. Makiya, R. *et al*, Ap. J., 728 (2011).

7. Siegal-Gaskins, J. M. *et al*, Mon. Not. Roy. Astron. Soc., 415 (1964).

8. Calore, F. *et al*, Ap. J., 796 (2014).

9. Miniati, F., Mon. Not. Roy. Astron. Soc., 337 (2002).

10. Keshe, U. *et al*, Ap. J., 585 (2003).

11. Ahn, K. *et al*, Phys. Rev. D17, 12 (2005).

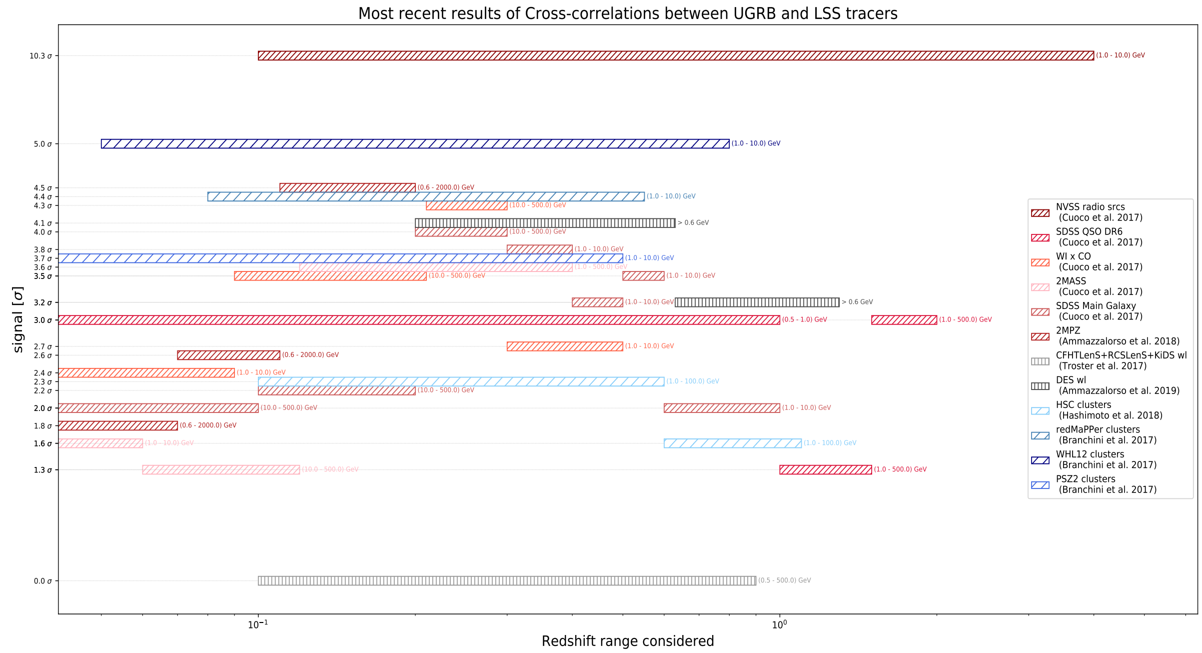

Figure 2: *Summary of Cross-Correlation signal between the extragalactic gamma-ray sky and LSS probes.*

12. Rasera, Y. *et al*, Phys. Rev. D74, 10 (2006).
13. Casanova, S. *et al*, Proceedings: Gamma-Ray Bursts 2007, 1000 (2008).
14. Ando, S. *et al*, Ap. J., 689 (2008).
15. Abdo, A.A. *et al*, Phys. Rev. Lett., 104 (2010).
16. Xia, J.-Q. *et al*, Mon. Not. Roy. Astron. Soc., 416 (2011).
17. Xia, J.-Q. *et al*, Ap. J. Suppl., 217 (2015).
18. Cuoco, A. *et al*, Mon. Not. Roy. Astron. Soc., 416 (2017).
19. Ammazzalorso, S. *et al*, Phys. Rev. D98, 10 (2018).
20. Ackermann, M. *et al*, Phys. Rev. Lett. 121, 24 (2018).
21. Branchini, E. *et al*, Astrophys. J. Suppl. 228, (2017).
22. Hashimoto, D. *et al*, Mon. Not. Roy. Astron. Soc., 448, 4 (2019).
23. Shirasaki, M. *et al*, Phys. Rev. D90 (2014).
24. Shirasaki, M. *et al*, Phys. Rev. D97, 12 (2018).
25. Tröster, T. *et al*, Mon. Not. Roy. Astron. Soc., 467 (2017).
26. Ammazzalorso, S. and others., arXiv:1907.13484 (2019)
27. Fornengo, N. *et al*, Ap. J 802 (2015)

Frascati Physics Series Vol. 69 (2019)
PHOTON 2019 - International Conference on the Structure and the Interactions of the Photon
Jun 3-7, 2019

THE γ-RAY HALO AROUNG GEMINGA IN FERMI-LAT DATA AND IMPLICATIONS FOR THE POSITRON FLUX AT EARTH

Mattia Di Mauro[1], Silvia Manconi[2,3*], Fiorenza Donato[2,3]
[1]*NASA Goddard Space Flight Center, Greenbelt, MD 20771, USA*
[2]*Dipartimento di Fisica, Università di Torino, via P. Giuria 1, 10125 Torino, Italy,*
[3]*Istituto Nazionale di Fisica Nucleare, Sezione di Torino, Via P. Giuria 1, 10125 Torino, Italy*

Abstract

In this contribution we present a detailed study of the GeV gamma-ray halo around Geminga and Monogem, and show the constraints found for the contribution of these PWNe to the cosmic-ray positron excess, combining Milagro and HAWC data with measurements from the Fermi-LAT for the first time. We report the detection of a significant emission from Geminga PWN, derived by including the proper motion of its pulsar. We demonstrate that using gamma-ray data from the LAT is of central importance to provide a precise estimate for a PWN contribution to the cosmic positron flux.

1 Introduction

In the last few years, the flux of cosmic-ray electrons and positrons ($e^{\pm}$) has been measured with unprecedented precision from about 0.1 GeV up to TeV energies, thanks to the data provided by PAMELA, Fermi-LAT, AMS-02, DAMPE and CALET experiments [1, 2, 3, 4, 5]. The interpretation of these data is still debated, and is of central importance to reach a full understanding of the cosmic-ray acceleration and propagation in the Galaxy. Among the different leptonic fluxes, the origin of the antimatter component (i.e., the e^+ flux) has received particular attention. In fact, the e^+ observed above 10 GeV cannot be explained by the tipycal expectations from the secondary production, i.e. the e^+ produced by spallation reactions of primary cosmic rays with the Interstellar Medium (ISM) [6]. This *excess* of cosmic-ray e^+ has been intepretated invoking different mechanisms (see [7, 8] for recent reviews), such as the pairs emitted by pulsars and their Pulsar Wind Nebulae (PWNe) [9], the secondary emission in Supernova Remnants (SNRs) [10], modifications in the secondary production mechanism [11], or the annihilation or decay of dark matter particles in our Galaxy (see [12] and references therein). The idea that pulsars might be factories of cosmic-ray $e^{\pm}$ in our Galaxy dates back to 30 years ago [13]. Multiwavelength observations of several PWNe confirm the presence of very-high energy $e^{\pm}$ pairs [14]. The spectral energy

* *speaker*

distribution (SED) of these objects, from radio to γ-ray energies, provides valuable information about the population of $e^{\pm}$ produced by these sources [8]. Nevertheless, the details of the acceleration and release of pairs from PWNe in the interstellar medium are still under investigation, and are of major interest for assessing a possible contribution of PWNe to the cosmic-ray $e^{\pm}$ detected at Earth. Recently, the Milagro and HAWC experiments have reported the detection of an extended γ-ray emission at energies larger than 5 TeV from the direction of Geminga and Monogem PWNe, with an angular size of about 2° [15, 16]. Geminga and Monogem (or J0633+1746 and B0656+14) pulsars are among the closest (distances of 0.250 kpc and 0.288 kpc, and ages of 342 kyr and 111 kyr, respectively) and most powerful sources in the ATNF catalog [17]. With a spin-down power of $W_0 \sim 3 \times 10^{34}$ erg s^{-1}, they have been considered for long among the main candidates to contribute to the e^+ flux at Earth [18, 19]. These γ-ray measurements can be used to precisely quantify the contribution of these PWNe to the cosmic-ray e^+ flux at Earth [20, 21]. In fact, the extended TeV γ-ray emission seen by HAWC and MILAGRO has been interpreted as inverse Compton scattering (ICS) emission of $e^{\pm}$ accelerated, and then released, by these sources and interacting with the interstellar radiation field (ISRF) [22]. The ISRF, composed of the cosmic microwave background (CMB), infrared (IR) and starlight (SL), is then scattered up to γ-ray energies. The angular extension of this TeV γ-ray emission, together with the age of the sources, suggest that these ICS photons are produced by $e^{\pm}$ pairs escaped from the PWNe, at a distance of few tens of parsec. However, the γ rays between $5-40$ TeV detected by HAWC are produced via ICS off the ISRF by $e^{\pm}$ at average energies of at least tens of TeV. Since the e^+ AMS-02 excess is between a few tens up to hundreds of GeV, the HAWC data cannot test directly the origin of this excess. The use of HAWC γ-ray data in order to predict the e^+ flux at AMS-02 energies is indeed an extrapolation, which can affect significantly the conclusion on the e^+ flux, depending on the assumptions made. Moreover, data from the Fermi-LAT experiment in the energy range of $10-1000$ GeV are perfectly suited in order to constrain more precisely the Monogem and Geminga contribution to the e^+ at $E > 100$ GeV, since ICS photons in this energy range are produced by $e^{\pm}$ detected at Earth with average energies in the range $350-1500$ GeV. In this contribution we discuss the search for an extended γ-ray emission in the direction of Geminga and Monogem using *Fermi*-LAT data, which can be attributed to the ICS of the accelerated $e^{\pm}$ pairs off the ISRF.

2 PWNe: positron and photon flux

Highly energetic $e^{\pm}$ pairs are believed to be produced in PWNe under the influence of winds and shocks around the pulsars, then accelerated up to very high energies, and finally injected into the ISM, typically after a few tens of kyr [13, 23]. We here consider a continuous injection scenario to describe the emission mechanism of $e^{\pm}$ in PWNe, where the particles are emitted with a rate that follows the pulsar spin-down energy, which is translated in the energy of $e^{\pm}$ pairs with an efficiency η. This time-dependent $e^{\pm}$ injection spectrum $Q(E,t)$ is obtained as described in Refs [24, 25].

Once produced at the source, the $e^{\pm}$ that propagate in the Galaxy and produce γ rays through ICS with the Galactic ISRF, which is composed of the CMB, the IR light, and the SL. The ISRF energy density in the local Galaxy is taken as in [22]. We model the photon flux emitted for the ICS around the pulsar as [26, 27], using the definition of the power of photons emitted by a single $e^{\pm}$ for ICS as in [26, 28]. In general, the dominant effects for energetic ($E > 10$ GeV) $e^{\pm}$ propagating in our Galaxy are the energy losses, through synchrotron emission and inverse Compton scattering on the above mentioned radiation fields, and the spatial diffusion, caused by the random scattering on the Galactic magnetic field irregularities. This last effect is tipically described by means of a diffusion coefficient of the form $D(E) = D_0(E/1\text{ GeV})^{-\delta}$, where the parameters D_0 and δ are tipically constrained throughout

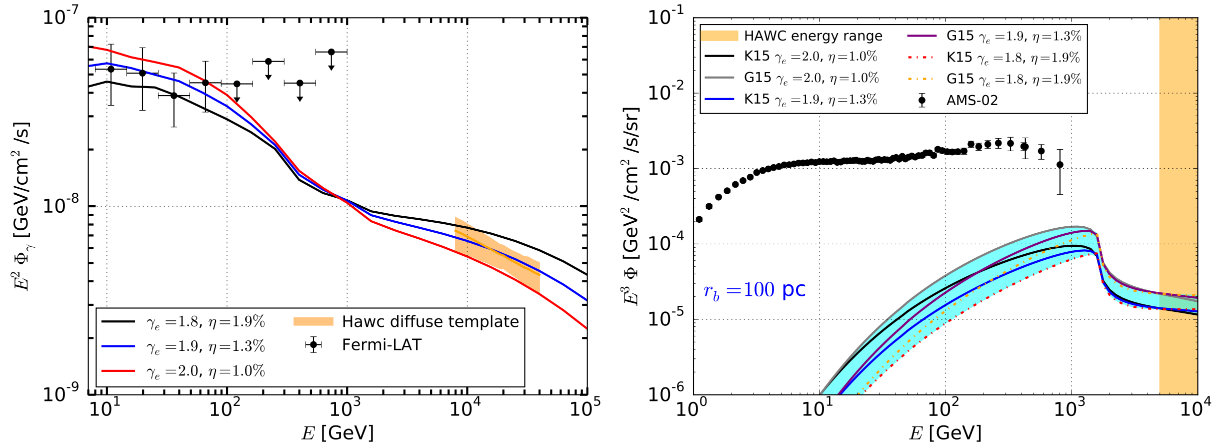

Figure 1: *Left panel: The γ-ray flux for ICS from Geminga. The Fermi-LAT data we derived are shown as black dots. We report the HAWC data (obtained using a diffuse template) as an orange band* [16]*. The curves are the flux predictions obtained for different values of γ_e and η. Right panel: e^+ flux at Earth from Geminga as computed within a two-zone diffusion model, and for the γ_e, η values compatible with Fermi-LAT data. Blue (purple) curves are for G15 (K15) propagation model and for $r_b = 100$ pc. The cyan band embeds the differences in the results considering these two propagation parameters and the choice of γ_e.*

the measurements of the ration between secondary and primary cosmic rays, since the first are almost only produced during the propagation of primary cosmic rays, and thus trace the propagation properties of the Galaxy. The HAWC data suggest that the diffusion coefficient ($D(E) = D_0(E/1\text{ GeV})^{-\delta}$) in the vicinity of Geminga and Monogem PWNe may be ~ 500 times smaller than the one usually derived for the average of the Galaxy [16]. We take into account this observation by using a two-zone diffusion model [29], where the region of inefficient diffusion is contained around the source, and delimited by an empirical radius r_b. For this two-zone diffusion model, we use the definition of the diffusion coefficient, as well as the solution for the $e^\pm$ density at the Earth position, as derived in Ref. [29]. As for the regions in the Galaxy for $r > r_b$, we use the propagation parameters obtained in [30] (K15) and [31] (G15). For more details on our model for the emission of $e^\pm$ and γ-rays from PWNe we address to Ref. [25].

3 Fermi-LAT data analysis setup

The point-like pulsed emissions from the Monogem and Geminga pulsars is included in *Fermi*-LAT source catalogs [32] [1]. A multiple-degree extended emission has instead never been claimed. In order to search for such a signal, we analyze 115 months of *Fermi*-LAT Pass 8 data, in the energy range $E = [8, 1000]$ GeV, passing standard data quality selection criteria, belonging to the Pass 8 `SOURCE` event class, and using the instrument response functions `P8R3_SOURCE_V2`. We consider energies above 8 GeV, because at lower energies the interstellar emission model (IEM), as well as the pulsed emission from the pulsar, dominate the γ-ray data. Our region of interest (ROI) is of $70^\circ \times 70^\circ$, and it is centered at RAJ2000$= 95^\circ$ and DEJ2000$= 13^\circ$. The data are binned with a pixel size of 0.06°, and 6 bins per energy decade.

We expect that the morphology of ICS emission is energy dependent. In particular, the larger the

[1]See `https://fermi.gsfc.nasa.gov/ssc/data/access/lat/8yr_catalog/` for the most recent Fermi-LAT source catalog obtained with 8 years of data.

value of D_0, the more extended will be the ICS emission. The extension decreases significantly for higher energies, and is about 3° in the HAWC energy range. The energy dependence of the spatial morphology of the ICS emission is taken into account by creating a *mapcube* template, a three dimensional table that, for each energy bin, gives the γ-ray intensity in Galactic longitude and latitude. For simplicity, we assume a one-zone diffusion model for the γ-ray ICS halo. This is a reasonable choice, since for the energies considered in our analysis the low-diffusion zone dominates our ROI. In addition, we include the effect on the ICS γ-ray morphology coming from the proper motion of the Geminga pulsar, which is relevant for energies below a few hundred GeV [29, 25]. In fact, the Geminga pulsar has a proper motion of 178.2 ± 1.8 mas/year, corresponding to a transverse velocity of $v_T \approx 211(d/250\text{pc})$ km s^{-1} [33].

Our model fit to the data includes the IEM (with free normalization and spectral shape), the isotropic template (with free normalization) and cataloged sources (with free normalization and spectral shape) from the preliminary 8 years list [2]. We employed the IEM released with Pass 8 data [34] (i.e., `gll_iem_v06.fits`). We also repeated the analysis using 10 different IEM (see [25]), in order to derive the systematics in the result associated to this choice. As for the templates of the Monogem and Geminga ICS halos, we vary D_0 in the range $10^{25} - 10^{29}$ cm^2/s, as well as their spectral slope, and perform our analysis for different values of D_0.

4 Results

We detect the Geminga ICS halo in Fermi-LAT data with $TS = 65 - 143$[3] and $D_0 = 1.6 - 3.5 \cdot 10^{26}$ cm^2/s, depending on the considered IEM. The value we find for D_0 is compatible within 2σ errors with the result by the HAWC Collaboration ($D_0 = 6.9^{+3.0}_{-2.2} \cdot 10^{25}$ cm^2/s). In addition, our analysis significantly detects the motion of Geminga pulsar by fitting its ICS halo. In fact, the fit in which we include the effect of the proper motion in the ICS template is preferred at $4.7 - 7.1\sigma$, depending on the IEM model. The Monogem halo is not detected in Fermi-LAT data, regardless of the value of D_0. We derive the 95% lower limit on the value of the diffusion coefficient to be $D_0 > 1 - 10 \cdot 10^{26}$ cm^2/s, which is compatible with Ref. [16]. The flux values for the Geminga ICS halo are reported in Fig. 1 (left panel). They are evaluated independently in different energy bins, by leaving free to vary the SED parameters of the sources in the model, as well as of the IEM and the isotropic templates. The *Fermi*-LAT measures the Geminga ICS halo with a precision of about 30% from 8 GeV up to 100 GeV. As for the remaining explored energies, we obtain upper limits. We also report our predictions for the SED derived using the modeling described in Sec. 2. By fitting the *Fermi*-LAT data, we derive the efficiency of spin-down energy conversion (η) for different e^+ spectral indices. For $\gamma_e = [1.8, 1.9, 2.0]$, we find $\eta = [0.019, 0.013, 0.010]$, respectively. We note that the chosen γ_e values bracket the HAWC measurements. An analogous analysis for Monogem for $\gamma_e = 1.9$ and 2.1 results in $\eta \leq 0.008$ and 0.006, respectively.

We now use our findings to predict the contribution of Geminga and Monogem to the e^+ flux at Earth. The e^+ flux is computed implementing the η fitted on the *Fermi*-LAT data, for the different e^+ spectral indices. Since the e^+ emitted from the Geminga and Monogem PWNe travel in both the low and high-diffusion zones before reaching the Earth, a two-zone diffusion model is used (see Sec. 2 and reference therein). The results are shown in Fig. 1 (righ panel) for $r_b = 100$ pc, and using for $r > r_b$ the K15 and G15 Galactic propagation models. The different γ_e and η give very similar predictions at hundreds of GeV up to TeV energies, where the *Fermi*-LAT γ rays calibrate the progenitor leptons. Therefore, at lower e^+ energies softer injection spectra give higher e^+ flux. The Geminga PWN, as constrained now

[2] `https://fermi.gsfc.nasa.gov/ssc/data/access/lat/fl8y/gll_psc_8year_v5.fit`

[3] (Test Statistic (TS) defined as twice the difference in maximum log-likelihood between the null hypothesis (i.e., no source present) and the test hypothesis: $TS = 2(\log \mathcal{L}_{\text{test}} - \log \mathcal{L}_{\text{null}})$.)

by *Fermi*-LAT data, contributes at a few per-cent level to the positron flux at 100 GeV. The highest contribution from Geminga is about 10% of the last AMS-02 energy data point at around 800 GeV. As for Monogem (not present in this figure, but see [25]), it can produce at most 3% of the flux at the highest energy measured e^+ flux. Additional tests that validate the detection of the Geminga ICS halo in *Fermi*-LAT data against different systematics are discussed in Ref. [25].

5 Conclusions

We reported the first detection of a counterpart of the Geminga γ-ray halo seen by HAWC in *Fermi*-LAT data from 8 GeV up to hundreds of GeV [25]. As for Monogem, we derived stringent upper limits. We accurately modeled the ICS emission from $e^\pm$ pairs produced in PWNe, as well as the effects of the proper motion of Geminga pulsar, as this affects the spatial morphology of the ICS γ-ray halo at GeV energies. We demonstrated that using *Fermi*-LAT data, together with HAWC measurements, can significantly constrain the e^+ flux from these two sources. We conclude that these sources alone, as bound now by *Fermi*-LAT data, cannot be the major contributors to the e^+ excess. However, a Galactic population of pulsars with efficiency in the range of $1-3\%$ and physical spin-down properties has been recently demonstrated to explain the e^+ flux excess [35]. This result, together with the results discussed in [9] for cataloged pulsars, suggest that the cumulative e^+ emission from Galactic PWNe remains a viable interpretation for the e^+ excess.

The *Fermi* LAT Collaboration acknowledges generous ongoing support from a number of agencies and institutes that have supported both the development and the operation of the LAT as well as scientific data analysis. These include the National Aeronautics and Space Administration and the Department of Energy in the United States, the Commissariatá l'Energie Atomique and the Centre National de la Recherche Scientifique / Institut National de Physique Nucléaire et de Physique des Particules in France, the Agenzia Spaziale Italiana and the Istituto Nazionale di Fisica Nucleare in Italy, the Ministry of Education, Culture, Sports, Science and Technology (MEXT), High Energy Accelerator Research Organization (KEK) and Japan Aerospace Exploration Agency (JAXA) in Japan, and the K. A. Wallenberg Foundation, the Swedish Research Council and the Swedish National Space Board in Sweden. Additional support for science analysis during the operations phase is gratefully acknowledged from the Istituto Nazionale di Astrofisica in Italy and the Centre National d'Etudes Spatiales in France. This work performed in part under DOE Contract DE- AC02-76SF00515.

MDM acknowledges support by the NASA Fermi Guest Investigator Program 2014 through the Fermi multi-year Large Program N. 81303 (P.I. E. Charles). The work of FD and SM is supported by the "Departments of Excellence 2018 - 2022" Grant awarded by the Italian Ministry of Education, University and Research (MIUR) (L. 232/2016). FD and SM acknowledge financial contribution from the agreement ASI-INAF n.2017-14-H.0 and the Fondazione CRT for the grant 2017/58675.

References

1. O. Adriani et al., *Nature* **458**, pp. 607–609 (2009).
2. M. Ackermann et al., *Physical Review Letters* **108**(1), pp. 011103 (2012).
3. M. Aguilar, L. Ali Cavasonza, G. Ambrosi, et al., *Phys. Rev. Lett.* **122**, pp. 041102 (2019).
4. G. Ambrosi et al., *Nature* **552**, pp. 63–66 (2017).
5. O. Adriani, Y. Akaike, K. Asano, et al., *Phys. Rev. Lett.* **120**, pp. 261102 (2018).

6. T. Delahaye, F. Donato, N. Fornengo, et al., *Astron. Astrophys.* **501**, pp. 821–833 (2009).
7. Pasquale D. Serpico, *Astropart. Phys.* **39-40**, pp. 2–11 (2012).
8. A. M. Bykov, E. Amato, A. E. Petrov, et al., *Space Sci. Rev.* **207**(1-4), pp. 235–290 (2017).
9. M. Di Mauro, F. Donato, N. Fornengo, et al., *JCAP* **4**, pp. 6 (2014).
10. P. Blasi, *Physical Review Letters* **103**(5), pp. 051104 (2009).
11. Nicola Tomassetti and Fiorenza Donato, *Astrophys. J.* **803**(2), pp. L15 (2015).
12. M. Di Mauro, F. Donato, N. Fornengo, et al., *JCAP* **5**, pp. 031 (2016).
13. X. Chi, K. S. Cheng, and E. C. M. Young, *ApJL* **459**, pp. L83 (1996).
14. B. M. Gaensler and P. O. Slane, *Ann. Rev. Astron. Astrophys.* **44**, pp. 17–47 (2006).
15. A. A. Abdo, B. T. Allen, T. Aune, et al., *ApJL* **700**, pp. L127–L131 (2009).
16. A. U. Abeysekara et al., *Astrophys. J.* **843**(1), pp. 40 (2017).
17. R. N. Manchester, G. B. Hobbs, A. Teoh, et al., *AJ* **129**, pp. 1993–2006 (2005).
18. Dan Hooper, Pasquale Blasi, and Pasquale Dario Serpico, *JCAP* **0901**, pp. 025 (2009).
19. Silvia Manconi, Mattia Di Mauro, and Fiorenza Donato, *JCAP* **1701**(01), pp. 006 (2017).
20. H. Yüksel, M. D. Kistler, and T. Stanev, *Physical Review Letters* **103**(5), pp. 051101 (2009).
21. A. U. Abeysekara et al., *Science* **358**(6365), pp. 911–914 (2017).
22. Silvia Vernetto and Paolo Lipari, *Phys. Rev.* **D94**(6), pp. 063009 (2016).
23. P. Blasi and E. Amato, *Astrophysics and Space Science Proceedings* **21**, pp. 624 (2011).
24. Hasan Yuksel et al., *Phys. Rev. Lett.* **103**, pp. 051101 (2009).
25. Mattia Di Mauro, Silvia Manconi, and Fiorenza Donato, (arXiv:1903.05647).
26. G. R. Blumenthal and R. J. Gould, *Reviews of Modern Physics* **42**, pp. 237–271 (1970).
27. Marco Cirelli, Gennaro Corcella, Andi Hektor, et al., *JCAP* **1103**, pp. 051 (2011).
28. T. Delahaye, J. Lavalle, R. Lineros, et al., *A&A* **524**, pp. A51 (2010).
29. Xiaping Tang and Tsvi Piran, *Mon. Not. Roy. Astron. Soc.* **484**(3), pp. 3491–3501 (2019).
30. Rolf Kappl, Annika Reinert, and Martin Wolfgang Winkler, *JCAP* **1510**(10), pp. 034 (2015).
31. Y. Genolini, A. Putze, P. Salati, et al., *Astron. Astrophys.* **580**, pp. A9 (2015).
32. M. Ackermann et al., *Astrophys. J. Suppl.* **209**, pp. 34 (2013).
33. J. Faherty et al., *Astrophysics and Space Science* **308**, pp. 225230 (2007).
34. F. Acero et al., *Astrophys. J. Suppl.* **223**(2), pp. 26 (2016).
35. Ilias Cholis, Tanvi Karwal, and Marc Kamionkowski, *Phys. Rev.* **D98**(6), pp. 063008 (2018).

Frascati Physics Series Vol. 69 (2019)
PHOTON 2019 - International Conference on the Structure and the Interactions of the Photon
Jun 3-7, 2019

THE MULTI-MESSENGER APPROACH FOR CURRENT AND FUTURE TRANSIENT SEARCHES AT VERY HIGH ENERGIES

Alessio Berti on behalf of the MAGIC Collaboration
INFN Torino, Torino, Italy

Abstract

The very high energy sky comprises many astrophysical sources originating from explosive or flaring events on different timescales, from fraction of seconds to years. These transient sources are largely observed and monitored in different bands of the electromagnetic spectrum, including very high energy (VHE, $E > 100$ GeV) gamma rays. Furthermore, transient sources are associated with systems of compact objects like black holes and neutron stars. Other non-photonic messengers, like gravitational waves and neutrinos, are expected to be produced in these extreme environments. Therefore the detailed characterization of the sources and environments of transient events should benefit from a multi-messenger approach for such searches. In this context, Cherenkov telescopes like MAGIC face many challenges in the observation of transient sources at VHE, stemming in particular from their low duty cycle and limited field of view. Nonetheless, the planning of targeted follow-up strategies proved to be successful in the observation of transients. In this contribution, a particular highlight will be given to the synergies between MAGIC and facilities like LIGO/Virgo and IceCube, providing alerts on GW and neutrino events respectively. Such synergies are the key to many outstanding results, as demonstrated by the detection of the flaring blazar TXS 0506+06 in coincidence with a high energy neutrino and the first time detection of a Gamma-Ray Burst at VHE by MAGIC, GRB 190114C. Finally, the future CTA experiment will open a new window in transient searches, thanks to its improved sensitivity, especially for short timescales.

1 Introduction

The current astrophysics panorama is rapidly changing thanks to the rise of the so-called multi-messenger observations, where data coming from different experiments and messengers are collected and analyzed. In some cases, this approach is the best one to try to find an answer to some pending questions of modern astrophysics, like the origin of ultra high energy cosmic rays or high energy neutrinos. Despite the limitations of the techniques used to detect the different messengers, the simultaneous analysis of the data

in the multi-messenger approach can partially compensate for the individual weaknesses. For the multi-messenger technique to work, a coordination of different experiments is extremely important, especially in providing information about interesting events to be followed-up. Consequently, each experiment can build its own follow-up strategies according to the information which is received.
The link between multi-messenger astrophysics and transient sources is quite straightforward. Different messengers are usually produced in catastrophic and highly energetic events, involving compact objects like black holes (BH) and neutron stars (NS). Such systems may exhibit an explosive or flaring behavior, giving rise to transient events on different timescales and energy ranges, such as gamma-ray bursts (GRBs), high energy neutrinos, gravitational waves, fast radio bursts (FRBs) and many more. Many transient sources are known or expected to be emitters of very high energy (VHE, $E \gtrsim 100\,\mathrm{GeV}$) photons. In such an energy range, one of the best instruments for the observations of transient sources are Cherenkov telescopes.
In this contribution I will describe on the challenges in the follow-up of some classes of transient sources with Cherenkov telescopes and highlighting some recent findings in such a rich and rapidly evolving field, focusing on the results of the MAGIC telescopes.

2 The MAGIC telescopes

The MAGIC[1] (*Major Atmospheric Gamma Imaging Cherenkov*) collaboration, composed by nearly two hundred people (scientists, engineers, technical and administration staff) from 12 countries across South America, Europe and Asia, operates two Cherenkov telescopes located at 2200 m a.s.l in the Canary island of La Palma, Spain [1]. The MAGIC telescopes use the Imaging Atmospheric Cherenkov Technique (IACT) to detect indirectly very high energy gamma rays produced from different astrophysical sources. This technique exploits the short (on nanosecond timescale) Cherenkov light flash emitted by highly energetic secondary particles produced by the interaction of a primary particle in the upper layers of the atmosphere. This light is collected by a large reflective surface (composed of segmented mirrors) and focused towards an imaging camera comprising a large number of light detectors, usually photomultipliers. From the topology and features of the image created by the triggered detector elements, the properties of the primary particle can be estimated, like its nature (gamma-ray or cosmic ray), energy and arrival direction. This technique can be improved using an array of several telescopes, giving a stereoscopic view of the same event and improving final angular and energy resolution and sensitivity. This approach is currently adopted by MAGIC since 2009. The most striking features of the MAGIC telescopes can be summarized as follows [2]: a) energy threshold as low as $50\,\mathrm{GeV}$ for observations performed near the zenith; b) angular resolution of $0.06°$ ($0.1°$) at $1\,\mathrm{TeV}$ ($100\,\mathrm{GeV}$); c) energy resolution of 15% (24%) at $1\,\mathrm{TeV}$ ($100\,\mathrm{GeV}$); d) sensitivity equal to about 0.7% of the Crab Nebula flux above $220\,\mathrm{GeV}$, giving a 5σ detection in 50 hours; e) field of view of $3.5°$ diameter; f) light-weight structure to allow fast repositioning of the telescopes ($180°$ rotation in 25 seconds); g) possibility to observe with moonlight with a contained reduction of the performances [3]. As explained in the following, these figures of merit of the MAGIC telescopes make them well suited for the follow-up of transient source.

3 The MAGIC transients program

Starting from their original concept, the MAGIC telescopes were designed to be able to detect the VHE emission expected from GRBs. While GRBs are still one of the key target in the general MAGIC science

[1] `https://magic.mpp.mpg.de/`

program, in order to adequately respond to the beginning of the operations of several new facilities for the observation of different messengers, the MAGIC transient scientific program currently comprises the follow-up of sources emitting high energy neutrinos, gravitational waves or bursts of radio waves. The fraction of time dedicated to this effort has been increased during the years given the global effort put into multi-wavelength and multi-messenger astrophysics and the possible high scientific reward from key discoveries in such a field.

3.1 The MAGIC automatic alert system

The response to transient events should be, in the general case, as fast as possible. Many transient sources exhibit an explosive behavior, where the bulk of the emission lasts a very brief period of time. Therefore, in most cases, planning observations is not possible. Moreover, Cherenkov telescopes have some downsides when considering the follow-up of transients, mainly their low duty cycle and small field of view. Indeed, the onset and sky position of transient events cannot be predicted: telescopes like MAGIC need to rely on external triggers provided by instruments with survey capabilities, which can pinpoint with reasonable localization the position of a transient event. For this reason, the Gamma-ray Coordinate Network (GCN) system receives the information about transient sources from different facilities (both ground-based and space-born) and distributes it to interested partners, including MAGIC, in the form of electronic alerts. In order to process these alerts, MAGIC developed an automatic alert system which checks the visibility of the target from the MAGIC site according to predefined criteria. In some cases (GRBs, neutrino alerts), if the conditions are fulfilled, the telescopes are automatically repointed to the position of the target contained in the alert (the so-called transient alert follow-up procedure). Originally developed only for the follow-up of GRBs, this system was adapted to process alerts coming from neutrino and gravitational wave experiments, making it a multi-messenger system.

3.2 Gamma-ray bursts

Gamma-ray bursts are transient sources releasing a large amount of energy in a short period of time as electromagnetic radiation. The emission from GRBs is divided in two phases: the prompt and the afterglow, both featuring typically non thermal spectra. In the former the bulk of emission is produced, usually in the keV-MeV band. The latter follows the prompt (but there can be a superposition) and comprises a fainter emission decreasing with time which can be observed in different bands, from radio to GeV.

While emission up to high energies (tens of GeV) was detected from GRBs, the search for VHE emission, predicted to be present by theoretical models, led to many unsuccessful attempts, until 2019. The difficulty of reaching a detection of a GRB at VHE depends on many aspects, related to their sudden appearance, typical high redshift, fast fading and heterogeneous characteristics. In particular, from the observation point of view, the detection of VHE emission from very distant sources is challenging due to the absorption of the VHE gamma-ray flux by the extragalactic background light (EBL). Such an effect increases with energy of the gamma-rays and distance of the source, producing a cutoff in the observed spectrum at increasingly lower energies as redshift increases. Therefore having a low threshold such as MAGIC's is important to collect photons in a region of the spectrum less affected by the effect of the EBL.

As anticipated, the year 2019 saw the first detection of VHE emission from a GRB, GRB 190114C, by a Cherenkov telescope i.e. MAGIC. Despite the non-optimal observing conditions (moderate moonlight and high zenith angles), MAGIC could detect a very strong VHE emission above 0.3 TeV, with a significance

of 20 standard deviations in the first 20 minutes of observation [4, 5]. This event, being the first of this kind, will help to learn more about GRB physics, from the process producing the VHE emission to the characteristics of the GRB jet.
Another interesting event in the sample of MAGIC GRBs is GRB 160821B, a short and close GRB at $z = 0.16$, since it is associated with a kilonova [6, 7] and because the MAGIC data shows a possible hint of detection. The latter, if real, could have strong implications for the detection of the counterparts of binary neutron star mergers in the VHE range.

3.3 High energy neutrinos

The discovery of a diffuse flux of neutrinos by Icecube has led to the search for the sources of such particles [8]. Furthermore, the detection of high energy neutrinos is a signature of the presence of hadronic processes involving ultra high energy cosmic rays (UHECRs). In such a scenario, electromagnetic radiation is expected to be produced. Therefore the detection of an electromagnetic counterpart of a high energy neutrino can help in the identification of the sources of UHECRs. For this reason, MAGIC is deeply involved in the follow-up of high energy candidate events released by IceCube. Such a task is simplified thanks to the IceCube realtime alert system [9], in operation since 2016, which automatically distributes alerts on high energy neutrinos to the follow-up community. Such an alert stream has been updated recently in order to release events with a high probability of being astrophysical and improved localizations. Neutrino alerts are publicly released via the Astrophysical Multimessenger Observatory Network (AMON) and the GCN. The MAGIC alert system receives these alerts and, as for GRBs, the reaction is completely automatic. Given the angular resolution of IceCube, around $0.2°–1°$, the localizations are comparable with the field of view of MAGIC. Therefore new analysis methods are being developed and tested to provide the identification of point-like sources or the computation of upper limits in an extended region of the field of view [10].
A milestone in the follow-up of neutrino events is IC170922A, a high energy neutrino (most probable energy of 290 TeV at 90% confidence level) detected by IceCube on 22nd September 2017. The position of the neutrino event was consistent with the one of a blazar, TXS 0506+056. After a week from the event, the Fermi-LAT instrument detected a flare from the source, a known emitter in the high energy range. This triggered additional follow-up observations, in which MAGIC eventually detected a significant VHE signal above 400 GeV from 13 hours of data collected between 28th September and 4th October 2017. For the first time, a gamma-ray flux was found found to be correlated to an astrophysical neutrino [11]. The extensive multi-wavelength observations performed was crucial to build the broadband spectral energy distribution, the starting point for theoretical modeling of the emission of both high-energy neutrino and electromagnetic radiation. The presence of the neutrino can be justified if at least part of the gamma-ray emission is hadronic in origin, therefore leading to several lepto-hadronic models proposed to explain the emission from TXS 0506+056 [12, 13, 14]. Considering the energy of the neutrino, the protons accelerated in the blazar and abel to escape from the acceleration region can plausibly reach 10^{19} eV. As a conclusion, TXS 0506+056 can be a source of UHECRs [12].

3.4 Gravitational waves counterparts

After the discovery of the first gravitational wave signal from a binary black hole system [15] and of the first electromagnetic counterpart to a gravitational wave event from a binary neutron star system [16, 17], the follow-up of GW candidate events is growing even more, with more and more facilities joining in the effort. MAGIC started to perform follow-up of GW events released by LIGO and Virgo since 2015 through a dedicated memorandum of understanding, performing the first follow-up by a Cherenkov telescope for GW151226 [18]. Currently, the interferometers LIGO and Virgo are in their third observational run (O3), started on 1st April 2019 and expected to last 12 months. While in O1 and O2 GW alerts were distributed via a private GCN stream only to partners with a signed memorandum of understanding, in O3 alerts are being distributed publicly via GCN, given the increased rate of expected events (about one per week and one per month for BBH and BNS systems respectively). This change in the distribution of alerts led MAGIC to set up a (semi-)automatic procedure in order to cope with different scenarios. Given the network of three interferometers, events with a localization region of few tens of square degrees can be expected. In such a case the region can be covered with a scan, where pointings have a duration tuned to the desired sensitivity level. This kind of events (like GW170817/GRB 170817A) may also be quite close, so that complete galaxy catalogs can be used to search for a correlation with the distance information provided by GW instruments. If an electromagnetic counterpart is discovered by other facilities, its observation has the priority. The reaction can be automatic or manual, depending on the way the alert is distributed. In the latter case, a fast target of opportunity strategy has been approved to let experts on duty change the night schedule to prioritize the observation of the counterpart. This follow-up strategy is also applied when the localization region is larger, namely hundreds or thousands of square degrees, where a scan with few pointings is not feasible. The last observational case cover the case of electromagnetic delayed emission on timescales of weeks/months, as seen in GW170817/GRB 170817A. The information provided by radio, optical and X-ray facilities are crucial in such a scenario in order to carefully plan an observation.

As O3 is reaching almost half of its duration, some developments are expected before its conclusion. One of the most interesting ones will happen when KAGRA will join the GW network, helping in providing better localization for an easier follow-up [19]. In view of such changes, MAGIC strategy will be refined in order to be as most automatic as possible, selecting the best mode of observation and target(s) as soon as possible after the GW trigger.

4 Conclusions and prospects

MAGIC is strongly contributing to the advances in the study of transient sources, thanks to the solutions adopted in hardware, software and technology aspects of the experiment. This led to milestone discoveries as the first gamma-ray source in coincidence with a high energy neutrino and the first detection of a GRB in the VHE range, which are helping in the advance of our knowledge in those fields. The collaboration is putting a lot of effort in maintaining and updating its follow-up strategies, including also new transient phenomena like Fast Radio Bursts [20]. In the multi-messenger panorama, more sensitive facilities are expected to come online in the next decade, providing more events to be followed-up and increasing the number of potential discoveries. In view of such developments, MAGIC is always improving the telescopes capabilities and refining observational strategies, possibly coordinating with other facilities for multi-wavelength or multi-messenger observations.

References

1. Aleksić, J. et al., *The major upgrade of the MAGIC telescopes, Part I: The hardware improvements and the commissioning of the system*, Astropart. Phys. **72** (2016) 61 [astro-ph.IM/1409.6073]

2. Aleksić, J. et al., *The major upgrade of the MAGIC telescopes, Part II: A performance study using observations of the Crab Nebula*, Astropart. Phys. **72** (2016) 76 [astro-ph.IM/1409.5594]

3. Ahnen, M. L. et al., *Performance of the MAGIC telescopes under moonlight*, Astropart. Phys. **94** (2017) 29 [astro-ph.IM/1704.00906]

4. Mirzoyan, R. et al., *MAGIC detects the GRB 190114C in the TeV energy domain.*, GCN 23701 (2019)

5. Razmik Mirzoyan, *First time detection of a GRB at sub-TeV energies; MAGIC detects the GRB 190114C*, The Astronomer's Telegram 12390 (2019)

6. Lamb, G. P. et al., *Short GRB 160821B: a reverse shock, a refreshed shock, and a well-sampled kilonova*, arXiv astro-ph.HE/1905.02159

7. Troja, E. et al., *The afterglow and kilonova of the short GRB 160821B*, arXiv astro-ph.HE/1905.01290

8. Aartsen, M. G. et al., *Observation and Characterization of a Cosmic Muon Neutrino Flux from the Northern Hemisphere Using Six Years of IceCube Data*, ApJ **833** (2016) [astro-ph.HE/1607.08006]

9. Aartsen, M. G. et al., *The IceCube realtime alert system*, Astropart. Phys. **92** (2017) 30 [astro-ph.HE/1612.06028]

10. Fattorini, A. et al., *Analysis Methods for Neutrino Follow Up Observations with MAGIC*, this conference proceedings

11. IceCube Collaboration et al., *Neutrino emission from the direction of the blazar TXS 0506+056 prior to the IceCube-170922A alert*, Science **361** (2018) 147 [astro-ph.HE/1807.08794]

12. Ansoldi, S. et al., *The Blazar TXS 0506+056 Associated with a High-energy Neutrino: Insights into Extragalactic Jets and Cosmic-Ray Acceleration*, ApJ **863** (2018) L10 [astro-ph.HE/1807.04300]

13. Keivani, A. et al., *A Multimessenger Picture of the Flaring Blazar TXS 0506+056: Implications for High-energy Neutrino Emission and Cosmic-Ray Acceleration*, ApJ **864** (2018) 84 [astro-ph.HE/1807.04537]

14. Gao, S. et al., *Modelling the coincident observation of a high-energy neutrino and a bright blazar flare*, Nature Astronomy **3** (2019) 88 [astro-ph.HE/1807.04275]

15. Abbott, B. P. et al., *Observation of Gravitational Waves from a Binary Black Hole Merger*, PRL **116** (2016) 061102

16. Abbott, B. P. et al., *GW170817: Observation of Gravitational Waves from a Binary Neutron Star Inspiral*, PRL **119** (2017) 161101

17. Goldstein, A. et al., *An Ordinary Short Gamma-Ray Burst with Extraordinary Implications: Fermi-GBM Detection of GRB 170817A*, ApJL **848** (2017) 2

18. de Lotto, Barbara et al., *MAGIC electromagnetic follow-up of gravitational wave alerts*, New Frontiers in Black Hole Astrophysics **324** (2017) 287

19. Abbott, B. P. et al., *Prospects for observing and localizing gravitational-wave transients with Advanced LIGO, Advanced Virgo and KAGRA*, Living Reviews in Relativity, **21** (2018) 1

20. Acciari, V. et al., *Constraining very-high-energy and optical emission from FRB 121102 with the MAGIC telescopes*, Mon. Not. R. Astr. Soc. **481** (2018) 2479 [astro-ph.HE/1809.00663]

Frascati Physics Series Vol. 69 (2019)
PHOTON 2019 - International Conference on the Structure and the Interactions of the Photon
Jun 3-7, 2019

GAMMA-RAY AND NEUTRINO ASTROPHYSICS CONNECTION

Dario Gasparrini
INFN - Roma Tor Vergata Via della Ricerca Scientifica, 1. I-00133 Rome - Italy
ASI Space Science Data Center Via del politecnico, snc. I-00133 Rome - Italy
Sara Buson
University of Würzburg, Emil-Fischer-Str. 31 D-97074 Würzburg - Germany
on behalf of Fermi-LAT Collaboration

Abstract

The recent discovery of a diffuse neutrino flux of astrophysical origin by IceCube started the search to identify the cosmic sources of the emission. Synergy with other experiments could be a useful mean of investigation and in particular, the combination of neutrino/gamma-ray information is motivated by the fact that both radiations may be produced in the same astrophysical particle-cascade scenario, arriving us undeflected from the source. With these assumptions, we can place limit on the known astrophysical source classes contribution to the diffuse neutrino flux. Another ground of discovery in this field is the search for transients and variable neutrino/ electromagnetic sources, in which case the atmospheric neutrino and the muon background can be reduced by taking time- and space-coincidence.

1 Introduction

The detection of a diffuse high-energy neutrino flux of cosmological origin in the range from 30 TeV to 2 PeV [1]) by the IceCube observatory has prompted the quest for the identification of of the astrophysical sources responsible of it. The observed signal is consistent with an isotropic distribution, suggesting that the majority of the contribution is from extragalactic origin [2]). The production of high energy neutrinos involves the acceleration of cosmic rays. Two main categories of high-energy neutrino / cosmic rays production models have been proposed: ”cosmic-ray accelerators”, where neutrino are produced within the cosmic ray source and mesons are typically produced by interactions of cosmic rays with radiation, and ”cosmic-ray reservoirs”, where neutrinos are produced by inelastic hadronuclear collisions while confined within the environment surrounding the cosmic ray source (for more details see e.g. [3])). For instance, the former models have been suggested for relativistic jets of gamma-ray bursts and blazars, while the second one for starburst galaxies, galaxy clusters and active galactic nuclei (AGN).

2 AGN as Multi-Messenger Sources

AGN with relativistic jets, powered by accretion of mass onto the central massive black hole (SMBH), have long being endorsed and, in turn, neutrino emitters [4]. Blazars, AGN with jet pointing close to the line of sight of the observer are the most numerous sources in the extragalactic GeV-TeV γ-ray sky (e.g., [5]). Their powerful jets are capable of accelerating electrons to relativistic energies, and their electromagnetic emission is often explained within the framework of leptonic scenarios.

However, it is reasonable assuming that in such environments hadrons are present too and, at least at some extent, accelerated as well. the idea has fostered the development of lepto-hadronic scenarios, where emission by hadrons interactions contribute to the electromagnetic radiation observed at the highest energies. In hadronic interactions, high energy photon / pairs and neutrinos are produced in equal powers making gamma-ray blazars plausible source candidates of the observed high-energy neutrinos.. It has been shown that one-zone blazar emission models, where neutrinos are produced in photo-hadronic interactions, typically predict the peak of neutrino spectra at or beyond PeV-energies [6].

2.1 A promising hint

In literature, several studies claim a hint for connection between gamma-ray blazars and high energy neutrino events, although with marginal correlation significance. One example is the blazar PKS 1424-418 which flare was found correlated at 2-3σ of significance with a 2 PeV neutrino [7].

To date, the most compelling correlation is in the observation of IceCube event IceCube-170922A in spatial and time coincidence with the flaring gamma ray blazar [8]. Information about its sky localization were reported by the IceCube collaboration to the astrophysical community almost in real time and prompted an extensive multi-messenger campaign to pinpoint the potential counterpart. High energy gamma-ray emission from the candidate neutrino counterpart, the blazar TXS 0506+056, was first reported by the *Fermi*-Large Area Telescope [9], and further confirmed by the MAGIC and VERITAS Cherenkov detectors [10], [11]. At the time of the neutrino detection TXS 0506+056 was undergoing an enhanced activity state (see fig. 1). Assuming a direct correlation between the gamma-ray and neutrino emission, a spatial chance coincidence of the neutrino and blazar was disfavored at 3 σ significance. The rich multiwavelenght dataset collected enabled an avalanche of theoretical efforts directed to model the neutrino emission in coincidence with electromagnetic blazar flare (see e.g [10])

A subsequent follow up analysis of the IceCube arrival data evidenced the presence of additional neutrinos positionally coincident with TXS0506+056 [2]. The neutrino excess was constituted by 13 low-energy events clustered in a four months time interval, between October 2014 and March 2015. The energy of the events was on average 10 TeV, and the most energetic one had a deposited energy of 20 TeV. The spatial coincidence and previous gamma-ray/neutrino connection had motivated the idea that the blazar could be responsible also for these observed neutrinos. Intriguingly, during this period of time, the source did not show remarkable activity over the gamma ray spectrum and its emission is compatible with a quiescent state (green shaded area in fig.1).

2.2 A complicated interplay

Many theoretical models that have been applied to the spectral energy distribution (SED) of TXS0506+-56 successfully explain the multi wavelength emission and the neutrino detection from the blazar. However, the detection of one single neutrino event makes it difficult to derive robust estimates on the neutrino spectrum. The latter is a necessary ingredient to anchor any theoretical model. The archival neutrino

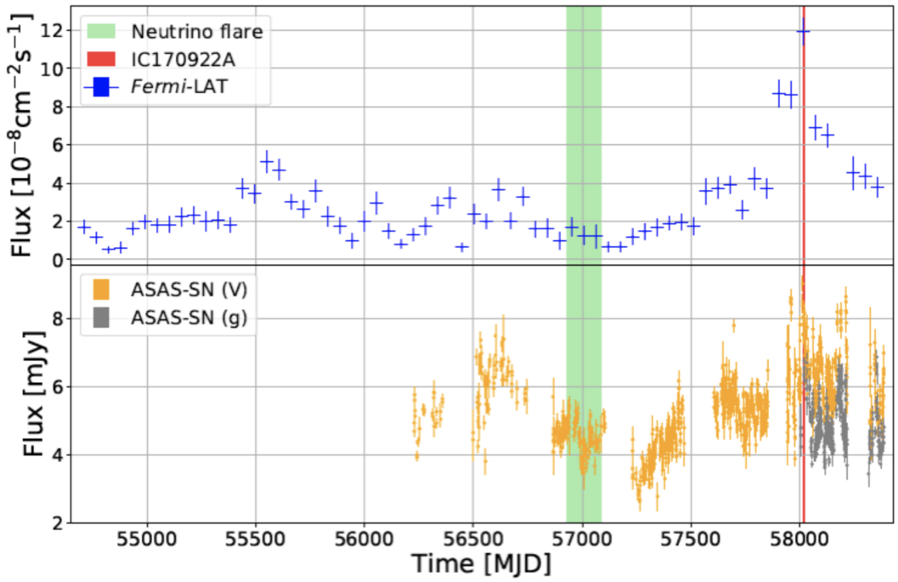

Figure 1: *Light curve of TXS 0506+056 in the-gamma-ray (top, Fermi-LAT) and optical band (bottom, ASAS-SN). The vertical red line indicates the arrival time of IceCube-170922A, The green shaded area highlights the period if time when in 2014-15 IceCube observed an excess of low-energy neutrinos ("neutrino flare"). From* [12]

excess observed in 2014-15 offers an ideal opportunity in this case; it includes a sufficient statistics to derive special constrains and thus allows us to test predictions for photo-hadronically produced neutrinos from TXS 0506+056 and place constrains on the associated broad-band electromagnetic SED.

In the photo-hadronic scenario of a jetted AGN, the high energy photons and electron-positron pairs accompanying the neutrino emission are expected to develop electromagnetic cascades. It can be shown that the efficiency is directly linked to the observed neutrino production rate and the observable photon radiation is theoretically expected to be shifted in the keV to MeV band.

Efforts have been directed into comparting the contemporaneous neutrino and electromagnetic observations for October 2014/March 2015 dataset. During the archival neutrino flare only sparse observations in optical, X-rays, and gamma-rays are available. Nevertheless, this limited information accessible are yet remarkably constraining for photon-hadronic predictions.

3 Future perspective

The progress made in the past years have turned neutrino astrophysics into a promising ground for future discoveries. the Possible TXS 0506+056 / IceCube-170922A association is a tantalizing clue in support of hadronic acceleration in blazar, and the identification of the first neutrino emitter. Nevertheless, detailed investigation of the 2014/2015 blazar/neutrino dataset suggest that a correlation between gamma-ray flaring activity and neutrino emission is not straightforward and needs further investigation. The signature of the expected cascade electromagnetic emission accompanying the neutrino production are likely encoded in X-ray - soft gamma-ray band, making the keV band and above the crucial energy range to solve the multi messenger case. Current wide-field instruments such like INTEGRAL [13] and

MAXI/GSC [14] provide larger sky coverage offering a good complement to more sensitive instruments like *Swift* and *NuSTAR*. Significant progress are expected in the future, when instruments like IXPE [15] and hopefully AMEGO [16] will provide the first X-ray/gamma-ray polarimetry results and coverage of the sub MeV band helping to disentangle leptonic and hadronic contribution in the blazar SED. New neutrino observatories planned for the upcoming decade, such as KM3NeT [17] and GVD [18] in the northern hemisphere and the upgrade of IceCube in the South Pole will have a sensitivity similar or improved by a factor of two to the current IceCube detector. These next generation observatories promise to shed the light in the identification of hadronic sources, providing the first definite clues into Universe PeV accelerators.

4 Acknowledgements

The *Fermi*-LAT Collaboration acknowledges support for LAT development, operation and data analysis from NASA and DOE (United States), CEA/Irfu and IN2P3/CNRS (France), ASI and INFN (Italy), MEXT, KEK, and JAXA (Japan), and the K.A. Wallenberg Foundation, the Swedish Research Council and the National Space Board (Sweden). Science analysis support in the operations phase from INAF (Italy) and CNES (France) is also gratefully acknowledged. This work performed in part under DOE Contract DE-AC02-76SF00515.

References

1. Aartsen, M.G. *et al*, Science, **342**, 1242856 (2013).
2. Aartsen M. G.*et al*, PhRvL, **113**, 101101 (2014).
3. Murase K., Waxman E., PhRvD, **94**, 103006 (2016).
4. Mannheim K., Stanev T., Biermann P. L., A&A, **260**, L1, (1992).
5. Ackermann M. *et al*, ApJS, **222**, 5 (2016).
6. Dermer C. D., Murase K., Takami H., ApJ, **755**, 147. (2012).
7. Kadler M. *et al*, NatPh, **12**, 807 (2016).
8. IceCube Collaboration *et al*, Sci, **361**, eaat1378 (2018).
9. Tanaka Y. T., Buson S., Kocevski D., ATel, **10791**, 1 (2017).
10. Ansoldi S. *et al*, ApJL, **863**, L10 (2018).
11. Abeysekara A. U. *et al*, ApJL, **861**, L20 (2018).
12. Reimer A., Böttcher M., Buson S., 2019, ApJ, **881**, 46 (2019).
13. Ubertini P., Bazzano A.,NIMPA, **742**, 47 (2014).
14. Kawamuro T. *et al*, ApJS, **238**, 32 (2018).
15. Weisskopf M. C., *et al*, ResPh, **6**, 1179 (2016).
16. Moiseev A., Amego Team, ICRC, **798**, ICRC...35 (2018).

17. Adrián-Martínez S., *et al*, JPhG, **43**, 084001 (2016).

18. Avrorin A. D., *et al*, EPJWC, **01006**, EPJWC.191 (2018).

Frascati Physics Series Vol. 69 (2019)
PHOTON 2019 - International Conference on the Structure and the Interactions of the Photon
Jun 3-7, 2019

OBSERVATION OF HIGH-ENERGY COSMIC PHOTONS WITH NEW-GENERATION SPACE TELESCOPES

Piergiorgio Fusco
Dipartimento di Fisica "M. Merlin" dell'Università e del Politecnico di Bari, I-70126 Bari, Italy
Istituto Nazionale di Fisica Nucleare (INFN) Sezione di Bari, I-70125 Bari, Italy

Abstract

While the Fermi gamma-ray telescope lives its 11^{th} year in orbit, new particle and gamma-ray space detectors are in operation as DAMPE (DArk Matter Particle Explorer), or are in the development stage as HERD (High Energy cosmic Radiation Detector). DAMPE was launched in 2015 by a collaboration of Chinese, Italian and Swiss scientific institutions and performs high-quality observations of cosmic electrons, protons, nuclei and gamma rays up to 10 TeV with good angular and energy resolution. HERD will be installed on board the Chinese Space Station to be launched in 2022 and will perform accurate measurements of energy and direction of cosmic rays and photons. An overview on these experiments and a summary of the main gamma-ray results and expectations will be presented.

1 Introduction

Cosmic photons of energy from a few 100 keV to about 1 PeV are produced in non-thermal processes involving the decay, the annihilation and the interaction of high-energy particles and nuclei. In particular, gamma rays are unique since they are free from thermal radiation and can propagate with negligible attenuation and deflection through the galaxy; however, they can not pass the atmosphere. Thus, the observation of gamma rays from space is of fundamental importance to achieve the clearest view onto non-thermal physics in local sources, as the Earth's limb, the Moon and the Sun; in galactic ones, like pulsars and supernova remnants; and in extragalactic ones, like blazars, gamma-ray bursts and gravitational waves production events. It can also shed light on exotic or unknown sources, like dark matter.

2 The DAMPE experiment

The DArk Matter Particle Explorer (DAMPE) [1] is a particle detector launched on 17 December 2015 in a Sun-synchronous orbit at a 500 km altitude. Its main scientific goals are the study of high energy cosmic electrons, positrons, photons, protons and nuclei; the observation of gamma rays from astrophysical sources; the search for dark matter signatures, for electromagnetic counterparts of gravitational waves and for exotic particles. DAMPE has been designed to have an excellent performance: it can detect particles with energy from some GeV up to tens of TeV with a good energy resolution, an accurate angular resolution and a large field of view.

2.1 The DAMPE instrument

DAMPE is composed by four sub-detectors (Figure 1): a Plastic Scintillator Detector (PSD), a Silicon-Tungsten Tracker (STK), a BGO Calorimeter (CALO) and a Neutron Detector (NUD).

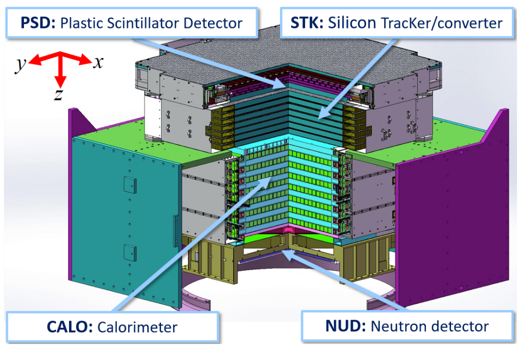

Figure 1: *The DAMPE instrument with its sub-detectors.*

The PSD detects charged particles and measures they charge number Z. It is made by two layers of orthogonal scintillator bars, providing information on the x and y coordinates. The STK is devoted to reconstruct the particle tracks and to convert photons into electron-positron pairs. It consists of 12 position-sensitive silicon detector planes (6 for the x-, 6 for the y-coordinate); 3 planes are equipped with 1 mm thick layers of tungsten to enhance the conversion of gamma rays. The BGO calorimeter measures the energy deposition of incident particles and analyzes the electromagnetic shower profile. It is composed of 308 BGO crystal bars arranged in 14 layers of 22 bars each; the bars of a layer are orthogonal to those of the adjacent one, to observe the shower in the xz and yz views. The total depth of the calorimeter is 32 radiation lengths and 1.6 nuclear interaction lengths. The last sub-detector is the NUD, made of four boron-loaded plastic scintillators, that improves the overall hadron identification efficiency.

We developed [2] a method to determine the absolute energy scale of DAMPE using the energy cutoff in the spectrum of cosmic-ray electrons and positrons that, below a certain rigidity, are bent back to space by the Earth's magnetic field. The expected cutoff was computed with a Monte Carlo simulation and compared with the measured one, yielding a correction factor of 1.2% to be applied to DAMPE data.

2.2 Observation of high-energy photons

DAMPE is a multi-purpose space detector and it has already produced relevant results in the study of cosmic electrons and positron, discovering a break in their spectrum [3], of cosmic protons, extending the study of their flux up to 100 Tev [4] and on the distribution of elements in cosmic rays [5]; other searches are ongoing on cosmic helium nuclei, on dark matter signatures, and many other subjects. However, DAMPE is also an excellent gamma-ray space telescope and many searches are done on cosmic photons.

The photon selection is a challenging tasks, since the background of charged particles (electrons, protons and nuclei) has fluxes much higher than the galactic gamma-ray emission; the minimum rejection power required at 100 GeV is 10^5 for protons and 10^3 for electrons.

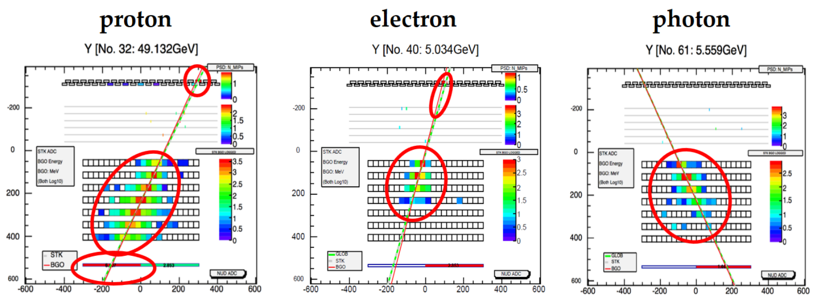

Figure 2: *Typical responses of DAMPE sub-detectors to various particles.*

The rejection techniques are based on the event topology (Figure 2). Protons are mainly suppressed using the PSD response and the shower profile in the BGO calorimeter with a contribution from the NUD, while electrons are mainly rejected using the PSD response and the first plane of the STK. Charged particles are detected by all planes of STK, while photons convert in e^+e^- couples mainly in tungsten layers and are detected only in the following planes. We are also testing the particle identification with Convolutional Neural Networks and Random Forest Classifiers [6]. Figure 3 shows the performance in photon detection, after the application of the selection criteria: the acceptance is over 0.1 m^2sr from 10 GeV to 1000 GeV and the angular resolution is 1° at 1 GeV, 0.1° at 100 GeV and 0.05° at 1 GeV.

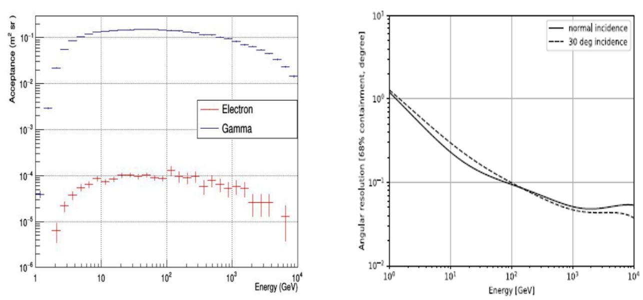

Figure 3: *DAMPE performance in photon detection: acceptance (left) and angular resolution(right).*

Figure 4 shows the gamma-ray sky as observed by DAMPE after 3 years: the main sources are well resolved and their positions agree with those measured by the Fermi/LAT.

DAMPE is also studying the gamma-ray emission of pulsars: counts maps, spectral energy distributions and pulse time profile are analyzed. For example, Figure 5 shows the results for Geminga.

DAMPE can detect the variability of some extragalactic sources, contributing to the study of transients. In some cases, for example with CTA 102, the detection was announced with an "Astronomer's Telegram" [7]. DAMPE also participates to the multi-messenger observation of high-energy cosmic phenomena: for example it has observed the extragalactic source TXS 0506+056 at 5.7 billion light-years that is the possible origin of the 290 TeV muon neutrino observed by IceCube in September 2017 [8], though no variability was detected due to the limited statistics.

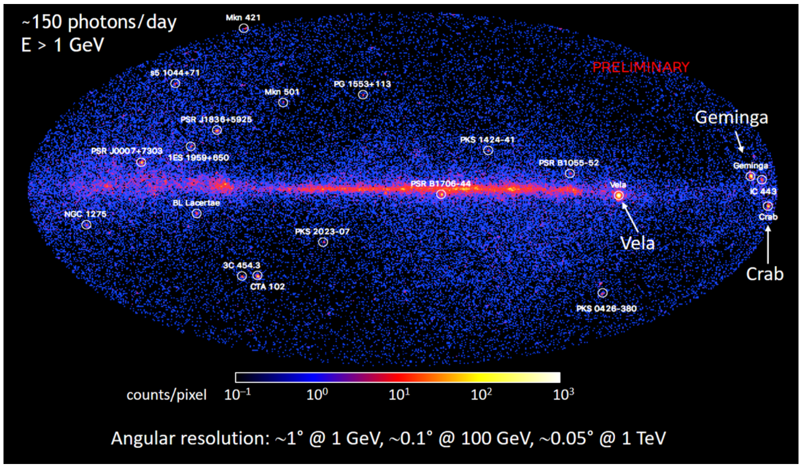

Figure 4: *The gamma-ray sky as observed by DAMPE. The major sources are well detected.*

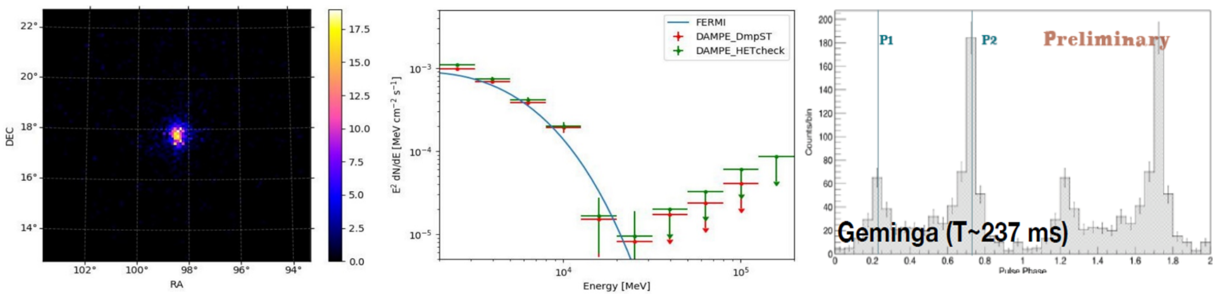

Figure 5: *The Geminga pulsar as observed by DAMPE: counts map (left), spectral energy distribution (center), phase profile (right).*

3 The HERD experiment

The High Energy cosmic Radiation Detector (HERD) [9] is a new-generation particle detector to be installed on the future Chinese Space Station in 2025. It will search for dark matter signatures and study cosmic rays, electrons, and gamma-rays. Its key features will be the large exposure (about 15 m^2sr yr, 10 times larger than previous space experiments) and an unprecedented gamma-ray sensitivity. It will perform high-statistics observations of electrons and photons from 100 GeV to 10 TeV and better spectral and composition measurements of cosmic rays from 300 GeV to 1 PeV.

3.1 The HERD instrument

HERD (Figure 6) will consist of a LYSO calorimeter (CALO) inside 5 sides of Silicon-Tungsten Trackers (STK) and 6 sides of Plastic Scintillator Detectors (PSD), plus a Transition Radiation Detector (TRD).

The trackers will be made of 7 layers (top) or 3 layers (sides) of SSDs with xy coordinates readout, interleaved with tungsten foils. They will be devoted to gamma-ray conversion and tracking, charge measurement, shower analysis and backsplash rejection. Optimization is ongoing, taking into account

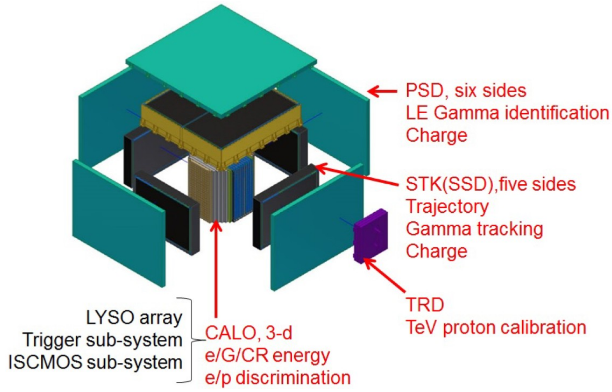

Figure 6: *An exploded view of the HERD instrument with its sub-detectors.*

that cosmic-ray calorimetry requires a shallow tracker, multiple energy measurements require many planes and gamma-ray acceptance requires a thick tracker. A depth of ~ 2 radiation lengths is expected.

The calorimeter will consist of more than 7500 LYSO crystals $3 \times 3 \times 3$ cm^3 each, with high light output and quick decay time, read by WLS fibers to be connected to image intensifiers and high resolution IsCMOS cameras. Its depth will be 55 radiation lengths and 3 nuclear interaction lengths. These features will allow an excellent energy resolution and a high-definition 3D imaging of the showers. A prototype has already been implemented and tested on particle beams at CERN in December 2018 [10]: Figure 7 shows the calorimeter energy resolution obtained for electrons, protons and photons.

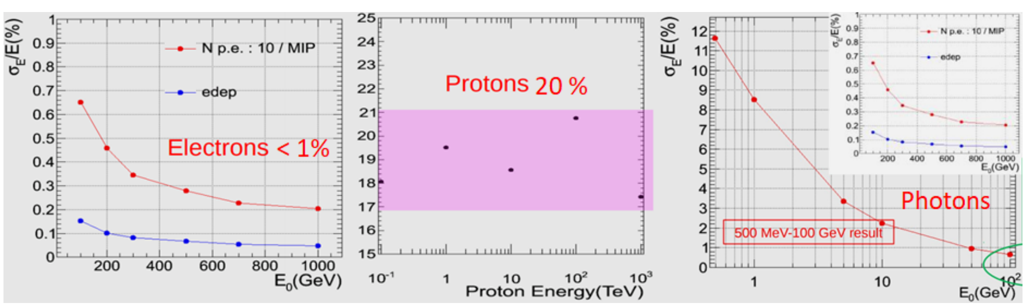

Figure 7: *HERD calorimeter beam tests results: electrons (left), protons (middle) and photons (right).*

The PSD will contribute in detecting charged particles, selecting gamma rays, building the trigger, and measuring the cosmic nuclei charges. It is being tested on particle and ion beams: several configurations and segmentations are under study to optimize performance and reduce background and backsplash. Finally, the TRD will be made of PP foils and will be devoted to the calibration at high energies.

3.2 HERD perspectives

The baseline HERD detector is defined and fulfills the requirements; further improvements and optimization are ongoing. The calorimetric detector with unprecedented depth and geometrical factor and the other high-performance sub-detectors will allow a significant improvement in cosmic-ray physics above the PeV, high-energy (and maybe also sub-GeV) cosmic photons observations and dark matter searches.

As an example, here we present our analysis of the expected sensitivity to a gamma-ray line signal: for monochromatic photons from a ~ 400 GeV dark matter particle, a sensitivity much greater than other experiments would allow to discriminate the signal over the other particles' background.

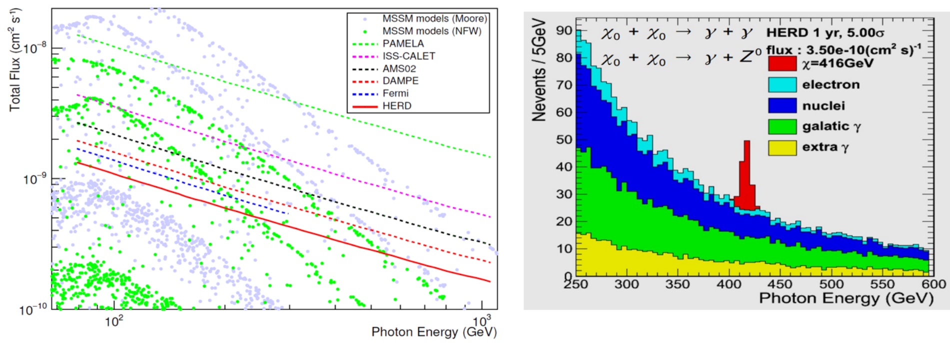

Figure 8: *The sensitivity of HERD to a gamma-ray line, compared to other instruments (left); a simulation of a ~ 400 GeV line over the background after 1 year of observations (right).*

4 Conclusions

DAMPE is operating stably since more than three years; 6 billion charged cosmic rays and 0.2 million gamma-rays have been collected over a wide energy range. Important results on charged particles have been obtained and others are expected. A significant contribution is given to photon studies: many sources and items are studied, more statistics is being accumulated and several publications are in preparation.

HERD will be taking data on board the CSS from 2025 for more than 10 years. It will be a calorimetric and tracking detector with unprecedented acceptance and will play a fundamental role in cosmic ray physics, dark matter search and gamma-ray astronomy. It will be the only high-energy gamma-ray detector operating in space in the next future, and with excellent performance.

References

1. J. Chang *et al*, Astropart. Phys. **95**, 6 (2017).
2. J. Zang *et al*, Proc. of Sci., PoS(ICRC2017), 197 (2017).
3. G. Ambrosi *et al*, Nature **552**, 63 (2017).
4. C. Yue *et al.*, Proc. of Sci., PoS(ICRC2019), 163 (2019).
5. T. Dong *et al*, Astropart. Phys. **105**, 31 (2019).
6. S. Garrappa *et al*, Proc. of Sci., PoS(ICRC2017), 603 (2017).
7. Z.L. Xu *et al*, Astronomer's Telegram No. 9901 (2016).
8. M.G. Aartsen *et al*, Science **361**, 6398 (2018).
9. S.N. Zhang *et al*, Proc. of SPIE **9144**, 91440X (2014).
10. Y. Dong *et al*, Proc. of SPIE **9905**, 99056D-1 (2016).

Frascati Physics Series Vol. 69 (2019)
PHOTON 2019 - International Conference on the Structure and the Interactions of the Photon
Jun 3-7, 2019

PROSPECTS FOR PHOTON-PHOTON MEASUREMENTS WITH TAGGED PROTONS IN ATLAS

Maciej Trzebiński
The Henryk Niewodniczański Institute of Nuclear Physics Polish Academy of Sciences
Radzikowskiego 152, 31-342 Cracow, Poland
on behalf of the ATLAS Collaboration*

Abstract

In 2017, ATLAS has been equipped with a new, dedicated detector system allowing measurements of forward protons scattered at small angles in diffractive and electromagnetic processes. These ATLAS Forward Proton detectors (AFP) can operate during the standard high-luminosity LHC runs and collect large amounts of integrated luminosity. This gives a possibility to study rare interactions, in particular, the two-photon processes. The physics programme includes measurements of photon-photon interactions present in the Standard Model, as well as using searches for new physics. In this paper, the AFP detectors and physics goals are briefly presented.

1 Introduction

In the majority of events of photon-photon and photon-proton scatterings at the LHC one or both outgoing protons stay intact. Since photon is a colourless object, such an exchange results in a presence of the rapidity gap between the centrally produced system and scattered protons. Thus, such events are of diffractive nature.

Diffractive processes are an important part of the physics programme at hadron colliders. This is also true for ATLAS [1)], where a large community works on both phenomenological and experimental aspects of diffraction. In such events, a rapidity gap[1] between the centrally produced system and scattered protons is present. Due to the exchange of a colourless object, a photon (in case of electromagnetic interaction) or Pomeron (strong force), one or both outgoing protons may stay intact.

[1] Rapidity gap is a space in rapidity devoid of particles.

2 Detection Techniques

The diffractive production may be recognized by the search for a rapidity gap in the forward direction or by the measurement of scattered protons. The first method is historically a standard one for the diffractive pattern recognition. It uses the usual detector infrastructure as trackers and forward calorimeters. Unfortunately, the rapidity gap may be destroyed by *e.g.* particles coming from the pile-up – parallel, independent collisions happening in the same bunch crossing. In addition, the gap may be outside the acceptance of a detector. In the second method, protons are directly measured. This solves the problems of gap recognition in the very forward region and a presence of pile-up. However, since protons are scattered at small angles (few hundreds microradians), additional devices called forward detectors are needed to be installed.

2.1 ATLAS Forward Proton Detectors

ATLAS is equipped with two sets of forward proton detectors: ALFA [2, 3] and AFP [4]. ALFA (Absolute Luminosity For ATLAS) detectors are designed to measure the properties of the elastic cross-section, soft diffraction and low-mass exclusive production. These topics are not in the scope of this report – readers interested in details should see *e.g.* Ref. [5, 6] (properties of the elastic scattering measured by ATLAS at $\sqrt{s} = 7$ and 8 TeV), Ref. [7] (general overview; soft diffraction), Ref. [8] (exclusive pion production) or Ref. [9] (diffractive bremsstrahlung).

AFP (ATLAS Forward Proton) consists of four detector stations placed symmetrically with respect to the ATLAS Interaction Point at 205 m and 217 m. In each AFP station there is a Roman Pot device allowing the units to move horizontally. Detectors located on the ATLAS C side are inserted into the beam 1 whereas the ones on the A side into the beam 2. The scheme of AFP detectors is shown in Figure 1.

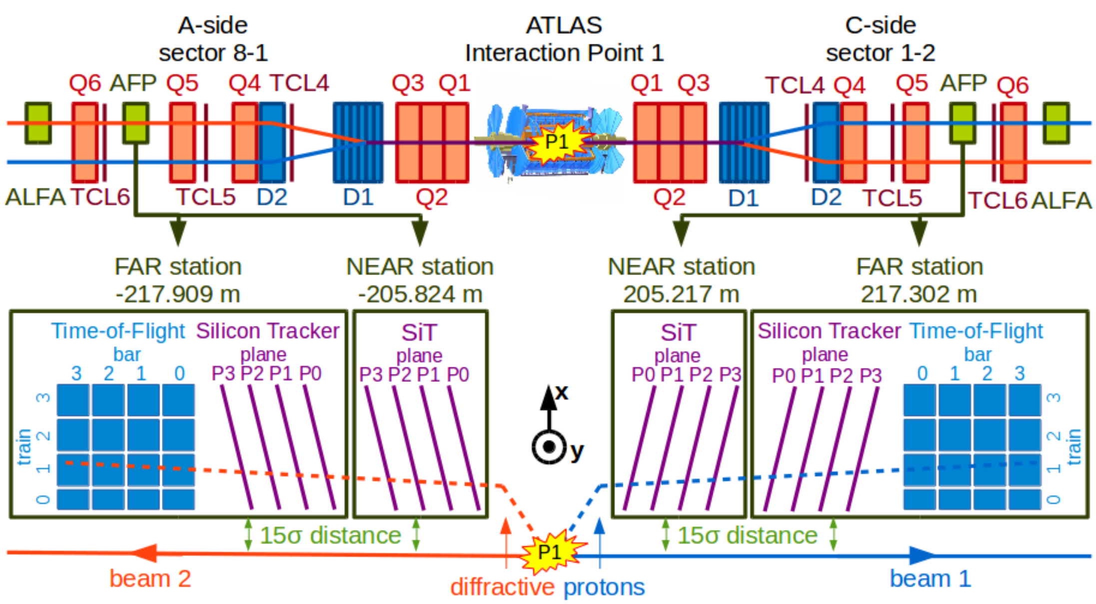

Figure 1: *Scheme of the ATLAS Forward Proton detectors.*

Each AFP station consists of four Silicon Trackers (SiT), which provide precise position measurements. The purpose of the AFP tracking system is to measure points along the trajectory of protons that were deflected during a proton-proton interaction. The readout chip was chosen to be FE-I4, which was originally designed for the IBL project [10]. There are four such chips installed in each station. The active area covered by the tracking detector is approximately 16×20 mm^2 with a pixel size of 50×250 μm^2. Detectors are tilted by 14 degrees. The resolution of a single plane was measured to be about 6 μm in x and about 30 μm in y [11]. By having two detectors on each side of the Interaction Point (IP) one can measure not only the position of the proton with respect to the beam, but also its elevation angle. These are connected to the proton kinematics at the interaction point – *i.e.* by measuring the proton properties in the AFP one can unfold its initial four-momentum [12].

Far stations host also the Time of Flight (ToF) detectors. The timing detectors measure the time of arrival of each proton, providing a trigger signal and allowing background reduction through the difference in proton time-of-flight measured on each side of the interaction point. The vertex calculated from ToF difference on both AFP sides can be compared to the primary interaction vertex. The resolution is expected to be between 20 and 30 ps [11].

2.2 LHC Optics

Between the AFP stations and ATLAS interaction point several LHC elements are placed. They have a significant impact on the proton trajectory and will influence its position in the AFP stations. These elements are:

- two dipole magnets (D1-D2) used for beam separation (bending),
- five quadrupole magnets (Q1-Q5) used for beam focusing,
- two collimators (TCL4, TCL5) used for magnet protection.

Settings of the LHC magnets are called optics and come from the requirements of the experiments in terms of luminosity and of the LHC machine protection. These settings may differ between the LHC fills. Due to the optics settings, the forward proton trajectories between the IP and AFP detectors are not straight lines. A typical situation ($\beta^* = 0.4$ m optics) for the high-luminosity ATLAS data taking is shown in Figure 2. Black rectangles represent dipole and quadrupole magnets, blue lines – collimators and red lines – AFP and ALFA stations. Assuming the proton transverse momentum equals zero, protons are bent accordingly to the energy lost during the collision: $\xi = \frac{E_{beam} - E_{proton}}{E_{beam}}$. As one can see, protons with very small energy loss are too close to the beam to be detected. With increasing energy loss, trajectories are further away from the beam and can be detected by AFP. However, if the energy loss is too big, forward protons will be filtered by collimators and will not reach the AFP station. The acceptance for a typical low-β^* optics covers $0.025 < \xi < 0.1$ [13], which corresponds to the proton energy loss of $160 < E_{proton} < 650$ GeV for $\sqrt{s} = 13$ TeV.

3 Photon Physics with Forward Proton Measurement

Photoproduction physics has so far been studied mainly in the electron accelerators. However, a high-energy bremsstrahlung from the proton at the LHC is a plentiful source of photons. Photoproduction processes can be studied using proton tagging.

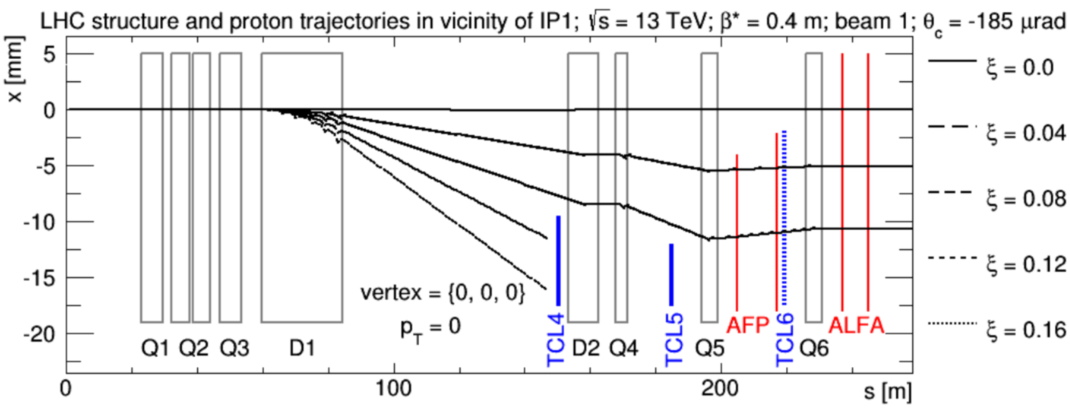

Figure 2: *Energy dependence of the proton trajectory in* (x, s) *plane for* $\sqrt{s} = 13$ *TeV,* $\beta^* = 0.4$ *m LHC optics in vicinity of ATLAS Interaction Point (IP1). Protons were generated at* $(0, 0, 0)$ *with transverse momentum* $p_{\mathrm{T}} = 0$*. The crossing angle in horizontal plane was set to 185* μ*rad. For details see Ref.* [13]*.*

3.1 Two Photon Processes: $\gamma\gamma \to \mu\mu$

A di-muon system can be produced in the exclusive mode: $p + p \to p\gamma^*\gamma^*p \to p\mu^+\mu^-p$, see Fig. 3. Such measurement was done by ATLAS without AFP [14]. The used data sample consisted of exclusive events and large irreducible background which was mainly coming from dissociated[2] events. Information about the presence of scattered protons should allow a significant reduction of this background.

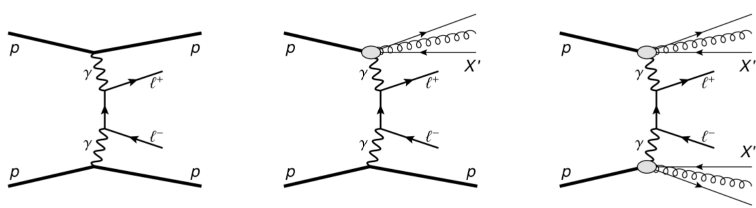

Figure 3: *Feynman diagrams for the exclusive di-muon photo-production.*

Due to the acceptance of AFP, double-tagged events have too small cross-section to be observed. However, a semi-exclusive (single tag) measurement should be possible assuming 40 fb^{-1} of collected data, minimal muon transverse momentum of 10 GeV and AFP positioned at about 2 mm from the beam. As was discussed in Ref. [4], such measurement can be used for the AFP detector alignment and optics calibration.

3.2 Anomalous Gauge Couplings

Measurement of W and Z boson pair production via the exchange of two photons (see left panel of Fig. 4) allows to perform a stringent test of the electroweak symmetry breaking [15]. Standard Model predicts

[2]Events in which one or both protons was destroyed due to interactions with other particles from the system. Such phenomena are described by a gap survival probability.

the existence of $\gamma\gamma WW$ quartic couplings while there is no $\gamma\gamma ZZ$ coupling. As was shown in Refs [16] and [17], collecting 30 – 300 fb^{-1} of data with the ATLAS detector and using protons measured in AFP should result in a gain in the sensitivity of about two orders of magnitude over a standard ATLAS analysis.

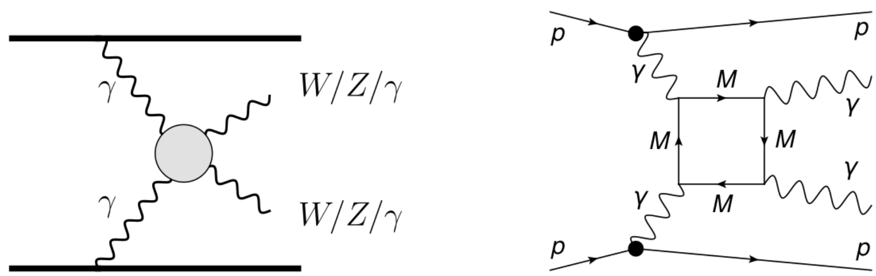

Figure 4: *Diagrams of anomalous gauge coupling (left) and magnetic monopole (right) production.*

3.3 New Physics Searches

Proton tagging may also serve as a powerful technique for the new physics searches as the backgrounds can be significantly reduced by the kinematic constraints coming from the AFP proton measurements. The general idea of background reduction was presented in Ref. [18, 19, 20] on a basis of the exclusive jet measurement.

Proton tagging technique might be also used for the invisible object searches. As an example, the case of magnetic monopoles produced by the photon exchange can be considered. From a diagram (see right panel of Fig. 4) one can conclude that, even if the centrally produced system escapes detection (or is not measurable) in ATLAS, one can measure scattered protons in AFP. In general, any production of new objects (with mass up to 2 TeV) via photon or gluon exchanges should be possible to be observed.

4 Summary

Since 2017 ATLAS is equipped with a full set of the AFP detectors, which collected data with a proton tag on both sides during the special and standard LHC runs. Even more data is planned to be collected during the LHC Run 3. Besides QCD measurements (rapidity gap survival, Pomeron structure, *etc.*), photon-induced processes can be measured. These include single-tagged exclusive muons ($pp \to p\mu^+\mu^- p$) and anomalous gauge couplings (W, Z and photon pairs). For the latter processes the use of the AFP detectors provides a significant gain in sensitivity as compared to the measurement based on the data from the central ATLAS detector. On top of that one can try to search for any production of new objects produced via photon or gluon exchanges (magnetic monopoles, invisible particles, ...). In such searches, forward proton measurements can be used for a background reduction.

References

1. ATLAS Collaboration, *The ATLAS Experiment at the CERN Large Hadron Collider*, JINST **3** (2008) S08003.

2. ATLAS Collaboration, *ATLAS Forward Detectors for Measurement of Elastic Scattering and Luminosity*, CERN-LHCC-2008-004, ATLAS-TDR-18, https://cds.cern.ch/record/1095847.

3. S. Abdel Khalek et al., *The ALFA Roman Pot Detectors of ATLAS*, JINST **11** (2016) P11013.

4. ATLAS Collaboration, *Technical Design Report for the ATLAS Forward Proton Detector*, CERN-LHCC-2015-009, ATLAS-TDR-024, https://cds.cern.ch/record/2017378.

5. ATLAS Collaboration, *Measurement of the total cross section from elastic scattering in pp collisions at $\sqrt{s} = 7$ TeV with the ATLAS detector*, Nuclear Physics B **889** (2014) 486.

6. ATLAS Collaboration, *Measurement of the total cross section from elastic scattering in pp collisions at $\sqrt{s} = 8$ TeV with the ATLAS detector*, Phys. Lett. B **761** (2016) 158.

7. K. Akiba et al., *LHC Forward Physics*, SLAC-PUB-16364, DESY 15-167.

8. R. Staszewski, P. Lebiedowicz, M. Trzebinski, J. Chwastowski, A. Szczurek, *Exclusive $\pi^+\pi^-$ Production at the LHC with Forward Proton Tagging*, Acta Physica Polonica B **42** (2011) 1861.

9. J. J. Chwastowski, S. Czekierda, R. Staszewski, M. Trzebinski, *Diffractive Bremsstrahlung at High-β^* LHC Case Study*, Eur. Phys. J. C **77** (2017) 216.

10. ATLAS Collaboration, *ATLAS Insertable B-Layer Technical Design Report*, CERN-LHCC-2010-013, ATLAS-TDR-19.

11. J. Lange et al., *Beam tests of an integrated prototype of the ATLAS Forward Proton detector*, JINST **11** (2016) P09005.

12. M. Trzebinski, R. Staszewski, J. Chwastowski, *LHC High Beta* Runs: Transport and Unfolding Methods*, ISRN High Energy Physics **2012** (2012) 491460.

13. M. Trzebinski, *Machine Optics Studies for the LHC Measurements*, Proc. SPIE 9290, Photonics Applications in Astronomy, Communications, Industry, and High-Energy Physics Experiments 2014, 929026.

14. ATLAS Collaboration, *Exclusive dilepton production at 7 TeV*, Physics Letters B **749** (2015) 242-261.

15. P. J. Dervan, A. Signer, W. J. Stirling, A. Werthenbach, *Anomalous triple and quartic gauge boson couplings*, J. Phys. G **26** (2000) 607.

16. E. Chapon, O. Kepka, C. Royon, *Anomalous quartic $WW\gamma\gamma$, $ZZ\gamma\gamma$, and trilinear $WW\gamma$ couplings in two-photon processes at high luminosity at the LHC*, Phys. Rev. D **81** (2010) 074003.

17. O. Kepka, C. Royon, *Anomalous $WW\gamma$ coupling in photon-induced processes using forward detectors at the LHC*, Phys. Rev. D **78** (2008) 073005.

18. ATLAS Collaboration, *Exclusive Jet Production with Forward Proton Tagging Feasibility Studies for the AFP Project*, ATL-PHYS-PUB-2015-003, https://cds.cern.ch/record/1993686.

19. M. Trzebinski, R. Staszewski, J. Chwastowski, *On the Possibility of Measuring the Single-tagged Exclusive Jets at the LHC*, Eur. Phys. J. C 75 (2015) 320.

20. M. Trzebinski, *Exclusive Jet Measurement in Special LHC Runs – Feasibility Studies*, Acta Phys. Pol. B **47** (2016) 1745.

Frascati Physics Series Vol. 69 (2019)
PHOTON 2019 - INTERNATIONAL CONFERENCE ON THE STRUCTURE AND THE INTERACTIONS OF THE PHOTON
Jun 3-7, 2019

PHOTON DETECTION WITH THE CMS ECAL IN THE PRESENT AND AT THE HL-LHC AND ITS IMPACT ON HIGGS-BOSON MEASUREMENTS

Marco Cipriani, on behalf of the CMS Collaboration
Sapienza Università di Roma & INFN, Roma

Abstract

The CMS experiment at the LHC features a high-resolution and homogeneous electromagnetic calorimeter (ECAL). The excellent performance of ECAL in the reconstruction of high-energy photons played a key role in the discovery of the Higgs boson and the measurement of its properties. The High-Luminosity LHC (HL-LHC) is expected to deliver an integrated luminosity 20 times larger than the LHC, allowing for the study of rare processes such as Higgs-boson pair production and self-coupling. During HL-LHC operations, up to 200 concurrent interactions per bunch collision are expected. In order to maintain its current performance in the harsher environment of the HL-LHC, an upgrade of the ECAL is planned. This contribution describes the ECAL performance in photon reconstruction and its impact on the measurement of the Higgs boson properties during the LHC Run II. Prospects for Higgs-boson measurements at the HL-LHC are presented as well.

1 Introduction

The Compact Muon Solenoid (CMS) [1] at the CERN Large Hadron Collider (LHC) is a general-purpose detector designed to discover the Higgs boson predicted by the Standard Model (SM) and search for new physics beyond the SM. The excellent performance of the CMS electromagnetic calorimeter (ECAL) [2] led to the observation of the Higgs boson through its decay into two photons [3], using data in proton-proton (pp) collisions collected at a center-of-mass energy of 8 TeV (Run I). After the discovery of this new particle, a rich physics program was established to characterize its production and decay cross section. In particular, the large amount of data collected at a center-of-mass energy of 13 TeV (Run II) allowed for the observation of the rare $t\bar{t}H$ production mode [4], where the Higgs boson is produced in association with a pair of top quarks.

At the LHC, the inclusive Higgs-boson production cross section is few tens of pb, nine orders of magnitude lower than the total pp inelastic cross section. Consequently, Higgs-boson analyses need to exploit decay channels that provide a distinctive experimental signature to achieve high background rejection. The diphoton decay channel has a very low branching ratio, about 0.2%, but it provides a clean signature with a pair of high-energy photons in the final state. The energy of the final-state photons can be measured with high precision thanks to the very good ECAL resolution, allowing the mass of Higgs boson candidates (m_H) to be measured with high resolution. This feature makes this channel particularly suitable to perform precision measurements of the Higgs boson properties.

The resolution of m_H is determined by the resolution of the energy of each photon and the resolution of the opening angle between them. The latter depends on the measured position of the interaction vertex along the beam line. As photons have no electric charge, they leave no signal in the tracker detector installed inside the ECAL. Therefore, the assignment of the two photons to the interaction point relies on other charged particles produced in association with the Higgs boson. However, the presence of several concurrent pp interactions (in-time pileup, PU) occurring in each beam crossing reduces the probability of identifying the correct diphoton vertex. The average number of PU interactions during Run II was about 40, with only one containing the interesting signature. Nevertheless, as long as the vertex is identified within 1 cm of the true one, the corresponding variation of m_H is negligible with respect to the one induced by the resolution of the photon energy. The diphoton vertex is selected as the one with the highest scalar sum of the transverse momenta (i.e. the projection of the momentum on the plane orthogonal to the beam axis) of all tracks originating from it. The efficiency of this algorithm to tag the correct vertex within 1 cm of the true one is about 80% for PU $\approx$ 25, and decreases linearly to about 70% at PU = 40.

During the High-Luminosity operation of the LHC (HL-LHC), foreseen to start in 2026, the luminosity of the machine will be increased by a factor 20 with respect to the current LHC conditions. The large data sample available for physics analyses will make it possible to carry out differential cross section measurements for the Higgs boson and enhance the experimental sensitivity to rare processes, such as Higgs-boson pair production and self-coupling. However, up to 200 concurrent interactions per bunch crossing are expected at the HL-LHC. At such PU levels, particle reconstruction and correct assignment to the primary interaction vertex will present a formidable challenge to the detectors, requiring an upgrade of the readout electronics or the replacement of some detector components.

The aim of this contribution is to describe the performance of the ECAL in photon reconstruction and identification during Run II, and its role in the context of Higgs-boson measurements. In addition, this paper provides an overview of the ECAL upgrade that is envisaged for the HL-LHC phase to maintain and possibly improve the physics performance achieved in Run II.

2 ECAL detector in Run II

CMS features a high-resolution, homogeneous electromagnetic calorimeter comprising 61200 crystals of lead tungstate ($PbWO_4$) arranged in a central barrel detector (EB) and complemented by 7324 crystals in each of the two endcaps (EE). The properties of $PbWO_4$ (Molière radius of 2.19 cm and radiation length X_0 = 0.85 cm) provide high granularity and excellent longitudinal containment of the electromagnetic shower of electrons and photons with energies up to the TeV scale. In addition, the decay time of scintillation light of about 25 ns guarantees a fast detector response.

The barrel covers the pseudorapidity (η) region within $|\eta|$ = 1.48, while the endcaps extend the coverage up to $|\eta|$ = 3.0. Avalanche photodiodes (APDs) and vacuum phototriodes (VPTs) are used as photodetectors in EB and EE, respectively. A preshower detector (ES), based on lead absorbers equipped with silicon strip sensors, is placed in front of EE. It covers the region $1.65 < |\eta| < 2.6$ and helps to resolve the signals of high-energy photons from the decays of neutral pions into two close photons, while also improving the measurement of the position of the electromagnetic shower in EE. ECAL is installed inside the CMS superconducting solenoid, which provides a magnetic field of 3.8 T. The CMS silicon tracker, located inside ECAL, detects charged particles up to $|\eta|$ = 2.5

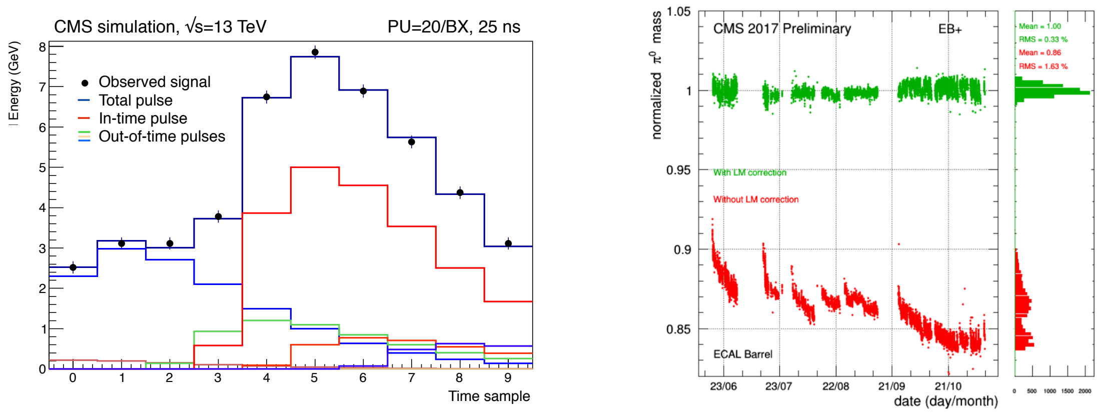

(a) pulse shapes in EE

(b) Energy scale stability

Figure 1: *a) Fitted pulse shapes in EE for simulated events. The total pulse (blue line), overlaid with the observed signal (black dots), is obtained as the sum of the fitted pulses (other colored lines). The in-time pulse (red line) peaks at the sixth time sample corresponding to the in-time bunch crossing. b) Stability of the energy scale in EB monitored using the diphoton mass in* $\pi^0 \to \gamma\gamma$ *decays before (red) and after (green) the laser corrections. Taken from* [5, 7].

and allows for the identification of electrons and photons.

2.1 Photon energy reconstruction

Electrons and photons deposit their energy in several ECAL crystals and are reconstructed through a clustering algorithm. The magnetic field bends the trajectory of electrons along the ϕ angle direction. Therefore, basic clusters extend along ϕ to form superclusters (SC) and recover additional energy deposits produced by electron bremsstrahlung or photon conversions in the tracker. The SC energy is measured as $E_{e,\gamma} = F_{e,\gamma}\, G\, \sum_i [S_i(t)\, C_i\, A_i]$, where $F_{e,\gamma}$ includes corrections to the clustered energy and G is an ADC-to-GeV conversion factor. The sum runs over the channels in the cluster: A_i is the amplitude measured in the i-th channel; $S_i(t)$ is a time-dependent correction for variations of channel response due to changes in crystal transparency; C_i is a relative calibration constant accounting for differences in the light yield and photodetector response of each channel.

The electrical signal from the photodetectors is amplified and shaped by a multi-gain preamplifier, and digitized by analog-to-digital converters (ADC) running at the LHC bunch crossing frequency of 40 MHz. The signal amplitude is then reconstructed from a series of 10 consecutive samples recorded by the ADC, one every 25 ns. The observed pulse shape is distorted by the energy deposited by particles originating from PU, but also from earlier or later bunch crossings (out-of-time pileup, OOT). In order to mitigate the bias on the measured amplitude due to OOT, an improved algorithm, named multifit, was deployed during Run II [5]. The multifit models the observed pulse shape as the sum of one in-time and up to nine out-of-time pulse amplitudes. The in-time signal amplitude is then extracted through the minimization of a χ^2 variable, which is fast enough to allow for the usage of the multifit also in the trigger software. All the pulse templates for each bunch crossing have the same shape and only differ by a 25 ns shift on the time axis. The total electronic noise and its covariance matrix enter the χ^2 definition and are measured from dedicated pedestal runs in the absence of signal pulses. An example of a fit in EE for simulated events is shown in Fig. 1a. The total pulse, overlaid with the observed signal, is obtained as the sum of the fitted pulses. The in-time pulse peaks at the sixth time sample corresponding to the in-time bunch crossing. The other out-of-time pulses peak at different time samples and represent the energy contribution from OOT.

The energy of an SC is further corrected using a multivariate analysis technique (MVA). The MVA is trained on simulations using as input, among other variables, the coordinates of the crystals and the shower shapes. The MVA addresses the non-perfect energy containment of the SC, and corrects for the energy loss due to interactions with material in front of ECAL and energy leakage in gaps between crystals. The output correction factor, $F_{e,\gamma}$, is tuned separately on electrons and photons to account for differences due to photon conversions in the material upstream of ECAL or electron bremsstrahlung. Finally, the absolute energy scale G is set to match the invariant mass from simulated $Z \to ee$ events.

2.2 ECAL response monitoring and calibration

The transparency of the ECAL crystals drifts continuously during periods of LHC operation because of radiation damage. This effect induces a change in the energy response of each channel, which is constantly monitored and corrected for by a dedicated laser system. The stability of the energy scale is monitored using the diphoton invariant mass distribution in events with $\pi^0 \to \gamma\gamma$ decays. Electrons from decays of Z and W bosons are used as well, exploiting either the $Z \to ee$ invariant mass or the ratio of the electron energy measured with ECAL and its momentum measured with the tracker. As shown in Fig. 1b, the time-dependent drift in the measured π^0 mass is removed after applying the laser monitoring correction. Each point in the π^0 monitoring history is obtained from a fit to about 5×10^5 π^0's collected every 5 minutes of data taking by a special trigger stream. W and Z bosons are selected with much lower rates, but the energy of the electrons from their decays is closer to the energy of photons in $H \to \gamma\gamma$ events. The energy scale during 2017 was stable within 0.1% (0.2%) in EB (EE) [7].

The energy resolution for photon showers from Higgs bosons is limited by the constant term, whose main contribution stems from the accuracy of the inter-calibration (IC) constants. The IC procedure has the purpose of equalizing the variations of the measured energy among different ECAL channels. This is accomplished by comparing a given observable, measured using only ECAL information, with a physics reference. Several methods based on physical processes are used to provide an IC constant for each channel [6]: $\pi^0 \to \gamma\gamma$, $Z \to ee$ and E/p methods. The calibration with π^0's exploits the position of the peak of the invariant-mass distribution of unconverted photon pairs. The E/p method uses prompt electrons from decays of W and Z bosons and is based on the comparison of the electron energy measured with ECAL (E) and its momentum measured with the tracker (p). The $Z \to ee$ method is similar to the π^0 one, but relies on the invariant mass of the Z resonance. Preliminary IC constants were derived using data collected in 2017. The IC precision obtained from the combination of all methods is better than 0.3% for $|\eta| <0.8$ and lower than 1% in the rest of EB.

2.3 Energy resolution and impact on $H \to \gamma\gamma$

The calibration based on 2017 data helped improve the energy resolution with respect to the calibration conditions available at the end of 2017. Figure 2a shows the energy resolution measured for low bremsstrahlung electrons, as a function of the electron pseudorapidity. The observed resolution gets worse at higher η in EB due to the larger amount of material upstream of ECAL, although a general improvement bigger than 10% is observed in the entire acceptance region. In 2017, a mass resolution of less than 1.5% was achieved in $H \to \gamma\gamma$ events. A better resolution will be achieved after a new calibration campaign of the full Run II dataset that is currently ongoing. It should be stressed that the energy resolution is assessed using electrons from W and Z bosons because of the lack of high-mass resonances decaying into photons other than the Higgs boson. The non-linearity of the energy scale from the Z peak to m_H, as well as the extrapolation from electrons to photons, affects the energy of photons in $H \to \gamma\gamma$ events by less than 0.5%, and is accounted for as a systematic uncertainty. Figure 2a shows the measured diphoton mass spectrum using data collected in 2016 and 2017. The lower panel shows the residuals after the subtraction of the non-resonant background component.

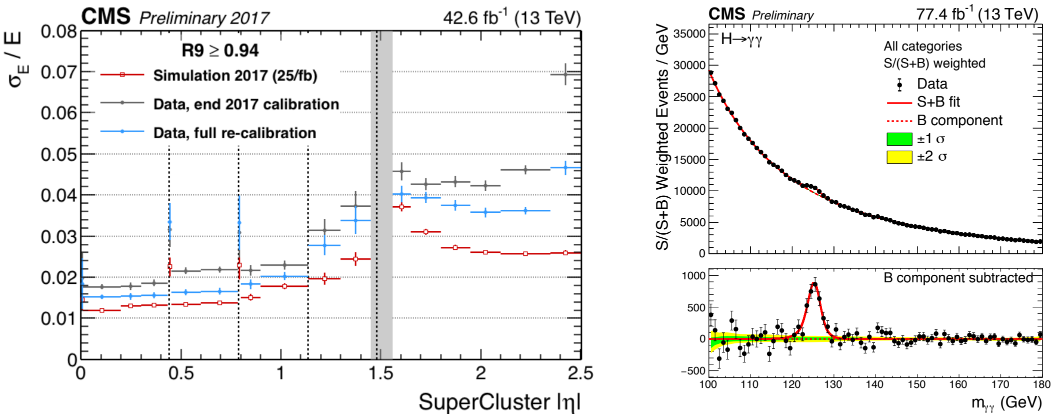

(a) Electron energy resolution (b) $H \to \gamma\gamma$ mass spectrum

Figure 2: *a) Energy resolution measured from the invariant mass of electron pairs in $Z \to ee$ events for low bremsstrahlung electrons ($R_9 > 0.94$), as a function of the leading electron $|\eta|$. The shower shape variable R_9 is defined as the ratio of the energy measured in a 3×3 matrix of crystals centered on the SC crystal with the highest energy and the total SC energy* [6]*. b) Observed diphoton mass spectrum using 2016 and 2017 data. The Higgs-boson peak is distinctly visible. Taken from* [7, 8].

3 ECAL upgrade for HL-LHC

HL-LHC will provide *pp* collisions with unprecedented intensity, resulting in harsher data-taking conditions, with average PU reaching a factor 5 higher than in Run II. This will pose serious challenges to the detectors due to heavier radiation damage. It will also imply a significant increase in the trigger rate and latency time, which could not be sustained by the current systems. This section will focus on the upgrade of the ECAL barrel [9]. The endcaps are going to be replaced by a new High-Granularity Calorimeter, described in [10].

In order to comply with the strict trigger requirements imposed by the HL-LHC conditions, the EB very-front-end electronics (VFE), which provides pulse amplification, shaping, and digitization functions, will be replaced by new faster electronics based on trans-impedance amplifiers (TIA). The main advantage of the upgraded VFE is in the reduction of the signal pulse length. The multifit algorithm will then be used to model the pulse shapes using more time samples, leading to a mitigation of OOT, while also improving the measurement of the signal arrival time. It will also provide better discrimination of anomalous signals (spikes) caused by particles showering directly in the photodetectors, thus generating earlier signals than the physics ones.

The data processed by the first stage of the CMS trigger (Level-1 Trigger, L1) will be read in streaming through new off-detector electronics based on FPGA processors. While the legacy on-detector architecture provides trigger information with 5×5 crystal granularity, with no tracking information and limited capability to identify spikes, the new one will provide single-crystal information, with significant benefits in terms of background rejection. The detector will operate at 9° instead of the present 18°, as the lower temperature will reduce the radiation-induced noise in the APD and enhance the light yield by 20%.

An important issue for Higgs physics at the HL-LHC stems from the degradation of the performance to locate the diphoton vertex in a 200 PU environment. To cope with the worsening of the m_H resolution, an upgrade of the EB timing capability is foreseen. Achieving a time resolution of 30 ps can help to identify the correct vertex with a space uncertainty lower than about 1 cm through triangulation, restoring the effective PU conditions of Run II for which standard vertex-tagging algorithm are optimized. If the photons are well separated in η, the estimated improvement on the $m_{\gamma\gamma}$ resolution is 10% compared to no timing. More robust algorithms are going to be deployed during the HL-LHC to further improve the physics performance. Preliminary studies have shown that the upgrade of the ECAL barrel will preserve the resolution of m_H achieved during Run II.

The large statistics offered by the HL-LHC program will permit the investigation of rare Higgs-boson pair production, which is also sensitive to the Higgs self-coupling. The highest sensitivity to these processes is obtained using events where one Higgs boson decays into a photon pair, and the other one into a pair of b quarks. Indeed, the signal selection can benefit from both the good photon energy resolution and the better vertex-finding efficiency, thanks to the production of other charged particles arising from the hadronization of b quarks.

4 Conclusions

ECAL has shown excellent performance in the reconstruction and identification of high-energy photons and electrons during Run II, and played a key role in many physics analyses involving these particles in their final states. In particular, the high resolution of the energy of photons has been a fundamental ingredient to perform detailed studies of the properties of the Higgs boson in the diphoton decay channel.

Maintaining and possibly improving the performance achieved during Run II is vital for the Higgs physics program during the HL-LHC phase. The higher particle rate induced by the increase in the instantaneous luminosity at the HL-LHC will require an upgrade of the whole ECAL detector. The barrel will be equipped with new faster front-end electronics, while the endcaps will be replaced by a new detector. The improved time tagging planned for the barrel will increase the efficiency to locate the diphoton vertex in $H \to \gamma\gamma$ events, offsetting the degradation of the m_H resolution caused by the larger PU. Preliminary studies on simulated events with the HL-LHC conditions hold the promise to preserve the photon energy resolution achieved during Run II.

References

1. S. Chatrchyan *et al.* [CMS Collaboration], JINST **3**, S08004 (2008).
2. S. Chatrchyan *et al.* [CMS Collaboration], JINST **5**, T03010 (2010).
3. V. Khachatryan *et al.* [CMS Collaboration], Eur. Phys. J. C **74**, 3076 (2014).
4. A. M. Sirunyan *et al.* [CMS Collaboration], Phys. Rev. Lett. **120**, 231801 (2018).
5. E. Di Marco [CMS Collaboration], *CMS electromagnetic calorimeter calibration and timing performance during LHC Run I and future prospects*, CMS-CR-2014-410 (2014); http://cds.cern.ch/record/1975982.
6. S. Chatrchyan *et al.* [CMS Collaboration], JINST **8**, P09009 (2013).
7. CMS Collaboration, CMS-DP-2018-015 (2018); https://cds.cern.ch/record/2319285.
8. CMS Collaboration, *Measurements of Higgs boson production via gluon fusion and vector boson fusion in the diphoton decay channel at* $\sqrt{s} = 13\,TeV$, CMS-PAS-HIG-18-029 (2019); https://cds.cern.ch/record/2667225.
9. CMS Collaboration, *The Phase-2 Upgrade of the CMS Barrel Calorimeters*, CERN-LHCC-2017-011, CMS-TDR-015; https://cds.cern.ch/record/2283187/.
10. A. Martelli, *The CMS HGCAL detector for HL-LHC upgrade*, in proceedings of *LHCP2017 conference*, arXiv:1708.08234v1 [physics.ins-det].

Frascati Physics Series Vol. 69 (2019)
PHOTON 2019 - International Conference on the Structure and the Interactions of the Photon
Jun 3-7, 2019

TWO-PHOTON FUSION HIGGS PRODUCTION IN COLLISIONS WITH PROTON AND ION BEAMS AT THE LHC, HE-LHC, AND FCC

David d'Enterria
CERN, EP Department, 1211 Geneva, Switzerland
Daniel E. Martins
UFRJ, Univ. Federal do Rio de Janeiro, 21941-901, Rio de Janeiro, RJ
Patricia Rebello Teles
ERJ, Univ. do Estado do Rio de Janeiro, 20550-900, Rio de Janeiro, RJ

Abstract

The production of the Higgs boson in ultraperipheral collisions (UPCs) of proton and nuclear beams at three future colliders — the high-luminosity Large Hadron Collider (HL-LHC), the high-energy LHC (HE-LHC), and the Future Circular Collider (FCC) — is studied. The cross sections for the process $\mathrm{AA}\xrightarrow{\gamma\gamma}\mathrm{(A)H(A)}$, with the Higgs particle produced via two-photon fusion at midrapidity and the hadron(s) A surviving the interaction, are computed with MADGRAPH 5 extended with the corresponding coherent γ fluxes for Pb-Pb, Xe-Xe, Kr-Kr, Ar-Ar, O-O, p-Pb, and p-p collisions over $\sqrt{s_{_{\rm NN}}} \approx$ 3–100 TeV. Taking into account the expected luminosities for all colliding systems, the yields and significances for observing the Higgs boson in UPCs, on top of the $\gamma\gamma \rightarrow \mathrm{b\bar{b}, c\bar{c}, q\bar{q}}$ continuum backgrounds, at the three future colliders are estimated. At HL-LHC and HE-LHC, the systems with larger Higgs significance are Ar-Ar(6.3 TeV) and Kr-Kr(12.5 TeV) respectively. However, evidence for $\gamma\gamma \rightarrow \mathrm{H}$ production would require $\times 200$ and $\times 30$ times larger integrated luminosities at both machines. Factors of ten can be gained by running for a year, rather than the typical 1-month heavy-ion run at the LHC, but the process will likely remain unobserved unless a higher energy collider such as the FCC is built. In the latter machine, a 5σ observation of $\gamma\gamma \rightarrow \mathrm{H}$ is warranted in just the first nominal Pb-Pb and p-Pb runs.

1 Introduction

Heavy ions accelerated at high energies are surrounded by huge electromagnetic (e.m.) fields generated by the collective action of their Z individual proton charges. In the equivalent photon approximation (EPA) [1)], such strong e.m. fields can be identified as quasireal photon beams with very low virtualities $Q^2 < 1/R_A^2$ and large longitudinal energies of up to $\omega_{\max} \approx \gamma_L/R_A$, where R_A is the radius of the emitting charge and $\gamma_L = E_{\rm beam}/m_{N,p}$ is the beam Lorentz factor for nucleon or proton mass $m_{N,p} =$ 0.9315, 0.9382 GeV [2, 3)]. On the one hand, since the photon flux scales as the squared charge of each colliding particle, photon-photon cross sections are enhanced millions of times for heavy ions (up to $Z^4 \approx 5 \cdot 10^7$ for Pb-Pb) compared to proton or electron beams. On the other hand, proton (and lighter ions) feature larger $\omega_{\max}$ values thanks to their lower radii R_A and larger beam γ_L factors, and can thereby reach higher photon-photon c.m. energies. At LHC energies, photons emitted from nuclei (with radii $R_A \approx 1.2\,A^{1/3}$ fm) are almost on-shell (virtuality $Q < 0.06$ GeV, for mass numbers $A > 16$), and reach longitudinal energies of up to hundreds of GeV, whereas photon fluxes from protons ($R_A \approx 0.7$ fm) have larger virtualities, $Q \approx 0.28$ GeV, and longitudinal energies in the TeV range [3]. Table 1 summarizes the relevant characteristics of $\gamma\,\gamma$ collisions in ultraperipheral collisions (UPCs) of proton and nuclear beams at the HL-LHC, HE-LHC, and FCC. The beam-beam luminosities are from the estimates of Refs. [4, 5], whereas for p-p collisions, we take $\mathscr{L}_{\rm int} = 1$ fb^{-1} as the value potentially integrated under low-pileup conditions that allow for exclusive $\gamma\,\gamma$ measurements. One can see that, in all cases, the maximum photon-photon c.m. energies reach above the kinematical threshold for Higgs boson production, $\sqrt{s_{\gamma\gamma}^{\rm max}} \gtrsim m_{\rm H} = 125\,{\rm GeV}$.

Table 1: Main features of photon-photon collisions in UPCs with proton and nuclear beams at the HL-LHC, HE-LHC, and FCC: (i) Nucleon-nucleon c.m. energy $\sqrt{s_{_{\rm NN}}}$, (ii) integrated luminosity per run $\mathscr{L}_{\rm int}$, (iii) beam energies $\rm E_{beam}$, (iv) Lorentz factor γ_L, (v) effective charge radius R_A, (vi) photon "maximum" energy $\omega_{\max}$ in the c.m. frame, and (vii) "maximum" photon-photon c.m. energy $\sqrt{s_{\gamma\gamma}^{\rm max}}$. The last two columns list the $\gamma\,\gamma \to$ H cross sections and number of events expected for the quoted $\mathscr{L}_{\rm int}$ per system.

System	$\sqrt{s_{_{\rm NN}}}$	$\mathscr{L}_{\rm int}$	$E_{\rm beam1} + E_{\rm beam2}$	γ_L	R_A	$\omega_{\max}$	$\sqrt{s_{\gamma\gamma}^{\rm max}}$	$\sigma(\gamma\gamma \to {\rm H})$	$\rm N(\gamma\gamma \to H)$
Pb-Pb	5.5 TeV	10 nb^{-1}	2.75 + 2.75 TeV	2950	7.1 fm	80 GeV	160 GeV	15 pb	0.15
Xe-Xe	5.86 TeV	30 nb^{-1}	2.93 + 2.93 TeV	3150	6.1 fm	100 GeV	200 GeV	7 pb	0.21
Kr-Kr	6.46 TeV	120 nb^{-1}	3.23 + 3.23 TeV	3470	5.1 fm	136 GeV	272 GeV	3 pb	0.36
Ar-Ar	6.3 TeV	1.1 pb^{-1}	3.15 + 3.15 TeV	3400	4.1 fm	165 GeV	330 GeV	0.36 pb	0.40
O-O	7.0 TeV	3.0 pb^{-1}	3.5 + 3.5 TeV	3750	3.1 fm	240 GeV	490 GeV	35 fb	0.11
p-Pb	8.8 TeV	1 pb^{-1}	7.0 + 2.75 TeV	7450, 2950	0.7, 7.1 fm	2.45 TeV, 130 GeV	2.6 TeV	0.17 pb	0.17
p-p	14 TeV	1 fb^{-1}	7.0 + 7.0 TeV	7450	0.7 fm	2.45 TeV	4.5 TeV	0.18 fb	0.18
Pb-Pb	10.6 TeV	10 nb^{-1}	5.3 + 5.3 TeV	5700	7.1 fm	160 GeV	320 GeV	150 pb	1.5
Xe-Xe	11.5 TeV	30 nb^{-1}	5.75 + 5.75 TeV	6200	6.1 fm	200 GeV	400 GeV	60 pb	1.8
Kr-Kr	12.5 TeV	120 nb^{-1}	6.25 + 6.25 TeV	6700	5.1 fm	260 GeV	530 GeV	20 pb	2.4
Ar-Ar	12.1 TeV	1.1 pb^{-1}	6.05 + 6.05 TeV	6500	4.1 fm	320 GeV	640 GeV	1.7 pb	1.9
O-O	13.5 TeV	3.0 pb^{-1}	6.75 + 6.75 TeV	7300	3.1 fm	470 GeV	940 GeV	0.11 pb	0.33
p-Pb	18.8 TeV	1 pb^{-1}	13.5 + 5.3 TeV	14 400, 5700	0.7, 7.1 fm	4.1 TeV, 160 GeV	4.2 TeV	0.45 pb	0.45
p-p	27 TeV	1 fb^{-1}	13.5 + 13.5 TeV	14 400	0.7 fm	4.1 TeV	8.2 TeV	0.30 fb	0.30
Pb-Pb	39 TeV	110 nb^{-1}	19.5 + 19.5 TeV	21 000	7.1 fm	600 GeV	1.2 TeV	1.8 nb	200
p-Pb	63 TeV	29 pb^{-1}	50. + 19.5 TeV	53 300, 21 000	0.7,7.1 fm	15.2 TeV, 600 GeV	15.8 TeV	1.5 pb	45
p-p	100 TeV	1 fb^{-1}	50. + 50. TeV	53 300	0.7 fm	15.2 TeV	30.5 TeV	0.70 fb	0.70

The possibility to produce the Higgs boson by exploiting the huge photon field in UPCs of ions, $\rm AA \xrightarrow{\gamma\gamma} (A)H(A)$, where the scalar boson is produced at midrapidities and the colliding ions (A) survive their electromagnetic interaction (first diagram in Fig. 1 top-right), was first considered in several studies 30 years ago [6]. The observation of such $\gamma\,\gamma \to$ H process would provide an independent measurement of the H–γ loop-induced coupling based not on Higgs decays but on its s-channel production mode, as well as a model-independent extraction of the total Higgs width combining this process with the $\rm H \to \gamma\,\gamma$ decay channel measured at future $\rm e^+e^-$ Higgs factories. Detailed studies of the actual measurement of the Higgs boson in its dominant $\rm b\bar{b}$ decay mode, including realistic experimental acceptance and efficiencies for the signal and the $\gamma\,\gamma \to \rm b\bar{b}, c\bar{c}, q\bar{q}$ continuum backgrounds (second diagram in Fig. 1 top-right), were first presented in Ref. [7] for ultraperipheral proton-nucleus (p-A) and nucleus-nucleus (A-A) collisions at LHC energies. This work showed that, for the nominal integrated luminosities, the scalar boson was unobservable in UPCs at the LHC unless one integrated at least $\times 300$ times more luminosity than that expected for the standard 1-month heavy-ion operation. Although the LHC beam luminosities for p-p are 7 orders of magnitude larger than for Pb-Pb, the running conditions with 50 or more pileup p-p collisions per bunch crossing make it impossible to select exclusive photon-photon events with central masses at 125-GeV unless one installs very forward proton taggers (at 420 m inside the LHC tunnel) with 10-picosecond time resolution [8]. On the other hand, similar studies [9] carried out within the CERN Future Circular Collider (FCC) project [5], indicated that the observation of Higgs production in UPCs was clearly possible in just the first nominal run of Pb-Pb and p-Pb collisions at $\sqrt{s_{_{NN}}} = 39$ and 63 TeV respectively. This writeup provides a summary of the more detailed studies reported in Ref. [10] for a Higgs boson measurement in the High-Luminosity phase of the LHC (HL-LHC), as well as at the proposed High-Energy LHC (HE-LHC) with twice larger c.m. energies [4], including not only higher luminosities but also collisions of lighter ions (Xe-Xe, Kr-Kr, Ar-Ar, O-O).

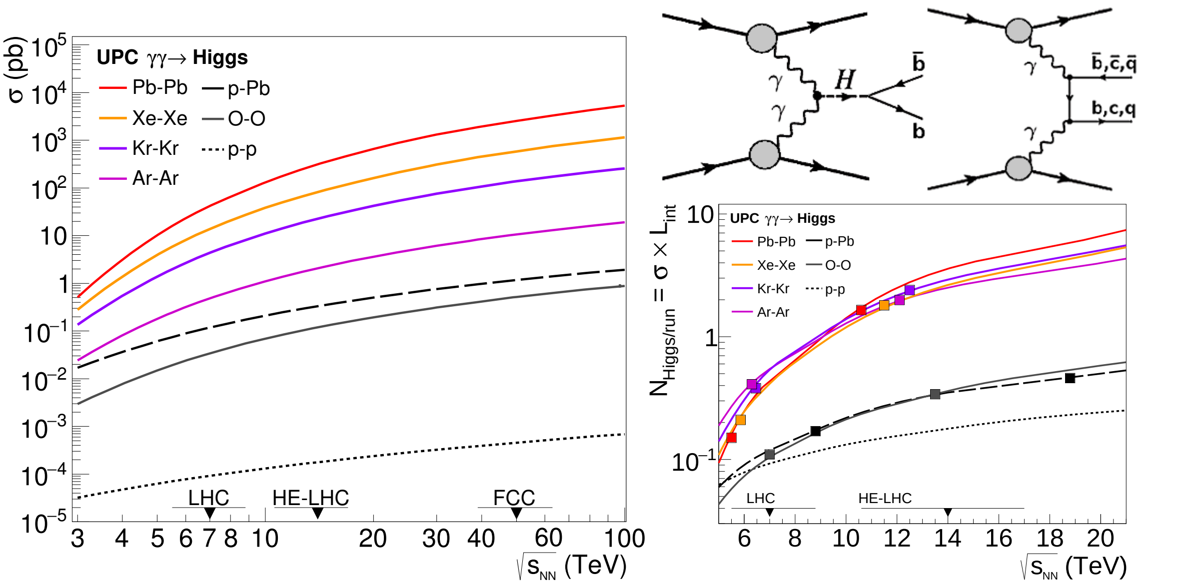

Figure 1: *Left: Two-photon fusion Higgs boson cross section versus nucleon-nucleon c.m. energy in nuclear and proton collisions over $\sqrt{s_{_{NN}}} = 3$–100 TeV. Right-top: Diagrams for the two-photon production of the Higgs boson (*$b\bar{b}$ *decay) and of the b-,c-,light-quark pair backgrounds. Right-bottom: Number of Higgs bosons produced per month in UPCs of various colliding systems in the HL-LHC/HE-LHC energy range.*

2 Theoretical setup

The MADGRAPH 5 (v.2.5.4) Monte Carlo (MC) event generator [11] is employed to compute the UPC Higgs boson cross sections, following the implementation discussed in detail in [7], from the convolution of the Weizsäcker-Williams EPA photon fluxes for the proton and/or ions, and the elementary $\gamma\,\gamma \to \mathrm{H}$ cross section (with H-γ coupling parametrized in the Higgs effective field theory [12]):

$$\sigma_{\mathrm{A_1 A_2 \to H}} = \int dm_{\mathrm{H}}\, dy_{\mathrm{H}}\, \frac{2m_{\mathrm{H}}}{s}\, f_{\gamma/A_1}(x_1) f_{\gamma/A_2}(x_2)\, \hat{\sigma}_{\gamma\,\gamma \to \mathrm{H}}\ ; \tag{1}$$

where $x = \omega/E$ is the beam energy fraction carried by the photon. For protons, the MADGRAPH 5 default γ flux is given by the energy spectrum of Ref. [13]:

$$f_{\gamma/p}(x) = \frac{\alpha}{\pi}\, \frac{1 - x + 1/2x^2}{x} \int_{Q^2_{\mathrm{min}}}^{\infty} \frac{Q^2 - Q^2_{\mathrm{min}}}{Q^4} |F(Q^2)|^2 dQ^2\ , \tag{2}$$

where $\alpha = 1/137$, $F(Q^2)$ is the proton e.m. form factor, and the minimum momentum transfer $Q_{\rm min}$ is a function of x and the proton mass m_p, $Q^2_{\rm min} \approx (x\, m_p)^2/(1-x)$. For ions of charge Z, the photon energy spectrum, integrated over impact parameter b from $b_{\rm min} = R_A$ to infinity, is [14]:

$$f_{\gamma/A}(x) = \frac{\alpha\, Z^2}{\pi}\, \frac{1}{x} \left[2x_i K_0(x_i) K_1(x_i) - x_i^2 (K_1^2(x_i) - K_0^2(x_i))\right], \quad (3)$$

where $x_i = x\, m_N\, b_{\rm min}$, K_0, K_1 are the zero- and first-order modified Bessel functions of the second kind, and for the different nuclear radii R_A, we use the data from elastic lepton-nucleus collisions [15]. We exclude nuclear overlap by imposing $b_1 > R_{A_1}$ and $b_2 > R_{A_2}$ for each photon flux, and applying a correcting factor on the final cross section that depends on the ratio of Higgs mass over $\sqrt{s_{_{\rm NN}}}$ [16].

After cross section determination, the event generation is carried out for the dominant Higgs decay mode, $\rm H \to b\bar{b}$ with 56% branching fraction [17], as it is the final state that provides the largest number of signal events. The same setup is used to generate the exclusive two-photon production of $\rm b\bar{b}$ and (misidentified) $\rm c\bar{c}$ and light-quark ($\rm q\bar{q}$) jet pairs, which constitute the most important physical backgrounds for the $\rm H\to b\bar{b}$ measurement. For the HL-LHC and HE-LHC system, the analysis is carried out at the parton level only, whereas for FCC energies, we have further used PYTHIA 8.2 [18] to shower and hadronize the two final-state b-jets generated, which are then reconstructed with the Durham k_t algorithm [19] (exclusive 2-jets final-state) using FASTJET 3.0 [20].

3 Total Higgs cross sections

The ultraperipheral Higgs boson cross sections as a function of $\sqrt{s_{_{\rm NN}}}$ are shown in Fig. 1 (left) and listed in the before-last column of Table 1 for all p-p, p-A, and A-A systems considered. The theoretical cross sections have a conservative 20% uncertainty (not quoted) to cover different charge form factors and nuclear overlap conditions. As expected, the bigger the charge of the colliding ions the larger the UPC cross sections, but such advantage is mitigated by the correspondingly reduced beam-beam luminosities for heavier ions. Figure 1 (right-bottom) shows the product of Higgs UPC cross section times the integrated luminosities for each colliding system in the HL-LHC and HE-LHC energy range. At the LHC, we see that, despite the fact that Pb-Pb features the largest Higgs cross section, $\sigma(\gamma\,\gamma \to \rm H) = 15$ pb, there are about 2.5 times more scalar bosons per month in Ar-Ar and Kr-Kr collisions (0.40 versus 0.15, last column of Table 1) thanks to the comparatively larger luminosities and c.m. energies of the latter compared to lead beams. At HE-LHC, the Higgs cross sections are about a factor of 10 larger than at the LHC, and most colliding systems feature 1.5–2.5 Higgs bosons produced per month. The most competitive systems to try a measurement of UPC Higgs production are Ar-Ar and Kr-Kr at HL-LHC and HE-LHC respectively. At the FCC, the cross sections are two orders of magnitude larger than at the LHC, reaching $\sigma(\gamma\,\gamma \to \rm H) = 1.75$ nb and 1.5 pb in Pb-Pb and p-Pb collisions at $\sqrt{s_{_{\rm NN}}} = 39$ and 63 TeV which, for the nominal $\mathscr{L}_{\rm int} = 110$ nb^{-1} and 29 pb^{-1} per-month integrated luminosities, yield ∼200 and 45 Higgs bosons produced (corresponding to 110 and 25 bosons in the $\rm b\bar{b}$ decay mode, respectively).

4 Data analysis and Higgs boson significances

The observation of the Higgs boson in UPCs relies on the measurement of two exclusive b-jets with invariant masses peaked at $m_{\rm H}$, on top of a background of $\gamma\gamma \to \rm b\bar{b}, c\bar{c}, q\bar{q}$ continuum pairs, where charm and light ($\rm q = u, d, s$) quarks are misidentified as b-quarks. For all colliding systems and at all $\sqrt{s_{_{\rm NN}}}$, the pure MC-level background continuum cross sections over $m_{\rm H} \approx 100$–150 GeV, computed with the same MADGRAPH 5 setup, are about 25, 200, and 10^3 times larger respectively than the Higgs signal.

The data analysis follows closely the study of Ref. [7], with the following acceptance and reconstruction performances assumed: jet reconstruction over $|\eta| < 2.5$ (< 5 for FCC), 7% b-jet energy resolution (resulting in a dijet mass resolution of ~6 GeV at the Higgs peak), 70% b-jet tagging efficiency, and 5% (1.5%) b-jet mistagging probability for a c (light-flavour q) quark. For the double b-jet final-state of interest, these lead to a ~50% efficiency for the MC-generated signal ($\mathscr{S}$), and a total reduction of the misidentified $c\bar{c}$ and $q\bar{q}$ continuum backgrounds ($\mathscr{B}$) by factors of ~400 and ~4500 respectively. The sum of remaining continuum backgrounds can be reduced through proper kinematical cuts: (i) requiring jets with $p_T \approx m_H/2 = 55$–67 GeV (as expected for jets from the decay of an UPC Higgs produced almost at rest) suppresses more than 95% of the continuum, while removing only half of the signal; (ii) requiring $|\cos\theta_{j_1 j_2}| < 0.5$ — to exploit the fact that the angular distribution in the helicity frame of the Higgs decay b-jets is isotropic while the continuum (with quarks propagating in the t- or u- channels) is peaked in the forward–backward directions — further suppresses the backgrounds while leaving almost untouched the signal; and (iii) the pair jet mass to be within $\pm 1.4\sigma_{jj}$ around the Higgs mass (i.e. $116 \lesssim m_{b\bar{b}} \lesssim 134$ GeV). For all systems, the overall loss of Higgs signal events due to the acceptance and kinematical cuts (i.e. without accounting for (mis)identification efficiencies) is around a factor of two, whereas the backgrounds are reduced by factors of 30 to 100, resulting in a final $\mathscr{S}/\mathscr{B} \approx 1$ for all colliding species.

Table 2: Summary of the cross sections after each event selection step, and final number of events expected (for the nominal integrated luminosities quoted) for signal and backgrounds in the $\gamma\gamma \to H(b\bar{b})$ measurements in Ar-Ar at HL-LHC, Kr-Kr at HE-LHC, and Pb-Pb and p-Pb at FCC.

Ar-Ar at $\sqrt{s_{_{NN}}} = 6.3$ TeV	cross section (b-jet (mis)tag effic.)	visible cross section after $\eta^j, p_T^j, \cos\theta_{jj}, m_{jj}$ cuts	N_{evts} ($\mathscr{L}_{int} = 1.1$ pb^{-1})
$\gamma\gamma \to H \to b\bar{b}$	0.20 pb (0.10 pb)	0.045 pb	0.05
$\gamma\gamma \to b\bar{b}$ [$m_{b\bar{b}}$=100−150 GeV]	8.2 pb (4.0 pb)	0.06 pb	0.06
$\gamma\gamma \to c\bar{c}$ [$m_{c\bar{c}}$=100−150 GeV]	60 pb (0.15 pb)	0.006 pb	0.006
$\gamma\gamma \to q\bar{q}$ [$m_{q\bar{q}}$=100−150 GeV]	70 pb (0.016 pb)	–	–
Kr-Kr at $\sqrt{s_{_{NN}}} = 12.5$ TeV			N_{evts} ($\mathscr{L}_{int} = 0.12$ pb^{-1})
$\gamma\gamma \to H \to b\bar{b}$	11 pb (5.5 pb)	2.5 pb	0.30
$\gamma\gamma \to b\bar{b}$ [$m_{b\bar{b}}$=100−150 GeV]	365 pb (180 pb)	2.8 pb	0.34
$\gamma\gamma \to c\bar{c}$ [$m_{c\bar{c}}$=100−150 GeV]	2.7 nb (6.7 pb)	0.24 pb	0.03
$\gamma\gamma \to q\bar{q}$ [$m_{q\bar{q}}$=100−150 GeV]	3.1 nb (0.70 pb)	–	–
Pb-Pb at $\sqrt{s_{_{NN}}} = 39$ TeV			N_{evts} ($\mathscr{L}_{int} = 110$ nb^{-1})
$\gamma\gamma \to H \to b\bar{b}$	1.0 nb (0.50 nb)	0.19 nb	21.1
$\gamma\gamma \to b\bar{b}$ [$m_{b\bar{b}}$=100−150 GeV]	24.3 nb (11.9 nb)	0.23 nb	25.7
$\gamma\gamma \to c\bar{c}$ [$m_{c\bar{c}}$=100−150 GeV]	525 nb (1.30 nb)	0.02 nb	2.3
$\gamma\gamma \to q\bar{q}$ [$m_{q\bar{q}}$=100−150 GeV]	590 nb (0.13 nb)	0.002 nb	0.25
p-Pb at $\sqrt{s_{_{NN}}} = 63$ TeV			N_{evts} ($\mathscr{L}_{int} = 29$ pb^{-1})
$\gamma\gamma \to H \to b\bar{b}$	0.87 pb (0.42 pb)	0.16 pb	4.8
$\gamma\gamma \to b\bar{b}$ [$m_{b\bar{b}}$=100−150 GeV]	21.8 pb (10.7 pb)	0.22 pb	6.3
$\gamma\gamma \to c\bar{c}$ [$m_{c\bar{c}}$=100−150 GeV]	410 pb (1.03 pb)	0.011 pb	0.3
$\gamma\gamma \to q\bar{q}$ [$m_{q\bar{q}}$=100−150 GeV]	510 pb (0.114 pb)	0.001 pb	0.04

Table 2 lists the cross sections after each event selection step, and final number of events expected (for the nominal integrated luminosities quoted) for signal and backgrounds in the systems with larger signal strength at each collider (Fig. 1, right-bottom): Ar-Ar at $\sqrt{s_{_{NN}}} = 6.3$ TeV, Kr-Kr at $\sqrt{s_{_{NN}}} = 12.5$ TeV, and Pb-Pb at $\sqrt{s_{_{NN}}} = 39$ TeV. Since the FCC case has been studied with more detail [9], we include also in the table the results obtained in p-Pb at $\sqrt{s_{_{\rm NN}}} = 63$ TeV. The Ar-Ar and Kr-Kr numbers quoted after each set of cuts are realistic estimates based on the overall signal and background losses derived in the complete MC studies of Refs. [7, 9]. The listed Pb-Pb and p-Pb results at FCC are those obtained in the full MC analysis described in Ref. [9]. The last column of Table 2 lists the final number of signal and background events expected after all selection criteria for the nominal 1-month run operation. The expected number of Higgs events per month, after cuts, at HL-LHC and HE-LHC are below unity and one would need to integrate at least factors of $\times 300$ and $\times 20$ more luminosities, respectively, in order to see a 3σ evidence of UPC Higgs production (Fig. 2). These factors are derived simply by requiring that the $\mathscr{S}/\sqrt{\mathscr{B}}$ ratio around the Gaussian Higgs peak ($116 < m_{\rm b\bar{b}} < 133$ GeV), is above 3. A factor of $\times 10$ in $\mathscr{L}_{\rm int}$ could be gained by running for the time typical of a proton-proton run, instead of the nominal 1-month heavy-ion run operation. Such a longer run, motivated by Higgs- rather than heavy-ion physics, at HE-LHC would allow for an evidence of the process, by combining two experiments. Achieving the same significance at the HL-LHC seems out of reach, unless an extra factor of ten enhancement in the instantaneous Ar-Ar luminosity is accomplished by some (currently unidentified) means.

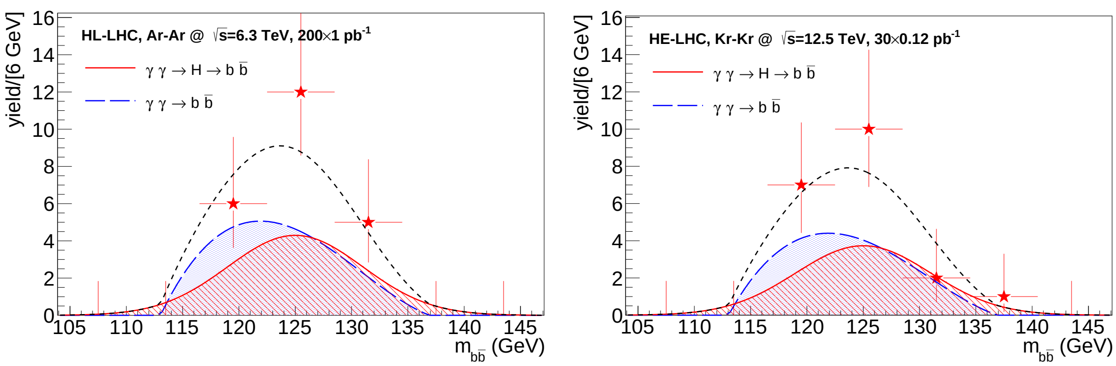

Figure 2: *Expected invariant mass distributions for b-jet pairs from two-photon-fusion Higgs signal (red Gaussian) over the* $\rm b\bar{b}+c\bar{c}+q\bar{q}$ *continuum (hatched blue area) in ultraperipheral Ar-Ar (*$\sqrt{s_{_{\rm NN}}} = 6.3$ *TeV, left) and Kr-Kr (*$\sqrt{s_{_{\rm NN}}} = 12.5$ *TeV, right) collisions, after event selection criteria with integrated luminosities* $\times 200$ *and* $\times 30$ *larger than the nominal ones for each system.*

At the FCC, Pb-Pb collisions at $\sqrt{s} = 39$ GeV with the integrated luminosity of $\mathscr{L}_{\rm int} = 110$ nb^{-1} per nominal 1-month run, results in about $\sim$21 signal counts over $\sim$28 for the sum of backgrounds in a window $m_{\rm b\bar{b}} = 116$–133 GeV around the Higgs peak. Reaching a statistical significance of 5σ (Fig. 3, right) would require to combine two different experiments (or doubling the luminosity in a single one). Similar estimates for p-Pb at 63 TeV (29 pb^{-1}) yield about 5 signal events after cuts, over a background of 6.7 continuum events. Reaching a 5σ significance for the observation of $\gamma\gamma \to$ H production (Fig. 3, left) would require in this case to run for about 8 months (instead of the nominal 1-month run per year), or running 4 months and combining two experiments.

5 Conclusion

Prospective studies for the measurement of the two-photon production of the Higgs boson in the $\rm b\bar{b}$ decay channel in ultraperipheral Pb-Pb, Xe-Xe, Kr-Kr, Ar-Ar, O-O, p-Pb, and p-p collisions at the HL-LHC, HE-LHC, and FCC, have been presented. Cross sections have been obtained with MADGRAPH 5 including nuclear and proton equivalent photon fluxes and requiring no hadronic overlap of the colliding beams, at nucleon-nucleon c.m. energies over $\sqrt{s_{_{\rm NN}}} = 5$–100 TeV. The same setup is used to generate

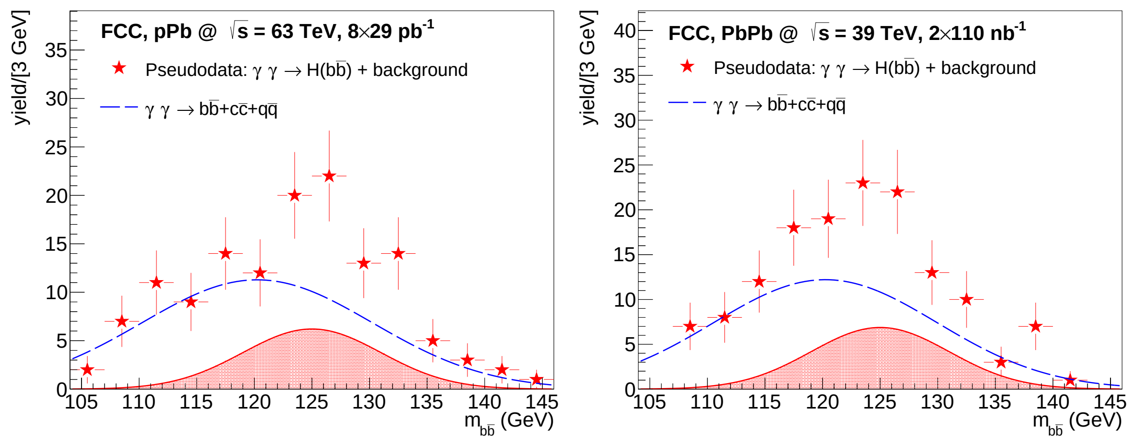

Figure 3: *Expected invariant mass distributions for b-jet pairs from two-photon-fusion Higgs signal (red Gaussian) over the* $\mathrm{b\bar{b}} + \mathrm{c\bar{c}} + \mathrm{q\bar{q}}$ *continuum (hatched blue area) in ultraperipheral p-Pb* ($\sqrt{s_{_{\rm NN}}} = 63$ *TeV, left) and Pb-Pb* ($\sqrt{s_{_{\rm NN}}} = 39$ *TeV, right) collisions, after event selection criteria with the quoted integrated luminosities (see text).*

the exclusive two-photon production of $\mathrm{b\bar{b}}$ and (misidentified) $\mathrm{c\bar{c}}$ and light-quark ($\mathrm{q\bar{q}}$) jet pairs, which constitute the most important physical backgrounds. By assuming realistic jet acceptance, reconstruction performances, and (mis)tagging efficiencies, and applying appropriate kinematical cuts on the jet p_T and angles in the helicity frame, we can reconstruct the $\mathrm{H(b\bar{b})}$ signal on top of the dominant $\gamma\gamma \to \mathrm{b\bar{b}}$ continuum background with $\mathscr{S}/\mathscr{B} \approx 1$ signal-over-background ratios. On the one hand, reaching 3σ evidence of UPC Higgs-production at HL-LHC and at HE-LHC, requires factors of about $\times 200$ and $\times 30$ more integrated luminosities in Ar-Ar and Kr-Kr collisions, respectively, than currently planned for both machines. Factors of ten in integrated luminosity can be gained running for the duration (10^7 s) typical of a p-p run, rather than the nominal 1-month heavy-ion operation, but would still fall too short for any feasible measurement at the HL-LHC. On the other hand, the measurement of $\gamma\gamma \to \mathrm{H} \to \mathrm{b\bar{b}}$ would yield about 20 (5) signal counts after cuts in Pb-Pb (p-Pb) collisions at the FCC for their nominal integrated luminosities per run. Observation of the two-photon-fusion Higgs production at the 5σ-level is thereby achievable in the first FCC run by combining the measurements of two experiments. The feasibility studies presented here indicate the Higgs physics potential opened up to study in $\gamma\gamma$ ultraperipheral ion collisions at current and future CERN hadron colliders, eventually providing an independent measurement of (i) the H-γ coupling not based on Higgs decays but on a s-channel production mode, as well as (ii) its total width by combining this $\gamma\gamma \to \mathrm{H}$ measurement with the $\mathrm{H} \to \gamma\gamma$ decay branching ratio measured at future $\mathrm{e^+e^-}$ Higgs factories.

Acknowledgments – P. R. T. acknowledges financial support from the CERN TH Department and from the FCC project. We thank I. Helenius and L. Harland-Lang for useful discussions on PYTHIA 8 and/or photon-photon collisions, as well as J. Jowett for feedback on running conditions for light-ions at the HL-LHC and HE-LHC, and to E. Chapon on statistical methods.

References

1. C. von Weizsäcker *Z. Physik* **88** (1934) 612; E. J. Williams, Phys. Rev. **45** (1934) 729. E. Fermi *Nuovo Cimento* **2** (1925) 143.
2. C. A. Bertulani and G. Baur, Phys. Rept. **163** (1988) 299.
3. A. J. Baltz *et al.*, Phys. Rept. **458** (2008) 1. [arXiv:0706.3356 [nucl-ex]]
4. Z. Citron *et al.*, arXiv:1812.06772 [hep-ph]; A. Abada *et al.* [FCC Collab.], CERN-ACC-2018-0059.
5. A. Dainese *et al.*, CERN Yellow Report **3** (2017) 635, doi:10.23731/CYRM-2017-003.635 [arXiv:1605.01389 [hep-ph]]; D. d'Enterria *et al.*, QM'17 Proceeds., Nucl. Phys. A **967** (2017) 888 [arXiv:1704.05891 [hep-ex]]; and A. Abada *et al.* [FCC Collab.], CERN-ACC-2018-0058.
6. M. Grabiak *et al.*, J. Phys. G **15** (1989) L25; E. Papageorgiu, Phys. Rev. D **40** (1989) 92; M. Drees *et al.*, Phys. Lett. B**223** (1989) 454; K. J. Abraham *et al.*, Phys. Lett. B **251** (1990) 186.
7. D. d'Enterria and J. P. Lansberg, Phys. Rev. D **81** (2010) 014004 [arXiv:0909.3047 [hep-ph]].
8. M. G. Albrow *et al.* [FP420 R&D Collab.], JINST **4** (2009) T10001.
9. D. d'Enterria, D. Martins, P. Rebello Teles, CERN-Proceeds-2018-001.33; arXiv:1712.10104 [hep-ph].
10. D. d'Enterria, D. E. Martins and P. Rebello Teles, arXiv:1904.11936 [hep-ph].
11. J. Alwall *et al.*, JHEP **09** (2007) 028 [arXiv:0706.2334 [hep-ph]].
12. M. A. Shifman, A. I. Vainshtein, M. B. Voloshin and V. I. Zakharov, Sov. J. Nucl. Phys. **30**, 711 (1979) [Yad. Fiz. **30** (1979) 1368]; B. A. Kniehl and M. Spira, Z. Phys. C **69** (1995) 77; S. Dawson and R. Kauffman, Phys. Rev. D **49** (1994) 2298.
13. V. M. Budnev, I. F. Ginzburg, G. V. Meledin, V. G. Serbo, Phys. Rept. **15** (1975) 181.
14. J.D. Jackson, *Classical Electrodynamics*, 2nd edition, John Wiley & Sons (1975).
15. H. De Vries, C. W. De Jager and C. De Vries, Atom. Data Nucl. Data Tabl. **36** (1987) 495.
16. R. N. Cahn and J. D. Jackson, Phys. Rev. D **42**, 3690 (1990).
17. M. Spira, Nucl. Instrum. Meth. A **389** (1997) 357; A. Djouadi, J. Kalinowski and M. Spira, Comput. Phys. Commun. **108** (1998) 56; A. Djouadi, J. Kalinowski, M. Mühlleitner and M. Spira, arXiv:1003.1643 [hep-ph]; `http://people.web.psi.ch/spira/hdecay/`.
18. T. Sjöstrand *et al.*, Comput. Phys. Commun. **191** (2015) 159.
19. S. Catani, Y. L. Dokshitzer, M. H. Seymour and B. R. Webber, Nucl. Phys. B **406** (1993) 187.
20. M. Cacciari, G. P. Salam and G. Soyez, Eur. Phys. J. C **72** (2012) 1896. [arXiv:1111.6097 [hep-ph]].

Frascati Physics Series Vol. 69 (2019)
PHOTON 2019 - International Conference on the Structure and the Interactions of the Photon
Jun 3-7, 2019

ELECTROWEAK PRECISION TESTS OF THE SM

Jens Erler
PRISMA$^+$ Cluster of Excellence, Johannes Gutenberg-University, 55099 Mainz, Germany
on sabbatical leave from
Departamento de Física Teórica, IF–UNAM, 04510 CDMX, México

Abstract

A global survey of weak mixing angle measurements at low and high energies is presented. Then I will discuss theoretical uncertainties in precision observables with special emphasis on their correlations. The important role of vacuum polarization in global fits will also be addressed before fit results are presented.

1 Weak mixing angle, W and Higgs boson masses, and associated theory uncertainties

I will start with a survey of measurements of the weak mixing angle, $\sin^2\theta_W$, as its accurate determination is becoming a global endeavor. One can compute and measure $\sin^2\theta_W$ and relate it to the W boson mass, M_W. Thus, one has 3 ways of obtaining it, yielding a doubly over-constrained system at sub-per mille precision. As this system involves relations between couplings and masses of the Standard Model (SM) particles, this is *the* key test of electroweak symmetry breaking. Moreover, comparisons of measurements at different scales or between different initial or final states provide a window to physics beyond the SM that would remain closed with only one kind of determination, even if that would be extremely precise.

One approach to measure $\sin^2\theta_W$ is to tune to the Z resonance, where one can measure forward-backward (FB) or left-right (LR) asymmetries (the latter if one has at least one polarized beam) in e^+e^- annihilation around the Z boson mass, M_Z. Or one can reverse initial and final states and measure the FB asymmetry in pp or $p\bar{p}$ Drell-Yan annihilation in a larger window around M_Z.

A very different route is to go to lower energies, and consider purely weak processes. Using neutrinos in the deep inelastic regime (νDIS), where scattering occurs to first approximation off individual quarks, rates are relatively large. Very recently the process called Coherent Elastic Neutrino Nucleus Scattering (CEνNS) as has been observed for the first time by the COHERENT Collaboration [1] at Oak Ridge.

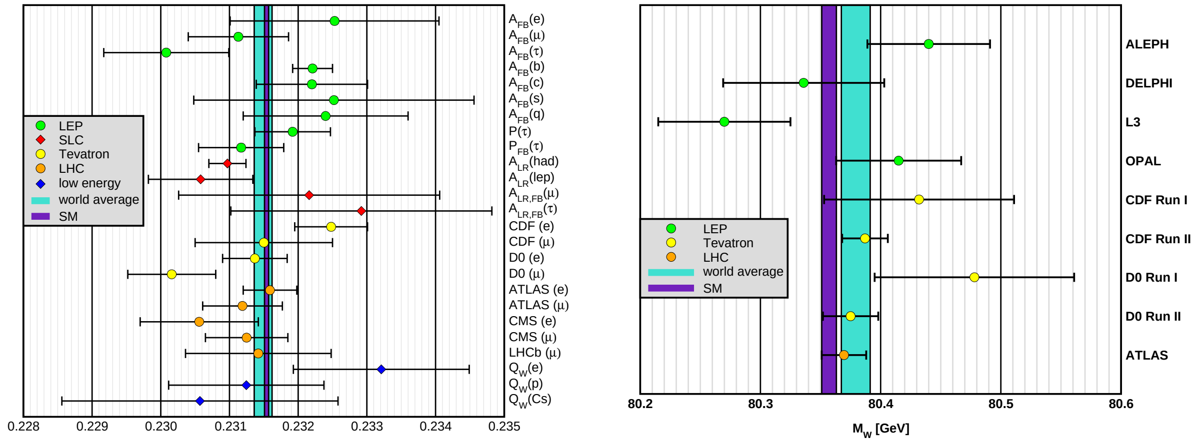

Figure 1: *Survey of measurements of the effective weak mixing angle (left) and the W boson mass (right).*

An alternative strategy to eliminate the electromagnetic interaction is to perform experiments in polarized and therefore parity-violating electron scattering [2] (PVES), measuring tiny cross section asymmetries between left-handed and right-handed polarized initial states,

$$A_{LR} = \frac{\sigma_L - \sigma_R}{\sigma_L + \sigma_R} \ . \tag{1}$$

Just as for the neutrino case, one may consider a purely leptonic process, specifically polarized Møller scattering, $\vec{e}^- e^- \to e^- e^-$ [3]. And again one can scatter deep inelastically (eDIS), but there is an important difference to νDIS. Because of the small cross sections in ν scattering one needs large nuclei, which leads to complications from nuclear physics effects, while in eDIS one may use a target as small and simple as the deuteron, as done, *e.g.,* by the PVDIS Collaboration [4] at JLab. In fact, polarized eDIS was the process that established the SM [5], and a high-precision measurement will be possible with SoLID at the upgraded CEBAF. The PVES analog of CEνNS on a proton target has been completed very recently by JLab's Qweak Collaboration [6] and provided the first direct measurement of the weak charge of the proton [7], $Q_W(p)$. The future P2 experiment [8] at the MESA facility at the JGU Mainz, will reduce the error in $Q_W(p)$ by a factor of 3, and may also run using a ^{12}C target which is a interesting, because it is spherical and iso-scalar and has therefore only one nuclear form factor. Thus, $Q_W(^{12}\text{C})$ would be easier to interpret, especially if form factor effects can be constrained by additional run time at larger momentum transfer Q^2. PVES would then be able to disentangle the weak charges of the proton and the neutron, and consequently the effective vector couplings of the up and down quarks to the Z boson.

Another newcomer are isotope ratios in atomic parity violation (APV). Now, APV in single isotopes is a traditional way to address the weak neutral-current, and has been studied successfully in alkali atoms [9]. But one faces atomic physics complications, since one needs to understand the atomic structure in heavy nuclei from sophisticated many-body calculations [10] to a few per mille accuracy. But most of the atomic physics effects cancel in isotope ratios. The first such measurement has been achieved very recently at the JGU Mainz [11] where the weak charges of Yb showed the expected isotope dependence.

Fig. 1 shows the most precise determination of $\sin^2\theta_W$. The LEP and SLC measurements in e^+e^- annihilation near the M_Z pole [12] yield the combined result, $\sin^2\theta_W = 0.23153 \pm 0.00016$. There was a change in the extraction from the FB asymmetry for $b\bar{b}$ pairs at LEP, as the two-loop QCD correction necessary to extract the pole asymmetry is now known with its b quark mass dependence [13], reducing the largest LEP discrepancy with the SM by $\approx 1/4\ \sigma$. Another change affected the extraction from APV in ^{133}Cs [9], for which the Stark vector transition polarizability has been re-measured [14] very recently, shifting $|Q_W(^{133}\mathrm{Cs})|$ which was 1.4 σ lower than the SM value much closer to the prediction.

The leptonic FB asymmetries at the Tevatron combine to the value [15] $\sin^2\theta_W = 0.23148 \pm 0.00033$. The average [16] of those at the LHC, $\sin^2\theta_W = 0.23131 \pm 0.00033$, by ALTAS, CMS, and LHCb, assumes that the smallest theory uncertainty (± 0.00025 for ATLAS) is common to all three detectors. Since rather different aspects of parton distribution functions are necessary for the extraction of $\sin^2\theta_W$ at $p\bar{p}$ and pp colliders, the uncertainties can be assumed to be uncorrelated, and we find the world average, $\sin^2\theta_W = 0.23149 \pm 0.00013$, in excellent agreement with the global fit result, $\sin^2\theta_W = 0.23153 \pm 0.00004$.

Fig. 1 also shows a comparison of M_W results. In contrast to $\sin^2\theta_W$, one observes better mutual agreement among the various measurements at LEP [17], the Tevatron [18], and by ATLAS [19], but their average, $M_W = 80.379 \pm 0.012$ GeV, is 1.5 σ higher than the SM prediction, $M_W = 80.361 \pm 0.005$ GeV.

The indirect and global fit results for M_W and $\sin^2\theta_W$ account not only for theory errors but also include an implementation of theoretical correlations [16]. There are various kinds of such errors entering the fits, where the most important ones are from unknown higher order contributions to the gauge boson self-energies. They can be estimated by considering the expansion parameters involved, including various enhancement factors [16]. We translate these loop factors into uncertainties in the oblique parameters [20] $S = S_Z$, T, and $U = S_W - S_Z$, which have been originally introduced to parameterize potential new physics contributions to electroweak radiative corrections. Denoting these uncertainty parameters by ΔS_Z, ΔT and ΔU, and assuming them to be sufficiently different (uncorrelated) *induces* theory correlations between different observables. We find $\Delta S_Z = \pm 0.0034$, $\Delta T = \pm 0.0073$, and $\Delta U = \pm 0.0051$.

The top quark mass determined from global fits to all data except m_t from the Tevatron and LHC, including (excluding) these uncertainties, is $m_t = 176.5 \pm 1.9$ (1.8) GeV. This represents a 1.8 (1.9) σ larger value than the direct measurement [16] $m_t = 172.90 \pm 0.47$ GeV. Similarly, global fits to all data except for the direct $M_H = 125.10 \pm 0.14$ GeV constraint [16] from the LHC, give $M_H = 90^{+17}_{-15}$ GeV and $M_H = 91^{+18}_{-16}$ GeV, showing only slightly increased central value and uncertainty and reduced tension with the directly measured value once theory uncertainties are included.

2 Vacuum polarization in global fits

The electromagnetic coupling at the Z peak, $\alpha(M_Z)$, is needed to predict M_W and $\sin^2\theta_W$. To this end, three different groups have analyzed hadron production data in e^+e^- annihilation, and in some cases τ decay spectral functions which by approximate isospin symmetry yield additional information on the former. Or one can use perturbation theory for at least part of the calculation, and only rely on data in the hadronic region up to about 2 GeV, and then perform a renormalization group evolution [21] (RGE), which depends on the strong coupling α_s, and the charm and bottom quark $\overline{\mathrm{MS}}$ masses, $\hat{m}_c$ and $\hat{m}_b$. The results of the different approaches agree well, where for references and a discussion, I refer to Ref. [21].

The data used for the hadronic part also enter other observables present in global electroweak fits, inducing another source of uncertainty correlation. *E.g.,* they are crucial for the SM prediction of the muon anomalous magnetic moment, a_μ, where they enter first at two loops and generate a correlation with $\alpha(M_Z)$, and both are in turn anti-correlated with three-loop vacuum polarization in a_μ. Because the muon mass scale is rather low, most of the evaluation of the hadronic vacuum polarization contribution to a_μ is based on data. However, there is a fraction that can be computed perturbatively. In particular, the heavy quark contributions are fully accessible in perturbation theory [22], which for the charm contribution yields, $a_\mu^c = (14.6 \pm 0.5_{\mathrm{PQCD}} \pm 0.2_{\hat{m}_c} \pm 0.1_{\alpha_s})10^{-10}$, and where the errors are from the truncation of the

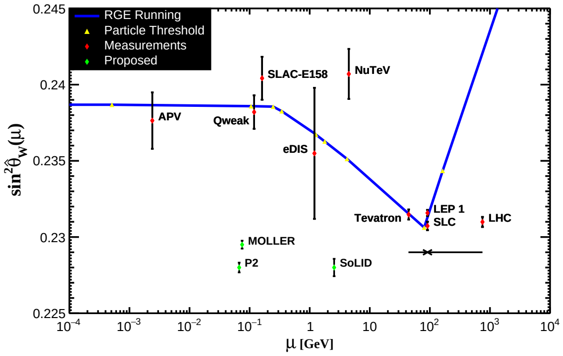

Figure 2: *Renormalization group evolution (running) of the weak mixing angle (updated from Ref.* [21]*).*

perturbative series at $\mathcal{O}(\alpha_s^2)$, and the parametric errors in $\hat{m}_c(\hat{m}_c)$ and α_s. This in excellent agreement with the very recent lattice result in Ref. [23] and of very similar precision. Similarly, $a_\mu^b = 0.3 \times 10^{-10}$, which has not been computed on the lattice, yet. Note, that Ref. [23] finds a rather large total hadronic vacuum polarization contribution, so that if confirmed, there would cease to be a conflict between the measurement of a_μ and the SM, which currently amounts to more than 3 σ. But then there would be a new discrepancy between the dispersive and lattice gauge theory approaches to vacuum polarization.

$\sin^2\theta_W(0)$ enters many low-energy electroweak observables, and Fig. 2 shows that future low-energy PVES experiments will be at the precision level of the LEP and SLC measurements. To compute the RGE in the non-perturbative region, one needs the same kind of data that enters the calculation of $\alpha(M_Z)$. This part needs to be subdivided into two pieces because the vector couplings of the Z boson differ from the electric charges, implying that there is a piece that is not directly related to $\alpha(M_Z)$ and necessitating a study of the effect and uncertainty associated with the corresponding flavor separation. Estimates of the singlet piece and isospin breaking effects are also required. The overall uncertainty is negligible compared to any upcoming low-energy determination of $\sin^2\theta_W$ in the foreseeable future [21].

The final application of vacuum polarization are heavy quark mass determinations. If one employs as input quantities only the electronic decay widths of the narrow resonances, and compares two different moments of the relevant vacuum polarization function, one obtains simultaneous information on the quark mass and the continuum contribution. The constraint on the latter can then be compared with the experimental determination of electro-production of the open heavy quark. This results in an over-constrained system, where any residual difference can be taken as an error estimate [24] of non-perturbative effects which are supposedly small but possibly not entirely negligible. This strategy has been applied to $\hat{m}_c$ resulting in the precision determination [24], $\hat{m}_c(\hat{m}_c) = 1272 \pm 8 + 2616[\alpha_s(M_Z) - 0.1182]$ MeV, where the central value is in very good agreement with recent lattice results [25] and of comparable precision.

3 Results and conclusions

A simple example to illustrate how global fits constrain physics beyond the SM is the ρ_0 fit, where one assumes that the new physics is mainly affecting the ρ parameter, quantifying the neutral-to-charged current interaction strengths. *E.g.,* any electroweak doublet with a mass splitting, $\Delta m^2 \geq (m_1 - m_2)^2$, contributes to ρ_0 positive definitely. It might appear that there is no decoupling, so that even a doublet with Planck scale masses but electroweak size splitting may give observable effects in experiments at

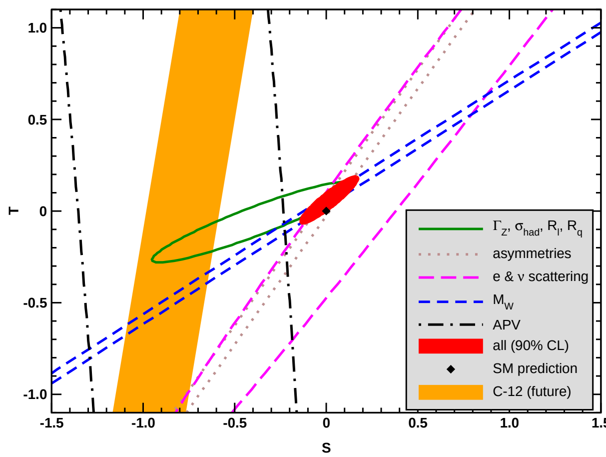

Figure 3: T vs. S *for various data sets. Also shown is the impact that the* ^{12}C *PVES measurement would have if it could be performed with a relative error of* 0.3%*. This yields a different slope in the* ST*-plane.*

much lower energies, but this is not the case, as there is a see-saw type suppression of Δm^2 in any given model. Indeed, the leading contributors to ρ_0 in the SM effective field theory are dimension 6 operators, so that these effects are suppressed by at least two powers of the scale of new physics. The global fit yields [26] $\rho_0 = 1.00039 \pm 0.00019$, which is 2 σ higher than the SM value, $\rho_0 \equiv 1$, and a manifestation of the tension in M_W discussed earlier. It is amusing to point out that at face value, one even finds a non-trivial 95% CL *lower* bound on the sum of all such mass splittings. This strongly disfavors, *e.g.,* zero hypercharge, $Y = 0$, Higgs triplets for which $\rho_0 < 1$. On the other hand, a Higgs triplet with $|Y| = 1$ is consistent with the data provided its vacuum expectation value is around 1% of that of the SM doublet.

Another example is a fit [26] to the S and T parameters [20], $S = 0.02 \pm 0.07$ and $T = 0.06 \pm 0.06$ with a correlation of 81%,. It is illustrated in Fig. 3. $U = 0$ is fixed, as it is generally suppressed by 2 extra factors of the new physics scale [27] compared to S and T. Remarkably, with these 2 extra degrees of freedom, the minimum χ^2 drops by 4.2 units. One can interpret the S and T parameters in a variety of new physics models, if one assumes that non-oblique effects are absent or small. *E.g.,* the mass of the lightest Kaluza-Klein state [28] in warped extra dimensions [29] should satisfy the bound $M_{KK} \gtrsim 3.2$ TeV, while the lightest vector state in minimal composite Higgs models [30] is bound by $M_V \gtrsim 4$ TeV [26].

To conclude, both, the LHC and low-energy measurements are approaching LEP and SLC precision in $\sin^2\theta_W$. There are new players represented by COHERENT [1], Qweak [6], and APV isotope ratios [11], where with the lower precision of these first measurements, it is currently more interesting to assume the validity of the SM, and to use them to constrain neutron skins (the difference of the neutron and proton radii in nuclei), or more generally form factor effects.

Acknowledgements

This work is supported by CONACyT (México) project 252167–F, the German–Mexican research grant SP 778/4–1 (DFG) and 278017 (CONACyT), and by PASPA (DGAPA–UNAM). I gratefully acknowledge the hospitality and support by the Helmholtz-Institute and the THEP group at the Institute of Physics at the JGU Mainz. Finally, I thank Rodolfo Ferro-Hernández for updating Fig. 2, and I am indebted to Werner Bernreuther and Long Chen for a dedicated update and a private communication w.r.t. Ref. [13].

References

1. COHERENT: D. Akimov *et al.*, Science **357**, no. 6356, 1123 (2017).
2. J. Erler, C. J. Horowitz, S. Mantry and P. A. Souder, Ann. Rev. Nucl. Part. Sci. **64**, 269 (2014).
3. SLAC–E158: P. L. Anthony *et al.*, Phys. Rev. Lett. **95**, 081601 (2005).
4. JLab–PVDIS: D. Wang *et al.*, Nature **506**, no. 7486, 67 (2014).
5. SLAC–E122: C. Y. Prescott *et al.*, Phys. Lett. **84B**, 524 (1979).
6. JLab–Qweak: D. Androić *et al.*, Nature **557**, no. 7704, 207 (2018).
7. J. Erler, A. Kurylov and M. J. Ramsey-Musolf, Phys. Rev. D **68**, 016006 (2003).
8. JGU–P2: D. Becker *et al.*, Eur. Phys. J. A **54**, 208 (2018).
9. C. S. Wood *et al.*, Science **275**, 1759 (1997).
10. B. M. Roberts, V. A. Dzuba and V. V. Flambaum, Ann. Rev. Nucl. Part. Sci. **65**, 63 (2015).
11. D. Antypas *et al.*, Phys. Rev. A **100**, no. 1, 012503 (2019).
12. ALEPH, DELPHI, L3, OPAL, SLD and LEP EWWG: S. Schael *et al.*, Phys. Rept. **427**, 257 (2006).
13. W. Bernreuther, L. Chen, O. Dekkers, T. Gehrmann and D. Heisler, JHEP **1701**, 053 (2017).
14. G. Toh *et al.*, arXiv:1905.02768 [physics.atom-ph].
15. CDF and DØ: T. A. Aaltonen *et al.*, Phys. Rev. D **97**, no. 11, 112007 (2018).
16. J. Erler and M. Schott, Prog. Part. Nucl. Phys. **106**, 68 (2019).
17. ALEPH, DELPHI, L3, OPAL and LEP EWWG: S. Schael *et al.*, Phys. Rept. **532**, 119 (2013).
18. CDF and DØ: T. A. Aaltonen *et al.*, Phys. Rev. D **88**, no. 5, 052018 (2013).
19. ATLAS: M. Aaboud *et al.*, Eur. Phys. J. C **78**, no. 2, 110 (2018).
20. M. E. Peskin and T. Takeuchi, Phys. Rev. D **46**, 381 (1992).
21. J. Erler and R. Ferro-Hernández, JHEP **1803**, 196 (2018).
22. J. Erler and M. Luo, Phys. Rev. Lett. **87**, 071804 (2001).
23. A. Gérardin *et al.*, Phys. Rev. D **100**, no. 1, 014510 (2019).
24. J. Erler, P. Masjuan and H. Spiesberger, Eur. Phys. J. C **77**, no. 2, 99 (2017).
25. FLAG: S. Aoki *et al.*, arXiv:1902.08191 [hep-lat].
26. PDG: J. Erler and A. Freitas, in M. Tanabashi *et al.*, Phys. Rev. D **98**, 030001 (2018).
27. B. Grinstein and M. B. Wise, Phys. Lett. B **265**, 326 (1991).
28. M. Carena, E. Ponton, J. Santiago and C. E. M. Wagner, Nucl. Phys. B **759**, 202 (2006).
29. L. Randall and R. Sundrum, Phys. Rev. Lett. **83**, 3370 (1999).
30. A. Pich, I. Rosell and J. J. Sanz-Cillero, JHEP **1401**, 157 (2014).

Frascati Physics Series Vol. 69 (2019)
PHOTON 2019 - International Conference on the Structure and the Interactions of the Photon
June 3-7, 2019

THE MUON g-2 EXPERIMENT AT FERMILAB

Matteo Sorbara* on behalf of the Muon g-2 Collaboration†
Università di Roma "Tor Vergata" and INFN Sezione Roma Tor Vergata

Abstract

The muon anomaly, $a_\mu = \frac{g-2}{2}$, is a low energy observable that can be both measured and computed with high precision. Therefore it provides an important test of the Standard Model (SM) and it is a sensitive probe for new physics. The a_μ value has been measured to a precision of 0.54 ppm by the E821 experiment at the Brookhaven National Laboratory (BNL). This result shows a difference greater than $3\,\sigma$ compared to the SM prediction. In an effort to clarify this discrepancy between experimental measurement and theoretical calculation, the Muon g-2 (E989) experiment at Fermilab aims to reduce the experimental error on a_μ by a factor of four. E989 collected a dataset with the same statistical power of the BNL experiment during the Run 1 data taking (2018). The analysis of data is ongoing and the first result should become available in early 2020. In this paper, I will discuss the experimental setup and report on the status of the Run 1 analysis.

1 Introduction

The muon anomaly $a_\mu = (g-2)_\mu/2$ can be computed and measured with high precision. Therefore it can provide a test for the SM and, any deviation from the predicted value can be hint of new physics. From the theoretical point of view, there is a great effort to reduce the uncertainty in the hadronic contribution (this contribution has the major uncertainty). The latest theoretical value for the anomaly is [1]:

$$a_\mu^{SM} = (11\ 659\ 182.04 \pm 3.56) \times 10^{-10}\ . \tag{1}$$

*matteo.sorbara@roma2.infn.it
†http://muon-g-2.fnal.gov

From the experimental point of view, the world average of a_μ^{exp} is dominated by the measurement at BNL. The current average is [2]

$$a_\mu^{exp} = (11\ 695\ 208.0 \pm 5.4_{stat} \pm 3.3_{syst}) \times 10^{-10}\ . \tag{2}$$

The measured value has a total uncertainty (statistics dominated) of 0.54 *ppm*. The difference with the most recent prediction is:

$$a_\mu^{exp} - a_\mu^{SM} = (25.96 \pm 7.26) \times 10^{-10}\ . \tag{3}$$

This difference corresponds to a 3.7 σ discrepancy from the Standard Model's prediction. If the discrepancy is confirmed, it could be the evidence of new physics processes contributing to the g-2 value. Great effort is coming from the new Muon $g-2$ experiment at Fermilab (E989) to achieve 21 times the statistics of BNL experiment and to reduce the uncertainty by a factor 4 (to 0.14 *ppm*).

1.1 The Measurement

The a_μ measurement is based on the extraction of two frequencies: the anomalous precession frequency of the muon's spin in a magnetic field (ω_a) and the free proton precession frequency (ω_p) related to the magnetic field magnitude. We can define the anomalous precession frequency as the difference between the spin precession frequency and the cyclotron frequency. For relativistic muons, assuming that the magnetic field $\vec{B}$ is uniform and the betatron oscillations of the beam are negligible, the $\vec{\omega}_a$ can be written as:

$$\vec{\omega}_a = \vec{\omega}_s - \vec{\omega}_c = -\frac{q}{m}\left[a_\mu \vec{B} - \left(a_\mu - \frac{1}{\gamma^2 - 1}\right)\frac{\vec{\beta} \times \vec{E}}{c}\right] \tag{4}$$

where $\vec{\beta}$ is the particle speed in units of c, and γ is the Lorentz factor. The term $\vec{\beta} \times \vec{E}$ represents the contribution of the electric field. For the specific value of $\gamma = 29.3$ (i.e. $p_\mu = 3.094\ Gev$), called the *magic momentum*, the electric field term in equation 4 vanishes (corrections due to the momentum spread are considered during data analysis), leaving just the B field term. Precision measurement of ω_a and of the magnetic field leads then to a measure of a_μ:

$$a_\mu = \frac{g_e}{2}\frac{m_\mu}{m_e}\frac{\mu_p}{\mu_e}\frac{\omega_a}{\omega_p}\ , \tag{5}$$

where g_e is the electron's gyromagnetic ratio, m_μ/m_e is the ratio between muon's and electron's masses and μ_e/μ_p is the ratio of proton's and electron's magnetic moment.

2 E989 experiment at FNAL

2.1 The storage ring

The main component of the experiment is a 14 m diameter superconducting storage ring producing a 1.45 T uniform magnetic field recommissioned from the E821 experiment. A highly pure beam of polarized (96%) positive muons produced by FNAL's accelerator chain is injected into the ring via a superconducting inflector magnet. Three fast kicker magnets put the injected muons onto the closed orbit needed for the storage. Electrostatic quadrupoles provide vertical focussing of the beam. The beam is collimated to remove the off-momentum muons.

To ensure the uniformity of the magnetic field, a shimming process was applied to the storage magnet. Figure 2 shows how this process improved the magnetic field uniformity that is kept under ± 25 *ppm* variation.

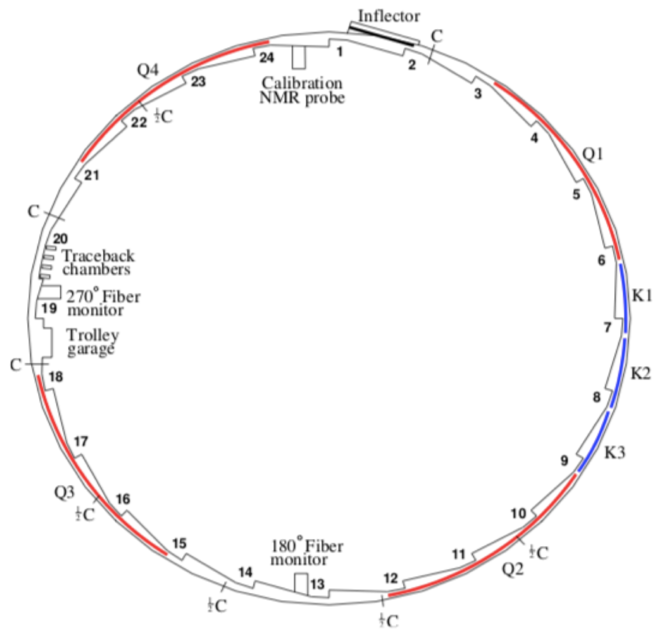

Figure 1: *Schematics of the Muon g-2 storage ring.* Q_{1-4} *represent the electrostatic quadrupoles,* K_{1-3} *are the kickers. Collimators (C), inflector and one tracker station are also shown.*

The field is measured during the run by fixed NMR probes placed around the ring under and over the vacuum chamber. Regular trolley runs are performed: a cylinder equipped with 17 NMR probes is placed inside the vacuum chamber in the muons storing region and moved along all the ring to measure the field magnitude inside the storage region. The total uncertainty related to the field measurement is shown in figure 5b.

The calorimeter system precisely measures the arrival time and the energy of the decay positrons curling into the ring due to the magnetic field. There are 24 calorimeters outside the vacuum chamber along the inner circumference of the ring. Each calorimeter is placed right behind a radial window (figure 3a) that allows positrons to exit the vacuum chamber minimizing the path in air.

A single calorimeter is composed of 54 PbF_2 Čerenkov crystals ($2.5 \times 2.5 \times 14\ cm^3$) arranged in

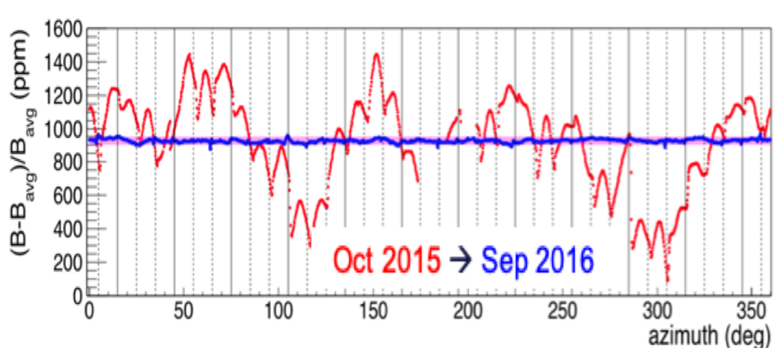

Figure 2: *Magnetic field measurements before and after the shimming. This process improved the field uniformity by reducing the fluctuations.*

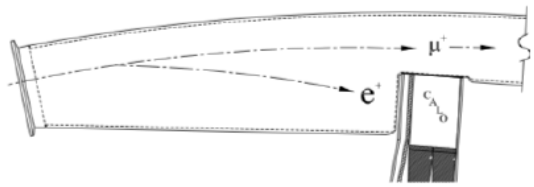

(a) *Calorimeter positioning outside the vacuum chamber.*

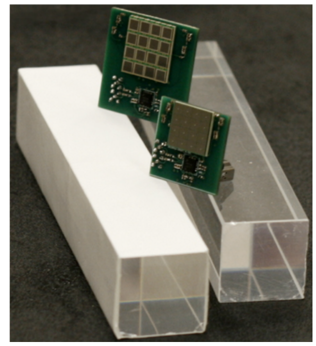

(b) *Lead fluoride crystals with large area SiPMs used to read Čerenkov light.*

Figure 3: *The Muon g-2 calorimeter system.*

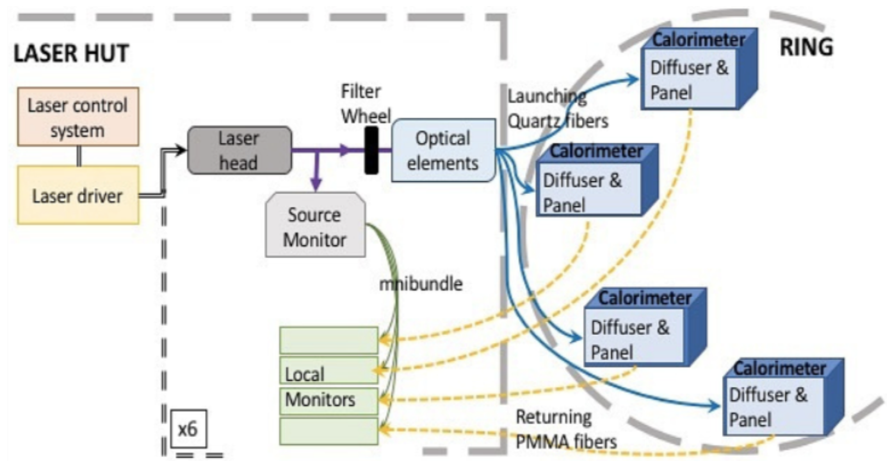

Figure 4: *Laser system scheme. Laser pluses are sent to calorimeters via optical fibers. A source monitor checks the stability of the laser pulse, and a local monitor checks the stability of the distribution system.*

a 9×6 matrix. Lead fluoride has good features for the g-2 measure: high density ($7.77\ g/cm^3$), low Molière radius ($1.8\ cm$ for the Čerenkov light), low radiation length ($X_0 = 0.93\ cm$) and low magnetic susceptibility. Crystals are wrapped in black Tedlar absorbtive wrapping to trasmit only the direct light. The light from each crystal is read by a Large Area Silicon Photomultiplier (SiPM) working in Geiger mode. Each SiPM has an active area of $1.2 \times 1.2\ cm^2$ with $50\ \mu m$ pixels that is well-matched with the crystal area. [3] A laser system, shown in figure 4, is used to keep track of and correct for the gain variation of the SiPMs.

Each laser fires a light pulse with the same wavelength of the Čerenkov radiation emitted by the crystals ($405\ nm$) and the light is evenly distributed to all the crystals. Before the muon injection (fill), on 1 over 10 fills and between fills, laser pulses are sent to the calorimeters and their response is measured. Any variation in the laser intensity is checked with two PIN diodes in the Source Monitor. A third light detector is an 8 mm diameter photomultiplier, used to double check the diodes' stabilities. The PMT stability is checked with a low counts ^{241}Am source. A Local Monitor system measures the light coming back from the calorimeters to correct for variations in the light distribution system. The laser system is measured to be stable at the sub per-mill level in the time period of the measure (700 μs). See ref. [4] and references there in for details. The gain changes in the calorimeter should have a final uncertainty of 20 *ppb*, as shown in figure 5a. [3]

Category	E821 [ppb]	E989 Improvement Plans	Goal [ppb]
Gain changes	120	Better laser calibration	
		low-energy threshold	20
Pileup	80	Low-energy samples recorded	
		calorimeter segmentation	40
Lost muons	90	Better collimation in ring	20
CBO	70	Higher n value (frequency)	
		Better match of beamline to ring	< 30
E and pitch	50	Improved tracker	
		Precise storage ring simulations	30
Total	180	Quadrature sum	70

(a) ω_a *measure.*

Source of uncertainty	2001	E989
Systematics of calibration probes	50	35
Calibration of trolley probes	90	30
Trolley measurements of B_0	50	30
Interpolation with fixed probes	70	30
Uncertainty from muon distribution	30	10
Inflector fringe field uncertainty	–	–
Time dependent external B fields	–	5
Others †	100	30
Total systematic error on ω_p	170	70

(b) ω_p *measure.*

Figure 5: Systematics uncertainty budget for the new E989 experiment. [3]

2.2 ω_a Analysis

The anomalous precession frequency ω_a can be measured due to the parity violating decay of muons. From angular momentum conservation and helicity considerations, there is a strong correlation between the high energy positrons momentum direction and the muon spin. So ω_a can be measured by counting the number of high energy positrons ($E > 1.7\ GeV$) along the muon's momentum axis. The result is the so called "Wiggle Plot" shown in figure 6a): the muon's decay exponential modulated by the anomalous precession frequency.

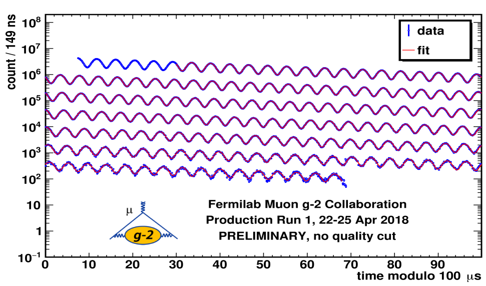

(a) *PRELIMINARY Wiggle plot of the Muon g-2 experiment (E989) using* ~60 *hour data. The curve is fitted with equation 6.*

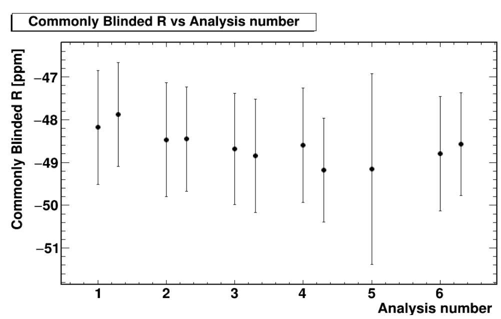

(b) *PRELIMINARY Comparison between* ω_a *results from six different working groups. The uncertainty is statistics dominated and it's* ~ 1.33 *ppm. The value is hardware blinded and the points have still a common offset.*

Figure 6: 60h dataset, part of run 1, analysis.

The equation used for the fit, including corrections is:

$$N(t) = N_0 e^{-\frac{t}{\tau}} \left[1 - A\cos(\omega_a t + \phi)\right] \cdot C(t) \cdot V(t) \cdot \Lambda(t) \tag{6}$$

which includes corrections related to the beam dynamics. $C(t)$ accounts for the time dependent radial CBO effect and $V(t)$ for the vertical waist. $\Lambda(t))$ is the muon loss term. CBO terms are evaluated using a tracking detector. Two tracker stations detect positrons in front of two different calorimeters. The track is used to reconstruct the position of the beam during the fills without affecting the beam itself. From the position of the beam, both CBO and vertical oscillation can be parametrized and used as corrections in the fitting function. The lost muon function is evaluated from triple coincidences in consecutive calorimeters and with the application of energy and timing cuts according to MIP behaviour.

The precession frequency value is both hardware and software blinded to avoid biases. The hardware blinding is done by applying an offset in the range ± 25 ppm to the 40 MHz clock frequency. The offset is common to all the analyses and unknown by the analyzers. In the fit, ω_a is blinded according to:

$$\omega_a = 2\pi \cdot 0.2291\ MHz \cdot [1 - (R - \Delta R) \cdot 10^{-6}] \tag{7}$$

where ΔR is different for each group.

Six different working groups are performing independent analyses to extract the anomalous precession frequency. The final result will be the combination of each group value. Last February, the 60h dataset was analysed and the results from each group were compared after unblinding the software offset. Results are in good agreement showing consistency of the analyses (see fig. 6b). The total uncertainty is ~ 1.33 ppm and it is statistics dominated.

2.3 Conclusions

The new Muon g-2 E989 experiment at Fermilab will provide the measurement of the muon's anomalous magnetic moment with a precision of 0.14 ppm. A precise measurement of the anomalous precession frequency both with a high precision magnetic field measurement will lead to this goal. During Run 1 (2018), the experiment collected almost 1.4 times the positrons collected at the BNL experiment. Recently Run 2 data taking was completed and, after a summer shutdown to improve the system, Run 3 is expected to start in October 2019. A first result with almost the same statistical power as the BNL result is expected in early 2020.

Acknowledgments

This work was supported by the Department of Energy offices of HEP and NP (USA), the National Science Foundation (USA), the Istituto Nazionale di Fisica Nucleare (Italy), the Science and Technology Facilities Council (UK), the Royal Society (UK), the European Union's Horizon 2020 research and innovation programme under the Marie Skłodowska-Curie grant agreements No. 690835 (MUSE), No. 734303 (NEWS), MOST and NSFC (China), MSIP and NRF (Republic of Korea).

References

1. A. Keshavarzi *et al.*, Phys. Rev. D **97** 114025(2018).
2. G. W. Bennet *et al. (Muon g-2 Collaboration)*, Phys. Rev. D **73** 072003 (2006).
3. E989 collaboration, Muon g-2 Technical Design Report, arXiv:1501.06858v2 [physics.ins-det].
4. A. Anastasi *et al.*, arXiv:1906.08432 [physics.ins-det].

Frascati Physics Series Vol. 69 (2019)
PHOTON 2019 - International Conference on the Structure and the Interactions of the Photon
Jun 3-7, 2019

SuperKEKB AND Belle II STATUS, AND PROSPECTS ON TWO-PHOTON PHYSICS

B.Shwartz
Budker Institute of Nuclear Physics,
Novosibirsk State University
Novosibirsk 630090, Russia
on behalf of Belle II collaboration

Abstract

At present experiments with a new Belle II detector at SuperKEKB collider have started at KEK (Japan). These new experiments will continue and widen the studies began at the previous experiments with the Belle detector. The luminosity of the SuperKEKB collider will exceed the previous one by about 40 times, amounting to $8 \times 10^{35}\mathrm{cm}^{-2}\mathrm{s}^{-1}$. The main features of the collider and detector as well as the current status of the SuperKEKB/Belle II project are reported in this talk. Main physics motivations, goals and perspectives of this experiment for two-photon physics are discussed as well.

1 Introduction

Experiments with the Belle detector [1] at the KEKB e^+e^- energy-asymmetric collider [2] were continued from 1999 to 2010. In these experiments which were conducted at the center-of-mass energy around the $\Upsilon(4S)$-meson mass the world highest luminosity, $2.1 \times 10^{34}\mathrm{cm}^{-2}\mathrm{s}^{-1}$, was achieved and total integrated luminosity of about 1 ab^{-1} was collected. The main goal of the Belle experiment, a discovery of the CP-violation (CPV) in B meson decays, was achieved in 2001 [3]. Based on full collected statistics CPV parameters in various channels of B meson decays were measured with high accuracy [4].

Due to high KEKB luminosity and the quality of the Belle detector, in addition to the main task, many other important results were obtained, including precise measurement of the hadronic cross sections in $\gamma\gamma$ and e^+e^- processes. Belle results on two-photon hadron production concentrate mostly on two body processes and about 10 different channels were studied. However, other important results, on π^0 transition form factor (TFF) and study of the charmonium and exotic states, were obtained as well. Recent results on two-photon processes obtained by the Belle are presented by Dr.Wenbiao Yan in his talk at this conference [5]

Recently, first experimental runs were conducted with new detector, Belle II, at the new collider, SuperKEKB. This asymmetric e^+e^- collider ($E^+ = 4$ GeV, $E^- = 7$ GeV) built in the same KEKB tunnel has to achieve the luminosity exceeding the previous one (KEKB) by about 40 times, amounting to $8 \times 10^{35}\mathrm{cm}^{-2}\mathrm{s}^{-1}$. The Belle II is deeply upgraded Belle detector. By now the Belle II collaboration gathered about 900 researchers from 26 countries.

This note describes the current status and perspectives of the SuperKEKB/Belle II project for two-photon physics.

2 Super KEKB collider and the Belle II detector

New SuperKEKB collider is constructed in the KEKB tunnel utilizing many elements of the previous B-factory. However, considerable part of both rings, magnets and beam pipes, were replaced by new ones. Injector for KEKB is upgraded as well. Special damping ring is constructed to produce high intensive positron beams with low emittance.

The Belle II detector contains new vertex detector, central drift chamber and particle identification system. The K_L-meson and muon identification subsystem (KLM) is partially upgraded. The ECL scintillation crystals and mechanical structure of the electromagnetic crystal calorimeter (ECL) is kept unchanged from the previous experiment.

Schematic view of the Belle II detector is presented in Fig. 1.

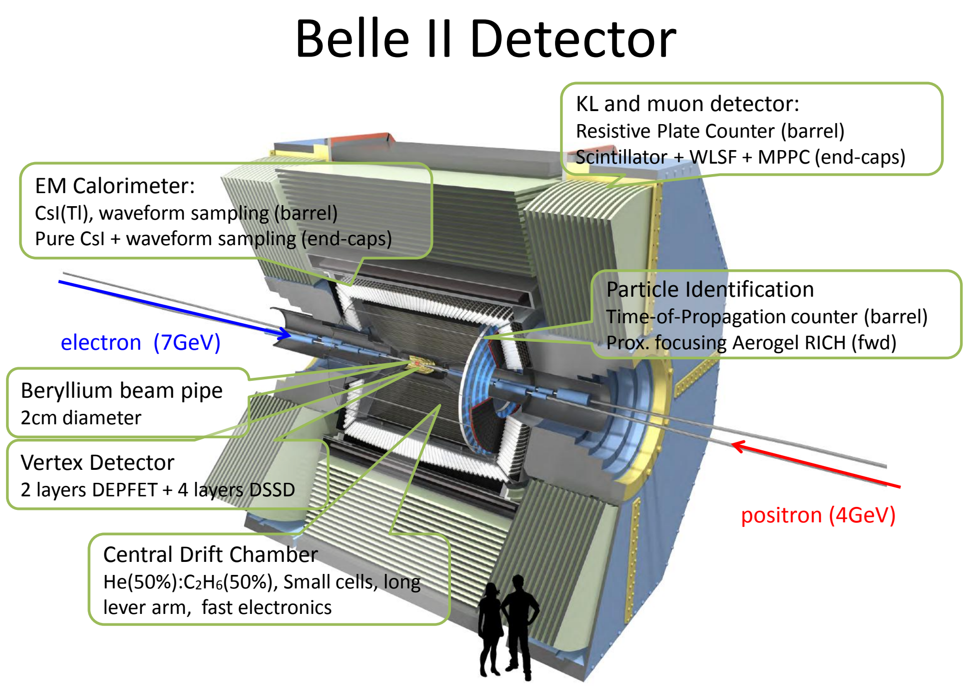

Figure 1: *Schematic view of the Belle II detector.*

The tracking system of the Belle II detector consists of the Vertex Detector (VXD) and the Central Drift Chamber (CDC). The VXD contains the two layer Pixel Detector (PXD) and four layer Silicon Vertex Detector (SVD). The PXD is based on DEPFET technology which allows to produce very thin (down to 50 μm) sensors.

The central drift chamber (CDC) provides track reconstruction and its precise momentum measurement; a measurement of the ionization losses of the charged particles for the identification purposes; a generation of the signals for the trigger system. The momentum resolution of the Belle II with CDC and SVD is $\sigma_{p_t}/p_t = 0.11\% \cdot p_t[\mathrm{GeV/c}] \oplus 0.30\%/\beta$, which it much better than that for the Belle detector. The expected dE/dx resolution is about 5%.

Main charged particle identification (PID) at Belle are based on the Cherenkov ring detection. In the barrel part of the Belle II detector the time-of-propagation (TOP) counters [7] are employed. This system will provide a good pion-kaon separation in the momentum range up to 3.5 GeV/c. Identification of charged particles in the forward endcap region will be performed by the proximity-focusing aerogel ring-imaging Cherenkov detector (ARICH). This system allows to obtain 99% of kaon identification efficiency at 1% of pion misidentification for particles with 4 GeV/c momentum.

The existent CsI(Tl) crystal Electromagnetic Calorimeter (ECL) are planned to be used together with the same PIN photo-diodes, preamplifiers and cables connected them to shapers. The baseline of the upgrade of the ECL is the electronics modification following the general strategy of the Belle upgrade.

A superconducting solenoid providing a magnetic field of 1.5 T as well as an iron yoke will be reused from the Belle detector. The Belle KL&Muon detector (KLM) is integrated with the iron yoke of the magnet. For the Belle II detector the end cap KLM parts as well as two innermost layers of the barrel KLM part are replaced to the system based on the plastic scintillators. Remaining barrel part keeps the RPC system.

Experiments with the Belle II detector started in 2018 by the physics run without final vertex detector. In this run the integrated luminosity of about 0.5 fb^{-1} were collected that allowed to commission the collider and to test all detector subsystems. The physics run with full detector has been performed in March - June of 2019. In this run the collider achieved the luminosity of about 1.1×10^{34} cm^{-2}s^{-1} and about 5 fb^{-1} of integrated luminosity was collected. The data analysis is ongoing. Data taking as well as further collider tuning will continue from October of this year.

3 Study of Two-Photon Physics at Belle II

The Belle II experiment should obtain new valuable results on many processes including two-photon hadronic production due to expected high luminosity as well as considerably improved detector characteristics. The project parameters of the tracking and particle identification at the Belle II are much better than those were at the Belle and BaBar. Thus, we can hope for the drastic improvement of the corresponding contributions to the systematic uncertainties. High data statistics expected at Belle II experiment will provide a possibility of the careful comparison of the simulation and experimental efficiencies and determination of the corresponding corrections which should improve systematics as well. An important issue is much more sophisticated and flexible neutral trigger.

In this note we discuss only two most interesting two-photon studies:

- Transition form factors of π^0, η and $\eta\prime$ mesons via single and double tagged events. These are particularly important for light-by-light contribution to muon (g-2) theoretical calculation;

- Study and search for charmonium and charmonium-like states in the two-photon collisions.

3.1 Study of π^0, η and $\eta\prime$ mesons transition form factors

Precise measurement of the π^0, η and $\eta\prime$ transition form factors provides possibilities to test the theoretical models of light hadrons, in particular, the assumptions about wave functions of these hadrons [8]. These measurements give also an important input for theoretical analysis of the hadronic-light-by-light (HLbL) contribution to the anomalous magnetic moment of the muon $(g-2)$ [9, 10]. It should be noted that this subject is especially interesting since high precision measurements of this value, a_μ, performed at Brookhaven National Laboratory [11] differs from theoretical calculations via the Standard Model [12, 13, 14] by more than 3.5 standard deviations.

The $\pi^0(\eta,\ \eta\prime)$ transition form factor is measured in the process $e^+e^- \to e^+e^-\gamma^*\gamma \to e^+e^-\pi^0$ where γ^* means the virtual photon with high virtuality. Then one of the initial particles, electron or positron, is scattered at large angle into detector that determines the momentum transfer, Q^2, of the virtual photon. This approach is usually referred as "single-tag measurement".

Such measurements were performed by the Belle collaboration [15]. The results of this study is presented in Fig. 2(left) together with data from BaBar [16] and CLEO [17] in comparison with different theoretical models [8]. As seen from the figure the Belle results are consistent with the pQCD prediction

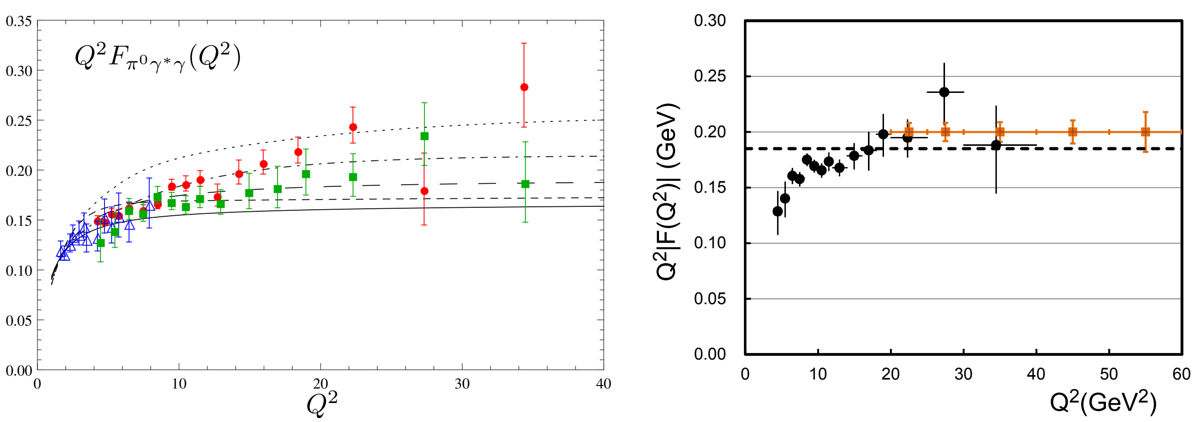

Figure 2: *Left plot: The pion transition form factor measured by Belle [15] (squares), BaBar [16] (circles) and CLEO [17] (open triangles). Lines correspond to various theoretical models [8], solid line presents the pQCD asymptotic. Right plot: Present Belle results on the π^0 transition form factor (black circles) and expectations for Belle II (red squares) at 50 ab^{-1} of collected luminosity. The error bars present the quadratic sum of the statistical and estimated systematic uncertainties. The dashed line is the asymptotic of the TFF.*

while behaviour of the BaBar data is rather different. This discrepance induced large interest of theorists and new precise measurements are certainly desirable.

A single-tag measurement mentioned above implies the events contains one electron (or positron) and two photons from π^0 decay. Unfortunately, events of this type were strongly suppressed by the Belle trigger system which included a special veto signal to prescale the Bhabha events. This decreased the trigger efficiency for studied events to about 10% and considerably enlarged the statistical and systematic uncertainties.

At the Belle II the trigger system was designed taking into account these important measurements and the trigger efficiency should be drastically improved. As a result, we expect by factor from 3 to 5 better precision in the measurement of π^0 TFF as shown in Fig. 2b. TFF of η and $\eta\prime$ mesons will be measured as well.

3.2 New-Charmonium (or XYZ) production

Another important task in the considered field is a study of the production and properties of the charmonium states with a mass above 3.6 GeV like $\eta_c(2S)$, $\chi_{c2}(2P)$ etc. as well as a search for exotic states.

During the last decade in the charmonium mass range about ten new states which cannot be clearly explained by the conventional quark-antiquark structire were discovered. Two of them, $X(3915)$ and $X(4350)$ were observed by Belle in B decays and two-photon processes [18, 19] (see Fig. 3). As can

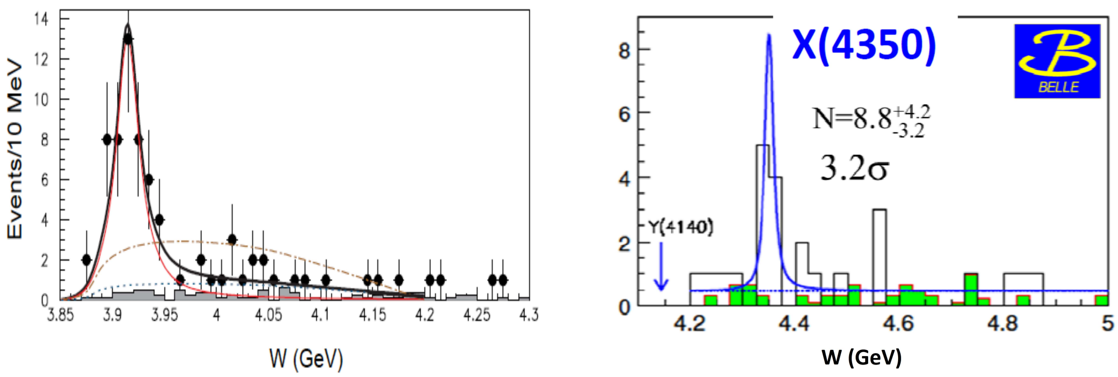

Figure 3: *Distributions over $J/\Psi\omega$ (left) and $J/\Psi\phi$ (right) in $\gamma\gamma$ production* [18, 19].

be seen from the Fig. 3 the statistics is very limited (less than 100 events) and we expect considerable improvement of these studies at Belle II.

Another important study in this field is a search for exotic baryons in $\gamma\gamma \to \overline{p}pK^+K^-$ process. Such a study was performed by Belle [20] resulted in an upper limit on theproduction. This study will be substantially widen with high statistics expected at Belle II.

4 Conclusion

- Last decade demonstrated the fruitfulness and efficiency of the flavor "factory" approach in the particle physics.
- Huge number of results were obtained at the B-factories, but many new questions appeared and the large field of researches will be opened by the super B factory.
- High luminosity to be brought by SuperKEKB/Belle II will make various analyses possible for two-photon physics:
  - Further study of light hadrons production and their characteristics.
  - QCD tests with exclusive processes at high W, at high Q^2, with Single and Double tag.
  - Study of charmonia/XYZ above 3.6 GeV.

References

1. A. Abashian *et al.*, Nucl. Instr. and Meth. A **479**, 117 (2002).
2. S. Kurokawa *et al.*, Nucl. Instr. and Meth. A **499**, 1 (2003).
3. Belle Collab. (A. Abashian *et al.*), Phys. Rev. Lett. **86**, 2509 (2001).
4. I.Adachi et al. (Belle collaboration), Phys. Rev. Lett **108** , 171802 (2012).
5. Wenbiao Yan, Recent results from two-photon processes at Belle, talk at this conference
6. T. Abe *et al.*, Belle II technical design report, KEK Report 2010-1 (2010).
7. K. Inami *et al.*, Nucl. Instr. and Meth. A **595**, 96 (2008).
8. G.P. Lepage and S.J. Brodsky, Phys. Lett. B **87**, 359 (1979);
   V.L. Chernyak and I.R. Zhitnitsky, Nucl. Phys., B **345**, 137 (1990);
   S.V. Mikhailov *et al.*, Phys. Rev. D **93**, 114018 (2016).
9. E. Kou *et al.*, The Belle II Physics Book, KEK Preprint 2018-27 (2018), arXiv:1808.10567 [hep-ex].
10. G. Colangelo *et al.*, JHEP **09**, 91 (2014), arXiv:1402.7081;
    G. Colangelo *et al.*, JHEP **04**, 161 (2017), arXiv:1702.07347.
11. G.W. Bennett *et al.*, Phys. Rev. D **73**, 072003 (2006).
12. C. Bouchiat and L. Michel, J. Phys. Radium **22** 121 (1961).
13. M. Gourdin and E. de Rafael, Nucl. Phys. B **10**, 667 (1969).
14. T. Teubner *et al.*, arXiv:1001.5401 (2010).
15. S. Uehara *et al.*, Phys. Rev. D **86**, 092007 (2012), arXiv:1205.3249.
16. B. Aubert *et al.*, Phys. Rev. D **80**, 052002 (2009), arXiv:0905.4778.
17. J. Gronberg *et al.*, Phys. Rev. D 57, 33-54 (1998), arXiv:hep-ex/9707031.
18. S. Uehara *et al.* (Belle Collaboration), Phys. Rev. Lett. 104, 092001 (2010).
19. PRL 104, 112004 (2010) C.P. Shen *et al.* (The Belle Collaboration) Phys. Rev. Lett. **104**, 112004 (2010).
20. C.P. Shen *et al.* (Belle Collaboration), Phys. Rev. D **93**, 112017 (2016).

Frascati Physics Series Vol. 69 (2019)
PHOTON 2019 - International Conference on the Structure and the Interactions of the Photon
Jun 3-7, 2019

GAMMA-GAMMA COLLIDER WITH $W_{\gamma\gamma} \leq 12$ GEV BASED ON EUROPEAN XFEL

V.I. Telnov
Budker Institute of Nuclear Physics, Novosibirsk, Russia
Novosibirsk State University, Novosibirsk, Russia

Abstract

Using Compton scattering of 0.5 μm laser photons on existing 17.5 GeV electron beams from European XFEL one can obtain a $\gamma\gamma$ collider with $W_{\gamma\gamma} \leq 12$ GeV. Such a collider will be a nice place for application of modern technologies: powerful lasers, optical cavities, superconducting linacs and low-emittance electron sources. Physics program: spectroscopy of $C = +$ resonances in various J^P states ($b\bar{b}$, four quark states, quark molecules and other exotica). Variable circular and linear polarizations will help to determine quantum numbers and to measure separately polarization components of the $\gamma\gamma$ cross section ($\sigma_\perp, \sigma_\parallel, \sigma_0, \sigma_2$).

1 Introduction

Gamma-gamma collisions have already long history. Since 1970 two-photon processes were studies at e^+e^- storage rings in collisions of virtual photons (γ^*). Physics here is interesting and complementary to that in e^+e^-, but not competitive because the number of virtual photons per one electron is rather small: $dn_\gamma \sim 0.03\, d\omega/\omega$, therefore $L_{\gamma\gamma} \ll L_{e^+e^-}$.

At future e^+e^- linear colliders beams are used only once which makes possible $e \to \gamma$ conversion using Compton back scattering of laser light just before the interaction point and thus obtaining $\gamma\gamma$,γe collider (or the photon collider) with a luminosity comparable with that in e^+e^- collisions. [1, 2] The maximum energy of scattered photons

$$\omega_m = \frac{x}{x+1}E_0; \quad x \approx \frac{4E_0\omega_0}{m^2c^4} \simeq 15.3 \left[\frac{E_0}{\mathrm{TeV}}\right] \left[\frac{\omega_0}{\mathrm{eV}}\right] = 19 \left[\frac{E_0}{\mathrm{TeV}}\right] \left[\frac{\mu\mathrm{m}}{\lambda}\right]. \tag{1}$$

For example: $E_0 = 250$ GeV, $\omega_0 = 1.17$ eV ($\lambda = 1.06\ \mu m$) $\Rightarrow x = 4.5$ and $\omega_m/E_0 = 0.82$. So, most powerful solid-state lasers with $1\,\mu$m wavelength are perfectly suited for e^+e^- linear colliders with the energies $2E_0$ =100–1000 GeV, which are actively developed since 1980s (VLEPP, NLC, JLC, TESLA-ILC, CLIC). For the $\gamma\gamma$ collider one needs lasers with ps duration, several Joules flash energy and the pulse structure similar to that of a basic e^-e^- collider. Modern laser technology allows to build the required laser system, though it is not easy.

Since the late 1980s $\gamma\gamma$ colliders are considered as a natural part of all linear collider projects, conceptual [4, 6, 5] and pre-technical designs [7, 8] have been published. Just after the Higgs discovery the photon collider was considered as one of Higgs factory options, [9, 10] a dozen variants of $\gamma\gamma$ Higgs factories were proposed beside those based on ILC and CLIC. The photon collider is attractive because it does not need positrons and the energy required to produce the Higgs is somewhat lower that in e^+e^- collisions. However, e^+e^- colliders are better for the Higgs study due to the unique reaction $e^+e^- \to$ ZH which allows to detect almost all Higgs decays, even invisible (by missing mass).

If the linear collider (ILC or CLIC) is ever built, at first it will work in the e^+e^- mode, so the photon collider can appear only in 3–4 decades. Such perspective cannot inspire people who want to do something interesting already now.

In April 2017, Chinese physicists organized ICFA Mini-Workshop on Future $\gamma\gamma$ Collider with invitation of world experts in particle, laser and accelerators physics to discuss what can be made reasonable in this direction. In my review talk, I have proposed to construct a photon collider based on electron linacs of existing (or future) free electron lasers. [11] The first candidate is the European XFEL with 17.5 GeV electron beams which is in operation since 2017. Using 0.5 μm laser one can obtain compliment it with a photon collider on the energy $W_{\gamma\gamma} \leq 12$ GeV. The region $W_{\gamma\gamma} < 4$–5 GeV can be studied at e^+e^- Super B-factory (in $\gamma^*\gamma^*$ collisions), but in the region $W_{\gamma\gamma} = 5$–12 GeV the photon collider has no competitors. Possible circular and linear polarizations make such photon collider an unique machine for the study of $\gamma\gamma$ physics in the $b\bar{b}$ energy region with many new states, including exotic. Beside the Mini-Workshop in China [11] this suggestion was reported at several recent conferences-workshops, [12, 13] the present paper is the first one on this subject.

2 Possible parameters of $\gamma\gamma$ collider based on European XFEL

The European XFEL has the following parameters of electron beams: [14] beam energy $E_0 = 17.5$ GeV, the number of particles in the bunch $N = 0.62\cdot 10^{10}$ (1 nC), the bunch length $\sigma_z = 25$ μm, the normalized transverse emittance $\epsilon_n = 1.4$ mm·mrad, the bunch rate 27 kHz (trains 10 Hz, 2700 bunches in one train, about 100 m between bunches in the train). To obtain the photon collider, the electron beams from the XFEL should be sequentially deflected into two arches with a radius of about 100 m and then converted by lasers to high-energy photons just before the interaction point.

The general scheme of the photon collider is shown in Fig. 1. Laser photons scatter on electrons at the distance $b \sim \gamma\sigma_y$ which is about 2 mm for the considered project. Increasing of $\rho = b/\gamma\sigma_y$ leads to some degree of monochromatization and suppression of low energy collisions. After crossing the conversion region, electrons have a broad energy spectrum and large disruption angles due to deflection of low-energy electrons in the field of the opposing beam. The "crab crossing" scheme of collisions solves the problem of the beam removal without hitting final quads.

In order to have the energy of Compton scattered photons close to the electron energy the parameter x should be optimally somewhat below $x = 4.8$ (when $\omega_m = 0.82E_0$) or $\lambda = 4.2E_0[\mathrm{TeV}]$ μm. [7] It is $\lambda \approx 0.074$ μm for $E_0 = 17.5$ GeV. In this case the maximum $W_{\gamma\gamma}$ would be $35 * 0.8 = 28$ GeV. We do not consider such ultimate case because 1) such a short wavelength laser system with the required peak (TW) and average (100 kW) power is technically unfeasible and 2) there is no interesting physics in the region

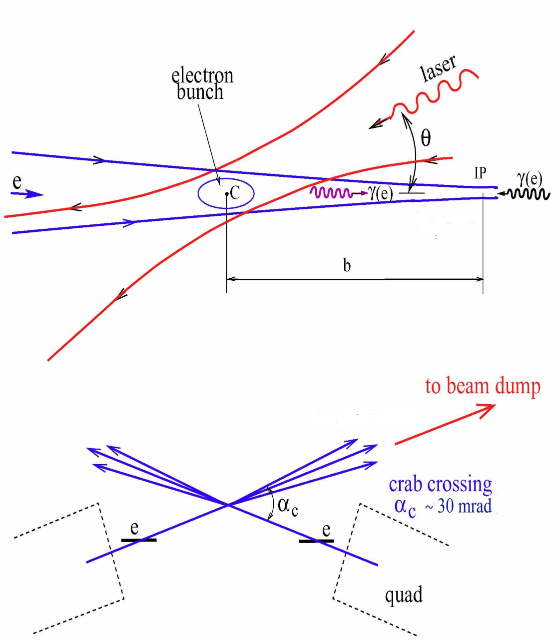

Figure 1: *(top)* The general scheme of a $\gamma\gamma$ γe photon collider. *(below)* A crab-crossing collision scheme for the removal of disrupted beams from the detector to the beam dump.

$W_{\gamma\gamma} = 12$–28 GeV. In our consideration we assume the laser wavelength $\lambda = 0.5$ μm, having in mind the laser system with an external optical cavity like at the ILC photon collider, [8] pumped by a frequency doubled 1 μm laser. In this case the parameter $x = 0.65$ and the ratio $\omega_m/E_0 = x/(x+1) \approx 0.394$. The laser intensity in the conversion region is limited by nonlinear effects in Compton scattering, described by the parameter ξ^2 (see ref. [7]). We assume $\xi^2 = 0.05$, which reduces ω_m/E_0 by 3%, down to 0.38. In this case $W_{\gamma\gamma,\max} = 13.3$ GeV (peak at 12 GeV), that covers the region with b-quark resonances.

In calculation of an the optimal pulse duration and flash energy we assume the laser system similar to that at the ILC based $\gamma\gamma$ collider (optical resonator, laser mirrors outside electron beams). [8] The required flash energy is smaller than in the ILC case by a factor of 3 due to larger Compton cross section at smaller x.

One of serious problems at $\gamma\gamma$ colliders is removal of used beams which are disrupted by the opposing electron beam. The disruption angle is proportional to $\sqrt{N/\sigma_z}$. In order to keep disruption angles acceptable we assume the electron bunch length longer than at XFEL, 70 μm instead of 25 μm.

Simulation of processes at the interaction and collision points was done by my code used since 1995 for simulation of photon colliders at the NLC, CLIC, TESLA-ILC. [7] We consider both unpolarized electron beams (existed at the XFEL) and 80% longitudinally polarized (here low emittances is a problem to be solved). The laser beam is circularly polarized, $P_c = \pm 1$ (when circularly polarized high energy photons are needed). Collisions of linearly polarized photons is also interesting for physics, for that linearly polarized laser beams should be used. The degree of polarization in the high energy part of spectrum is almost 100% for circular polarization and about 85% for linear polarization (in the considered case of $x = 0.65$).

The $\gamma\gamma$ luminosity spectra for non-polarized and longitudinally polarized electrons are shown in Fig. 2. Spectra are decomposed to the states with total helicity of the colliding photons $J_z = 0$ or 2. The total luminosity is the sum of the two spectra. The luminosities with the cut on the relative longitudinal momentum of produced systems are also shown. This cut suppress boosted collisions of Compton and beamstrahlung photons with very different energies. Luminosity distributions similar to those in Fig. 2 but for various distances between the conversion and interaction points are shown in Fig. 3. One can see that with the increase of ρ the luminosity spectra become more cleaner and energetic at at the cost of some reduction in luminosity. Resulting parameters of the photon collider are given in Table 1.

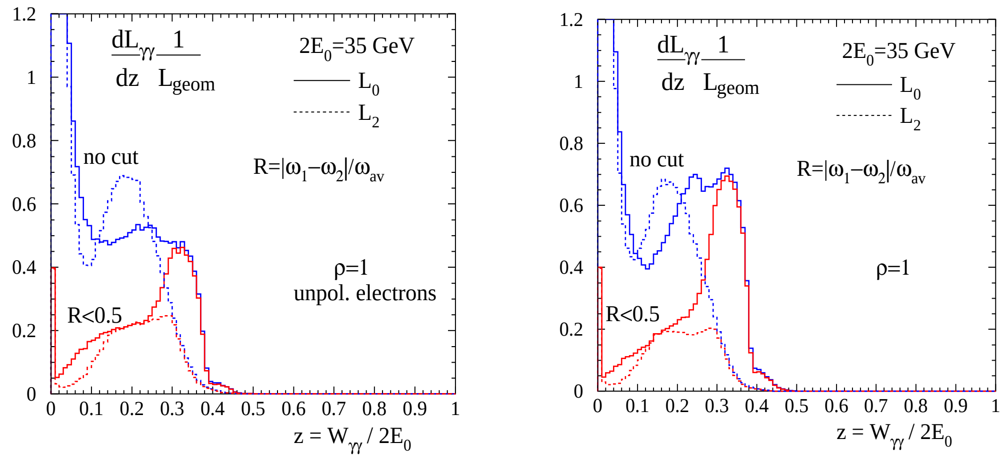

Figure 2: $\gamma\gamma$ luminosity distributions. Left: unpolarized electrons; right: longitudinal electron polarization $2\lambda_e = 0.8$ (80%). In both cases laser photons are circularly polarized, $P_c = -1$. Solid lines for J_z of two colliding photons equal to 0, dotted lines for $J_z = 2$. Red curves are luminosities with the cut on longitudinal momentum.

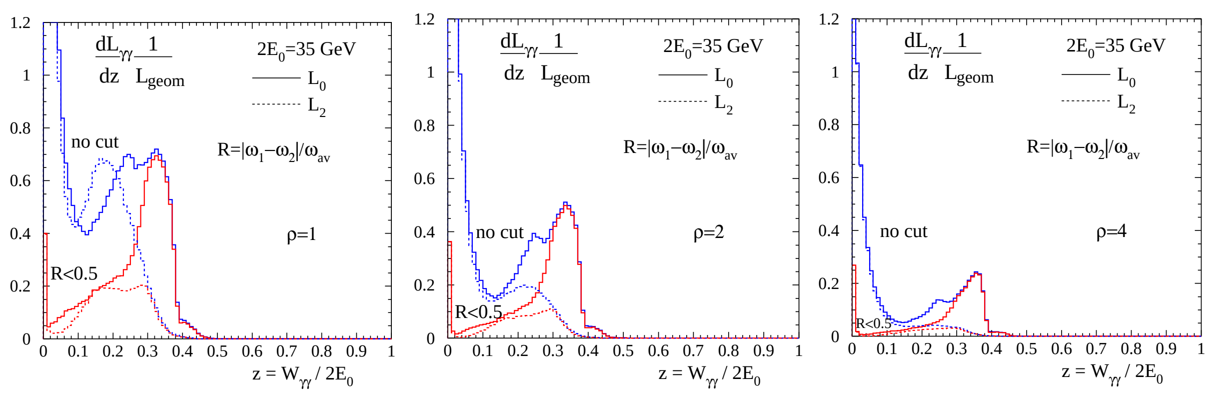

Figure 3: $\gamma\gamma$ luminosity distributions on invariant mass $W_{\gamma\gamma}$ for various distances b between conversion and interaction points (characterized by the parameter $\rho = b/(\gamma\sigma_y)$. See other explanations in Fig. 2.

3 Physics at a 0.1-12 GeV photon collider

A photon, like an electron, is a point-like particle participating in electromagnetic interactions. The cross section for a lepton pair production in $\gamma\gamma$ collisions is $\sigma_{\gamma\gamma} \approx (q/e)^4/W_{\gamma\gamma}^2[\,\mathrm{GeV}^2] \cdot 10^{-30}$ cm^2 for $W_{\gamma\gamma} \gg mc^2$ and $|cos\theta| < 0.9$ while in e^+e^- collisions $\sigma_{e^+e^-} \approx 0.085(q/e)^2/W_{e^+e^-}^2[\,\mathrm{GeV}^2] \cdot 10^{-30}$ cm^2.

Beside, photons spends some time in the form of virtual lepton pairs, quark pairs (or vector mesons) and behaves in $\gamma\gamma$ collisions as a hadron. The cross section $\sigma(\gamma\gamma \to hadrons)$ =(0.4–0.6)$\cdot 10^{-30}$ cm^2 (at

Table 1: Parameters of the photon collider.

$2E_0$	GeV	35
N per bunch	10^{10}	0.62
Coll. rate	kHz	15
σ_z	μm	70
$\epsilon_{x,n}/\epsilon_{y,n}$	mm-mrad	1.4/1.4
β_x/β_y at IP	μm	70
σ_x/σ_y at IP	nm	53/53
Laser λ	μm	0.5
Parameters x and ξ^2		0.65, 0.05
Laser flash energy	J	3
Laser pulse duration	ps	2
f# of laser system		27
Crossing angle	mrad	~ 30
b,(CP-IP distance)	mm	1.8
$L_{\mathrm{ee,geom}}$	$10^{33}\,\mathrm{cm}^{-2}\mathrm{s}^{-1}$	1.6
$L_{\gamma\gamma}(z > 0.5 z_m)$	$10^{33}\,\mathrm{cm}^{-2}\mathrm{s}^{-1}$	0.21
$W_{\gamma\gamma}$(peak)	GeV	12

$W_{\gamma\gamma} > 1\,\mathrm{GeV}$) does not decrease with the energy and exceeds the point like quark pair production cross section.

A nice feature of both e^+e^- and $\gamma\gamma$ collisions is a single resonance production of hadrons. In e^+e^- these resonances have the photon quantum numbers: $J^{PC} = 1^{--}$, that are $\ldots J/\Psi, \Upsilon \ldots$. Two real photons can produce $C = +$ resonances with the following states: [16] $J^P = 0^+, 0^-, 2^+, 2^-, 3^+, 4^+, 4^-, 5^+ \ldots$ ($\pi^0, \eta \ldots, H-$boson), forbidden numbers are $J^P = 1^{\pm}$ and (odd $J)^-$. So, the $\gamma\gamma$ collider presents much richer possibility for study of hadronic resonances.

Cross sections of resonance production in $\gamma\gamma$ collisions depend on the total helicity of two photons $J_z = 0$ or 2. If C and P-parities conserve, then resonances are produced only in certain helicity states: [16] $J_z = 0$ for $J^P = 0^{\pm}$, (even $J)^-$; $J_z = 2$ for (odd$J \neq 1)^+$; $J_z = 0$ or 2 for J^P=(even $J)^+$. The value of J_z is set in the experiment by varying the laser photon helicities (and the longitudinal electron beam polarization, if it is not zero).

Photon polarization is characterized by the photon helicity λ_γ, the linear polarization l_γ and the direction of the linear polarization. Any $\gamma\gamma$ process is described by 16 cross sections, but only three most important which do not vanish after averaging over spin states and azimuthal angles of final particles [3, 15], that are $\sigma^{np} = 0.5(\sigma_\parallel + \sigma_\perp) = 0.5(\sigma_0 + \sigma_2); \tau^c = 0.5(\sigma_0 - \sigma_2); \tau^l = 0.5(\sigma_\parallel - \sigma_\perp)$.

The number of events

$$d\dot{N} = dL_{\gamma\gamma}(d\sigma^{np} + \lambda_\gamma \tilde{\lambda}_\gamma \, d\tau^c + l_\gamma \tilde{l}_\gamma \cos 2\Delta\phi \, d\tau^l) \,, \tag{2}$$

where the tilde sign marks the second colliding beam, $\Delta\phi$ is the angle between directions of linear polarizations of colliding photons. For example, for $J = 0$ resonance always $\sigma_2 = 0$, while $\sigma_\parallel$ and $\sigma_\perp$ depend on CP-parity: for $CP = 1$ $\sigma_\parallel = \sigma_0$, $\sigma_\perp = 0$, for $CP = -1$ resonances $\sigma_\parallel = 0$, $\sigma_\perp = \sigma_0$. The cross section in this case

$$\sigma \propto 1 + CP \cdot l_{\gamma,1} l_{\gamma,2} \cos 2\Delta\phi. \tag{3}$$

Scalar particles are produced when photon lineaar polarizations are parallel, while pseudoscalar scalars are produced when polarization are perpendicular. So, the circular and linear photon polarizations help a lot for J^P determination and allow to measure all important polarization components of $\gamma\gamma$ cross sections.

Photon colliders have broad luminosity spectra with complicated polarization properties. All this characteristics can be measured and calibrated experimentally using QED processes with known cross section. [7, 15]

At $\gamma\gamma$ collider in $W < 12$ GeV, (u, d, s, c, b-quarks energy region), a high degree of circular and linear polarizations of scattered photons is available. It is determined mainly by the polarization of the laser. Longitudinal polarization of electrons (there are sources with 85% polarization) is desirable to enhance photon helicities and make larger ratio L_0/L_2 (or opposite), see Fig. 2.

Observation of $\gamma\gamma$ resonances is one of most interesting task for the $\gamma\gamma$ collider. The cross section for a resonance production is proportional to its partial width $\Gamma_{\gamma\gamma}$, which says a lot about its structure and nature. Most of observed $\gamma\gamma$ resonances are $q\bar{q}$ states, there are also several candidates for 4-quark states. Glueballs, composed from two gluons, are predicted but not observed yet.

Particles with $C = +$ are observed at e^+e^- colliders in decays of other heavier particles ($J/\Psi, \Upsilon$ and their excited states. Decay branchings are not small only in decays of narrow states. $J/\Psi(\Upsilon)$ excited states with masses above $D\bar{D}(B\bar{B})$ thresholds are broad therefore their branching to $C = +$ states are very small. Photon collider allows not only to observe directly $C = +$ states but also simultaneously to measure their $\Gamma_{\gamma\gamma}$.

One example. The $\eta_b(9398)$ $C = +$ state was observed at B-factories in radiative decay of $\Upsilon(1S)$, but its $\Gamma_{\gamma\gamma}$ width is unknown yet because its expected branching to $\gamma\gamma$ is less then 10^{-4}. At the photon collider the production rate of a resonance with $J = 0$ is

$$\dot{N} = \frac{dL_{\gamma\gamma}}{dW_{\gamma\gamma}} \frac{4\pi^2\Gamma_{\gamma\gamma}(1+\lambda_1\lambda_2)(\hbar c)^2}{(Mc^2)^2} \approx 8\cdot 10^{-27}\frac{\Gamma_{\gamma\gamma}L_{ee}}{E_0M^2[\,\mathrm{GeV}^2]}, \tag{4}$$

where we put $(dL_{\gamma\gamma}/dW_{\gamma\gamma})(2E_0/L_{ee}) \approx 0.5$ (see Fig. 2 for unpolarized electrons), photon helicities $\lambda_{1,2} = 1$. For $E_0 = 17.5$ GeV, $\Gamma_{\gamma\gamma}(\eta_b) = 0.5$ keV, $M_{\eta_b} = 9.4$ GeV, $L_{ee} = 1.6\cdot 10^{33}$ cm^{-2}s^{-1} and $t = 10^7$ s we get 40000 events. Electron polarization increase the production rate by factor of 1.5.

The collider LEP-2 had enough energy to produce η_b in $\gamma^*\gamma^*$ collisions but it was not observed because the production rate at $L_{e^+e^-}$(LEP-2) $= 10^{32}$ cm^{-2}s^{-1} was about 700 times lower than at considered $\gamma\gamma$ collider. In order to have the same production rate of $\gamma\gamma$ states in central region at e^+e^- collider with $2E_0 \sim 100$ GeV its luminosity should be approximately $L_{e^+e^-} \sim 10^{35}$ or 70 times higher than the geometric luminosity $L_{ee} \sim 1.6\cdot 10^{33}$ at the $\gamma\gamma$ collider.

Observation of single $C = +$ resonances in $\gamma\gamma$ collisions needs detection of all final particles that can be checked by requiring the total transverse momentum to be near to zero. These events will be central with more or less isotropic distribution of particles. The non-resonance hadronic background is large but can be suppressed using a cut on $\sum|p_{i,\perp}|$ and particle identification (b, c-quark tagging). Note, at the photon collider only the high energy part of the luminosity spectra has good polarization properties. In order use these good properties in a whole energy region one has to do an energy scan by changing the electron beam energy.

4 Conclusion

Photon colliders are very cost effective additions for e^+e^- linear colliders. However perspectives of the high energy linear colliderss are unclear already many decades. It makes sense to build a photon collider on smaller energy, $W_{\gamma\gamma} < 12$ GeV (b,c regions). The $\gamma\gamma$ physics here is very rich. The required linac already exist, it is SC linac of European XFEL with the energy 17.5 GeV. The photon collider can use electron beams after XFEL which now are sent to the beamdump (though for some experiments time sharing will be desirable). Such $\gamma\gamma$ collider will be a nice place for application of modern outstanding accelerator and laser technologies. It does not need positrons and damping rings. The required laser system is identical to that needed for the photon collider at the ILC. One can not promise some breakthrough discoveries at this collider (this applies to other projects as well), but there are many arguments (scientific, technical, financial and social) in favor of such collider of a new type.

References

1. I. F. Ginzburg, G. L. Kotkin, V. G. Serbo, and V. I. Telnov, Pizma ZhETF, 34 (1981) 514; JETP Lett. 34 (1982) 491.
2. I. F. Ginzburg, G. L. Kotkin, V. G. Serbo and V. I. Telnov, *Nucl. Instrum. Meth.* **205** (1983) 47.
3. I.F. Ginzburg, G.L. Kotkin, S.L. Panfil, V.G. Serbo, and V.I. Telnov. Nucl. Inst. Meth., **A219**, 5 (1984). *Nucl. Instrum. Meth.* **A 219** (1984) 5.
4. The NLC Design Group, *Zeroth-Order Design Report for the NLC*, SLAC-474, SLAC, 1996.
5. R. Brinkmann et al, Nucl. Instr. Meth., **A406**, 13 (1998), hep-ex/9707017.
6. N. Akasaka et al, JLC Design Study, KEK-REPORT-97-1;
   I. Watanabe, et al, KEK-REPORT-97-17.
7. B. Badelek *et al. Int. J. Mod. Phys. A*, **19** (2004) 5097, [hep-ex/0108012].
8. V. I. Telnov, *Acta Phys. Polon. B* **37** (2006) 1049, [physics/0604108].
9. V. I. Telnov, PoS IHEP **-LHC-2012** (2012) 018, arXiv:1307.3893 [physics.acc-ph]
10. V. I. Telnov, JINST **9** (2014) no.09, C09020, arXiv:1409.5563 [physics.acc-ph].
11. V.I. Telnov, talk at ICFA Mini-Workshop on Future $\gamma\gamma$ Collider, Tsinghua Univ, Beijing, April 2017.
12. V.I. Telnov, talk at PHOTON 2017, CERN, May 22, 2017.
13. V.I. Telnov, talk at the Intern. conf. Probing strong-field QED in electron-photon interactions, 21-23 August 2018, DESY, Hamburg.
14. M. Altarelli et.al.,The European X-tay Free-Electron Laser, Technical design report, DESY=2006-097, July 2007.
15. A.V. Pak, D.V. Pavluchenko, S.S. Petrosyan, V.G. Serbo and V.I. Telnov, Nucl. Phys. Proc. Suppl.**126** (2004) 379, hep-ex/0301037.
16. V.B. Berestetskii, E.M. Lifshitz, and L.P. Pitaevskii. Quantum electrodynamics. Pergamon Press, Oxford, 1982.

Frascati Physics Series Vol. 69 (2019)
PHOTON 2019 - International Conference on the Structure and the Interactions of the Photon
Jun 3-7, 2019

THE PADME EXPERIMENT AT LNF

Clara Taruggi
Dipartimento di fisica, Università di Roma Tor Vergata - Roma, Italy
INFN, Laboratori Nazionali di Frascati - Frascati (RM), Italy

Abstract

Among the theoretical models addressing the dark matter problem, the category based on a secluded sector is attracting increasing interest. The PADME experiment, at the Laboratori Nazionali di Frascati (LNF) of INFN, is designed to be sensitive to the production of a low mass gauge boson A' of a new $U(1)$ symmetry holding for dark particles. This 'dark photon' is weakly coupled to the photon of the Standard Model, and it provides an experimental signature for one of the simplest implementations of the dark sector paradigm. The DAΦNE Beam-Test Facility of LNF provides a high intensity, mono-energetic positron beam impacting on a low Z target. The PADME detectors are designed to measure with high precision the momentum of a photon, produced along with A' boson in e^+e^- annihilation in the target, thus allowing to measure the A' mass as the missing mass in the final state. This technique, particularly useful in case of invisible decays of the A' boson, is adopted for the first time in a fixed target experiment. Simulation studies predict a sensitivity on the interaction strength (ϵ^2 parameter) down to 10^6, in the mass region 1 MeV $< M_{A'} <$ 22.5 MeV, for one year of data taking with a 550 MeV beam. In Winter 2018-2019 the first run took place, providing useful data to study the detector performance, along with the beam and background conditions. Intense activity is taking place to deliver preliminary results on the PADME data quality. This talk will review the status of the experiment and the prospects.

1 Introduction

The observation of cosmological phenomena (e.g., gravitational lensing or anisotropies in the Cosmic Microwave Background) suggests the existence of a new kind of matter, which interacts at least gravitationally with particles of the Standard Model (SM). In the last decades, many experiments tried to detect this kind of matter, commonly known as Dark Matter (DM). The extremely difficult detection of DM could be explained if SM particles and DM particles would live in two separate sectors, connected by a portal. The simplest model for this theory introduces a $U(1)$ symmetry, acting as a portal, between these two sectors [1]. The vector boson mediator of this interaction could be massive, and is called dark photon (marked as A'), in analogy with SM photon. We can think three main ways to produce a dark photon using electron and/or positron interactions:

1. annihilation $e^+e^- \to \gamma A'$
2. Bremsstrahlung $e^{+,-}N \to e^{+,-}A'$
3. meson decay (in which mesons are produced by e$^+$, e$^-$ interactions) $\pi^0, \eta, ... \to \gamma A'$

Dark photon decay depends on DM mass properties. If only DM particles with $m_{DM} > m_{A'}/2$ exist (where m_{DM} is DM mass and $m_{A'}$ is dark photon mass respectevely), then dark photon will decay in SM particles (visible decay). Otherwise, if $m_{DM} \leq m_{A'}/2$, dark photon will predominantly decay in DM particles (invisible decay).

2 The PADME experiment

2.1 The experimental technique

The PADME experiment [2], [3] will search for a dark photon exploiting the annihilation $e^+e^- \to \gamma A'$ of a positron beam on a target making the hypothesis of invisible decay channels of A'. If the positron beam energy is known and target is at rest, the detection of the SM photon in the final state allows to close the kinematic of the process, and to search for the dark photon as a peak in the missing mass distribution:

$$m^2_{miss} = (P_{e^+} + P_{e^-} - P_\gamma)^2 \tag{1}$$

with P_i 4-momentum of the positron, the electron and the SM photon, depending on the index.

The only assumption the experiment makes is that A' couples to leptons. Since the invisible decay of A' is considered, no restrictions on the decay time of A' are needed: the signature of the experiment is a single photon in the electromagnetic calorimeter. Moreover, the experiment can set new limits on the coupling for any kind of particles that can be produced in e$^+$e$^-$ annihilations.

2.2 Description of the detector

PADME is installed at the Beam Test Facility of the Laboratori Nazionali di Frascati [4]. The experiment (see fig. 1 for a scheme of the detector) is using a 550 MeV positron beam (20k e$^+$ per bunch, 200 ns duration, 49 Hz), which allows to reach dark photon masses up to 22.5 MeV. The beam hits an active diamond target where the annihilation process takes place. The target is made of a 20×20×0.1 mm^3 policrystalline diamond: 16 x graphitic strips on one side, and 16 y graphitic strips on the other provide information about beam position and multiplicity [5]. The low Z of carbon and the small thickness (100 μm) of the target minimize multiple scattering and background from Bremsstrahlung.
After the interaction point, a magnetic field (∼0.5 T) in a vacuum chamber (10^{-6} bar) bends positrons and electrons towards the charged particles veto system of the experiment. The system consists of three veto stations, each made of 1.1×1×17.8 mm^3 plastic scintillating bars coupled to optical fibers and SiPMs [6]. 90 bars are placed on the left side (beam point of view) of the vacuum chamber and work as positrons veto (PVeto), while 90 bars are place on the right side, working as electrons veto (EVeto). 16 bars are placed to the left side of the calorimeters, working as high energy positrons veto (HEPVeto).

Photons fly unhindered to the Electromagnetic Calorimeter (ECal), and to the Small Angle Calorimeter (SAC). The SM Bremsstrahlung radiation rate would not fit with the long decay time (300 ns) of BGO crystals, "blinding" the calorimeter most of the time. For this reason, ECal has a central hole of $\sim$105 mm side, which allows radiation to reach the faster SAC. ECal is made of 616 $21\times21\times230$ mm^3 BGO crystals, coupled to HZC Photonics XP1911 photomultipliers (readout sampling: 1 GHz, 1024 samples) [7]. The scintillating units are arranged in a cylindrical shape (radius $\sim$ 300 mm).
SAC consists of 25 $30\times30\times140$ mm^3 PbF_2 Cherenkov crystals, coupled to Hamamatsu R13478UV photomultipliers (readout sampling: 2.5 GHz, 1024 samples) [8]. PbF_2 time resolution ($\sim$ 100 ps) allows us to reconstruct Bremsstrahlung events. The distance between the target and ECal is approximately 3.45 m, while between ECal and the SAC front faces is $\sim$ 50 cm. A TimePix3 silicon pixels detector monitors the exhausted beam. The detector consists of 12 sensors, each made of a 256×256 pixels matrix. With a 8.4×2.8 cm^2 surface, it's the biggest TimePix3 array used so far in particle physics.

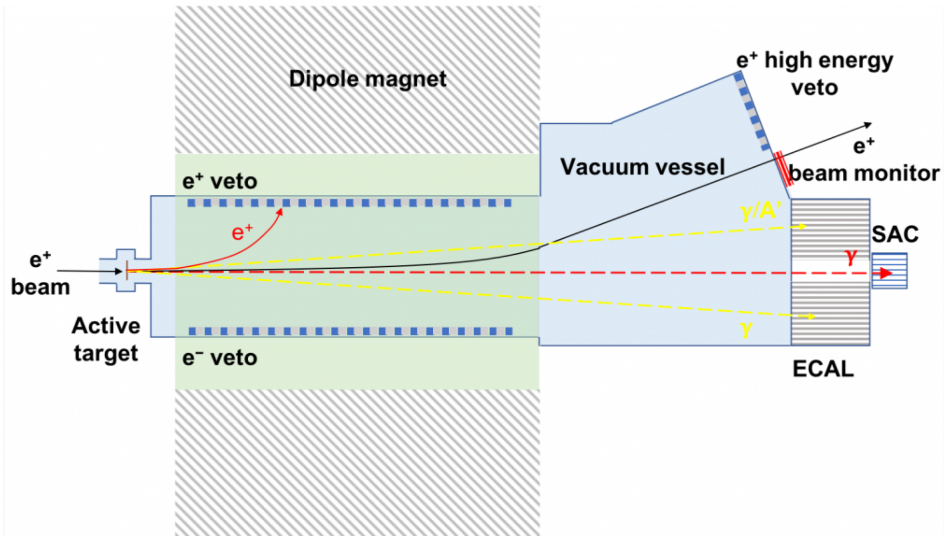

Figure 1: *A schematic of PADME. The positron beam hits the target, where the annihilation happens; charged particles are deflected in vacuum by the magnetic field towards the vetoes, while photons arrive to the calorimeters (see text for more details).*

2.3 Data taking run I and future prospects

The first run of the experiment lasted from October 2018 to March 2019. Priorities for first run has been set to:

1. the development of an online monitor system for the experiment, in order to have reliable information about the experiment during data taking
2. calibrations studies for every detectors, a crucial point for the events reconstruction, performed with beam (target and veto) and cosmic rays (ECal and SAC)
3. finding the best beam configuration, moving from a secondary beam, where beam positrons are obtained by the collision of accelerated electrons on a target, to a primary beam, where positrons are accelerated after the production

4. performing background studies, in order to compare them to the Montecarlo of the experiment
5. providing information about the number of positrons arriving on target
6. collect a sample of 10^{12} positrons on target (POT): a preliminary estimate on the result we obtained gave us $\sim 7 \cdot 10^{12}$ POT for the first run, but we must include uncertainty to this number.

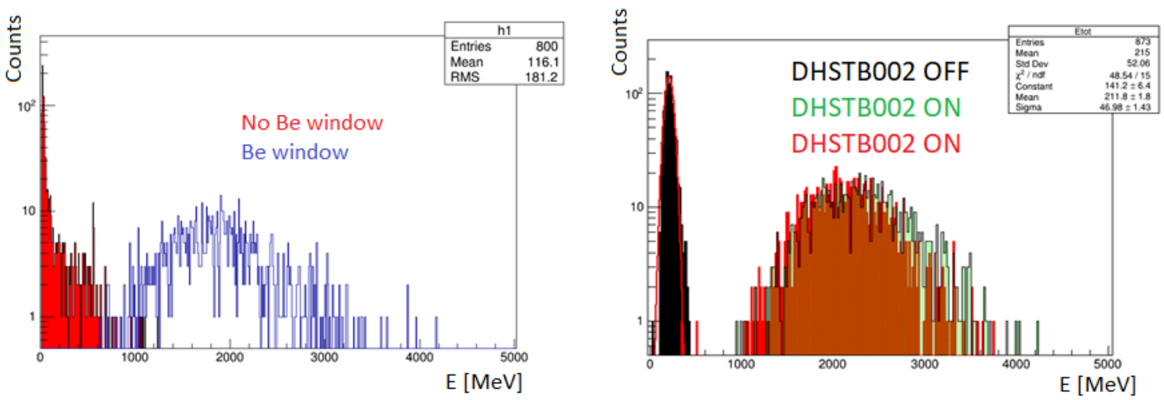

Figure 2: *On the left, the total energy distribution of the Montecarlo of the experiment, with and without the beryllium window; on the right, the total energy distribution of the collected data (DHSTB002 is the last dipole of the transfer line before the target).*

One of the most important task was to better understand the beam-induced background of the experiment. In first place, a 3 times smaller background has been obtained switching from secondary to primary beam. In second place, data analysis suggested that the main cause for this kind of background was due to the beam hitting the beryllium window separating BTF vacuum from PADME vacuum. The addition of the beam line and of the beryllium window to the Montecarlo of the experiment provided us a more reliable simulation of the collected data. In fig. 2 it's possible to note the similar behaviour of the total energy distribution in the Montecarlo and in data, once the beryllium window is added to the simulation.
A second calibration tool is going to be placed on ECal: it will use a ^{22}Na source, that will be moved in front every scintillating units also to monitor the performance of the calorimeter during data taking. Promising results on beam background decrease have been obtained with a different beam configuration, and the shift of the beryllium window should guarantee further improvements. The collaboration asked for a second physics run in order to reach 10^{13} positrons on target.

3 Conclusions

The PADME experiment at Laboratori Nazionali di Frascati started its search for the possibile mediator A' of a new interaction between dark matter and standard matter. The particle, called "dark photon" in analogy with the Standard Model photon, will be searched as a peak in the missing mass distribution of the annihilation process $e^+e^- \to \gamma A'$. A first run of the experiment was performed from October 2018 to March 2019, allowing the study the background of the experiment and to perform calibration studies of the detectors. We collected 10^{12} positrons on target during Run I, and the collaboration asked for additional time to reach the goal of 10^{13}.

References

1. J. Alexander et al., arXiv:1608.0863 (2016).
2. M. Raggi, V. Kozhuharov, Adv. High Energy Phys. 2014, 959802 (2014).
3. M. Raggi, V. Kozhuharov, P. Valente, EPJ Web Conf. 96, 01025 (2015).
4. P. Valente *et al*, arXiv:1603.05651 [physics.acc-ph] INFN-16-04-LNF (2016).
5. F. Oliva *et al*, Nucl. Instrum. Meth. A936, 697 (2019).
6. F. Ferrarotto *et al*, IEEE Trans. on Nucl. Science 65, 8 (2018).
7. M. Raggi *et al*, Nucl. Instrum. Meth. A862, 31 (2017).
8. A. Frankenthal *et al*, Nucl. Instrum. Meth. A919, 89 (2019).

Frascati Physics Series Vol. 69 (2019)
PHOTON 2019 - International Conference on the Structure and the Interactions of the Photon
Jun 3-7, 2019

SEARCH FOR AN INVISIBLE VECTOR BOSON FROM π^0 DECAYS AT NA62

Letizia Peruzzo
Johannes Gutenberg University Mainz, Staudingerweg 7, 55128 Mainz (Germany)
on behalf of the NA62 Collaboration *

Abstract

The high-intensity setup, trigger system flexibility and detector performance make the NA62 experiment at CERN particularly suitable to perform direct searches for long-lived hidden-sector particles, such as dark photons, dark scalars, axion-like particles, and heavy neutral leptons, using kaon and pion decays as well as operating the experiment in dump mode. Results from NA62 will be presented on a search for π^0 decays to one photon and an invisible massive dark photon. From about 400 M π^0 decays, no signal is observed beyond the expected fluctuation of the background and limits are set in the plane of the dark photon coupling to ordinary photon versus the dark photon mass. The analysis has been also interpreted in terms of the branching ratio for the electroweak decay $\pi^0 \to \gamma\nu\bar{\nu}$.

* The NA62 Collaboration: R. Aliberti, F. Ambrosino, R. Ammendola, B. Angelucci, A. Antonelli, G. Anzivino, R. Arcidiacono, T. Bache, M. Barbanera, J. Bernhard, A. Biagioni, L. Bician, C. Biino, A. Bizzeti, T. Blazek, B. Bloch-Devaux, V. Bonaiuto, M. Boretto, M. Bragadireanu, D. Britton, F. Brizioli, M.B. Brunetti, D. Bryman, F. Bucci, T. Capussela, J. Carmignani, A. Ceccucci, P. Cenci, V. Cerny, C. Cerri, B. Checcucci, A. Conovaloff, P. Cooper, E. Cortina Gil, M. Corvino, F. Costantini, A. Cotta Ramusino, D. Coward, G. D'Agostini, J. Dainton, P. Dalpiaz, H. Danielsson, N. De Simone, D. Di Filippo, L. Di Lella, N. Doble, B. Dobrich, F. Duval, V. Duk, J. Engelfried, T. Enik, N. Estrada-Tristan, V. Falaleev, R. Fantechi, V. Fascianelli, L. Federici, S. Fedotov, A. Filippi, M. Fiorini, J. Fry, J. Fu, A. Fucci, L. Fulton, E. Gamberini, L. Gatignon, G. Georgiev, S. Ghinescu, A. Gianoli, M. Giorgi, S. Giudici, F. Gonnella, E. Goudzovski, C. Graham, R. Guida, E. Gushchin, F. Hahn, H. Heath, E.B. Holzer, T. Husek, O. Hutanu, D. Hutchcroft, L. Iacobuzio, E. Iacopini, E. Imbergamo, B. Jenninger, J. Jerhot, R.W. Jones, K. Kampf, V. Kekelidze, S. Kholodenko, G. Khoriauli, A. Khotyantsev, A. Kleimenova, A. Korotkova, M. Koval, V. Kozhuharov, Z. Kucerova, Y. Kudenko, J. Kunze, V. Kurochka, V. Kurshetsov, G. Lanfranchi, G. Lamanna, E. Lari, G. Latino, P. Laycock, C. Lazzeroni, M. Lenti, G. Lehmann Miotto, E. Leonardi, P. Lichard, L. Litov, R. Lollini, D. Lomidze, A. Lonardo, P. Lubrano, M. Lupi, N. Lurkin, D. Madigozhin, I. Mannelli, G. Mannocchi, A. Mapelli, F. Marchetto, R. Marchevski, S. Martellotti, P. Massarotti, K. Massri, E. Maurice, M. Medvedeva, A. Mefodev, E. Menichetti, E. Migliore, E. Minucci, M. Mirra, M. Misheva, N. Molokanova, M. Moulson, S. Movchan, M. Napolitano, I. Neri, F. Newson, A. Norton, M. Noy, T. Numao, V. Obraztsov, A. Ostankov, S. Padolski, R. Page, V. Palladino, A. Parenti, C. Parkinson, E. Pedreschi, M. Pepe, M. Perrin-Terrin, L. Peruzzo, P. Petrov, Y. Petrov, F. Petrucci, R. Piandani, M. Piccini, J. Pinzino, I. Polenkevich, L. Pontisso, Yu. Potrebenikov, D. Protopopescu, M. Raggi, A. Romano, P. Rubin, G. Ruggiero, V. Ryjov, A. Salamon, C. Santoni, G. Saracino, F. Sargeni, S. Schuchmann, V. Semenov, A. Sergi, A. Shaikhiev, S. Shkarovskiy, D. Soldi, V. Sugonyaev, M. Sozzi, T. Spadaro, F. Spinella, A. Sturgess, J. Swallow, S. Trilov, P. Valente, B. Velghe, S. Venditti, P. Vicini, R. Volpe, M. Vormstein, H. Wahl, R. Wanke, B. Wrona, O. Yushchenko, M. Zamkovsky, A. Zinchenko.

1 Introduction

The discovery of the Higgs boson at LHC completed the Standard Model of particle physics (SM) with the last missing piece. However, there are evidence that yet unknown particles or interactions are still needed in order to explain some observed phenomena, like the matter-antimatter asymmetry of the universe, the existence of the dark matter, neutrino masses and oscillations. So far, direct searches for new-physics at the energy frontier have not yet turned up any convincing evidence. In these searches, models with TeV energy scale have received most of the attention. However if physics beyond the SM is only very weakly coupled to the SM particles, some or all of the gaps might be filled in by the existence of light dark matter particles with the mediators of their interactions very weakly coupled to SM particles. One possible extension of the SM aimed to explain the dark matter abundance introduces a new $U(1)$ gauge-symmetry mediated by a vector field A', the dark photon. In a simple realization of this scenario [1, 2], the interaction between the A' field and the SM photon occurs through a kinetic-mixing Lagrangian with a coupling parameter $\epsilon << 1$,

$$\epsilon A'_{\mu\nu} F^{\mu\nu} \tag{1}$$

A consequence of this interaction [3] is the transition $\pi^0 \to \gamma A'$ with a branching ratio

$$\mathrm{BR}(\pi^0 \to \gamma A') = 2\epsilon^2 \left(1 - \frac{M_{A'}^2}{M_{\pi^0}^2}\right)^3 \times \mathrm{BR}(\pi^0 \to \gamma\gamma) \tag{2}$$

Additional interactions might accompany the above Lagrangian, with the dark photon coupled both with SM matter fields and with a hidden sector of possible dark matter candidate fields. If these are lighter than the A', the dark photon would decay mostly invisibly and a missing-energy signature might reveal its presence. Exploiting the extreme photon-veto capability and high resolution tracking of the NA62 experiment, the search for an invisible A' is performed with a missing-mass technique by fully reconstructing the decay chain

$$K^+ \to \pi^+\pi^0, \pi^0 \to \gamma A' \tag{3}$$

The results from a subsample of 2016 data are reported, corresponding to 1% of the statistics collected by NA62 in 2016–2018.

2 NA62 experiment

The NA62 experiment is the latest in a series of fixed-target experiments located at the CERN SPS using the decay-in-flight technique to explore kaon decays. The main goal of the experiment is to precisely measure the very rare decay $K^+ \to \pi^+\nu\bar{\nu}$ ($\mathrm{BR_{SM}} = (8.4 \pm 1.0) \times 10^{-11}$ [4]) with 10% accuracy. [5] The experiment uses the SPS proton beam (400 GeV/c), which hitting on a beryllium target produces a secondary hadron beam, with kaons contributing to only 6% of all particles. The beam has a momentum of (75 ± 1) GeV/c and a nominal intensity of 750 MHz. The beryllium target is followed by two 1.6 m long, water-cooled copper collimators (TAX) consisting on a series of graduated holes in which the beam passes trough, while the non interacting primary proton and unwanted secondary particles are absorbed. The detector apparatus (fig. 1) extends over 270 m from the target to the beam dump located at the end of the experiment. The kaon tagging and a precise timing measurement of the beam particles are provided by a Cherenkov detector (KTAG), followed by three silicon pixel stations which form the beam spectrometer (Gigatracker or GTK). A magnetic spectrometer of four STRAW chambers placed in vacuum provides the momenta and directions of the charged particles produced in the kaon decays. The particle identification is performed by a Ring Imaging Cherenkov (RICH) detector, an electromagnetic (LKr) calorimeter and a muon veto system (MUV). Large Angle (LAV) and Small Angle (IRC and SAC) Veto form together with the LKr calorimeter the high-efficiency photon veto system, covering angles from 0 to 50 mrad. A pair of charged hodoscopes (CHODs) complete the experimental apparatus. Detailed information on the detector layout and performances can be found in [6].

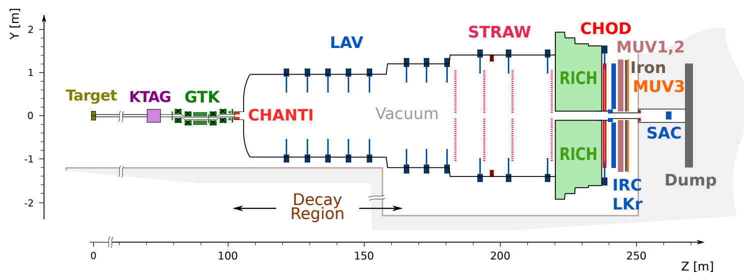

Figure 1: *NA62 experimental apparatus.* [6]

3 Dark photon analysis principle

The experimental signature for the events described in eq. 3, assuming a dominant invisible decay of the A' or a long-lived A' escaping the experimental apparatus, is given by a kaon decaying into a charged pion and a photon hitting the electromagnetic calorimeter (LKr) accompanied by missing energy and momentum. Given the kaon (P_{K^+}) and pion (P_{π^+}) 4-momenta measured by the GTK and STRAW respectively, the photon 4-momentum is obtained, assuming emission from the decay vertex, by measuring the photon position and energy in the LKr, the squared missing mass

$$M^2_{\text{miss}} = (P_{K^+} - P_{\pi^+} - P_\gamma)^2 \tag{4}$$

is expected to peak around the squared A' mass ($M^2_{A'}$) for the signal and around zero for the most relevant background $\pi^0 \to \gamma\gamma$ with one photon undetected (fig. 2).

A pure sample of $K^+ \to \pi^+\pi^0$ decays is selected by reconstructing only the K^+ and π^+ particles and requiring their missing mass $(P_{K^+} - P_{\pi^+})^2$ to be compatible with the squared π^0 mass. The number of $K^+ \to \pi^+\pi^0$ decays selected in control-sample data defines the statistics of tagged π^0 meson, which is about 4×10^8. For the $\pi^0 \to \gamma A'$ signal events, additional conditions are required in order to enforce the sole presence of a π^+ and one photon reconstructed in the final state:

- No additional signal from photons, except for the one reconstructed in the LKr, must be detected in the photon-veto system.
- No in-time activity must be detected in the hodoscope (NA48-CHOD) placed upstream the LKr, except for that associated to the π^+. This condition is particularly useful to reject events with one photon lost because of pair production upstream of the hodoscope.

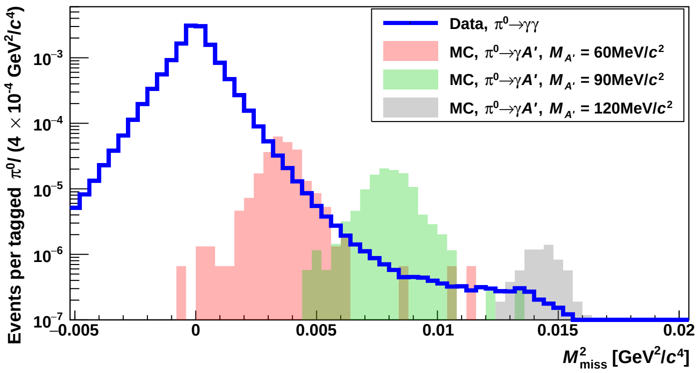

Figure 2: *Distribution of the squared missing mass evaluated from K^+ decays with on photon and one π^+ reconstructed. The blue line represents data from $\pi^0 \to \gamma\gamma$ decays with one photon (randomly chosen) assumed to be undetected. The expected spectra from Monte Carlo (MC) simulation of $\pi^0 \to \gamma A'$ are also shown. In the MC the coupling strength is set to $\epsilon^2 = 2.5 \times 10^{-4}$ and different A' mass are simulated: $M_{A'}$ =60 (red), 90 (green) and 120 MeV/c^2 (grey).*

- The missing momentum given in eq. 4 must point to the LKr calorimeter.
- The $K^+ \to \pi^+\nu\bar{\nu}$ trigger stream [5], which requires one-track and small forward energy in the final state, is used for the signal sample.

About 9×10^3 events pass the signal selection, and a peak scan is performed on the positive tail of $M^2_{\rm miss}$ distribution by comparing the number of events in a sliding $M^2_{\rm miss}$ window to the background expectation. The estimated number of signal events (n_{sig}) in a given $M^2_{\rm miss}$ window is normalized to the number of tagged π^0 meson (n_{π^0}) to give the branching ratio for $\pi^0 \to \gamma A'$ decays:

$$\mathrm{BR}(\pi^0 \to \gamma A') = \mathrm{BR}(\pi^0 \to \gamma\gamma) \times \frac{n_{sig}}{n_{\pi^0}} \frac{1}{\epsilon_{sel}\epsilon_{trg}\epsilon_{mass}} \tag{5}$$

where ϵ_{sel} accounts for the selection efficiency due to the additional requirements in the signal selection, ϵ_{trg} for the signal-trigger efficiency and ϵ_{mass} for the mass-window acceptance of the peak search in $M^2_{\rm miss}$. The three correction factors depend on $M_{A'}$ and are evaluated with a combination of Monte Carlo (MC) simulations and data control-sample. The geometrical acceptance and the π^0-tagging efficiency cancel in the ratio between signal and normalization.

4 Background evaluation

As shown by MC simulations, the most relevant background comes from $K^+ \to \pi^+\pi^0(\gamma)$ events with one photon from $\pi^0 \to \gamma\gamma$ undetected due to photon conversion. The expected background is evaluated with a data-driven approach: the same selection of the signal sample is applied with the exception of the NA48-CHOD extra activity condition, which is partially inverted. Events with in-time activity in the hodoscope not geometrically associated either with the π^+ or with the detected photon are selected. This requirement allows selecting a data control sample of $\pi^0 \to \gamma\gamma$ events with one photon detected in the LKr and the second lost because of conversion upstream the NA48-CHOD, without making any assumption on the shape of the $M^2_{\rm miss}$ tail and with no analytical extrapolation of the background. Since the presence of the second photon lost by conversion ensures no overlap with the signal sample and the signal pollution is verified to be below 1% with MC simulations, the enriched background sample is used to evaluate the expected $M^2_{\rm miss}$ background distribution. The background sample is scaled to the signal sample in a side-band region adjacent to but not overlapping with the A' signal region as shown in fig. 3 left.

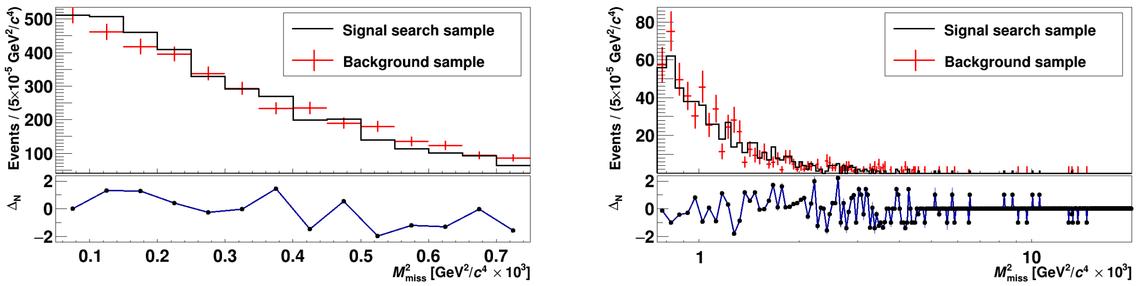

Figure 3: $M^2_{\rm miss}$ *distribution of the* A' *signal search sample (black) and background sample (red). The left panel shows the region used to evaluate the scaling factors, while the search region is shown in the right panel. In the bottom panels, the difference* Δ_N *between the two* $M^2_{\rm miss}$ *spectra is plotted in units of its standard deviation.*

5 Results

A peak search is performed on the $M^2_{\rm miss}$ distribution in the region $0.00075 < M^2_{\rm miss} < 0.01765$ GeV/c^4, corresponding to test the A' mass in the range 30–130 MeV/c^2. The observed data and the expected background events are evaluated for each of the $M_{A'}$ hypothesis by integrating the corresponding $M^2_{\rm miss}$ spectrum as shown in fig. 3 right. The width of the sliding window is set to $\pm 1\sigma_{M^2_{\rm miss}}$ around the tested mass hypothesis. In each mass hypothesis, the frequentist 90% confidence intervals are computed for the number of signal events using the CLs algorithm. [7] Given eq. 5, 90% confidence level (CL) upper limits are obtained on the coupling parameter ϵ^2 as a function of the A' mass as shown in fig. 4. The observed upper limits are compatible with fluctuations expected in the absence of signal and no statistically significant excess is detected. The result obtained improves the previous limits over the mass range 60–110 MeV/c^2 as shown in fig. 5. It must be underlined that the experimental technique used by NA62 is totally different than the one of the other recent results. Therefore, in general dark-photon models, the channel searched for by NA62 can be sensitive to possible new-physics effects notwithstanding the null result from other experiments (e.g. BaBar and NA64).

Slight modifications to the A' analysis allow performing a search for the decay $\pi^0 \to \gamma\nu\bar{\nu}$. The branching ratio of this process is expected to be of $\mathcal{O}(10^{-18})$ in the SM, while the present experimental limit [11] is BR($\pi^0 \to \gamma\nu\bar{\nu}$) $< 6\times10^{-4}$ at 90% CL. The strategy used for the A' search, based on the comparison of observed data and expected background events in a given $M^2_{\rm miss}$ interval, has been adopted. A peak search on the $M^2_{\rm miss}$ distribution is performed in the region 0.0054 GeV/c^4 $< M^2_{\rm miss} < M^2_{\pi^0}$, allowing to set an upper limit on the branching ratio of BR($\pi^0 \to \gamma\nu\bar{\nu}$) $< 1.9\times10^{-7}$ at 90% CL.

References

1. L. Okun, Sov. Phys. JETP **56**, 502 (1982).

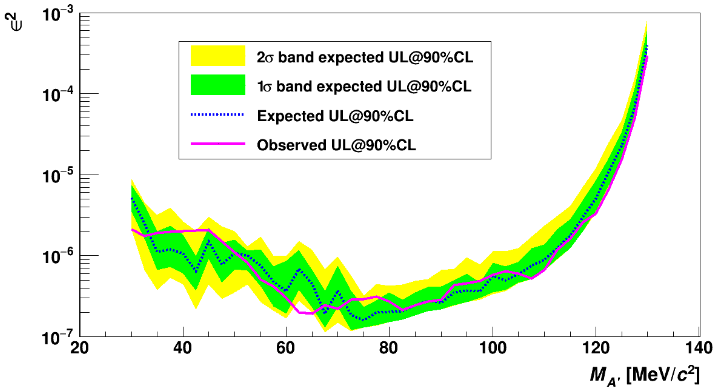

Figure 4: *Upper limit at 90% CL on the A' coupling strength as a function on the dark photon mass. The limit obtained from data (solid line) is compared to that expected in the absence of signal. The expected median of the upper limit is shown together with the bands at 68% and 95% coverage.*

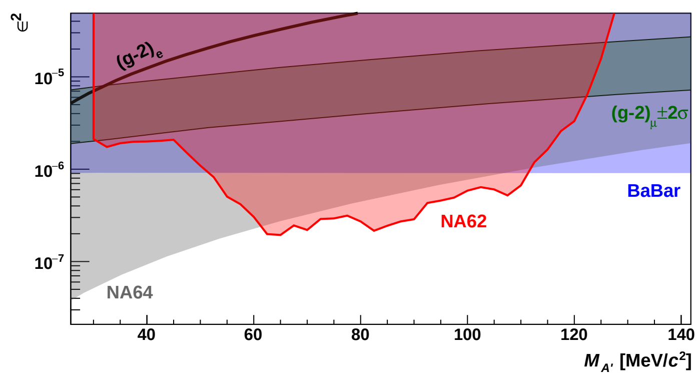

Figure 5: *Upper limit at 90% CL from NA62 (red region) in the ϵ^2 vs $M_{A'}$ plane, assuming a dark photon decaying into invisible final state. The limits from BaBar [8] (blue) and NA64 [9] (light grey) experiments are also shown. A new experimental technique is used by NA62 with respect to the previous experiments.*

2. B. Holdom, Phys. Rev. Lett. B **166**, 196 (1986).
3. Batell, Pospelov and Ritz, PRD **80**, 095024 (2009).
4. A. J. Buras, D. Buttazzo, J. Girrbach-Noe, R. Knegjens, JHEP **11**, 033 (2015).
5. E. Cortina Gill *et al.* [The NA62 Collaboration], Phys. Lett. B **778**, 137 (2018).
6. E. Cortina Gill *et al.* [The NA62 Collaboration], JINST **12**, P05025 (2017).
7. A. L. Read, J. Phys. G **28**, 2693 (2002).
8. J. P. Lees *et al.* [The BaBar Collaboration], Phys. Rev. Lett. **119**, 131804 (2017).
9. D. Banerjee *et al.* [The NA64 Collaboration], Phys. Rev. D **97**, 072002 (2018).
10. E. Cortina Gill *et al.* [The NA62 Collaboration], JHEP **05**, 182 (2019).
11. M.S. Atiya *et al.* [The E787 Collaboration], Phys. Rev. Lett. **69**, 733 (1992).

Frascati Physics Series Vol. 69 (2019)
PHOTON 2019 - International Conference on the Structure and the Interactions of the Photon
Jun 3-7, 2019

FULLY NEUTRAL FINAL STATES AT KLOE/KLOE-2

Marcin Berłowski
National Centre for Nuclear Research, Warsaw, Poland
on behalf of the KLOE-2 Collaboration

Abstract

In March 2018, the KLOE-2 experiment completed its data-taking at the e^+e^- DAϕNE collider in Frascati, collecting more than 5 fb^{-1} at the phi peak, thus extending the KLOE physics program with an upgraded detector. The KLOE detector is well suited for the study of fully neutral final states due to its large radius and a hermetic electromagnetic calorimeter, providing excellent timing and position resolution (50 ps and O(cm), respectively, at 1 GeV). The calorimeter energy resolution ($5\%/\sqrt{E}$) is greatly improved when kinematic constraints are applied. The upgraded KLOE-2 detector extends its acceptance coverage thanks to the new small angle calorimeters placed near the interaction region.
The latest results on prompt neutral final states will be presented, with particular emphasis on five photon final state, which is used to study the $\eta \to \pi^0\gamma\gamma$ decay. This process provides an important test of ChPT because of its sensitivity to the p^6 term on both the branching ratio and the $IM_{\gamma\gamma}$ spectrum. A preliminary KLOE measurement, based on 450 pb^{-1}, provided a much lower BR value than the most accurate determination from Crystal Ball. A new analysis with a larger data sample is in progress to confirm this result. The same five photon final state is also used to search for the B boson, a postulated leptophobic mediator of dark forces.

1 Introduction

KLOE and KLOE-2 detectors operated at DAFNE [1], an electron-positron collider phi-factory working at $\sqrt{s} \approx 1020\ MeV$ located in Frascati near Rome, Italy. The detector, consisting of a largest in the world cylindrical drift chamber (DC) [2], 4 m in diameter and 3.3 m long, filled with a light gas mixture of 90% helium and 10% isobutane was surrounded by an electromagnetic calorimeter (EMC) made of lead scintillating-fibers covering nearly 100% of 4π particle decay space [3]. DC and EMC were inside magnetic field of $\sim 0.5\ T$. In 2008 a new interaction scheme was introduced in order to increase the machine luminosity [4]. At that time KLOE-2 detector was upgraded with a new interaction region constituted by an inner cylindrical triple-GEM 4 layer tracker [5] for larger charge track acceptance at low $p_t's$ and to improve the vertex reconstruction. Also three new calorimeters were installed in the beamline region to improve acceptance for particles emitted at small polar angles [6, 7] and a scintillator stripes tagger placed after the first bending magnet of the machine designed for the search of $\gamma\gamma$ physics [8]. KLOE was taking data in the years 2001-2006, collecting 2.5 fb^{-1} of ϕ decays. The KLOE-2 dataset was collected in 2014-2018 and amounts to more than 5 fb^{-1}. Data recorded in both experiments is by now the largest sample of $e^+e^- \to \phi$ events collected in any e^+e^- collider, corresponding to about $2.4 \cdot 10^{10}$ produced ϕ mesons. A lot more information about perspectives and plans for the future of KLOE-2 experiment can be found in [9].

2 B boson searches

The dominating nowadays explanation for the observed anomalies in galaxy rotation curves, observations in gravitational lensing, the motion of galaxies within galaxy clusters etc. is postulate of existence of Dark Matter. It's still yet not being discovered directly and it's nature remains unknown mainly due to very small interaction with baryonic matter. The cosmological observations are postulating it to be $\sim 27\%$ of the total mass-energy of the universe, with $\sim 5\%$ ordinary matter and energy and the rest $\sim 68\%$ being an unknown form of energy known as dark energy. The primary candidate for cold dark matter particles is a new kind of weakly-interacting massive particle (WIMP). It's commonly proposed that the interaction would be mediated by a new vector gauge boson, the U boson or dark photon, which couple to photon via a kinetic-mixing term ϵ^2. This hypothetical boson, with mass in the $MeV - GeV$ range could be observed for example in e^+e^- colliders via processes like $e^+e^- \to U\gamma$ and additionally in hadron machines though $V \to P\gamma$ decays, where V and P are vector and pseudoscalar mesons respectively. Here we are focusing our search on a different kind of U boson, named B boson that couples to baryon number and arises from a new $U(1)_B$ gauge symmetry [10]. Analogically to coupling of U to the SM via kinetic mixing with the usual photon we can write the interaction Lagrangian:

$$\mathcal{L} \;=\; \tfrac{1}{3} g_B \bar{q}\gamma^\mu q B_\mu$$

where B_μ is the new gauge field coupling to baryon number and the gauge coupling g_B is universal for all quarks q. The B boson in this model carries the same quantum numbers as the ω meson: $I^G(J^{PC}) = 0^-(1^{--})$ and therefore shows as what kind of decays of B we should expect. The three main decay channels of ω with their Branching Ratios are: $BR(\omega \to \pi^+\pi^-\pi^0) \simeq 89\%, BR(\omega \to \pi^0\gamma) \simeq 8\%, BR(\omega \to \pi^+\pi^-) \simeq 1.5\%$. It's expected for the B decays to follow above scheme in the mass range: $m_\pi < m_B < GeV$, when above $B \to K\overline{K}$ channel opens. Below m_π dark photon searches for $U \to e^+e^-$ have sensitivity to the B boson as well, since it's expected that the pair of electrons is B's leading decay. In the mass range of m_π and $m_{3\pi} \simeq 620\ MeV$, a new channel opens with $B \to \pi^0\gamma$, which is not covered by dark photon searches and it's existence is expected to be seen as sharp, resonance peak in $\pi^0\gamma$ spectrum.

In KLOE we have currently exploring two possible channels with the B boson production: $\phi \to (\eta \to \gamma\gamma)(B \to \pi^0\gamma)$ and $\eta \to \gamma(B \to \pi^0\gamma)$ produced in $\phi \to \eta\gamma$ process (see next section). The $\phi \to \eta(B \to \pi^0\gamma)$ decay which is expected to be dominated by $\phi \to a_0(980)\gamma \to \eta\pi^0\gamma$ was already explored by KLOE collaboration [11] with the most precise branching ratio measurement up to date. The study can be extended and improved by looking for a sharp peak at m_B in $\pi^0\gamma$ invariant mass spectrum.

The new analysis exploring this possibility and taking an advantage of much bigger data sample (1.7 fb^{-1} compared to 450 nb^{-1} presented previously) is now carried over. We are looking for a signature coming from $\phi \to \eta\pi^0\gamma$ with η meson decay into two photons, therefore 5 aligned in time photons. The main backgrounds for this process are: $\phi \to (f_0 \to 2\pi^0)\gamma$, $\phi \to (a_0 \to \eta\pi^0)\gamma$, $e^+e^- \to (\omega \to \pi^0\gamma)\pi^0$, and $\phi \to (\eta \to 3\pi^0)\gamma$ when two of the photons are either merged, lost or both. The resolution is corrected by kinematic fit with nine constrains being energy-momentum conservation and times of flight of measured photons to be as expected from massless particles traveling with speed of light to the detector. We are using two more kinematic fits with additional constraints on masses of the final particles: η and π^0 for the signal selection and $2\pi^0$ for the background rejection. The global analysis efficiency by now is on the level of 13% with the remaining backgrounds consisting of $\phi \to (a_0 \to \eta\pi^0)\gamma$ and $\phi \to (\eta \to 3\pi^0)\gamma$. The fig.1 presents $IM(\pi^0\gamma)$ (left) and $IM(\pi^0\eta)$ (right) distributions. Extraction of an upper limit for

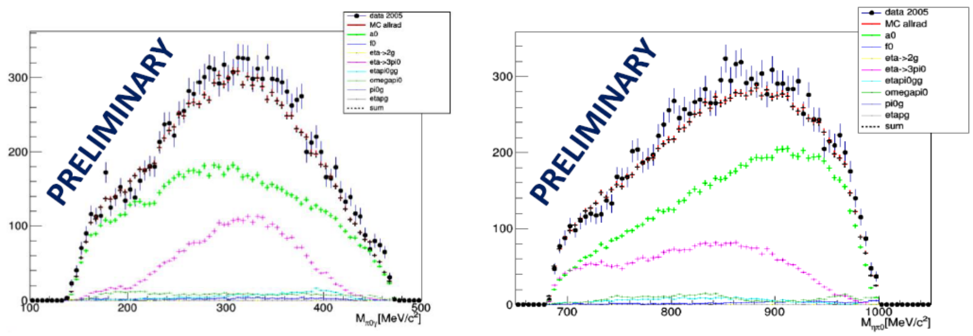

Figure 1: *Left: Invariant mass of $\pi^0\gamma$; Right: Invariant mass of $\pi^0\eta$. Black points are data shown with statistical error only, red points are sum of Monte Carlo contributions presented with different colors.*

the dark B mediator as well as systematic checks are ongoing. This analysis could be also used for an extraction of a new fit to $a_0(980)$ thanks to much bigger statistics.

3 $\eta \to \pi^0\gamma\gamma$ decay

The $\eta \to \pi^0\gamma\gamma$ decay was always in great interest of physicists since it's Branching Ratio (BR) and various characteristics can provide constrains for theoretical models which predict BRs that can vary in orders of magnitude (see left panel of fig.2). It is quite challenging since to measure it you have to have a great knowledge about possible backgrounds and good control about experimental conditions. The decay which is called Chiral Perturbation Theory (ChPT) "golden mode" can help to extract coefficient values at $O(p^6)$ and their signs which must be determined from the experiment. It's possible thanks to the fact that in this decay contributions at the level of p^2 are null, p^4 are equal to 0 on the tree level and are suppressed on 1-loop calculations by G-parity and large kaon mass with p^6 terms that dominate. Additionally the shape of $IM_{\gamma\gamma}$ distribution where photons are not coming from the π^0 decay can be used as a test of theoretical models (see right panel of fig.2).

In recent decades by increasing collected luminosities and improving detectors performance it's BR has been given by many experiments with growing precision with the latest value coming from AGS/Crystal Ball [23]:

$$BR(\eta \to \pi^0\gamma\gamma) = (2.21 \pm 0.24_{stat} \pm 0.38_{syst}) \cdot 10^{-4}$$

This measurement can be compared with the one coming from preliminary analysis by KLOE collaboration [22] giving the value which is more than 2σ lower: $(0.84 \pm 0.27_{stat} \pm 0.14_{syst}) \cdot 10^{-4}$. It was based on

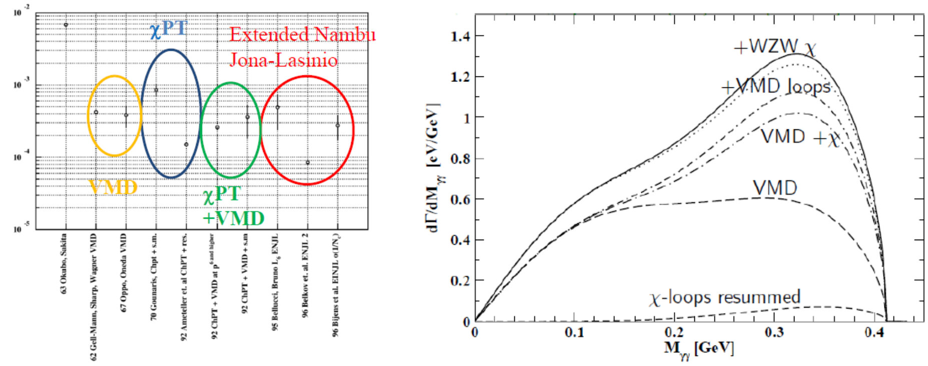

Figure 2: *Right: Theory predictions for $BR(\eta \rightarrow \pi^0\gamma\gamma)$ divided on different groups based on models used. Values are taken from* [13)–20)]. *Left: Contributions from different models to the two photon invariant mass distribution. For more information see* [12)].

a small sample of 450 nb^{-1} integrated luminosity with a signal significance at the level of 3σ. One of the aims of the new KLOE analysis was to increase data sample in order to confirm or deny the discrepancy between the two experiments.

At KLOE we are measuring the decay by looking for the process of $\phi \rightarrow \eta\gamma$, so the final state consists of exactly 5 aligned in time photons and no charged tracks. The two body decay of phi meson into $\eta\gamma$ is tagged using monochromatic photon of 363 MeV. The backgrounds for the $\eta \rightarrow \pi^0\gamma\gamma$ decay can be divided into three categories. The first one are the processes with less then 3 physical photons in the final state such as $\phi \rightarrow (\pi^0/\eta \rightarrow \gamma\gamma)\gamma$ or $e^+e^- \rightarrow \gamma\gamma$ with additional photons from cluster split-outs and/or accidental clusters coming from the machine background. The second one have the same number of prompt photons as our decay which are mainly $\phi \rightarrow (f_0 \rightarrow 2\pi^0)\gamma$, $\phi \rightarrow (a_0 \rightarrow \eta\pi^0)\gamma$ and $e^+e^- \rightarrow (\omega \rightarrow \pi^0\gamma)\pi^0$. The third category with more than five photons when some of them may be undetected or merge with other clusters which mainly is $\eta \rightarrow 3\pi^0$ produced via $\phi \rightarrow \eta\gamma$.

The new KLOE analysis is taking an advantage of much bigger data sample of 1.7 fb^{-1}. In order to correct measured variables the kinematic fit with nine constrains (energy-momentum conservation and times of flight of five photons to be consistent of massless particles) was used. It also allowed us to greatly improve the resolution in measured particles energies. To reduce the background three more dedicated kinematic fits were we constrained different particles masses were used. One of those was looking for events with two π^0 mesons in the final state to remove f_0 and ω events. The other one was suppressing a_0 by constraining η and π^0 both decaying into two photons. The last one was keeping only signal-like events under the hypothesis to have η meson decaying into $\pi^0\gamma\gamma$.

At this analysis level the background consists with more than (85%) with events coming from $\eta \rightarrow 3\pi^0$. Those events can be divided into three main classes: a) the ones with two lost photons, b) with 2 merged clusters either in one cluster or two different ones and c) with one lost and one merged photon. The next step was to use one of the TMVA methods [21)] (Boosted Decision Trees) to reject the events with at least one merged cluster. The procedure was based on the very basic reconstructed properties of clusters like different moments of distributions of cell positions in the cluster or total energy of the cluster. The right panel on fig.3 shows the distribution of one of the variables used in order to distinguish between merged and normal clusters. The method is divided into three steps: training using Monte Carlo simulations of $\eta \rightarrow \pi^0\gamma\gamma$ and $\eta \rightarrow 3\pi^0$, testing using independent data samples and evaluating the results on the analysis level. This technique allowed us to remove $\sim 50\%$ of the background originating from $\eta \to 3\pi^0$ with more than 85% rejection of category with two merged clusters, while keeping more than 85% efficiency for the signal. The global analysis efficiency on this level of analysis is 20% which is four times better than previous KLOE result. In left panel of fig.3 one can see the invariant mass of $\pi^0\gamma\gamma$ after removing part of merged events.

The next steps to be carried out are to use dedicated kinematic fits for $3\pi^0$ cases with lost photons which

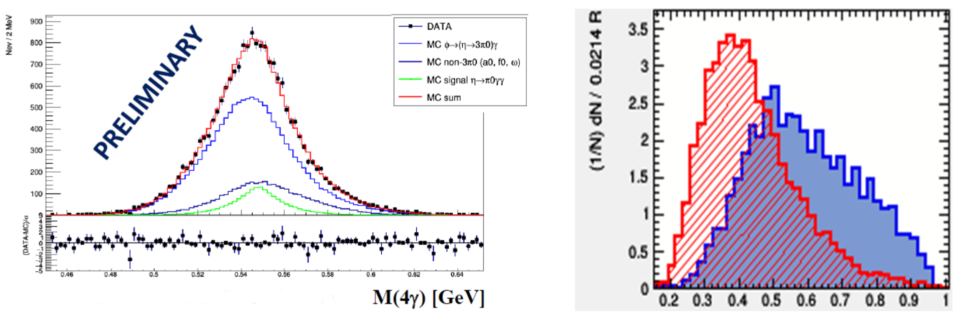

Figure 3: *Right: Invariant mass of $\pi^0\gamma\gamma$ after applying TMVA method to reject part of events with merged clusters. Black points are data presented with statistical error only, red line is fitted sum of Monte Carlo contributions shown with different colors. Left: An example of one of the variables used in TMVA analysis - the ratio between maximum cell energy and cluster energy. Red distribution is for the clusters which were merged, blue one for those without merging.*

are by now $\sim 75\%$ of the remaining background. We also want to normalize using a high statistics and almost background free $\eta \to 3\pi^0 \to 7\gamma$ which would also allow us to remove part of systematic effects. Then we are planning to remove the residual background contribution not coming from $3\pi^0$ decays and then finally to extract BR value for the decay. If we could obtain almost background free distributions we would be able to look into $IM_{\gamma\gamma}$ spectrum in order to put constrains on the ChPT models and $IM_{\pi^0\gamma}$ distribution would give us an access to search for a possible contribution coming from the B boson mentioned in the previous section.

4 Summary and perspectives

The KLOE-2 collaboration is still taking an advantage of high precision data taken in the first period of KLOE experiment. The studies will continue with increased statistics collected in the second KLOE-2 campaign which ended gathering more than 5 fb^{-1} integrated luminosity by March 2018. The new data will profit from detectors upgrade which for example will allow larger acceptance for photons emitted at small polar angles. In KLOE-2 we expect more than 10^8 η mesons produced which means for the presented analysis to have $\sim$ 1000 of $\eta \to \pi^0\gamma\gamma$ events assuming 5% global analysis efficiency, better background reduction for $\eta \to 3\pi^0$ thanks to increased detector's acceptance for photons coming at small angles, improvement of a factor of ~ 3.5 in $\pi^0\gamma$ invariant mass sensitivity for the $\phi \to \eta$ upper limit calculation. Preliminary results for both analysis are expected before the end of the 2019.

5 Acknowledgements

We warmly thank our former KLOE colleagues for the access to the data collected during the KLOE data taking campaign. We thank the DAFNE team for their efforts in maintaining low background running conditions and their collaboration during all data taking. We want to thank our technical staff: G.F. Fortugno and F. Sborzacchi for their dedication in ensuring efficient operation of the KLOE computing facilities; M. Anelli for his continuous attention to the gas system and detector safety; A. Balla, M. Gatta, G. Corradi and G. Papalino for electronics maintenance; C. Piscitelli for his help during major maintenance periods. This work was supported in part by the Polish National Science Centre through the Grant No. 2017/26/M/ST2/00697.

References

1. A. Gallo *et al*, Conf. Proc. **C060626**, 604-606 (2006).
2. M. Adinolfi *et al*, Nucl. Instrum. Meth. **A488**, 51-73 (2002).
3. M. Adinolfi *et al*, Nucl. Instrum. Meth. **A482**, 364-386 (2002).
4. G. Amelino-Camelia *et al*, Eur. Phys. J. **C68**, 619-681 (2010).
5. A. Balla *et al*, Nucl. Instrum. Meth. **A628**, 194-198 (2011).
6. M. Cordelli *et al*, Nucl. Instrum. Meth. **A718**, 81-82 (2013).
7. M. Cordelli *et al*, Nucl. Instrum. Meth. **A617**, 105-106 (2010).
8. D. Babusci *et al*, Nucl. Instrum. Meth. **A718**, 577-579 (2013).
9. A. Di Domenico, EPJ Web of Conferences Volume **166**, 00001 (2018).
10. S. Tulin, Phys. Rev. **D89**, 114008 (2014).
11. KLOE Collaboration (A. Aloisio *et al*), Phys. Lett. **B536**, 209-216 (2002).
12. E. Oset, J. R. Pelaez and L. Roca, Phys. Rev. **D77**, 073001 (2008).
13. S. Okubo and B. Sakita, Phys. Rev. Lett. **11**, 50 (1963).
14. M. Gell-Mann, D. Sharp, and W. G. Wagner, Phys. Rev. Lett. **8**, 261 (1962).
15. G. Oppo and S. Oneda, Phys. Rev. **160**, 1397 (1967).
16. G. J. Gounaris, Phys. Rev. **D1**, 1426-1431 (1970).
17. L. Ametller, J. Bijnens, A. Bramon, F. Cornet, Phys. Lett. **B276**, 185 (1992).
18. S. Bellucci and C. Bruno, Nucl. Phys. **B452**, 626 (1995).
19. A. A. Belkov, A. V. Lanyov, S. Scherer, J. Phys. **G22**, 1383 (1996).
20. J. Bijnens, A. Fayyazuddin and J. Prades, Phys. Lett. **B379**, 209 (1996).
21. A. Hoecker *et al*, PoS **A CAT**, 040 (2007).
22. B. Di Micco *et al*, Acta Phys. Slov. **56**, 403 (2006).
23. S. Prakhov *et al*, Phys. Rev. **C78**, 015206 (2008).

Frascati Physics Series Vol. 69 (2019)
PHOTON 2019 - International Conference on the Structure and the Interactions of the Photon
Jun 3-7, 2019

A LIGHT DARK MATTER PORTAL: THE AXION-LIKE PARTICLE

Federica Giacchino
Laboratori Nazionali di Frascati (LNF), Instituto Nazionale di Fisica Nucleare (INFN), Rome, Italy

Abstract

This article presents the Axion-like Particle (ALP) as a possible candidate for a portal to a light dark sector, with a special focus on the ALP research and phenomenology at accelerators such as PADME (Positron Annihilation into Dark Matter Experiment) at the Laboratori Nazionali di Frascati (LNF) of INFN.

1 Introduction

Cosmological and astrophysical evidence provides proofs of Dark Matter (DM) in a wide range of distance scales. If we assume that DM is a particle, we can affirm that none of the Standard Model (SM) particles is a good candidate. It is believed that Dark Matter is a manifestation of an entire Dark Sector (DS). The DS would be comprised of new particles not charged under SM gauge groups, and possibly new forces, linked with visible sector by a mediator known as *portal*. The simplified models are representative of a broader class of more complex UV-models considering few and relevant parameters, especially the portal, where the new terms in the Lagrangian should be renormalisable, and respect the Lorentz invariance, SM gauge invariance as well as the DM stability. This approach points out the importance of the portal as a door towards the dark sector because it opens the possibility to directly produce the mediator.

As alternative to the most famous candidate, the WIMP[1], the exploration of the hidden sector is well-motivated. Here the DM is lighter and/or much more weakly interacting (*feebly*) than usually

[1]The Weakly Interactive Massive Particle (WIMP) is a particle thermally produced in the early universe, with mass in the range GeV-TeV and annihilation cross-section at electroweak scale in order to produce the observed relic density [1)], $\Omega_{DM} h^2 = 0.1198 \pm 0.0015$.

assumed. These models could be an harbinger of new physics sector at a scales which would be experimentally inaccessible in WIMP searches. Therefore we need a high intensity source to produce light DM particle at a detectable rate. The search for new physics in low mass and coupling range is known as the *low-energy high-precision frontier*.

There are different candidates of portals for sub-GeV dark sectors, according to the nature of the particle [2]. This paper will consider a spin-0 mediator called Axion-like Particle and in particular the ALP production with e^+e^- annihilation at accelerators.

2 The Axion-like Particle

The axion-like particle is a light pseudoscalar particle, singlet under the SM gauge group, with a derivative coupling to the Standard Model. In essence, it is a pseudo Nambu-Goldstone boson of a general new spontaneously broken global symmetry. It is mainly motivated by string theories [3], or proposed in many extensions to the SM to address open problem as Strong-CP Problem [4] or Hierarchy Problem [5], as well as a possible solution for the muon magnetic moment anomaly [6]. It is not necessarily the QCD axion particle, so mass and couplings are independent parameters. For this reason ALPs scan a wide mass range: at masses below MeV scale they can have implications for cosmology and astrophysics [7], at masses larger than MeV scales they have interesting implications for particle physics. Consequently ALPs can have a different role in dark sector: a dark matter as weakly interactive *slim* particle (WISPy) [8] or as portal, respectively. This work will consider the latter hypothesis.

The effective Lagrangian that describes the simplified model considered is

$$\mathcal{L} = \mathcal{L}_{SM} + \frac{1}{2}\partial^{\mu}a\partial_{\mu}a - \frac{1}{2}M_a^2a^2 - \frac{g_{a\gamma\gamma}}{4}aF_{\mu\nu}\tilde{F}^{\mu\nu} - g_{a\psi\bar{\psi}}\partial_{\mu}a\bar{\psi}\gamma_{\mu}\gamma_5\psi + \mathcal{L}_{DM} \tag{1}$$

where the fourth term describes the interaction between the axion-like particle and the photons; $\tilde{F}_{\mu\nu}$ is the dual of electromagnetic strength $F_{\mu\nu}$; and the fifth term, assuming a leptophilic ALP, provides the interaction with the electrons, so $\psi \equiv e$ where e is the electron field[2]. The couplings $g_{a\gamma\gamma}$ and g_{aee}, which are real and dimensionful, and the ALP mass M_a are the free parameters to constraint with accelerators. The DM interaction will not be considered here.

3 ALP Production at accelerators

Over the past few years an increasing interest for experimental searches at accelerators has been given to ALPs in this mass range. In this work an ALP phenomenology in PADME [9] experiment will be described. The PADME setup (for more details about the experimental setup see [10]) is shown in fig.1.

Basically PADME searches the light dark particle (ALP as well as dark photon [9] [11]) using a positron beam on a thin diamond target, detecting the SM photon produced in the annihilation reaction: $e^+e^- \to \gamma + X$ where X is the light dark particle. The experiment aims to measure a peak in the missing mass spectrum for the invisible decay: $M^2_{miss} = (P_{e^+} + P_{e^-} - P_\gamma)^2$ where P_i are the 4-impulse of positron, electron and final photon respectively. The four momenta are reconstructed by knowing initial positron beam energy and position thanks to the active target, and measuring final photon energy and angle of recoiling thanks to 616 BGO crystals of the Electromagnetic Calorimeter (ECAL) and 25 PbF_2 crystals of Small Angle Calorimeter (SAC). The electron and positron coming from background processes,

[2]Developing the partial derivative, the fifth term can be written as $m_e g_{aee} a\bar{e}\gamma_5 e$.

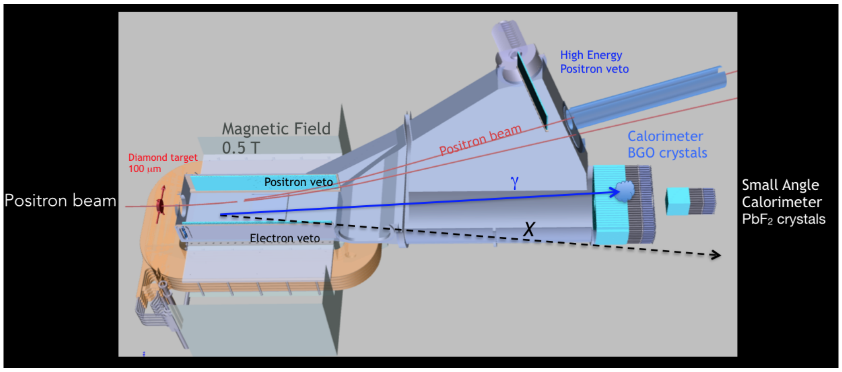

Figure 1: *Schematic view of the PADME setup.*

Bremsstrahlung or Bhabha scattering, or decaying particle, are bended from a dipole magnet of 0.49 T in which is integrated a P/E veto system.

At accelerators, after having produced the ALP from e^+e^- annihilation, two techniques of detection exist based on its mass range: for $M_a < 2M_{DM}$, the ALP decays to 2γ or e^+e^- pair, the so-called *visible* decay. The experimental signature is given by 3γ or a pair of e^+e^- plus an in-time photon; for $M_a > 2M_{DM}$ the ALP decays to DM-DM or for long-lived ALP, the so-called *invisible* decay. The observable of this process is a photon plus missing energy/momentum/mass according to the technique of the experiment.

The strategy for the dark particle identification is model-independent, unless the leptophilic assumption: only one cluster in ECAL, energy between $E_\gamma < 400\,\mathrm{MeV}$ for pile-up and $E_\gamma > 30\,\mathrm{MeV}$ for Bremsstrahlung, no signal in veto system (within $\pm 2\,\mathrm{ns}$), no cluster in SAC with energy above 50 MeV for residual 3γ events.

3.1 Cross-Section of positron-electron annihilation into ALP-photon at PADME

Taking into account the Lagrangian in eq.1, the production of ALP plus one photon from e^+e^- annihilation comes through two different Feynman diagrams: *s-channel* with photon mediator, and *t-* and *u-channel* with electron mediator, see fig.2.

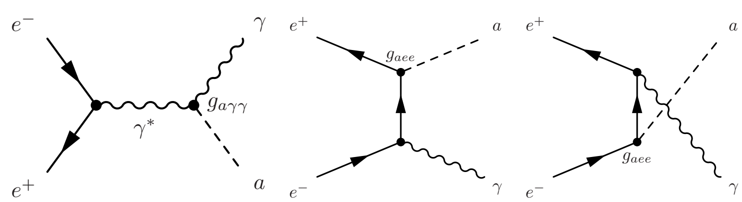

Figure 2: *Feynman diagrams of* $e^+e^- \to a + \gamma$*: (a) s-channel photon mediator; (b) t-channel and (c) u-channel electron mediator.*

The different contributions of the diagrams at the total cross-section are reported in the following plot (fig.3): in the left side the couplings are set to one, in right side the cross-sections are weighting the single contribution with opportune couplings according to the current limits [12) 13)]. In these plots the

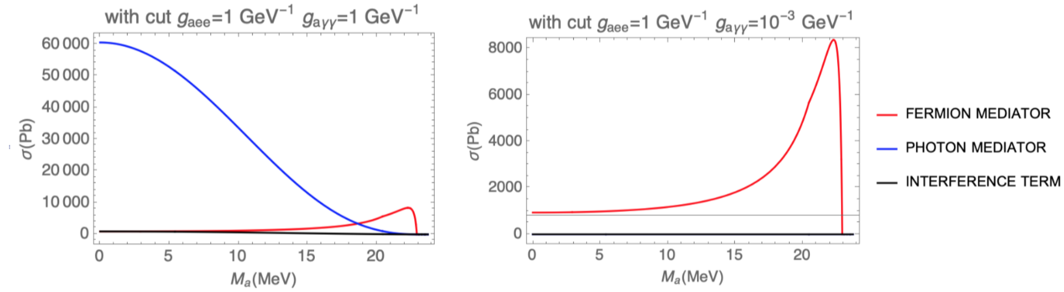

Figure 3: *Cross-sections as a function of the ALP mass setting the energy of the incident positron at* 550 MeV*, angular acceptance* $0.026 < \theta(\text{rad}) < 0.083$ *and photon energy threshold* $E_\gamma > 30\,\text{MeV}$*. "Fermion mediator", "Photon mediator" and "Interference term" corresponds to: left)* $g_{aee} = 1\, g_{a\gamma\gamma} = 0$*,* $g_{aee} = 0\, g_{a\gamma\gamma} = 1$ *and* $g_{aee} = 1\, g_{a\gamma\gamma} = 1$ *respectively, right)* $g_{aee} = 1\, g_{a\gamma\gamma} = 0$*,* $g_{aee} = 0\, g_{a\gamma\gamma} = 10^{-3}$ *and* $g_{aee} = 1\, g_{a\gamma\gamma} = 10^{-3}$ *respectively. All the couplings have dimension* GeV^{-1}.

positron beam energy at 550 MeV, the angular acceptance of ECAL ($0.026 < \theta(rad) < 0.083$) and the threshold gamma energy > 30 MeV are set.

The s-channel diagram would be the dominant contribution at the cross-section at small masses, while the fermion mediator increases more approaching to kinematical limit of $M_a = 23.7$ MeV. But taking into account the current limit on couplings, the fermion mediator is apparently the only relevant channel in all mass range. However $g_{a\gamma\gamma}$ constrians found in literature [12] are a naive recast of previous dark photon data. So a detailed study of detector acceptances and efficiencies is required before closing the parameter space area. The PADME analysis aims to fix direct limits on these couplings.

The probability that a single positron annihilate in the following process $e^+e^- \to \gamma + a$ in PADME is given by $N_e \sigma_{e^+e^- \to a+\gamma} = 6 d_t N_A \frac{\rho}{A} \sigma$, with N_e the total number of electrons in a unit surface area of target. These is found considering $d_t = 100\mu$m target thickness, N_A Avogadro number, $\rho = 3.5\,\text{g/cm}^3$ diamond density, $A = 12$ g/mol atomic mass. Assuming 2-years of data taking at 60% efficiency with bunch length of 200 ns, at 49 Hz and 20k e^+/bunch, we will collect around 10^{13} Positron-on-Target (POT). As is showed in fig.4 for $g_{aee} = 1$ and $M_a = 22$ MeV we expect around 1000 events.

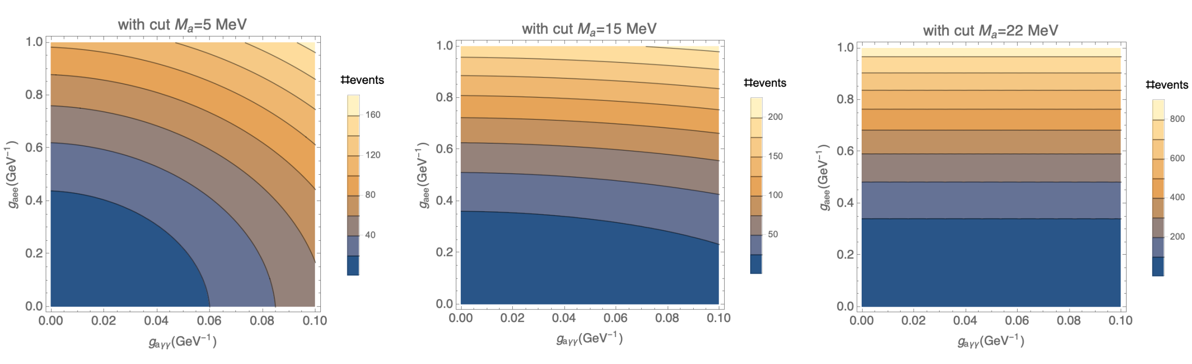

Figure 4: *Values of* g_{aee} *and* $g_{a\gamma\gamma}$ *couplings needed to get the number of events showed in the gradient color for three different ALP masses,* $M_a = 5, 15, 22\,\text{MeV}$.

3.2 ALP decays

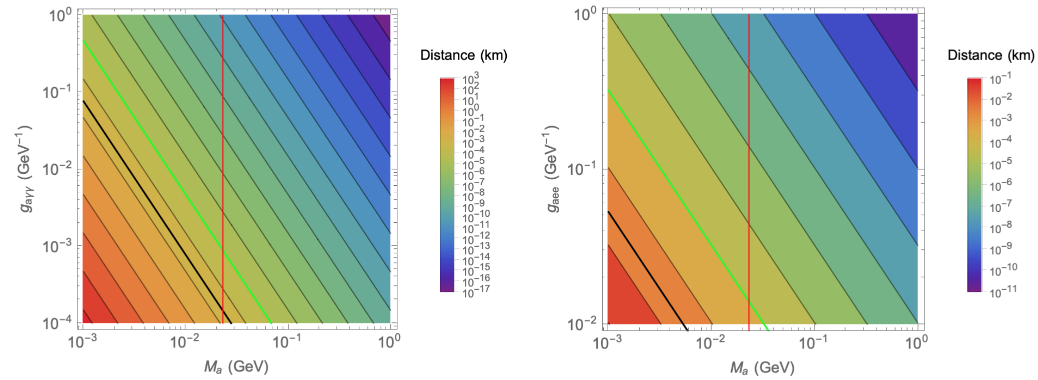

Figure 5: *Parameter Space analysis from ALP decays. Left: the grandient color is the values of decay length from $a \to \gamma\gamma$ for photon-ALP coupling $g_{a\gamma\gamma}$ in function of M_a; Right: the grandient color is the values of decay length from $a \to e^+e^-$ for fermion-ALP coupling g_{aee} in function of M_a. The red line represents the center-of-mass of experiment. The green line is the limit,* $10\,\mathrm{cm}$*, for having the visible decay mode. The black line is the size of experiment,* $3.7\,\mathrm{m}$.

In order to study the phenomenology of ALP in PADME, an analysis of the decay width of ALP in $\gamma\gamma$ and e^+e^- is needed:

$$\Gamma_{a\to\gamma\gamma} = \frac{g^2_{a\gamma\gamma} M_a^3}{64\pi}, \quad \Gamma_{a\to e^+e^-} \simeq \frac{g^2_{aee} M_a m_e^2}{8\pi} \tag{2}$$

Considering the boost $\gamma_a \simeq E_a/M_a$ with E_a the ALP mass, the decay length is $L_{a\to ij} = \gamma_a \hbar c/\Gamma_{a\to ij}$. In fig.5 a parameter scan (couplings vs ALP mass) is showed where the gradient color is the decay length of ALP in km. Only the regions to the left of the red line, the kinematical limit $M_a < 23.7\,\mathrm{MeV}$, are accessible to PADME. For a detector size $L_D = 3.7\,\mathrm{m}$ (black line), in the bottom left corner the ALP leaves the detector before decaying and the invisible decay mode can be explored. Conversely, above the green line (set at $10\,\mathrm{cm}$), the particle decays close to the point of annihilation and the final decay products, such as 2γ or e^+e^- pair, can be easily detected. Unfortunately the PADME veto measures only the absolute value of the momentum and not the direction, consequently the peak in the $M^2_{e^+e^-}$ distribution cannot be reconstructed, but installing a good spectrometer could be a future upgrade of PADME. In the middle region it is difficult to discriminate the signature and a tricky analysis is required.

4 Conclusions

After many years of high-energy accelerators, high-luminosity and ultra-sensitive detectors are investigating new and low energy scales of Dark Sector. A good candidate as pseudoscalar mediator is the axion-like particle. ALP is a generalisation of QCD axion with free mass and couplings. The PADME experiment is testing new physics at MeV-scales and it could produce a light portal, as the ALP, searching a peak in missing mass distribution. The analysis is new because both interactions, with photons and fermions, have been considering. The cross-section of $e^+e^- \to \gamma + a$ suggests that the fermionic mediator gives the dominant contribution since g_{aee} is not strong constrained by current limits. However, even if the photon coupling window is opened only around 10^{-3}, the constraints are only an approximation since they are a recast of dark photon analysis. PADME are exploring directly these regions. PADME is able to produce a relevant number of event. A direct analysis of acceptances is planning through computational tools such as MADGRAPH, and then later, to evaluate the experiment sensitivity for the invisible ALP decays, Monte Carlo simulations with GEANT4 will be performed. Data taking is started at the beginning of October 2018 for four months and we have collected $\sim 10^{12}$ POT. A run II is planned at the end on 2019 in order to reach $\sim 10^{13}$ POT.

5 Acknowledgements

I acknowledge the PADME collaboration. I wish to thank particularly E. Nardi (Laboratori Nazionali di Frascati (LNF), INFN) for very useful discussions, G. Corcella (Laboratori Nazionali di Frascati (LNF), INFN) and L. delle Rose (University of Florence, INFN) for computations.

References

1. **Planck** Collaboration P.A.R. Ade *et al*, Planck 2015 results. XIII. Cosmological parameters, Astron. Astrophys **594** (2019) A13.

2. R. Essig *et al.*, in Community Summer Study 2013: Snowmass on the Mississippi (CSS2013) Minneapolis, MN, USA, July 29-August 6, 2013 (2013).

3. A. Arvanitaki, S. Dimopoulos, S. Dubovsky, N. Kaloper, and J. March-Russell, String Axiverse, Phys.Rev. **D81** (2010) 123530.

4. R. D. Peccei and H. R. Quinn, CP conservation in the Presence of Instantons, Phys. Rev. Lett. **38** (1977) 1440 1443.

5. P.W. Graham, D.E. Kaplan and S. Rajendran, Cosmological Relaxation of the Electroweak Scale, Phys. Rev. Lett. **115** (2015) 221801.

6. W.J. Marciano, A. Masiero, P. Paradisi and M. Passera, Contributions of axionlike particles to lepton dipole moments, Phys. Rev. D **94** (2016) 115033.

7. D. Cadamuro and J. Redondo, Cosmological bounds on pseudo Nambu-Goldstone bosons, JCAP **1202** (2012) 032.

8. P. Arias, D. Cadamuro, M. Goodsell, J. Jaeckel, J. Redondo and A. Ringwald, WISPy Cold Dark Matter, JCAP **06** (2012) 013.

9. M. Raggi and V. Kozhuharov, Proposal to Search for a Dark Photon in Positron on Target Collisions at DAΦNE Linac, Adv. High Energy Phys. **2014** (2014) 959802.

10. C.Taruggi, The PADME experiment at LNF, in this proceeding.

11. R. Essig, P. Schuster and N. Toro, Probing Dark Forces and Light Hidden Sectors at Low-Energy e^+e^- Colliders, Phys. Rev. **D 80** (2009) 015003.

12. M.J. Dolan, T. Ferber, C. Hearty, F. Kahlhoefer and K. Schmidt-Hoberg, Revised constraints and Belle II sensitivity for visible and invisible axion-like particles, JHEP **12** (2017) 094.

13. D. S. M. Alves and N. Weiner, A viable QCD axion in the MeV mass range, JHEP **07**, 092 (2018).

Frascati Physics Series Vol. 69 (2019)
PHOTON 2019 - International Conference on the Structure and the Interactions of the Photon
Jun 3-7, 2019

VERY-FORWARD PHOTON PRODUCTION IN p-p AND p-Pb COLLISIONS MEASURED BY THE LHCf EXPERIMENT

Alessio Tiberio
Università degli Studi di Firenze and INFN, Sesto Fiorentino, Italy
on behalf of the LHCf Collaboration

Abstract

The main purpose of the LHCf experiment is to test the hadronic interaction models used in ground based cosmic rays experiments to simulate air-showers induced by ultra-high-energy cosmic rays in the Earth atmosphere. The LHCf experiment, situated at the LHC accelerator, is composed of two independent detectors located at 140 metres from the ATLAS interaction point (IP1) on opposite sides along the beam axis: the particular position of the detectors allows LHCf to measure neutral particles up to zero-degree with respect to the beam, with a pseudorapidity coverage of $\eta > 8.4$. Each detector is composed by two sampling and position sensitive calorimeters.

In this contribution the latest photon production measurements from LHCf will be compared with the predictions of DPMJET, EPOS, PYTHIA, QGSJET and SIBYLL Monte Carlo event generators, commonly used in air-shower simulations. The photon production cross section in proton-proton collisions at $\sqrt{s} = 13$ TeV and in proton-lead collisions at $\sqrt{s_{NN}} = 8.16$ TeV will be presented, including the preliminary combined analysis with ATLAS. There is not any hadronic interaction model well reproducing all the experimental data measured by the LHCf experiment. However, these data in the very-forward region will be useful in the tuning of the models and consequently reducing the discrepancy between their predictions.

1 Introduction

The LHC-forward experiment (LHCf) has measured neutral particles production in a very forward region in proton-proton and proton-lead collisions at the Large Hadron Collider. The main purpose of LHCf is to improve hadronic interaction models of Monte Carlo (MC) simulations used in cosmic rays indirect measurements. Highest energy cosmic rays can only be detected from secondary particles which are produced in the interaction of the primary particle with nuclei of the atmosphere, the so-called air showers.

Studying the development of air showers, it is possible to reconstruct the type and kinematic parameters of primary particles. To reproduce the development of air showers, MC simulations with accurate hadronic interaction models are needed. Since the energy flow of secondary particles is concentrated in the forward direction, measurements of particle production in the high pseudorapidity region (i.e. small angles) are very important. In the very forward region soft QCD interactions dominates and MC simulations of air showers utilize phenomenological models base on Gribov-Regge theory [1, 2]. Therefore, inputs from experimental data are crucial for the tuning of that models. The LHC accelerator gives the possibility to study a wide range of collision energies, from 0.9 TeV to 13 TeV in the center of mass frame, which corresponds to an energy range in the laboratory frame from 10^{14} eV to 0.9×10^{17} eV. This energy range covers the "knee" region of cosmic rays spectrum, which occurs around 10^{15} eV. Data collected by central detectors with 7 TeV collisions were already used for the tuning of hadronic interaction models widely used in air shower simulations (EPOS-LHC [3], QGSJET II-04 [4] and SIBYLL 2.3 [5]). However, discrepancies between observed data and MC simulations were observed also with these models [6].

2 The Detector

LHCf is composed of two independent detectors, called *Arm1* and *Arm2*. Arm1 is located 140 meters away from ATLAS interaction point (IP1) in the IP8 direction, while Arm2 is placed 140 meters away from IP1 in the opposite direction (toward IP2). Detectors are placed inside Target Neutral Absorber (TAN), where the beam pipe turns into two separates tubes. Since charged particles are deviated by the D1 dipole magnet (which bends colliding beams into the two separate beam pipes), only neutral particles, mainly photons and neutrons, reach the detector.

Each detector is made of two sampling and imaging calorimeters (called *towers* hereafter). Each tower is composed of 16 tungsten layers and 16 scintillator layers to measure the energy deposit and it also contains 4 position sensitive layers. During 0.9 TeV, 2.76 TeV and 7 TeV operations at the LHC, plastic scintillators (EJ-260) were used. Arm1 detector used scintillating fiber (SciFi) to measure position, while Arm2 used silicon microstrip detectors. For 13 TeV operation both detectors were upgraded: all the plastic scintillators were replaced by Gd_2SiO_5 (GSO) scintillators because of their radiation hardness; also the Arm1 SciFi were replaced by GSO bars. In Arm2 the signal of silicon detectors was reduced using a new bonding scheme of the microstrips to avoid saturation of readout electronics due to the higher energy deposit expected at $\sqrt{s} = 13$ TeV.

Transverse cross sections of towers are 20×20 mm^2 and 40×40 mm^2 for Arm1 and 25×25 mm^2 and 32×32 mm^2 for Arm2. Longitudinal dimension of towers is of 44 radiation lengths, which correspond to 1.6 nuclear interaction lengths. Energy resolution is better than 2% for photons above 200 GeV and of about 40% for neutrons. Position resolution for photons is 200 μm and 40 μm for Arm1 and Arm2, respectively, while position resolution for neutrons is of about 1 mm. Smaller tower of each detector is placed on the beam center and covers the pseudo-rapidity range $\eta > 9.6$, while larger tower covers the pseudo-rapidity range $8.4 < \eta < 9.4$. More detailed descriptions of detector performance are reported elsewhere [7, 8, 9, 10].

3 Physics Results With Proton-Proton Collisions At $\sqrt{s} = 13$ TeV

Results for inclusive photon energy spectrum in p-p collisions at $\sqrt{s} = 900$ GeV and 7 TeV have already been published [11, 12]. Proton-proton collisions at $\sqrt{s} = 13$ TeV were produced for the first time in 2015 at LHC. LHCf had a dedicated low-luminosity run from 9th to 13th of June 2015, with an instantaneous luminosity of $0.3 \div 1.6 \times 10^{29}\text{cm}^{-2}\text{s}^{-1}$. The data sample used in this analysis was obtained during the LHC Fill #3855 in a 3-hours run started at 22:32 on July 12. The instantaneous luminosity measured by ATLAS [13] ranged from 3 to 5 $\times 10^{28}\text{cm}^{-2}\text{s}^{-1}$ during this subset of the run. The beams had 29 colliding bunches, an half crossing angle of 145 μrad, a β^* of 19 m, and a pile-up parameter of $\sim$0.01. The integrated luminosity recorded was 0.191 nb^{-1} for both Arm1 and Arm2.

3.1 Photon inclusive energy spectrum

The inclusive energy spectrum of photon produced in p-p collisions at $\sqrt{s} = 13$ TeV [14] is presented in fig.1 for two pseudo-rapidity ranges together with the predictions of DPMJET 3.06 [15, 16], EPOS-LHC, PYTHIA 8.212 [17, 18], QGSJET II-04 and SIBYLL 2.3 hadronic interaction models. The LHCf data lie between MC predictions but there is not an unique model with a good agreement in the whole energy range and in both rapidity regions. In the pseudorapidity range $\eta > 10.94$, QGSJET and EPOS presents a good overall agreement with experimental data; SIBYLL predicts a lower yield of photons, even if it features a shape similar to data; PYTHIA spectrum agrees with data until $\sim$3.5 TeV but become harder at higher energies; DPMJET is generally harder than data. In the pseudorapidity range $8.81 < \eta < 8.99$, EPOS and PYTHIA spectra agree with data until $\sim$3 TeV, while they become harder at higher energies; SIBYLL has a good agreement until $\sim$ 2 TeV, then also it becomes harder than data; QGSJET presents a lower yield of photons, while DPMJET generally predict an harder spectrum than experimental data.

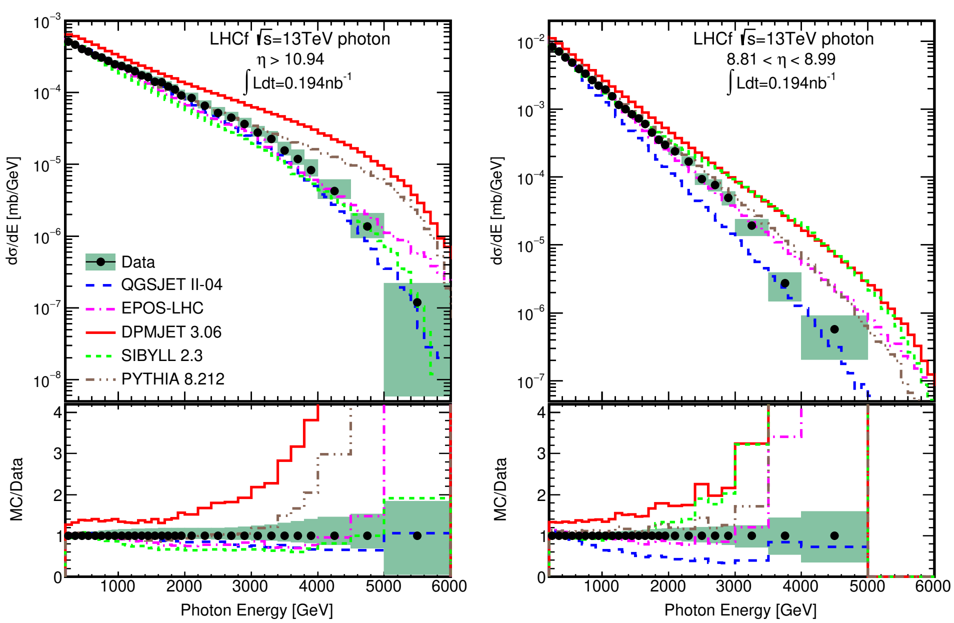

Figure 1: *Photon differential production cross section in the pseudorapidity regions $\eta > 10.94$ (left) and $8.81 < \eta < 8.99$ (right) for p-p collisions at $\sqrt{s} = 13$ TeV. Data are represented by black points while MC prediction from several models are represented by coloured histograms. Green shaded area represents statistical+systematic errors of data. Bottom panels show the ratio of MC predictions to data.*

3.2 LHCf-ATLAS combined analysis

The LHCf experiment alone does not have any information about the type of collision occured at the interaction point. Since 2013 LHCf and ATLAS [19] experiments exchange the trigger signals during LHCf dedicated runs, so it is possible to perform a combined analysis with the event information from both experiments. The number of tracks recorded by ATLAS detectors in the central region can be used to discriminate diffractive events from non-diffractive ones [20]. In particular, selecting events with no charged particles in the region $-2.5 < \eta < 2.5$ a pure sample of low-mass ($M_X < 20$ GeV) diffraction events can be selected.

The preliminary results [21] of the combined analysis are presented in fig.2, where the photon energy spectrum is shown for both the inclusive and the low-mass diffraction component. The diffraction spectrum of EPOS model has a good agreement with data in the $\eta > 10.94$ region, while PYTHIA has a better agreement for $8.81 < \eta < 8.99$.

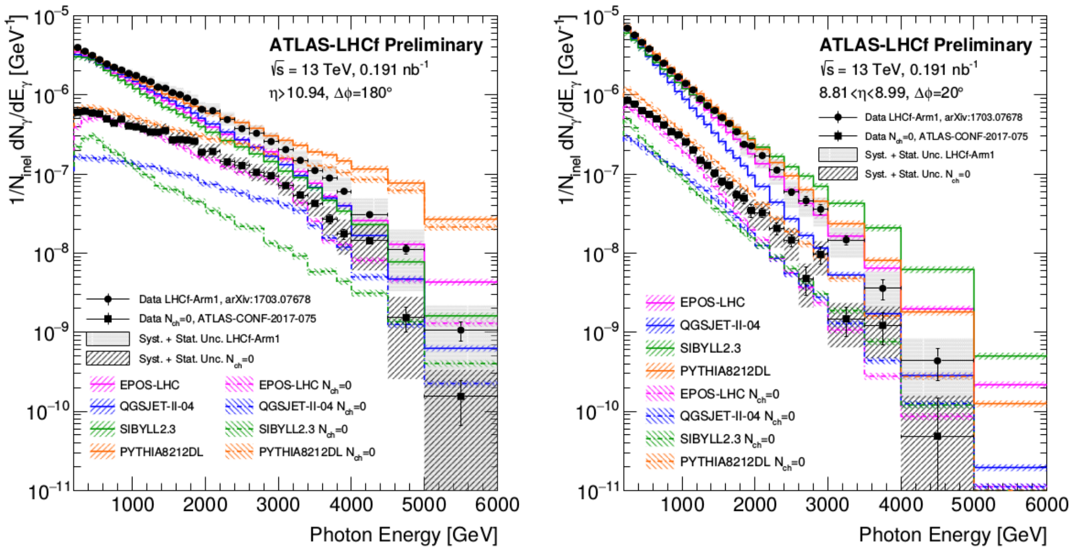

Figure 2: *Photon energy spectrum for pseudorapidity region* $\eta > 10.94$ *(left) and* $8.81 < \eta < 8.99$ *(right). Data are represented by black circles (inclusive) or black squares (low-mass diffraction), while MC predictions are represented by coloured solid (inclusive) or dashed (low-mass diffraction) lines. Hatched areas show statistical+systematic errors for data and statistical errors for MC. All the spectra are normalized to the total number of inelastic collisions.*

4 Physics Results With Proton-Lead Collisions At $\sqrt{s_{NN}} = 8.16$ TeV

A 9-hours-long low luminosity dedicated run for LHCf was performed on the 25th of November 2016 with proton-lead collisions at $\sqrt{s_{NN}} = 8.16$ TeV. Arm2 detector was installed on the proton-remnant side, while Arm1 detector was replaced by ATLAS ZDC. The data sample used to perform the photon production cross section analysis corresponds to an integrated luminosity of 8.1 μb^{-1} ($\sim$ 2 hours of operation). The instantaneous luminosity was $\sim 0.8 \times 10^{28} cm^{-2} s^{-1}$ with a pile-up parameter of 0.01.

The preliminary result of inclusive photon differential production cross section in p-Pb collisions at $\sqrt{s_{NN}} = 8.16$ TeV is presented in fig.3 for two pseudo-rapidity ranges together with the predictions of DPMJET 3.06, EPOS-LHC and QGSJET II-04 hadronic interaction models. Unlike the p-p case, in p-Pb collisions also Ultra Peripheral Collisions (UPC) can occur when the colliding proton interacts with a virtual photon of the strong electromagnetic field of the lead nucleus. UPC are simulated combining STARLIGHT [22] to estimate the virtual photon flux, SOPHIA [23] for low-energy proton-photon collisions, and either DPMJET 3.05 ora PYTHIA 6.428 for high-energy proton-photon collisions. UPC contribution in then added to hadronic interaction models predicitons.

In the $\eta > 10.94$ psedurapidity region EPOS and QGSJET show a good agreement with data while DPMJET predicts an harder spectrum. For $8.81 < \eta < 8.99$ EPOS has a good agreement with data up to 2 TeV, while QGSJET predicts a lower yield and DPMJET an harder spectrum.

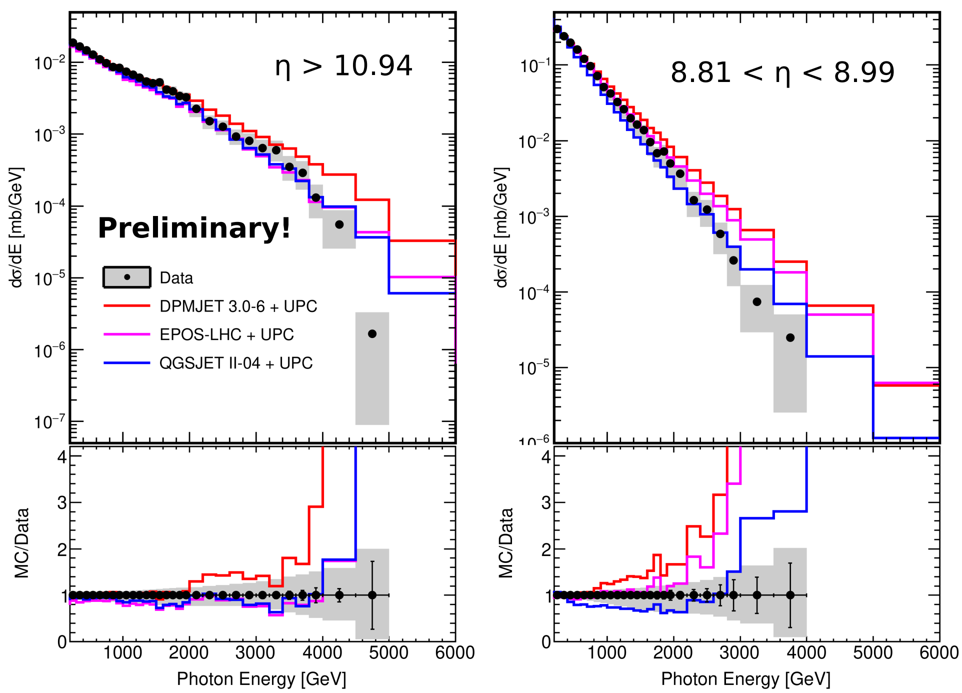

Figure 3: *Preliminary photon differential production cross section in the pseudorapidity regions $\eta > 10.94$ (left) and $8.81 < \eta < 8.99$ (right) for p-Pb collisions at $\sqrt{s_{NN}} = 8.16$ TeV. Data are represented by black points while MC prediction from several models are represented by coloured histograms. Grey shaded area represents statistical+systematic errors of data. Bottom panels show the ratio of MC predictions to data.*

5 Summary

LHCf experiment performed measurements on very forward photon production in proton-proton collisions at $\sqrt{s} = 13$ TeV and proton-lead collisions at $\sqrt{s_{NN}} = 8.16$ TeV at the LHC accelerator. These measurements are necessary to calibrate hadronic interaction models used in cosmic rays physics to understand the development of atmospheric showers. Measured photon inclusive production cross section in both p-p and p-Pb collisions indicates that there is not an unique model representing the data in the pseudorapidity regions $\eta > 10.94$ and $8.81 < \eta < 8.99$. However, the measured data lie between the prediction of DPMJET, EPOS, PYTHIA, QGSJET and SIBYLL hadronic interaction models. EPOS-LHC model has an overall better agreement with data than other models; QGSJET II-04 has a good agreement in the $\eta > 10.94$ region; PYTHIA 8.212 is consistent with data in the low energy region (below $\sim$3 TeV); SIBYLL 2.3 shows a good agreement below $\sim$2 TeV in the $8.81 < \eta < 8.99$ region; DPMJET 3.06 predicts an harder spectrum than data in both the rapidity regions. In the low-mass diffractition event sample selected with the LHCf-ATLAS combined analysis, EPOS has a good agreement in the $\eta > 10.94$ region, while PYTHIA is more accurate for $8.81 < \eta < 8.99$.

References

1. V. Gribov, Sov. Phys. J. Exp. Theor. Phys. **26**, 414 (1968).
2. T. Regge, Nuovo Cimento **14**, 951 (1959).
3. K. Werner, F.-M. Liu, and T. Pierog, Phys. Rev. C **74**, 044902 (2006).
4. S. Ostapchenko, Nucl. Phys. B, Proc. Suppl. **151**, 143 (2006).
5. F. Riehn, Felix *et al.*, PoS ICRC2015 (2016) 558.
6. The Pierre Auger Collaboration, PRL **117** (2016) 192001.
7. O. Adriani *et al.*, JINST **3**, S08006 (2008).
8. O. Adriani *et al.*, JINST **5**, P01012 (2010).
9. Y. Makino, A. Tiberio *et al.*, 2017 JINST **12** P03023.
10. K. Kawade *et al.*, JINST **9**, P03016 (2014).
11. O. Adriani *et al.*, Physics Letters B **703**, 128-134 (2011).
12. O. Adriani *et al.*, Physics Letters B **715**, 298-303 (2012).
13. ATLAS collaboration, Eur. Phys. J. C **76** (2016) 653.
14. O. Adriani *et al.*, Physics Letters B **780** (2018) 233–239
15. F. W. Bopp, J. Ranft, R. Engel, and S. Roesler, Phys. Rev. C **77**, 014904 (2008).
16. R. Engel, J. Ranft, and S. Roesler, Phys. Rev. D **55**, 6957 (1997).
17. T. Sjöstand, S. Mrenna, and P. Skands, J. High Energy Phys. **05** (2006) 026.
18. T. Sjöstand, S. Mrenna, and P. Skands, Comput. Phys. Commun. **178**, 852 (2008).
19. ATLAS Collaboration, The ATLAS Experiment at the CERN Large Hadron Collider, JINST **3** (2008) S08003.
20. Q. D. Zhou *et al.*, Eur. Phys. J. C **77** (2017) no.4, 212
21. The ATLAS and LHCf Collaborations, ATLAS-CONF-2017-075
22. http://starlight.hepforge.org
23. A. Mücke, R. Engel, J. P. Rachen, R. J. Protheroe, and T. Stanev, Comput. Phys. Commun. **124**, 290 (2000).

Frascati Physics Series Vol. 69 (2019)
PHOTON 2019 - International Conference on the Structure and the Interactions of the Photon
Jun 3-7, 2019

RARE AND RADIATIVE DECAYS AT LHCb

Miriam Calvo Gomez
La Salle, Universitat Ramon Llull. Barcelona, Spain
On behalf of the LHCb collaboration

Abstract

Rare and radiative b-hadron decays are sensitive probes of New Physics (NP). One sensitive measurement is the polarisation of the photon emitted in a $b \to s\gamma$ transition, predominantly left-handed in the Standard Model (SM). Recent results by the LHCb collaboration are presented: the first observation of $\Lambda_b^0 \to \Lambda\gamma$ and the time-dependent analysis of $B_s^0 \to \phi\gamma$, which provides constraints on right-handed currents contribution.

1 Introduction

In the Standard Model (SM) of particle physics, the radiative $b \to s\gamma$ transitions proceed via loop Feynman diagrams. The small size of the SM amplitude makes such process sensitive to the contribution of possible new virtual particles that can modify the decay rate or the helicity structure of the vertex. The emitted photons are produced predominantly with left-handed helicity in the SM due to parity violation in the weak interaction, with a small relative right-handed component proportional to the ratio of s- to b-quark masses. In many extensions of the SM, the right-handed component can be enhanced, leading to observable effects, for instance, in mixing-induced CP asymmetries and time-dependent decay rates of radiative B^0 and B_s^0 decays [1, 2, 3]. Figure 1 shows the dominant SM contribution as well as possible NP contributions.

The LHCb experiment has collected data in the first two runs of the Large Hadron Collider (LHC), during 2010-12 (Run 1) and 2015-18 (Run 2). In Run 1, the data sample corresponds to an integrated luminosity around 3 fb^{-1} collected in proton-proton (pp) collisions at center-of-mass energies of 7 and 8 TeV. For Run 2, the integrated luminosity is approximately 6 fb^{-1} and the pp collisions were at 13 TeV. The detector is ideally suited for b-hadron decay measurements due to its high trigger efficiency on the

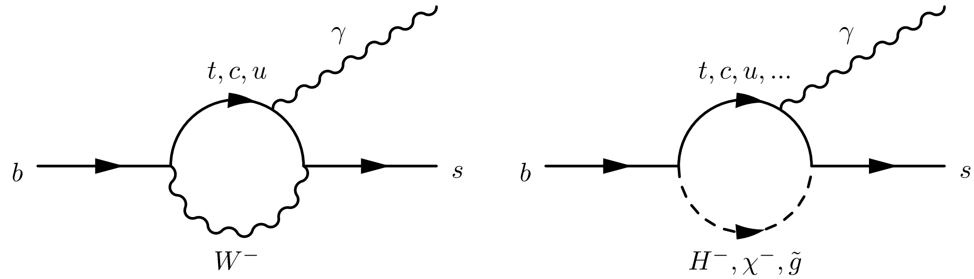

Figure 1: The $b \to s\gamma$ penguin diagram, mediated by SM particles (left) and possible new physics particles (right).

high E_T decay products and displaced vertices, as well as excellent tracking and particle identification performance [4].

Previous LHCb measurements regarding the photon polarisation with radiative decays are: the first observation of photon polarisation in $B^+ \to K^+\pi^+\pi^-\gamma$ decays [5]; the angular analysis of $B^0 \to K^{*0}e^+e^-$ in the low-q^2 region, where the virtual photon contribution is dominant [6], and the time-dependent analysis of $B_s^0 \to \phi\gamma$ decays [7]. Here the two most recent results from the LHCb collaboration are presented: the first observation of $\Lambda_b^0 \to \Lambda\gamma$ decays [8] and an update of the time-dependent analysis of $B_s^0 \to \phi\gamma$ decays [9].

2 First observation of $\Lambda_b^0 \to \Lambda\gamma$

Radiative b-baryon decays had never been observed so far. The study of these transitions offers a unique benchmark to measure the photon polarization due to the non-zero spin of the initial particle [10]. In particular, the $\Lambda_b^0 \to \Lambda\gamma$ decay has been proposed as a suitable mode for the study of the photon polarization [11, 12].

The $\Lambda_b^0 \to \Lambda\gamma$ decay is experimentally challenging to reconstruct. At hadron colliders the Λ_b^0 decay vertex cannot be determined directly due to the long lifetime of the weakly decaying Λ baryon and the unknown photon direction.

The SM prediction of the branching fraction lies in the range $(6–100)\times 10^{-7}$, where the large variation is due to different computations of the $\Lambda_b^0 \to \Lambda$ form factors at the photon pole [13, 14, 15, 16]. A precise measurement of the $\Lambda_b^0 \to \Lambda\gamma$ branching fraction allows discrimination between different approaches to the form-factor computation, and is an important step towards the measurement of the photon polarization in radiative b-baryon decays [17].

Here the first observation of $\Lambda_b^0 \to \Lambda\gamma$ decays is presented, with Λ reconstructed as $p\pi$. The $B^0 \to K^{*0}\gamma$ decay is used as a normalization mode to measure the branching fraction, with K^{*0} reconstructed in the $K^+\pi^-$ final state. The data sample used in this work corresponds to 1.7 fb^{-1} of integrated luminosity collected by the LHCb experiment in 13 TeV pp collisions during 2016. A dedicated reconstruction has been developed to study this mode and a Boosted Decision Tree algorithm is used to reduce the large combinatorial background.

Normalization and signal yields are obtained from a simultaneous extended unbinned maximum likelihood fit to data, shown in Fig. 2. The yields are found to be 65 ± 13 and 32670 ± 290 for $\Lambda_b^0 \to \Lambda\gamma$ and $B^0 \to K^{*0}\gamma$, respectively. The ratio of yields is given by the expression

$$\frac{N(\Lambda_b^0 \to \Lambda\gamma)}{N(B^0 \to K^{*0}\gamma)} = \frac{f_{\Lambda_b}}{f_{B_d}} \times \frac{\mathcal{B}(\Lambda_b^0 \to \Lambda\gamma)}{\mathcal{B}(B^0 \to K^{*0}\gamma)} \times \frac{\mathcal{B}(\Lambda \to p\pi)}{\mathcal{B}(K^{*0} \to K\pi)} \times \frac{\epsilon(\Lambda_b^0 \to \Lambda\gamma)}{\epsilon(B^0 \to K^{*0}\gamma)} \tag{1}$$

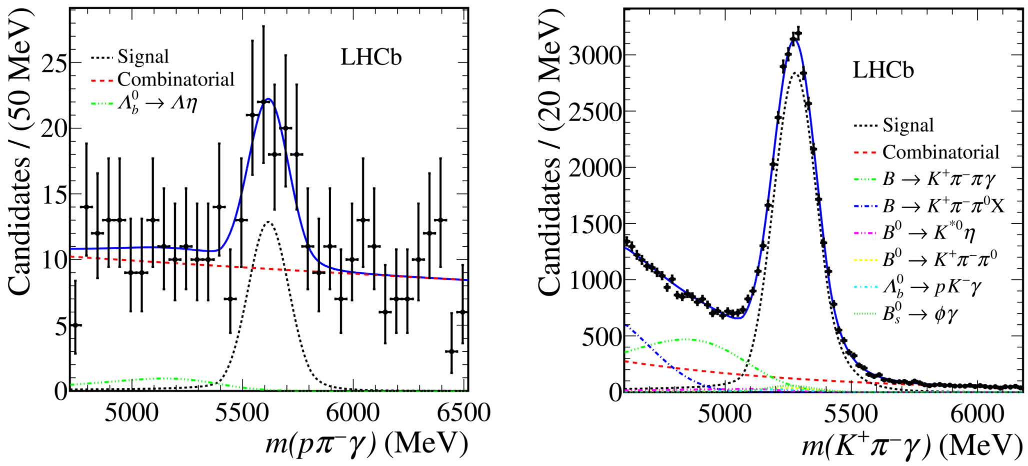

Figure 2: *Simultaneous fit to the (left) $\Lambda_b^0 \to \Lambda\gamma$ and (right) $B^0 \to K^{*0}\gamma$ invariant-mass distributions of selected candidates. The data are represented by black dots and the result of the fit by a solid blue curve while individual contributions are represented in different line styles (see legend).*

where $f_{\Lambda_b}/f_{f_{B_d}}$ is the ratio of hadronisation fractions [18], $\mathcal{B}$ is the branching fraction [19] and ϵ is the combined reconstruction and selection efficiency for the given decay computed from simulation and calibration samples.

The branching fraction of the $\Lambda_b^0 \to \Lambda\gamma$ decay is measured for the first time,

$$\mathcal{B}(\Lambda_b^0 \to \Lambda\gamma) = (7.1 \pm 1.5 \pm 0.6 \pm 0.7) \times 10^{-6}, \tag{2}$$

where the first uncertainty is statistical, the second systematic and the third is the systematic from external measurements, dominated by the ratio of hadronisation fractions. The significance for $\Lambda_b^0 \to \Lambda\gamma$ decays is found to be 5.6 standard deviations.

3 Time-dependent analysis of $B_s^0 \to \phi\gamma$

The decay rate of B_s^0 or $\bar{B}_s^0$ mesons to a CP even final state is given by:

$$\mathcal{P}(t) \propto e^{-\Gamma_s t}\{\cosh(\Delta\Gamma_s t/2) - A^{\Delta}\sinh(\Delta\Gamma_s t/2) + \zeta\, C\cos(\Delta m_s t) - \zeta\, S\sin(\Delta m_s t)\}, \tag{3}$$

where $\Delta\Gamma_s$ and Δm_s are the width and mass differences between the B_s^0 mass eigenstates, defined positively, Γ_s is the mean decay width between such eigenstates, and ζ takes the value of $+1$ (-1) for an initial B_s^0 $(\bar{B}_s^0)$ state. The coefficients A^{Δ} and S are sensitive to the photon helicity amplitudes and weak phases, while C is related to CP violation in the decay. The SM predictions for the three coefficients in the $B_s^0 \to \phi\gamma$ decay are close to zero [3]. The LHCb collaboration had previously measured $A^{\Delta} = -0.98\,^{+0.46}_{-0.52}\,^{+0.23}_{-0.20}$ from a time-dependent flavour-untagged analysis [7], which is compatible with the SM within two standard deviations.

This new analysis represents the first measurement of the CP-violating observables S and C from a radiative B_s^0 decay. An update of the A^{Δ} coefficient measurement is also provided. Results are based on data collected with the LHCb detector in pp collisions at center-of-mass energies of 7 and 8 TeV during the years 2011 and 2012, respectively, corresponding to an integrated luminosity of 3 fb^{-1}. Compared to the previous measurement, the current analysis benefits from a 20% higher event selection efficiency, a reoptimized calorimeter reconstruction and a new photon identification algorithm. Flavour-tagging algorithms [20, 21] are applied to determine the flavour of the initial eigenstate (B_s^0 or $\bar{B}_s^0$), which is essential to measure the S and C observables. The background is subtracted from a fit to the mass distribution of the B_s^0 candidates. A sample of untagged $B^0 \to K^{*0}(892)\gamma$ decays, reconstructed in the flavour-specific $K^{*0} \to K^+\pi^-$ final state, is used to control the decay-time-dependent efficiency, since its lifetime is well measured. Figure 3 shows the mass-fit of the signal and control mode candidates. A total of 5110 ± 90 $B_s^0 \to \phi\gamma$ and 33860 ± 250 $B^0 \to K^{*0}\gamma$ candidates are found.

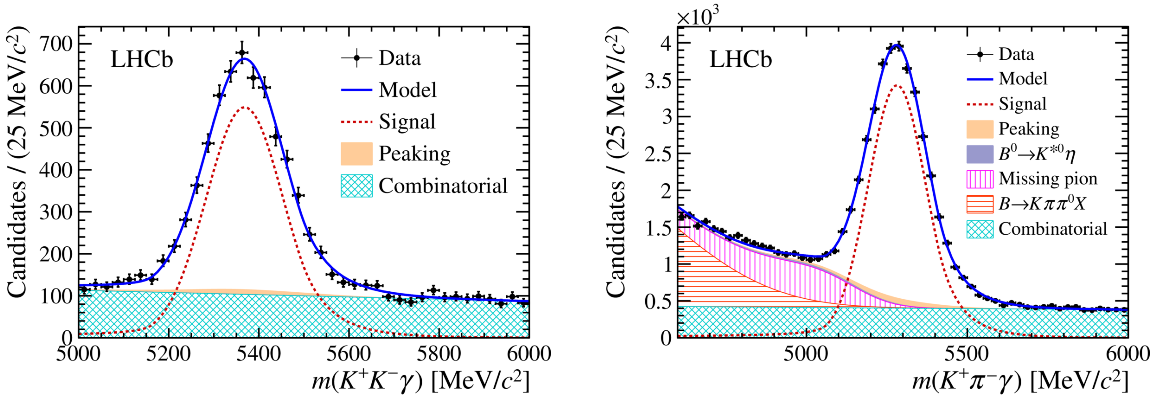

Figure 3: *Fits to the mass distributions of the (left) $B_s^0 \to \phi\gamma$ and (right) $B^0 \to K^{*0}\gamma$ candidates.*

From a simultaneous unbinned fit to the decay-time distributions of $B_s^0 \to \phi\gamma$ and $B^0 \to K^{*0}\gamma$ data samples, the following values are measured

$$S = 0.43 \pm 0.30 \pm 0.11,$$
$$C = 0.11 \pm 0.29 \pm 0.11,$$
$$A^{\Delta} = -0.67\,^{+0.37}_{-0.41} \pm 0.17,$$

where the first uncertainty is statistical (including the external parameters) and the second systematic. The larger systematic uncertainty for A^{Δ} is from the background modelling. For S and C parameters, the larger systematic uncertainties come from the decay-time resolution and the calibration of flavour-tagging algorithms. The fit projections are shown in Fig. 4. The results are compatible with the SM expectation [3] within 1.3, 0.3 and 1.7 standard deviations, respectively. The observables A^{Δ} and S provide constraints on the right-handed currents contribution in $b \to s$ transitions.

4 Summary

Radiative b-decays allow to probe NP at large energy scales through indirect measurements. The photon polarisation can be measured in several ways and allows to puts constraints on righ-handed components. The two lastest results from LHCb have been presented. The branching fraction of the $\Lambda_b^0 \to \Lambda\gamma$ decay is measured for the first time, opening the possibility of measuring the photon polarisation in b-baryon decays. Moreover, the CP-violating and mixing-induced observables S, C and A^{Δ} are measured from a time-dependent analysis of $B_s^0 \to \phi\gamma$ decay, and they are compatible with SM expectations.

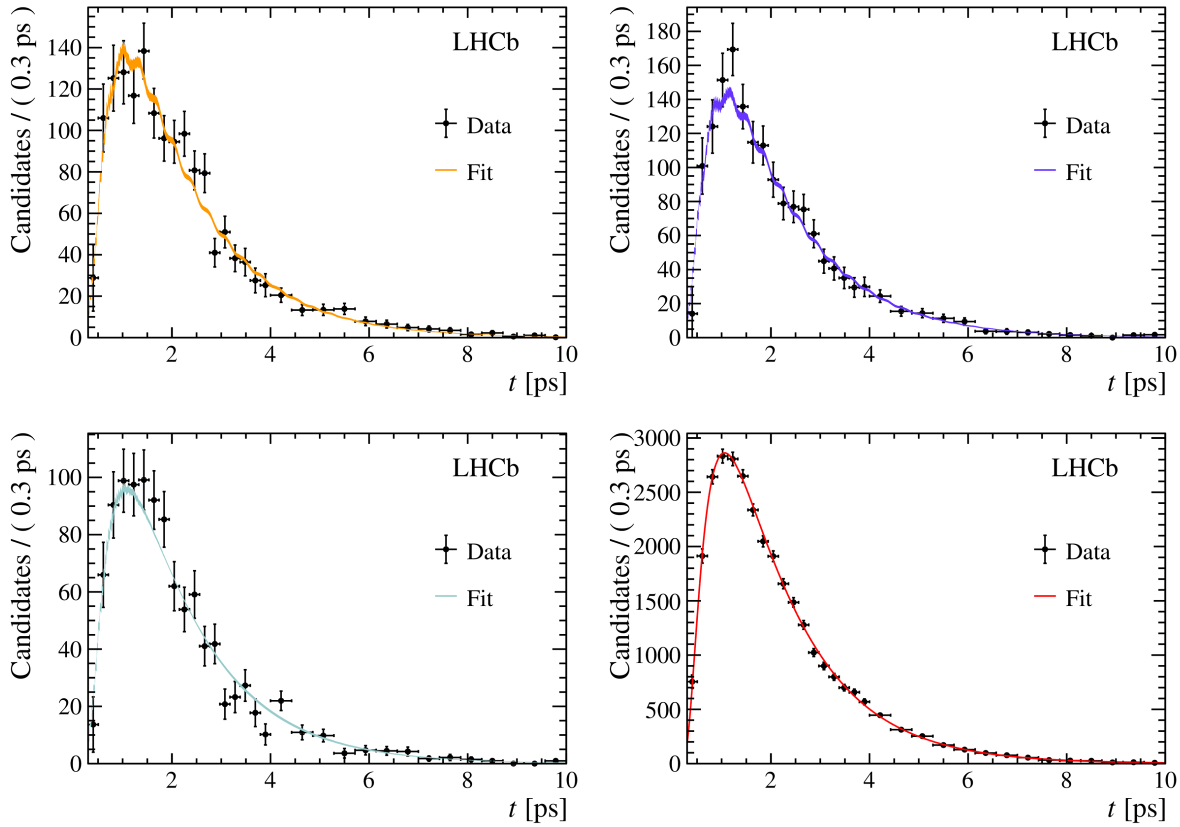

Figure 4: *Decay-time fit projections. The top row corresponds to the tagged (left) $B_s^0 \to \phi\gamma$ and (right) $\bar{B}_s^0 \to \phi\gamma$ candidates, while the bottom plots show the (left) untagged $B_s^0 \to \phi\gamma$ and (right) $B^0 \to K^{*0}\gamma$ candidates. The line is the result of the fit including statistical uncertainties.*

References

1. D. Atwood, M. Gronau, and A. Soni, Mixing-induced CP asymmetries in radiative B decays in and beyond the standard model. Phys. Rev. Lett. **79** 185 (1997).

2. D. Atwood, T. Gershon, M. Hazumi, and A. Soni, Mixing-induced CP violation in $B \to P_1P_2\gamma$ in search of clean new physics signals. Phys. Rev. D **71** 076003 (2005).

3. F. Muheim, Y. Xie, and R. Zwicky, Exploiting the width difference in $B_s^0 \to \phi\gamma$. Phys. Lett. B **664** 174 (2008).

4. The LHCb Collaboration, LHCb detector performance. Int. J. Mod. Phys. A **30**, 1530022 (2015).

5. The LHCb Collaboration, Observation of Photon Polarization in the $b \to s\gamma$ transition. Phys. Rev. Lett. **112** 161801 (2014).

6. The LHCb Collaboration, Angular analysis of the $B^0 \to K^{*0}e^+e^-$ decay in the low-q2 region. JHEP **04** 064 (2015).

7. The LHCb Collaboration, First experimental study of photon polarization in radiative B_s^0 decays. Phys. Rev. Lett. **118** 021801 (2017)

8. The LHCb Collaboration, First observation of the radiative decay $\Lambda_b^0 \to \Lambda\gamma$. Phys. Rev. Lett. **123** 031801 (2019).

9. The LHCb Collaboration, Measurement of the mixing-induced and CP-violating observables of $B_s^0 \to \phi\gamma$ decays. Phys. Rev. Lett. **123** 081802 (2019).

10. M. Gremm, F. Kruger, and L. M. Sehgal, Angular distribution and polarization of photons in the inclusive decay $\Lambda_b^0 \to X_s\gamma$. Phys. Lett. B **355** 579 (1995)

11. T. Mannel and S. Recksiegel, Flavour-changing neutral current decays of heavy baryons. The case $\Lambda_b^0 \to \Lambda\gamma$. J. Phys. G**24** 979 (1998)

12. G. Hiller and A. Kagan, Probing for new physics in polarized Λ_b^0 decays at the Z, Phys. Rev. D**65** 074038 (2002).

13. Y.-M. Wang, Y. Li, and C.-D. Lu, Rare decays of $\Lambda_b^0 \to \Lambda\gamma$ and $\Lambda_b^0 \to \Lambda l^+l^-$ in the light-cone sum rules, Eur. Phys. J. C **59** 861 (2009).

14. T. Mannel and Y.-M. Wang, Heavy-to-light baryonic form factors at large recoil. JHEP **12** 067 (2011).

15. L.-F. Gan, Y.-L. Liu, W.-B. Chen, and M.-Q. Huang, Improved light-cone QCD sum rule analysis of the rare decays $\Lambda_b^0 \to \Lambda\gamma$ and $\Lambda_b^0 \to \Lambda l^+l^-$. Commun. Theor. Phys. **58** 872 (2012).

16. R. N. Faustov and V. O. Galkin, Rare decays $\Lambda_b^0 \to \Lambda l^+l^-$ and $\Lambda_b^0 \to \Lambda\gamma$ in the relativistic quark model, Phys. Rev. D **96** 053006 (2017).

17. L. M. Garcia Martin *et al*, Radiative b-baryon decays to measure the photon and b-baryon polarization. arXiv:1902.04870v2

18. The LHCb collaboration, Measurement of b-hadron fractions in 13 TeV pp collisions. arXiv:1902.06794

19. M. Tanabishi *et al.*, Review of particle physics. Phys. Rev. D**98** 030001 (2018)

20. The LHCb collaboration, A new algorithm for identifying the flavour of B_s^0 mesons at LHCb. JINST **11** P05010 (2016).

21. The LHCb collaboration, Opposite-side flavour tagging of B mesons at the LHCb experiment. Eur. Phys. J. C **72** 2022 (2012).

Frascati Physics Series Vol. 69 (2019)
PHOTON 2019 - International Conference on the Structure and the Interactions of the Photon
Jun 3-7, 2019

INCLUSIVE PHOTON, PHOTON PLUS JETS AND DIPHOTON PRODUCTION MEASUREMENTS FROM ATLAS AND CMS

Ana Cueto, on behalf of the ATLAS and CMS Collaborations
Laboratoire d'Annecy de Physique des Particules (L.A.P.P.)

Abstract

The ATLAS and CMS Collaborations have made public in the last years several measurements of the production of isolated photons in proton-proton collisions. The latest ones at a centre-of-mass energy of $\sqrt{s} = 8$ and 13 TeV are presented.

1 Introduction

Measurements of the production of prompt photons provide useful inputs to test perturbative Quantum Chromodynamics (pQCD) with a hard colourless probe not affected by hadronisation effects. In proton-proton collisions, the production of isolated prompt photons proceeds mainly through the Compton scattering $qg \to q\gamma$ and, thus, it is sensitive to the density of gluons inside the protons. More detailed information for the constraint of the gluon parton density function (PDF) can be obtained by measuring the differential cross sections in different regions of the photon (and jet) rapidity in inclusive photon (photon plus jet) production. Since this process has been measured at different centre-of-mass energies, the ratios of cross sections, in which a significant reduction of the experimental and theoretical uncertainties can be achieved, represent an even more stringent test of the theory.

The production of prompt photons can also proceed through the fragmentation of a parton into a photon. This contribution is greatly suppressed by photon isolation requirements but can become relevant in determined regions of the phase space. When studied in association with jets, the measurements also provide insights to the dynamics of the photon plus jet system which are helpful to validate the description of this process by Monte Carlo (MC) generators or fixed-order calculations.

The photon pair production occurs mainly through quark-antiquark annihilation, $q\bar{q} \to \gamma\gamma$ and the loop process $gg \to \gamma\gamma$ due to the large density of gluons inside the proton. Variables of the diphoton system are sensitive to new physics (like the invariant mass, $m_{\gamma\gamma}$ and the absolute value of the cosine of the scattering angle, $|\cos\theta^{\star}|$), to higher-order corrections (like the opening angle between the photon pair in the azimuthal plane, $\Delta\phi_{\gamma\gamma}$ or the diphoton transverse momentum $p_{\mathrm{T},\gamma\gamma}$) or to soft-gluon emissions (like the transverse component of $p_{\mathrm{T},\gamma\gamma}$ with respect to the thrust axis, a_T and $\phi^{\star}_{\eta} = \tan\left(\frac{\pi-\Delta\phi_{\gamma\gamma}}{2}\right)\sin\theta^{\star}_{\eta}$.

Other Standard Model (SM) rare processes can be measured using photons. One example is the triphoton production. All these processes represent also an important background to beyond the Standard Model searches or other SM processes like the Higgs production decaying into a photon pair.

This manuscript presents the measurement of differential cross sections for inclusive isolated-photon and photon plus jet production at $\sqrt{s} = 13$ TeV reported by the ATLAS [1] and CMS [2] Collaborations [3, 4, 5], the measurement for cross section ratios for inclusive photon production between $\sqrt{s} = 8$ and 13 TeV [6] and measurements of isolated-photon pairs [7] and triphoton [8] production at $\sqrt{s} = 8$ measured with the ATLAS detector.

2 Inclusive photon and photon plus jet by CMS

Differential cross section measurements of inclusive photon production were measured by the CMS Collaboration with a total integrated luminosity of 2.26 fb^{-1} in a fiducial volume determined by photons with transverse momentum (E_{T}^{γ}) greater than 190 GeV, in the central region of the detector $|\eta^{\gamma}| < 2.5$ and isolated. The isolation requirement was implemented in a cone of radius $\Delta R = \sqrt{(\Delta\phi)^2 + (\Delta\eta)^2} = 0.4$ by imposing a maximum value of the sum of p_{T} of all particles inside the cone to be less than 5 GeV. For the photon plus jet measurements the described fiducial region was constrained to have a leading jet with $p_{\mathrm{T}}^{\mathrm{jet}}$ larger than 30 GeV and rapidity $|y^{\mathrm{jet}}| < 2.4$. The measurements of the inclusive-photon differential cross section were reported in four different regions of the photon rapidity, namely $|\eta^{\gamma}| < 0.8$, $0.8 < |\eta^{\gamma}| < 1.44$, $1.57 < |\eta^{\gamma}| < 2.1$ and $2.1 < |\eta^{\gamma}| < 2.5$. The photon plus jet differential cross sections measurement uses two ranges of the photon rapidity, namely $|\eta^{\gamma}| < 1.44$ and $1.57 < |\eta^{\gamma}| < 2.5$, and two regions of the jet rapidity, $|y^{\mathrm{jet}}| < 1.5$ and $1.5 < |y^{\mathrm{jet}}| < 2.4$.

The hadronic background was reduced by imposing criteria on the energy measured in the hadronic calorimeter, photon isolation and shower shape discriminating variables based on the characteristics of the photon energy deposits in the electromagnetic calorimeter. The background from electrons faking photons was suppressed by imposing tracking criteria. The residual hadronic background was subtracted using a boosted decision tree (BDT) utilising the photon kinematic variables, shower shapes information and the median energy density of the event as discriminating variables. The distributions of the BDT scores were used in a two-template binned likelihood fit to estimate the photon yield in each bin of η^{γ} and E_{T}^{γ}. The unfolding to particle level was perfomed though an iterative bayesian unfolding method.

The total systematic uncertainty without the luminosity uncertainty ranges between 5–8% in the central regions and increases to 9–17% in the forward regions. It is dominated by differences in the selection efficiency between data and MC simulations and the migrations in E_{T}^{γ} due to the uncertainties on the photon energy scale and resolution. The luminosity uncertainty is 2.3%.

The unfolded measurements were compared with the next-to-leading order (NLO) predictions from JetPhox using the NNPDF3.0NLO PDF set and BFG II photon fragmentation functions. The total theoretical uncertainty was estimated by adding in quadrature the uncertainties on the missing higher orders, the PDF- and α_s-induced uncertainties and the uncertainties on the extrapolation between particle and parton level. Fig. 1(a) shows the differential cross sections for the photon plus jet production compared to the NLO predictions of JetPhox in different regions of $|\eta^{\gamma}|$ and $|y^{\mathrm{jet}}|$. An adequate description of the measurement is provided by the NLO calculations within the experimental and theoretical uncertainties.

2.1 Inclusive photon by ATLAS

The measurement of inclusive photon production [4] was performed using data recorded by the ATLAS detector during 2015 corresponding to a total integrated luminosity of $\mathcal{L} = 3.2$ fb^{-1}. The measurements were unfolded to a fiducial volume given by $E_{\mathrm{T}}^{\gamma} > 125$ GeV, $|\eta^{\gamma}| < 2.37$ avoiding the crack region of the ATLAS detector ($1.37 < |\eta^{\gamma}| < 1.56$) and an isolation criteria imposed to the photon in which the transverse energy of all particles in a cone of radius $R = 0.4$ around the photon was limited to $E_{\mathrm{T}}^{\mathrm{iso}} < 0.0042 E_{\mathrm{T}}^{\gamma} + 4.8$ GeV. The differential cross sections were measured as functions of E_{T}^{γ} in four different regions of $|\eta^{\gamma}|$.

Photon candidates were required to satisfy photon identification requirements based on several shower shape variables and be isolated from additional energy in the calorimeters. The isolation criterion imposed at reconstruction level was the same one that defines the fiducial volume. After identification and isolation requirements a residual background coming mainly from jets misidentified as photons remains in the signal region. This remaining background was removed through the data-driven 2D-sideband method. The background from electrons faking photons was estimated using MC samples and was found to be negligible. The estimated signal yields were then unfolded to particle level using a bin-by-bin unfolding.

Several sources of systematic uncertainties were taken into account. Among them, the leading ones were the uncertainty on the photon energy scale and resolution, the uncertainty on the photon identification efficiency and the uncertainty on the assumption of uncorrelation between the photon isolation and identification variables for the background subtraction. The total systematic uncertainty was obtained as the sum in quadrature of all the uncertainties considered and amounts to $\sim 5\%$.

Fig. 1(b) shows the ratio of the measured unfolded cross sections compared to JetPhox using different PDF sets. The NLO calculations provide an adequate description of the data within uncertainties. The theoretical uncertainties tend to be much larger than the experimental ones in the regions where the measurements are not limited by statistics. Recently comparisons of these data with calculations at next-to-next-to-leading order (NNLO) can be found in [9] showing a better description of the distributions within the reduced theoretical uncertainties.

2.2 Inclusive photon cross-section ratios by ATLAS

As mentioned in Sec. 2.1, the size of the theory uncertainties limited the comparison between theory and data in inclusive photon measurements. Another venue, apart from going to higher orders, to be able to perform a more detailed test of the theory is measuring cross-section ratios. The measurements reported in [4] and [10] of inclusive photon production at $\sqrt{s} = 13$ and 8 TeV were performed in an overlapping phase-space region and following a very similar analysis strategy which eased the combination of the measurements. Furthermore, given that the measurement at 13 TeV was performed at the beginning of Run 2, many systematic uncertainties were extrapolated from those at 8 TeV or followed the same strategy for its estimation making clearer the correlation between both $\sqrt{s}$ in the measurement of the ratio of cross sections, $R_{13/8}^{\gamma}$.

The systematic uncertainties were treated as correlated between the different centre-of-mass energies when it was well justified. This affected the main uncertainty at both $\sqrt{s}$, the photon scale uncertainty. The uncertainty of the photon energy scale in the ratio of cross sections was no longer dominant in the whole phase space but comparable in size to other uncertainties. However, the luminosity uncertainty in the ratio, with a size of 2.8%, played a significant role.

To avoid the effect of the luminosity uncertainty, an additional measurement of the double ratio, $D^{\gamma/Z}_{13/8}$, of $R^{\gamma}_{13/8}$ over the ratio of the fiducial cross section for Z boson production at $\sqrt{s} = 13$ and 8 TeV was measured. The ratio of Z boson production was reported in [11] and has a value of $1.537 \pm 0.001(\text{stat}) \pm 0.01(\text{syst}) \pm 0.044(\text{lumi})$. The systematic uncertainties were treated as uncorrelated between the two processes, except for the luminosity uncertainty which cancels out in the ratio.

The predictions for $R^{\gamma}_{13/8}$ were obtained using JetPhox. All the theoretical uncertainties were treated as correlated between both $\sqrt{s}$. For $D^{\gamma/Z}_{13/8}$, the predictions of the Z ratio were computed using the Dyturbo program at NNLO accuracy. For the double ratio, the uncertainties arising from the variations of the scales were treated as uncorrelated for the different processes. A large reduction of the theoretical uncertainties was achieved compared to those of the individual inclusive photon predictions using this correlation scheme. They were reduced from a $10-15\%$ to a $2-4\%$.

Fig. 1(c) shows the ratio $D^{\gamma/Z}_{13/8}$ for the most central region of $|\eta^{\gamma}|$ with predictions from different PDF sets. Unfortunately, the main differences between PDF sets occur in the region of the phase space dominated by the statistical uncertainty. The predictions provide a good description of the ratios within the reduced uncertainties representing a very stringent and successful test of pQCD.

2.3 Photon plus jet by ATLAS

For this measurement, a more exclusive phase space than that used in the inclusive measurement described in Section 2.1 was explored while the same dataset was used. In addition to the requirements of the inclusive photon measurement, events were required to have a jet with $p_{\text{T}}^{\text{jet}} > 100$ GeV, $|y^{\text{jet}}| < 2.37$ and separated from the photon with $\Delta R_{\gamma-\text{jet}} < 0.8$. The isolation requirement at particle level corresponded to $E_{\text{T}}^{\text{iso}} < 0.0042 E_{\text{T}}^{\gamma} + 10$ GeV. The differential cross sections were measured as a function of E_{T}^{γ}, $p_{\text{T}}^{\text{jet}-\text{lead}}$, $\Delta\phi^{\gamma-\text{jet}}$, $m^{\gamma-\text{jet}}$ and $|\cos\theta^{\star}| = \tanh(\frac{\Delta y^{\gamma-\text{jet}}}{2})$.

The sources of experimental systematic uncertainties included also the jet energy scale and resolution, that is the dominant uncertainty in the measurement.

The measurements were compared to the fixed-order NLO predictions from Jetphox and the ME+PS@NLO QCD predictions from the Sherpa 2.2 generator as shown in Fig. 1(d) for $p_{\text{T}}^{\text{jet}}$. The latter include matrix elements of $\gamma + 1, 2$ partons at NLO accuracy and $\gamma + 3, 4$ partons at LO accuracy using a smooth-cone isolation for the photon at matrix-element level. The predictions agree with the measurements within the theoretical uncertainties. However, there are some regions of the phase space in which the predictions tend to overestimate the data. The disagreement disappears once higher-order corrections are included in the calculations as shown in [9].

3 Multi-photon measurements by ATLAS

In this section, two measurements of di- and triphoton production reported by the ATLAS Collaboration are presented. Both measurements used data collected at $\sqrt{s} = 8$ TeV with a total integrated luminosity of $\mathcal{L} = 20$ fb^{-1}.

3.1 Diphoton production

The production of photon pairs was studied as a function of several observables as described in the introduction. The leading (subleading) photon was required to have $E_{\text{T}}^{\gamma} > 40$ (30) GeV and fall in a region of $|\eta^{\gamma}| < 2.37$ avoiding the crack region of the detector. Both photons were required to be isolated with $E_{\text{T}}^{\text{iso}} < 11$ GeV and separated in the $\eta - \phi$ plane by $\Delta R_{\gamma\gamma} < 0.4$.

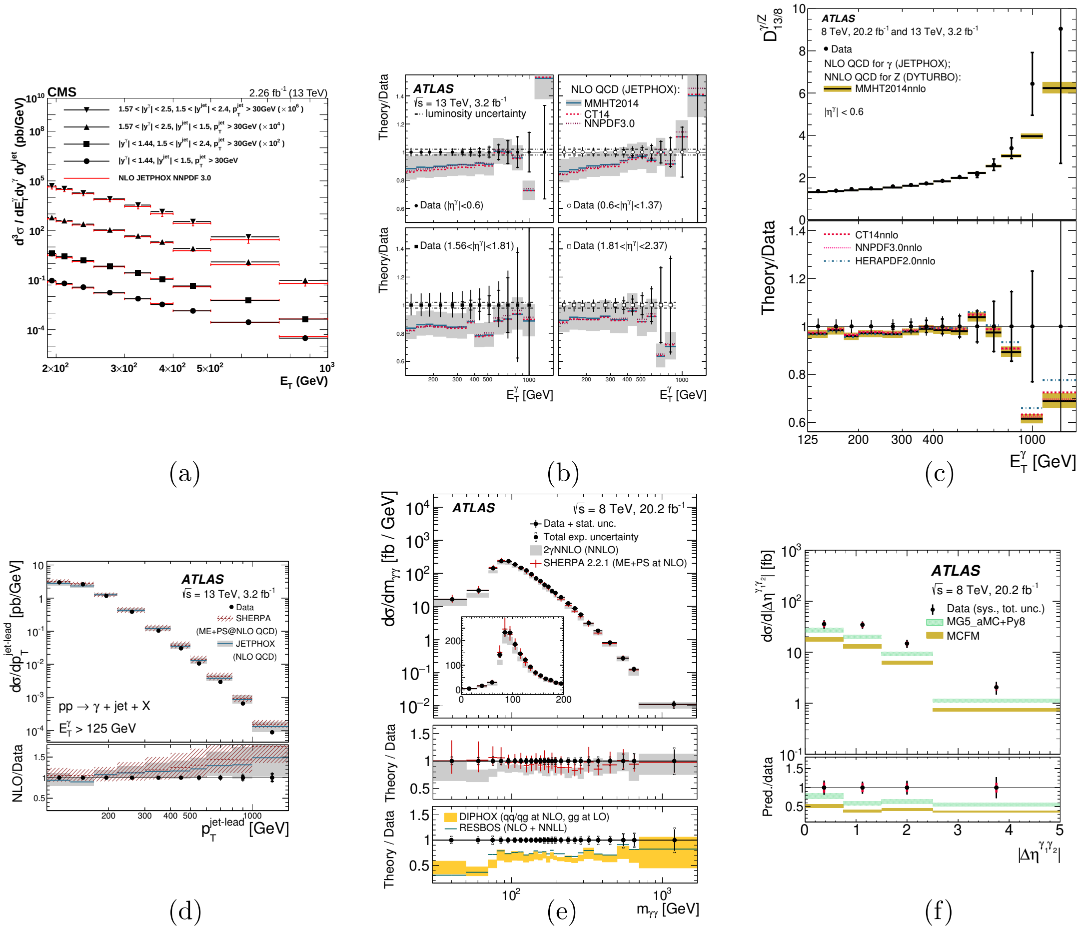

Figure 1: *Representative distributions from each of the measurements presented: (a) from [3], (b) from [4], (c) from [6], (d) from [5], (e) from [7] and (f) from [8]. See the text from description.*

After identification and isolation requirements, the signal yields are extracted using a data-driven two-dimensional template fit method consisting of an extended maximum-likelihood fit to the two-dimensional distributions of the calorimeter isolation variables of the photon pair passing the selection. The background from electron faking photons was also estimated in a data-driven way. The contribution from the Higgs boson was found to be negligible. The signal purity ranges from 60 to 98% across the bins of the various observables. The measurements were unfolded to particle level using an iterative Bayesian unfolding method.

The systematic uncertainties are dominated by the photon identification efficiency and the total uncertainty for the fiducial cross section measurements is around $\sim 5\%$.

The predictions from different generators were compared against the differential cross section measurements. Fig. 1(e) shows the differential cross sections for $m_{\gamma\gamma}$. The fixed-order NLO calculations from DIPHOX are not able to reproduce the data, the improvement brought by RESBOS including a resummation of the leading logarithms at next-to-next-leading-logarithmic accuracy is not enough in many regions of the phase space. The NNLO calculations from 2γNNLO are able to describe better the normalization of the data but fails to describe the shape of some observables. The ME+PS@NLO QCD predictions from SHERPA merging matrix elements for $\gamma\gamma + 0, 1$ parton at NLO and $\gamma\gamma + 2, 3$ partons at LO provide the best description of the data.

3.2 Triphoton production

The differential cross sections of three isolated photon production were measured as a function of several observables including the transverse momentum of each of the photons, invariant masses and angular distributions of the photons. The leading, subleading and subsubleading photons were required to have a transverse momentum larger than 27, 25 and 15 GeV respectively and fall in the central region of the detector. Photons were required to be isolated with $E_{\mathrm{T}}^{\mathrm{iso}} < 10$ GeV and separated from each other with $\Delta R_{\gamma\gamma} < 0.45$. Additionally, the invariant mass of the triphoton system was required to be larger than 50 GeV.

As in the previous measurements, the residual background after imposing isolation and identification criteria was subtracted using an extended 2D-sideband method for the three-photon case and using a likelihood approach to extract the signal yields. The electron background was estimated from MC samples and corresponds to a (6.5±0.2)% of the selected events. The typical value of the signal purity was found to be 55%. The signal yields were unfolded to particle level using a bin-by-bin unfolding technique.

The total systematic uncertainty for the fiducial cross section is 13% and is dominated by the photon identification efficiency and the uncertainties on the background subtraction.

The differential cross sections were compared against the fixed-order NLO predictions from MCFM and the NLO+PS predictions from MadGraph5+Pythia8 as in Fig. 1(e) for $|\Delta\eta^{\gamma_1\gamma_2}|$. Although both calculations underestimate the data, the predictions from MadGraph are closer to the data and describe better the shape of the angular observables. Higher-order predictions are needed to achieve a better description of this process.

Acknowledgement

This work was supported by the French Agence Nationale de la Recherche under the project "Photon-Portal" (ANR-16-CE31-0016).

References

1. ATLAS Collaboration, 2008 JINST 3 S08003
2. CMS Collaboration, JINST **3**, S08004 (2008).
3. CMS Collaboration, Eur. Phys. J. C **79** (2019) no.1, 20 [arXiv:1807.00782 [hep-ex]].
4. ATLAS Collaboration, Phys. Lett. B **770**, 473 (2017) [arXiv:1701.06882 [hep-ex]].
5. ATLAS Collaboration, Phys. Lett. B **780**, 578 (2018) [arXiv:1801.00112 [hep-ex]].
6. ATLAS Collaboration, JHEP **1904**, 093 (2019) [arXiv:1901.10075 [hep-ex]].
7. ATLAS Collaboration, Phys. Rev. D **95**, no. 11, 112005 (2017) [arXiv:1704.03839 [hep-ex]].
8. ATLAS Collaboration, Phys. Lett. B **781**, 55 (2018) [arXiv:1712.07291 [hep-ex]].
9. X. Chen, T. Gehrmann, N. Glover, M. Höfer and A. Huss, [arXiv:1904.01044 [hep-ph]].
10. ATLAS Collaboration, JHEP **1608**, 005 (2016) [arXiv:1605.03495 [hep-ex]].
11. ATLAS Collaboration, JHEP **1702**, 117 (2017) [arXiv:1612.03636 [hep-ex]].